Computational Fluid Dynamics-Based Fire-Side Modeling of Steam Cracking Furnaces

Yu Zhang

Promotors: Prof K. Van Geem, PhD, Prof G. B. Marin, PhD, Prof F. Qian, PhD
Doctoral thesis submitted in order to obtain the academic degrees of
Doctor of Chemical Engineering (Ghent University) and
Doctor of Process System Engineering (East China University of Science and Technology)

GHENT
UNIVERSITY

Department of Materials, Textiles and Chemical Engineering
Head of Department: Prof P. Kiekens, PhD
Faculty of Engineering and Architecture

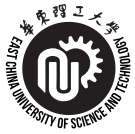

Department of Automation
Head of Department: Prof Z. Sun, PhD
School of Information Science and Engineering

Academic year 2016 - 2017

ISBN 978-94-6355-002-4
NUR 952
Wettelijk depot: D/2017/10.500/37

Promotoren:

prof. dr. ir. Guy B. Marin

Laboratorium voor Chemische Technologie

Vakgroep Materialen, Textiel en Chemische Proceskunde

Universiteit Gent

prof. dr. ir. Kevin M. Van Geem

Laboratorium voor Chemische Technologie

Vakgroep Materialen, Textiel en Chemische Proceskunde

Universiteit Gent

prof. dr. ir. Feng Qian

State Key Laboratory of Chemical Engineering

Department of Chemical Engineering

East China University of Science and Technology

Decaan: Prof. dr. ir. Rik Van de Walle

Rector: Prof. dr. Anne De Paepe

De auteur genoot tijdens de onderzoeksactiviteiten de financiële steun van de BOF Bilateral Scientific Cooperation (ECUST/LCT) en het China Scholarship Council (CSC).

EXAMENCOMMISSIE

Leescommissie

Prof. dr. ir. Xing-Gui Zhou
State Key Laboratory of Chemical Engineering
Department of Chemical Engineering
East China University of Science and Technology

Prof. dr. ir. Geraldine Heynderickx
Laboratorium voor Chemische Technologie
Vakgroep Materialen, Textiel en Chemische Proceskunde
Faculteit Ingenieurswetenschappen en Architectuur
Universiteit Gent

Prof. dr. ir. Bénédicte Cuenot
CFD/Combustion group
Centre Européen de Recherche et de Formation Avancée en Calcul Scientifique

Dr. ir. Ivana Stankovic
Mechanica van Stroming, Warmte en Verbranding
Faculteit Ingenieurswetenschappen en Architectuur
Universiteit Gent

Andere leden

Prof. dr. ir. Kevin Van Geem [promotor]
Laboratorium voor Chemische Technologie
Vakgroep Materialen, Textiel en Chemische Proceskunde
Faculteit Ingenieurswetenschappen en Architectuur
Universiteit Gent

Prof. dr. ir. Guy B. Marin [promotor]
Laboratorium voor Chemische Technologie
Vakgroep Materialen, Textiel en Chemische Proceskunde
Faculteit Ingenieurswetenschappen en Architectuur
Universiteit Gent

Prof. dr. ir. Feng Qian [promotor]
State Key Laboratory of Chemical Engineering
Department of Chemical Engineering
East China University of Science and Technology

Prof. dr. ir. Luc Taerwe [voorzitter]
Vakgroep Bouwkundige Constructies
Universiteit Gent

Acknowledgements

I would like to thank my domestic superior prof. dr. ir. Feng Qian for offering me a chance to be a doctoral researcher in East China University of Science and Technology. This later turns out to be a starting point of all the great days that I had during these years.

I would like to thank my promotors prof. dr. ir. Guy B. Marin and prof. dr. ir. Kevin M. Van Geem for giving me such a great opportunity to carry out research in Ghent University. My life of being a Ph.D. candidate would be completely different if I had never come to Belgium. Thank you for your guidance and examination throughout my thesis.

It is a great pleasure for me to have a double doctoral diploma from both UGent and ECUST. I would like to thank prof. dr. ir. Guy B. Marin, prof. dr. ir. Kevin M. Van Geem, prof. dr. ir. Feng Qian and prof. dr. ir. Wenli Du for putting a lot of efforts and reaching an agreement on this.

Ph.D. was never an easy ride but sometimes challenging. During my research, I had received a lot of help from many of my colleagues. Thanks go to Dr. Hu for leading me to the first glance of computational fluid dynamics. I also would like to thank Carl for his help with furnace simulations and my first publication. Discussions with David were often quite helpful no matter in the office or in the car back home. With respect to the convection section modeling, I thank Ismaël, Pieter V., Pieter R. and Andrés for offering many ideas to improve the code and Jühl for working together with me on it. Andrés is again thanked for your kindness cooperation in the COILSIM1D interactions between ECUST and UGent. I should not forget to thank prof. dr. ir. Kevin M. Van Geem for the freedom and encouragement that you gave me to explore new aspects. Special thanks come in the last to Pieter R. for quite some great discussions and shared experiences in various aspects directly or indirectly

relevant to my research. Thank you for taking care of many things when I was not in Ghent, especially during the recent days.

I would like to mention Ezgi and David for being my ‘office mate’ throughout my stay in Ghent. Thank you for the cheerful daily conversions we had together. I also would like to thank Natália, Laurien, Jens, Shekhar, Christina, and Diana. It was nice to have you in the office. Many thanks go to my other colleagues in LCT for the talks and laughs during lunch and coffee breaks, advices in research and life: Pieter R., Andrés, Amit, Ana, Hassan, Kaustav, Maria, Panos, Jelena, Marita, Max, Sri Bala, Stamatis, Marko, Nenad, Arturo, Konstantinos, Alexander, Pieter V., Ruben V.d.V., Ruben D.B., Carl, Nick, Thomas, Ismaël, Jiawei, Lukas, Songjun, Aditya D., Pieter D., Alper, Luis, Chanakya, Tapas, Gonzalo, Daria, Gilles, Georges, Nils, Vaios, Gaoping… I also would like to thank my colleagues Chaochun, Zhi, Xin, and Bin in ECUST.

It was a great journey to Belgium, which offered me the opportunities to meet a lot of great people. I would like to thank Hong, Zhimiao, Rik, Eva, Ning, and Bill. You gave me so many supports and joyfulness during my stay in Ghent, and most importantly, good friendships that I will always appreciate. Thanks also go to David and Roshanak for many dinner invitations and a fantastic wedding. Yunpeng is thanked for being a kindness and reliable flat mate, and tour pal as well. Thanks again to all of you for making my life brighter. I wish you a better future!

My special thanks go to Cindy, my girlfriend. Thank you for being with me. The days and moments we shared were so unique and unforgettable!

Last, I would like to send my most sincere thanks to my parents. Your love and support have always been the best gift I have ever received!

Yu Zhang
Ghent 2017

Contents

Notations

Roman

A	surface area	[m²]
A	eddy dissipation model constant, $A = 4.0$	[-]
A	band absorptance	[m^{-1}]
A^*	dimensionless band absorptance	[-]
A_{eff}	effective geometrical factor	[-]
a_i	weight factor of fictitious gray gas i	[-]
a_1	SST k-ω model constant, $a_1 = 0.31$	[-]
B	eddy dissipation model constant, $B = 0.5$	[-]
b	EWBM pressure parameter	[-]
$b_{i,j}$	EWBM temperature coefficient	[-]
C	species concentration	[mol m^{-3}]
C	production capacity	[kt h^{-1}]
C_{D1}	DEC model constant, $C_{D1} = 0.134$	[-]
C_{D2}	DEC model constant, $C_{D2} = 0.5$	[-]
C_2	constant for Planck function, $C_2 = 1.4388 \times 10^{-2}$	[m K]
C_2	Realizable k-ε model constant, $C_2 = 1.9$	[-]
$C_{1\varepsilon}$	RNG k-ε model constant, $C_{1\varepsilon} = 1.42$	[-]
$C_{2\varepsilon}$	RNG k-ε model constant, $C_{2\varepsilon} = 1.68$	[-]
C_μ	RNG k-ε model constant, $C_\mu = 0.0845$	[-]
c_p	heat capacity	[J mol^{-1} K^{-1}]
$D_{i,m}$	mass diffusion coefficient of species i	[m^2 s^{-1}]
$D_{T,i}$	thermal diffusion coefficient of species i	[kg m^{-1} s^{-1}]
d	inner diameter of reactor coil	[m]
d_i	inner diameter of reactor coil	[m]
d_o	outer diameter of reactor coil	[m]
E	specific total energy	[J kg^{-1}]
E_{prod}	ethene production rate	[t h^{-1}]

F	molar flow rate	[mol s^{-1}]
F_{feed}	feedstock mass flow rate	[kg s^{-1}]
$F_{m,i}$	mass flow rate in reactor coil i	[kg s^{-1}]
f	Fanning friction factor	[-]
$f(n\lambda T)$	fractional emissive power	[-]
g	gravitational acceleration	[m s^{-2}]
H_i	enthalpy of a species i	[J mol^{-1}]
ΔH	enthalpy of reaction	[J mol^{-1}]
h_c	convective heat transfer coefficient	[W m^{-2} K^{-1}]
h_i	specific enthalpy of species i	[J mol^{-1}]
I	radiation intensity	[W m^{-2}]
$\vec{J}_i$	diffusion flux of species i	[mol m^{-2} s^{-1}]
k	turbulent kinetic energy	[m^2 s^{-2}]
k_{eff}	effective conductivity	[W m^{-1} K^{-1}]
k_p	turbulent kinetic energy of the first near-wall node P	[m^2 s^{-2}]
L	path length	[m]
M	total number of reactor coils	[-]
M_w	molar mass	[kg mol^{-1}]
N_p	total number of products	[-]
N_R	total number of reactions	[-]
N_r	total number of reactants	[-]
N_s	total number of species	[-]
N_θ	discrete number of the polar angle θ	[-]
N_φ	discrete number of the azimuthal angle φ	[-]
n	refractive index	[-]
n	EWBM pressure parameter	[-]
$\vec{n}$	normal pointing out of the domain	[-]
P_{prod}	propene production rate	[t h^{-1}]
Pr_t	turbulent Prandtl number, $Pr_t = 0.85$	[-]
PE_i	propene to ethene mass ratio at the outlet of reactor coil i	[-]
PE_{mixing}	mixing-cup averaged propene to ethene mass ratio	[-]

p	total pressure	[Pa]
Q_{ab}	energy absorbed by all reactor coils	[W]
Q_{flue}	heat taken away by flue gas leaving the furnace	[W]
Q_{loss}	heat loss through furnace refractory	[W]
Q_r	thermal power release from reactions	[W]
q	heat flux	[W m^{-2}]
q_{conv}	convective heat flux	[W m^{-2}]
q_{emit}	radiative heat flux emitted from reactor coil surface	[W m^{-2}]
q_{flux}	total heat flux	[W m^{-2}]
q_i	total heat flux on the internal surface of the reactor coil	[W m^{-2}]
q_{in}	incident radiative heat flux on a wall	[W m^{-2}]
q_{inci}	incident radiative heat flux	[W m^{-2}]
q_o	tube external heat flux	[W m^{-2}]
q_{out}	radiative heat flux leaving a wall	[W m^{-2}]
q_{rad}	radiative heat flux	[W m^{-2}]
q_{re}	radiative heat flux reflected by reactor coil surface	[W m^{-2}]
R	universal gas constant, $R = 8.3145$	[J mol^{-1} K^{-1}]
R_{coke}	coking rate	[kg m^{-3} s^{-1}]
R_i	net production rate of species i	[mol m^{-3} s^{-1}]
r	intrinsic reaction rate	[mol m^{-3} s^{-1}]
$\vec{r}$	position vector	[-]
r_b	radius of the bend	[m]
Sc_t	turbulent Schmidt number, $Sc_t = 0.7$	[-]
S_E	energy source term	[J m^{-3} s^{-1}]
S_M	momentum source term	[kg m^{-2} s^{-2}]
$\vec{s}$	unit direction vector	[-]
$\vec{s}'$	scattering direction vector	[-]
T	temperature	[K]
T_{flue}	bridge wall temperature of flue gas	[K]
T_p	temperature of the first near-wall node P	[K]
$T_{w,i}$	internal tube metal temperature	[K]

$T_{w,o}$	external tube metal temperature	[K]
T^*	dimensionless temperature	[-]
Δt	time step size	[h]
t_d	decoking time	[h]
t_n	number of time steps	[-]
t_r	time step size for run length	[h]
$\vec{u}$	velocity	[m s^{-1}]
V	volume	[m^3]
V_m	molar volume	[m^3 mol^{-1}]
X	density path length	[kg m^{-2}]
Y	product composition	[wt%]
Y_i	mole fraction of species i	[mol mol^{-1}]
Y_P	mole fraction of any product species P	[mol mol^{-1}]
Y_R	mole fraction of a particular reactant R	[mol mol^{-1}]
y_p	distance from the wall to the first near-wall node P	[m]
y^*	dimensionless distance from the wall	[-]
x_i	mole fraction of species i	[mol mol^{-1}]

Greek

α	band strength parameter	[m^{-1}/kg·m^{-2}]
α	scaling factor	[-]
α_1	SST k-ω model constant, $\alpha_1 = 0.55$	[-]
α_2	SST k-ω model constant, $\alpha_2 = 0.44$	[-]
α_0	EWBM correlation parameter	[m^{-1}/kg·m^{-2}]
α_k	RNG k-ε model constant, $\alpha_k = 1.393$	[-]
α_ε	RNG k-ε model constant, $\alpha_\varepsilon = 1.393$	[-]
β	ratio of radiative heat flux to convective heat flux	[-]
β	RNG k-ε model constant, $\beta = 0.012$	[-]
β	line overlapping parameter	[-]
β^*	SST k-ω model constant, $\beta^* = 0.09$	[-]
β_0^*	EWBM correlation parameter	[-]

β_1	SST k-ω model constant, $\beta_1 = 0.075$	[-]
β_2	SST k-ω model constant, $\beta_2 = 0.828$	[-]
γ	specific heat ratio	[-]
γ	length fraction of fine structure in turbulent flow	[-]
ε	emissivity	[-]
ε	turbulent dissipation rate	[$m^2\ s^{-3}$]
ε_{ijk}	Levi-Civita symbol	[-]
δ_{ij}	Kronecker delta	[-]
δ_{coke}	coke thickness	[m]
ζ	Nekrasov factor for bends	[-]
θ	polar angle	[sr]
η	wavenumber	[cm^{-1}]
η_0	RNG k-ε model constant, η_0 =4.38	[-]
κ	absorption coefficient	[m^{-1}]
λ	wavelength	[μm]
λ_{coke}	thermal conductivity of coke	[W m^{-1} K^{-1}]
λ_w	thermal conductivity of tube metal	[W $m^{-1}K^{-1}$]
μ	viscosity	[Pa·s]
$\nu'_{R,j}$	stoichiometric coefficient for reactant *R* in reaction *j*	[-]
$\nu''_{P,j}$	stoichiometric coefficient for product *P* in reaction *j*	[-]
ρ	density	[kg m^{-3}]
σ	Stefan-Boltzmann constant, $\sigma = 5.67 \times 10^{-8}$	[W m^{-2} K^{-4}]
σ_k	Realizable k-ε model constant, $\sigma_k = 1.0$	[-]
σ_{k1}	SST k-ω model constant, $\sigma_{k1} = 0.85$	[-]
σ_{k2}	SST k-ω model constant, $\sigma_{k2} = 1.0$	[-]
σ_s	scattering coefficient	[m^{-1}]
σ_ε	Realizable k-ε model constant, $\sigma_\varepsilon = 1.2$	[-]
$\sigma_{\omega 1}$	SST k-ω model constant, $\sigma_{\omega 1} = 0.5$	[-]
$\sigma_{\omega 2}$	SST k-ω model constant, $\sigma_{\omega 2} = 0.856$	[-]
τ_0	optical thickness at the band center	[-]
$\bar{\bar{\tau}}$	stress tensor	[Pa]

Φ	scattering phase function	[-]
φ	azimuthal angle	[sr]
Ω	solid angle	[sr]
Ω	cross sectional surface area	[m^2]
ω	band width parameter	[m^{-1}]
ω_0	EWBM correlation parameter	[m^{-1}]

Subscript

b	black body
eff	effective
l	lower
t	turbulent
t	total
u	upper
w	wall
w	reactor coil surface
λ	spectral

Acronyms

ANN	artificial neutral network
BTX	benzene, toluene and xylenes
CCS	carbon capture and storage
CFD	computational fluid dynamics
CIP	coil inlet pressure, i.e. the process gas pressure at the inlet of the reactor, just upstream the radiation section
COP	coil outlet pressure, i.e. the process gas pressure at the outlet of the reactor, just upstream the adiabatic volume
COT	coil outlet temperature
CPU	central processing unit
CSTR	continuously stirred tank reactor
DNS	direct numerical simulation

DO	discrete ordinates
d-RMix	distributive reaction-mixing model
EDC	eddy dissipation concept
EDM	eddy-dissipation model
EWBM	exponential wide band model
FBP	final boiling point
IRHF	incident radiative heat flux
ISAT	in situ adaptive tabulation
LBLRTM	line-by-line radiative transfer models
LCT	laboratory for chemical technology
LES	large eddy simulation
LNAP	light naphtha
LPG	liquefied petroleum gas
IBP	initial boiling point
PDF	probability density function
P/E	propene to ethene mass ratio
PIONA	paraffins, iso-paraffins, olefins, naphthenes, aromatics
PSSA	pseudo-steady state assumption
PSS	pseudo-steady state
RANS	Reynolds-averaged Navier-Stokes
RNG	renormalization group
RTE	radiative transfer equation
SIMPLE	semi-implicit method for pressure-linked equations
SNB	statistical narrow band
SST	shear-stress-transport
TLE	transfer line exchanger, i.e. the heat exchanger of a steam cracking furnace downstream the adiabatic volume
TMT	tube metal temperature
TNF	turbulent non-premixed flames
TRI	turbulence-radiation interaction
UDF	user defined function
USC	ultra-selective conversion

WSGGM	weighted sum of gray gases model

Samenvatting

Stoomkraken is het belangrijkste petrochemische proces voor de productie van basischemicaliën zoals etheen, propeen en 1,3-butadieen. Voedingen gaande van ethaan en propaan tot nafta of zelfs gasolie worden omgezet naar deze waardevolle lichte olefines in buisreactoren opgehangen in grote, gasgestookte fornuizen. De koolwaterstoffen stromen eerst door een convectiesectie waar ze, indien nodig, worden verdampt en voorverwarmd tot een temperatuur van 770-950 K door warmte uit te wisselen met het warme rookgas afkomstig van de oven. Op een of meerdere plaatsen in de convectiesectie wordt stoom geïnjecteerd omwille van de volgende twee redenen: 1) in het geval van zware voedingen zorgt de stoom ervoor dat zelfs de componenten met een hoog kookpunt in de gasfase terechtkomen, dit om te voorkomen dat deze zware componenten de binnenkant van de buizen zouden vervuilen; en 2) de stoom verlaagt de partieeldruk van de koolwaterstoffen in de gasfase, wat de snelheid van ongewenste secundaire reacties in reactorbuis verlaagt. Vervolgens wordt het mengsel van koolwaterstoffen en stoom gelijk verdeeld over een groot aantal buisreactoren die zich in de oven bevinden. De gelijke verdeling wordt bewerkstelligd door gebruik te maken van ‘kritische’ venturi’s. Binnenin de reactorbuizen stijgt de temperatuur van het procesgas in een tijdspanne van 0.1-0.5 s tot 1050-1150 K aan de uitlaat van de reactor. De exacte verblijftijd en uitlaattemperatuur is afhankelijk van de voeding en de reactorgeometrie. De energie nodig voor de endotherme krakingsreacties wordt aangeleverd door het verbranden van een brandstof in branders aanwezig in de vloer of in de wanden van de oven. Warmteoverdracht van de oven naar het procesgas vindt hoofdzakelijk plaats via straling. De thermische efficiëntie in de oven van een stoomkraker varieert typisch tussen 40 % en 45 %. Na de passage door de buisreactoren wordt het procesgas snel

afgekoeld tot 630 K in een warmtewisselaar (de zogenaamde *transfer line exchanger*, TLE) om verlies aan selectiviteit naar de lichte olefines als gevolg van secundaire reacties te vermijden. Verderop wordt het effluent van de reactor verder afgekoeld om de zware producten en de verdunningsstoom te scheiden van de lichte koolwaterstoffen. In de scheidingssectie wordt de deze laatste stroom gefractioneerd in een opeenvolging van destillatiekolommen met de bedoeling om de gewenste producten te isoleren, de meest belangrijke zijnde etheen, propeen, 1,3-butadieen en de zogenaamde BTX componenten: benzeen, tolueen en xylenen.

In het algemeen verbruikt het stoomkraakproces ongeveer 8 % van het totale primaire energieverbruik van de chemische industrie. Bijna 65 % van deze energie wordt verbruikt in de oven om de nodige thermische energie aan te leveren aan de endotherme krakingsreacties. De steeds toenemende vraag naar lichte olefines, de sterk competitieve markt en een voortdurende bezorgdheid voor het milieu heeft de petrochemische industrie ertoe aangezet om de energie- en exergie-efficiëntie van het proces te verhogen en om de uitstoot van schadelijke componenten zoals NO_x en CO_2 te verminderen. Omwille van de complexiteit van de krakingsreacties die optreden in het procesgas en van de verbrandingsreacties die optreden in de oven kan een mathematisch model een sterke bijdrage leveren tot deze doelen. Dit model moet fungeren als basis voor het ontwikkelen, testen en verifiëren van nieuwe technologieën voor de oven, zowel tijdens de ontwerpfase als tijdens de operatie van de eenheid.

Een allesomvattend kader voor het modelleren van stoomkraakfornuizen bestaat enerzijds uit een model dat de conversie van de voeding in de buisreactoren beschrijft en anderzijds uit een model dat de stroming, verbranding en straling in de oven beschrijft. Beide modellen worden gelinkt via een koppelingsprocedure die de warmteuitwisseling tussen de oven en de

buisreactoren adequaat in rekening brengt. Voor het modelleren van de binnenkant van de reactorbuizen wordt het commerciële softwarepakket COILSIM1D gebruikt. Dit pakket is ontwikkeld aan het Laboratorium voor Chemische Technologie (LCT) en is gebaseerd op onderzoekservaring en data verzameld over een periode van meer dan 20 jaar. Gecombineerd met de moleculaire reconstructiemodule SIMCO, die commerciële indices zoals specifieke densiteit, gemiddelde molaire massa en PIONA gewichtsfracties omzet naar de meest waarschijnlijke gedetailleerde samenstelling, is COILSIM1D in staat om accuraat productopbrengsten en looptijden te voorspellen, in het bijzonder omwille van het gesofistikeerde reactienetwerk, bestaande uit honderden moleculen en duizenden elementaire reacties, dat is geïmplementeerd. Desalniettemin wordt de accuraatheid van de reactorsimulaties met COILSIM1D in belangrijke mate bepaald door de accuraatheid van de corresponderende warmtefluxprofielen gebruikt voor de simulatie. Dit laatste toont duidelijk de noodzaak aan van een breed toepasbaar model voor de oven dat in staat is om adequate randcondities te bepalen voor de reactorsimulaties.

De doelstelling van dit werk is het ontwikkelen van de allesomvattend kader gebaseerd op numerieke stromingsleer voor het simuleren van de oven van een industriële eenheid voor stoomkraken. Op basis van dit model kan de thermische koppeling tussen de oven en de buisreactoren onderzocht worden. Daarnaast kan het model ook worden gebruikt voor het ontwikkelen, testen en verifiëren van nieuwe technologie ontworpen om de thermische efficiëntie van de oven te verhogen, of om de productie van lichte olefines te verhogen en zelfs om de uitstoot van schadelijke componenten zoals NO_x te verlagen. Om dit te bewerkstellingen werden de volgende werkpakketten uitgevoerd: het ontwikkelen van een niet-grijs model voor de stralingseigenschappen van het rookgas zodat de warmteoverdracht door straling in de oven accuraat kan worden gemodelleerd; het optimaliseren van het

ontwerp via een bewust ongelijke verdeling van de voeding over de buisreactoren; het onderzoeken van de invloed van thermische herverdeling op de looptijdvoorspellingen en het ontwikkelen van een innovatieve methode voor het uitvoeren van looptijdvoorspellingen met een lagere rekenkost; het valideren en selecteren van onderliggende modellen voor het ontwikkelen en retrofitten van ultralage-NO_x branders. Alle simulaties gebaseerd op numerieke stromingsleer werden uitgevoerd met het softwarepakket ANSYS Fluent 14.5, waar nodig aangevuld met intern ontwikkelde modules die geïmplementeerd zijn als aanroepbare functies (*user defined functions)*.

In hoofdstuk 2 ligt de focus op het evalueren van de impact van de stralingseigenschappen van het rookgas op de thermische koppeling tussen de oven en de buisreactoren. Zogenaamde grijze modellen, momenteel nog altijd in gebruik voor het simulaties van grootschalige fornuizen voor stoomkraken, worden als onvoldoende accuraat beschouwd. Zo overschatten ze door de band de maximale vlamtemperatuur tot 100 K aangezien deze modellen geen rekening houden met de golflengteafhankelijkheid van de stralingseigenschappen van het rookgas. Om de niet-grijze stralingseigenschappen van het rookgas volledig in rekening te brengen, is een model voor de stralingseigenschappen van het rookgas ontwikkeld met negen banden (*exponential wide band mode,* EWBM*)*. De waarden voor totale emissiviteit verkregen met dit model met negen stralingsbanden komen goed overeen met de waarden voor totale emissiviteit gerekend aan de hand van de correlatie van Leckner en met benchmarkoplossingen berekend aan de hand van het zogenaamde *statistical narrow band* model voor warmteoverdracht door straling in een tweedimensionale rechthoekige ruimte. Het model met negen stralingsbanden werd vervolgens gereduceerd naar een model met vijf stralingsbanden door alle transparante banden, zijnde de banden in het golflengtespectrum waar de absorptiecoëfficiënt van het rookgas gelijk is aan nul, te combineren in een enkele

band. Simulaties van een industriële oven met ultraselectieve conversie (*ultra-selectieve conversion*, USC) werden uitgevoerd, gebruik makend van het niet-grijs model met vijf stralingsbanden aan de ene kant en het welbekende gewogen som van grijze gassen model (*weighted sum of gray gases*, WSGGM) aan de andere kant. De resultaten toonden aan dat verschillen in rookgastemperatuur van grootteorde 100 K worden voorspeld, wat ertoe leidt dat de gesimuleerde thermische efficiëntie van de oven 3.6 % verschilt en de gesimuleerde uitlaattemperatuur van het procesgas in de buisreactoren 44 K verschilt.

In hoofdstuk 3 staat de ongelijke verdeling van het thermische vermogen over de verschillende buisreactoren in de oven centraal. Deze ongelijke verdeling is een gevolg van geometrische factoren zoals branderpositie, schaduweffecten en de asymmetrie van de reactorbuizen. Het ontwerp van de oven op zich kan een inherent verschil in uitlaattemperatuur van het procesgas opleveren tot 29 K, en dat tussen verschillende buisreactoren binnen dezelfde module. Deze ongelijke verdeling van het vermogen is sterk ongewenst aangezien dit betekent dat maar een beperkt aantal buisreactoren kan worden geopereerd op volle capaciteit. Als maatregel tegen deze ongelijkheid, wordt het concept van een bewust ongelijke verdeling van de voeding over modules, zijnde groepen van buisreactoren, in een fornuis (*pass balancing*) verder uitgebreid naar een bewust ongelijke verdeling van de voeding over individuele reactoren. Vier verschillende schema's voor de verdeling van de voeding over de buisreactoren werden getest via simulaties op basis van de numerieke stromingsleer. Deze realiseerden respectievelijk een gelijke uitlaattemperatuur voor het procesgas, een gelijke verhouding van de massafracties van propeen en etheen aan de uitlaat van de reactor, een gelijke maximale snelheid van cokesvorming en een gelijke maximale buiswandtemperatuur. Door het toepassen van de bewust ongelijke verdeling over de reactoren kon de verwachte looptijd van de oven verlengd worden met 28 % en 13 %,

respectievelijk in de gevallen waar de maximale buiswandtemperatuur en de drukval over de reactor bepalend zijn voor de looptijd van de oven. De grootste winst werd geboekt met het schema dat een gelijke maximale snelheid van cokesvorming over alle reactoren bewerkstelligt, met een verwachte toename in de jaarlijkse productie van etheen en propeen met respectievelijk 1000 en 730 ton voor het USC fornuis met een jaarlijkse nominale productiecapaciteit voor etheen van 130 10^3 ton. Voor de praktische implementatie werd de zogenaamde vaste heterogene verdeling voorgesteld, aangezien de optimale verdeling over de individuele reactoren blijkt te gelden voor een breed scala aan voedingen. Het gewenste massadebiet aan koolwaterstoffen door elke reactor wordt gegarandeerd door de diameter van de keel van de venturi aanwezig tussen de convectiesectie en de buisreactor aan te passen, ofwel tijdens de ontwerpfase ofwel tijdens het installeren van nieuwe buisreactoren in de oven. Het is nuttig om stil te staan bij het feit dat de maximale snelheid van cokesvorming niet rechtstreeks gemeten kan worden terwijl de buisreactor opereren. Daarom werd het bewerkstellingen van een gelijke maximale buiswandtemperatuur voorgesteld als criterium voor het vastleggen van de bewust ongelijke verdeling van de voeding. Dit criterium vertoont een sterke correlatie met een gelijke maximale snelheid van cokesvorming, waardoor gelijkaardige resultaten worden verwacht. Tot slot werd voorgesteld om de beschikbare metingen van de maximale buiswandtemperatuur uit het verleden te combineren met gedetailleerde simulaties op basis van numerieke stromingsleer om zo tot een betrouwbaar kader te komen voor het bepalen van de beste verdeling van de voeding over de individuele reactoren.

In hoofdstuk 4 wordt invloed van thermische herverdeling onderzocht, zowel binnen een groep van reactoren als tussen verschillende groepen reactoren, dit aan de hand van een vergelijking van een volledig gekoppelde looptijdsimulatie gebaseerd op numerieke

stromingsleer en een ongekoppelde looptijdsimulatie van het USC fornuis. Dit is de eerste volledig gekoppelde looptijdsimulatie. De resultaten tonen aan dat de ongekoppelde looptijdsimulatie de looptijd van het USC fornuis in belangrijke mate onderschat (12 % korter) aangezien er in deze simulatiestrategie geen rekening kan worden gehouden met de thermische herverdeling die optreedt tijdens de looptijd. Om de rekenkost eigen aan een volledige gekoppelde looptijdsimulatie te reduceren, werd een alternatieve procedure ontwikkeld op basis van de invallende stralingswarmteflux (*incident radiative heat flux,* IRHF). De procedure gebruikt deze flux op de buitenwand van de reactor en correleert deze met de rookgastemperatuur tussen de oven en de convectiesectie berekenend aan de hand van een nuldimensionale warmtebalans. Een vergelijking met de resultaten van referentie looptijdsimulaties toont aan dat de nieuwe procedure gebaseerd op de invallende stralingswarmteflux accurate resultaten oplevert met relatieve verschillen kleiner dan 1 %. Daarenboven is de nieuwe procedure gebaseerd op IRHF meer dan 2000 keer sneller qua processortijd in vergelijking met de klassieke procedure, wat toelaat om de procedure te gebruiken voor optimalisatiedoeleinden.

Hoofdstuk 5 behandelt de validatie van onderliggende modellen voor turbulentie, straling en verbrandingschemie die gecombineerd moeten worden tot een allesomvattend kader voor het simuleren van niet vooraf gemengde turbulente verbranding in grootschalige fornuizen. Dit kader is ontwikkeld voor het ontwerpen en retrofitten van ultralage-NO_x branders. Verscheidene turbulentiemodellen werden gevalideerd door simulatieresultaten te vergelijken met experimentele data van een stroming met menglagen en een niet-reactieve ronde straal van propaan in meestromende lucht. Een aangepaste versie van het SST k-ω model was het best in staat om te turbulente eigenschappen van deze twee stromingen te beschrijven. Voor het valideren van het onderliggende model voor straling werd de impact van de

warmteoverdracht door straling onderzocht in de welbekende benchmarkvlam *Sandia flame D*. Het stralingsmodel met vijf banden ontwikkeld in hoofdstuk 2 gecombineerd met het discrete ordinatenmodel om de vergelijking voor stralingsoverdracht op te lossen, leverde de beste resultaten vergeleken met het gewogen gemiddelde van grijze gassen model gecombineerd met het discrete ordinatenmodel en met het zogenoemd optisch dun model. Vier reactiemechanismen voor verbrandingen, genaamd ChenCH4, ARM2, Lu21 en C1C2NO, werden vergeleken met experimentele data voor de *Sandia Flame D*. Een uitstekende overeenkomst tussen de gemeten en berekende NO-uitstoot werd gevonden gebruik makend van de mechanismen ChenCH4 en ARM2.

Tot slot werden de belangrijkste conclusies en werkpunten voor de toekomst samengevat in hoofdstuk 6. Deze laatsten zijn onder andere het potentieel voor het toepassen van coatings met een hoge emissiviteit, de golflengteafhankelijkheid van de emissiviteit van stralende oppervlakken in de oven, het effect van de turbulentie-chemie interactie en turbulentie-straling interactie voor het voorspellen van NO_x emissies en zogenaamde *oxy-fuel* verbranding waarbij gebruik gemaakt wordt van een zuivere zuurstofstroom als oxidans in plaats van lucht, wat toelaat om de CO_2 in het rookgas te stokkeren (*carbon capture and storage*, CCS).

Summary

Steam cracking is the principal petrochemical process to produce important base chemicals for the chemical industry such as ethene, propene and 1,3-butadiene. Hydrocarbon feedstocks ranging from ethane and propane up to naphtha or even gas oil are converted to these valuable light olefins in tubular reactors suspended in large gas-fired furnaces. The hydrocarbon feedstock is first fed into the convection section where it is evaporated, if necessary, and preheated to a temperature ranging between 770 K and 950 K by means of heat exchange with the hot flue gas. At one or more intermediate points in the convection section, dilution steam is injected into the process gas for the following two reasons: 1) for heavy feedstocks, steam injection ensures that even the components with the highest boiling point are entrained by the gas phase, thus limiting the fouling of the heat exchanger tubes by carbonaceous deposits; and 2) decrease the partial pressure of the hydrocarbons, thus decreasing the rate of unwanted secondary reactions in the reactor. Subsequently, the mixture of hydrocarbon feedstock and dilution steam is uniformly distributed via venturi nozzles over a large number of tubular reactors located in the radiant section. In the reactor coils, the process gas temperature rises rapidly up to 1050 – 1150 K at the coil outlet in a timeframe of about 0.1 – 0.5 s, depending on the type of feedstock and reactor geometry. The energy required for the highly endothermic cracking reactions is supplied via combustion of a fuel in burners located at the furnace floor and/or side walls. Heat transfer from the fire side to the process gas takes place primarily via radiation and the typical thermal efficiency in the radiant section ranges between 40% and 45%. The process gas leaving the reactor coils is rapidly quenched to around 630 K in transfer line exchanger (TLE) to prevent loss of selectivity towards the desired light olefins due to secondary reactions. Downstream, the effluent is further cooled to separate the heavy

products and the dilution steam from the light hydrocarbons and then directed towards a fractionation system where a sequence of distillation columns is used to fractionate the reactor effluent and isolate the desired products, the most important being ethene, propene, 1,3-butadiene and the so-called BTX, i.e. benzene, toluene and xylenes.

The overall steam cracking process accounts for about 8% of the chemical industry's primary energy consumption. Nearly 65% of that energy is required in the furnace section to provide the necessary thermal energy for reaction. The ever-increasing demand for light olefins, the highly competitive market and the continuous concern for the environment have driven the petrochemical industry to improve the energy and exergy efficiency of the process and reduce the emissions of pollutants such as NO_x and CO. Due to the complex nature of both the cracking process inside the tubular reactor and the combustion process in the furnace, clear opportunities can be provided by a mathematical modeling framework that fulfills the requirements for developing, testing and verifying new technologies for furnace and reactor optimization in both design and operation.

A comprehensive steam cracking furnace modeling framework usually consists of a model describing the process inside the tubular reactors and a model dedicated to calculating of flow, combustion and radiation in the furnace. These two parts of the framework are linked using a coupling procedure which ensures that the exchange of thermal power between the furnace and the reactor coils is adequately accounted for. For modeling the reactor side, a commercial software package COILSIM1D is available that has been developed at the Laboratory for Chemical Technology (LCT) based on more than 20 years of research experience and data. Combined with the molecular reconstruction module SIMCO, which translates commercial indices such as specific density, average molecular mass, PIONA mass fractions of a feedstock to its detailed composition, COILSIM1D is able to accurately predict

yields and run lengths thanks to an extensive and sophisticated reaction network consisting of hundreds of species and thousands of elementary reactions. However, the accuracy of the reactor simulations using COILSIM1D is strongly dependent on the accuracy of the heat flux profile provided for the calculation, indicating the need for a broadly applicable furnace model that is able to determine adequate boundary conditions for the reactor simulations.

The objective of this work is to construct a comprehensive computational fluid dynamics (CFD) based model for simulating the furnace of an industrial steam cracking unit. This model allows to investigate the thermal coupling between the furnace and the reactor coils and can fulfill the requirements of developing, testing and verifying new technologies designed to improve the furnace thermal efficiency, to increase production of light olefins, and to reduce NO_x emission. To this end, the following aspects were considered: development of a non-gray flue gas radiative properties model to describe radiative heat transfer inside the furnace; design optimization using flow distribution (pass balancing) technology; investigation of the impact of thermal redistribution on run length prediction and development of a novel coupling method to execute coupled run length simulations at a reduced computational cost; validation and selection of sub-models aimed at design and retrofit of ultra-low NO_x burners. All CFD simulations in this work were carried out using ANSYS Fluent 14.5, extended with in-house developed modules implemented as user defined functions.

Chapter 2 focuses on evaluating the impact of flue gas radiative properties on the thermal coupling between the furnace and the reactor coils. Gray gas models, currently still used in simulations of large-scale cracking furnaces, are reported to be too inaccurate, underpredicting the maximum flame temperature by up to 100 K as a result of the assumption that the flue gas radiative properties are independent of the wavelength. To fully account for

the non-gray characteristic of the flue gas, a nine-band model was developed for the radiative absorption coefficient based on the exponential wide band model (EWBM). Validation of this nine-band model shows good agreement with total emissivities calculated by the Leckner's correlation and with benchmark solutions calculated using the statistical narrow band (SNB) model for radiative heat transfer in a 2D rectangular enclosure. This model was then reduced to a five-band model by combining all transparent bands, i.e. radiative absorption coefficient equal to zero, into one band. Simulations of an industrial ultra-selective conversion (USC) furnace using the five-band non-gray gas model and the well-known gray implementation of the weighted sum of gray gases model (WSGGM) were carried out. Results showed that differences in flue gas bridge wall temperature in the order of 100 K are simulated , resulting in a 3.6% higher thermal efficiency and 44 K higher average coil outlet temperature for the reactors.

In addition to the radiative heat transfer, the uneven distribution of thermal power over different reactor coils in a furnace as a result of geometrical factors such as burner position, shadow effects and asymmetry of the reactor coil layout was investigated closely in Chapter 3. The furnace layout alone can induce a coil outlet temperature difference between different reactor coils in a module of up to 29 K, which is undesirable as this implies that only a limited number of coils can be operated at full potential. To reduce this non-uniformity, an extension of the flow distribution (pass balancing) technology, which adjusts the feedstock mass flow rate through reactor modules, i.e. groups of individual coils, was proposed. Four different flow distribution schemes realizing equal values for coil outlet temperature, propene to ethene mass ratio, maximum coking rate and maximum tube metal temperature (TMT) over all the reactor coils in a module were evaluated by coupled furnace-reactor CFD simulations. It was shown that applying flow distribution to the furnace yields 28% and 13% longer run length in

a tube metal temperature constrained and a coil inlet pressure constrained scenario, respectively. Achieving uniform coking rate proved to be the most optimal case, showing potential to increase the production of ethene and propene by 1000 and 730 metric tons respectively for the USC furnace with a nameplate ethene annual capacity of 130 10^3 metric tons. In terms of the practical implementation, a so-called fixed heterogeneous distribution was proposed since the most optimal feedstock flow distribution was found to be valid for a wide range of hydrocarbon feedstocks. In that case, the desired feedstock flow rate through each reactor coil is achieved by selecting the proper throat diameter of the venturi nozzle between the convection section outlet tube and the reactor coil in the design stage or when retubing the furnace. It is worth noting that the maximum coking rate cannot be measured on-stream. Therefore the maximum tube metal temperature, which is strongly correlated to the maximum coking rate, is proposed as the indicator for practical consideration. Finally, historically measured maximum tube metal temperature variations and detailed CFD simulation should be combined to offer a reliable framework to determine the optimal flow distribution.

In Chapter 4, inter-module and intra-module thermal redistribution was investigated by comparing a fully coupled CFD-based run length simulation and a standalone run length simulation of the USC furnace. No other fully coupled CFD-based run length simulations are reported in literature so this the first time such benchmark information has become available. Results showed that the standalone method significantly underpredicts the run length of the USC cracking furnace (12% shorter) due to its inability to capture the thermal redistribution phenomena. To reduce the prohibitively high computational cost associated with the fully coupled CFD-based run length simulation, an alternative method was developed, which utilizes the incident radiative heat flux (IRHF) on the reactor outer walls and correlates it to

the flue gas bridge wall temperature obtained from an overall zero-dimensional heat balance. Comparison with reference run length simulations showed that this IRHF-based method provides accurate results within a wide range of operating conditions or feedstock compositions, with relative differences between the IRHF-based method and the CFD-based method well below 1 %. Moreover, the new method is more than 2000 times faster in CPU time comparing to the CFD-based method, allowing the IRHF-based method to be used for optimization purposes.

Chapter 5 deals with validating sub-models for turbulence, radiation and combustion chemistry that are required to jointly establish a comprehensive framework for non-premixed turbulent combustion in large-scale furnaces. This framework is dedicated to design and retrofit of ultra-low NO_x burners. Different turbulence models were validated by comparing simulation results and experimental data of a mixing layer flow and a non-reacting round jet flow of propane into co-flowing air. A modified SST k-ω model showed the best performance in capturing the turbulence characteristics of these flows. For radiation model validation, the impact of radiative heat transfer was studied using the well-known benchmark case Sandia flame D. The five-band model developed in Chapter 2 combined with the discrete ordinates model to solve the radiative transfer equation provided superior results compared to the weighted sum of gray gases model combined with the discrete ordinates model and an optical thin model. Four combustion mechanisms, referred to as ChenCH4, ARM2, Lu21 and C1C2NO, were tested against the experimental data available from the Sandia flame D case. Excellent agreement between the measured and calculated NO emission were obtained by ChenCH4 and ARM2.

Finally, a summary of the main conclusions and future work were given in Chapter 6. The latter include but are not limited to the potential use of high emissivity coatings and the

associated wavelength dependence of the emissivity of radiating surfaces in the furnace, the effect of turbulence-chemistry interaction and turbulence-radiation interaction on the prediction of NO_x emission and oxy-fuel combustion as an alternative to air-fuel combustion to make the produced high purity CO_2 stream suited for carbon capture and storage.

Glossary

Absorption band	A spectral wavelength range for a gas species in which radiation energy can be emitted and/or absorbed due to the state transition of the atom or molecule from an initial state to a final state.
Choked flow	A compressible flow effect causing the velocity of a fluid to stop increasing with an increasing difference between upstream and downstream pressure when passing through a restriction.
COILSIM1D	Fundamental model for the simulation of steam cracking units developed at the Laboratory for Chemical Technology of Ghent University.
Coke	Solid carbonaceous residue that deposits inside the reactor and downstream equipment.
Computational fluid dynamics	A branch of fluid mechanics that uses numerical methods and algorithms to solve and analyze problems that involve fluid flow.
Emissivity	The effectiveness of a material in emitting energy compared to a black body at the same temperature.
Enthalpy	A thermodynamic quantity calculated from the internal energy U as $H = U + pV$, with p the pressure and V the volume of the system.
Entropy	A thermodynamic property related to the disorder of the system. A system with a larger number of possible states has a higher entropy.
Feedstock flow distribution	A technology to remedy nonunifomities in steam cracking

	furnaces by adjusting the feedstock mass flow rate through different (groups of) coils.
Gray gas model	A type of gas radiative properties model which assumes that the gas absorption coefficient is independent of the wavelength.
Molecular reconstruction	Deriving the detailed composition of a complex feedstock (or in fact any other mixture) from limited macroscopic information.
Non-gray gas model	A type of gas radiative properties models which expresses the gas absorption coefficient as a function of the wavelength.
Pseudo-steady state assumption	An approximation expressing that the rate of change of the concentration of a fast reaction species is equal to zero. Can be applied to multiple species in a reaction mechanism.
Pyrolysis	The uncatalyzed decomposition of organic components resulting from exposure to high temperature, in the absence of molecular oxygen.
Run length	Time of operation of a steam cracking furnace between two subsequent decoke operations.
Shale gas	Natural gas trapped in shale formations.
SIMCO	A module embedded in COILSIM1D for molecular reconstruction developed at the Laboratory for Chemical Technology of Ghent University.
Single-event microkinetic model	A kinetic model that consists of elementary reactions and accounts for all energetically equivalent reaction paths, i.e. single-events, to determine each reaction rate.
Shadow effects	The phenomenon that adjacent reactor coils in a steam cracking

	furnace shield each other from the radiation of the flame.
Spectral window	A spectral wavelength range for a gas species where it does not participate in radiative transfer, also called transparent band.
Steam cracking	A petrochemical process in which saturated hydrocarbons are converted into small unsaturated hydrocarbons by exposure to high temperature in the presence of steam.
Swirl flow	A whirling or eddying flow of fluid with a strong azimuthal velocity contribution.
Turbulence model	A model to predict the effects of turbulence. The continuity equations are often simplified by Favre-averaging, but models are needed to represent the scales of the flow that are not resolved.
3D reactor technology	Reactor technology that enhances heat transfer by small geometrical modification to the traditional straight, bare tube.

Chapter 1: Introduction

1.1 Steam cracking

Steam cracking of hydrocarbons is one of the most important petrochemical processes and the main route for producing light olefins such as ethene, propene and butadiene. These olefins are the building blocks of the chemical industry and their derivatives are widely used in everyday life. In the steam cracking process, hydrocarbon feedstocks ranging from ethane and propane up to naphtha or even gas oil are cracked in tubular reactors suspended in large-scale gas-fired furnaces. The spectrum of the products strongly depends on the feedstock composition. In general, lighter alkanes, e.g. ethane, propane, and LPG, mainly produce light olefins while for heavier hydrocarbon mixtures, a fair amount of aromatics such as benzene, toluene and para-xylene are obtained besides ethene and propene.

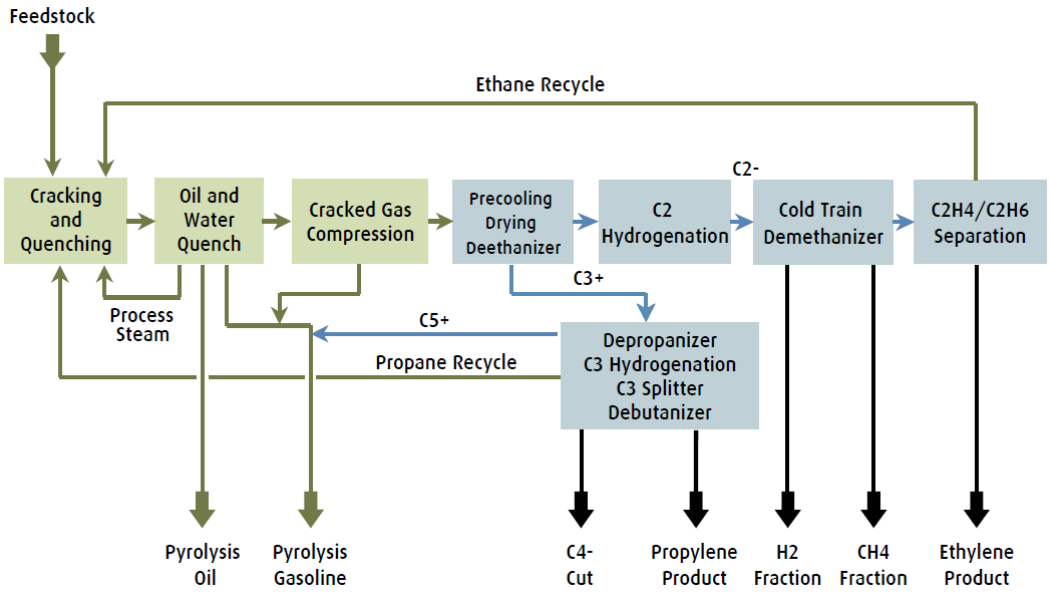

Figure 1-1: Schematic diagram of a typical steam cracking plant [1].

As shown in Figure 1-1, a typical steam cracking plant can be roughly divided into two sections: a hot section where the hydrocarbon feedstocks cracking takes place and a cold

section in which the products are separated and purified [2]. The hot section consists mainly of a furnace, a quenching system and a cracked gas compressor. In the cold section, the reactor effluent is dried and further processed in several distillation columns to separate the valuable components.

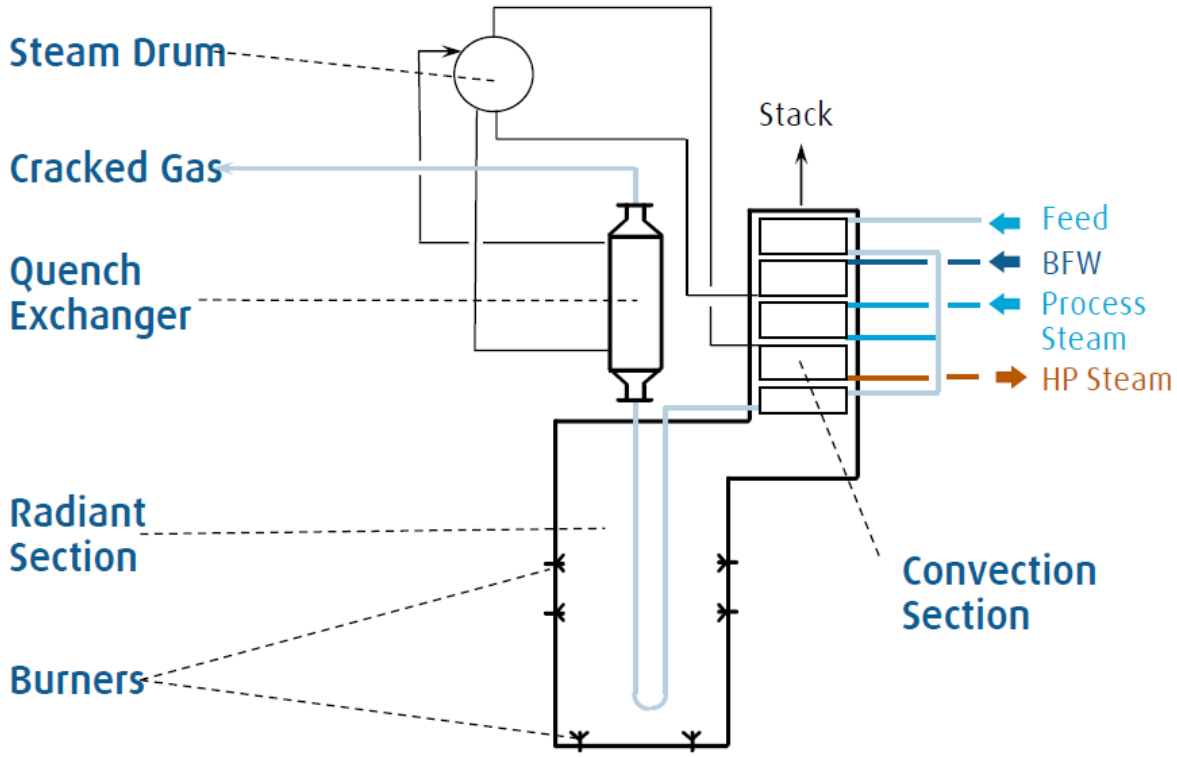

Figure 1-2: Schematic diagram of furnace of a steam cracking plant [1].

The furnace in the hot section of a steam cracking plant consists of a convection section, a radiant section and a transfer line exchanger (TLE), see Figure 1-2. A hydrocarbon feedstock is introduced into the convection section and preheated by means of heat exchange with the flue gas coming from the radiant section. During this process, dilution steam is mixed with the feedstock to reduce the partial pressure of the hydrocarbon, which disfavors secondary reactions between the light olefins and hence increases their selectivity. The diluted

hydrocarbon stream is further heated up to an incipient cracking temperature in the range of 770 – 950 K according to the type of the feedstock [3] and then distributed over a number of tubular reactors located in the radiant section, where the cracking occurs. The residence time of the reaction mixture in a coil is about 0.1 – 0.5 s. Within this short period, the hydrocarbon feedstock quickly breaks down into smaller molecules while the process gas temperature increases rapidly to 1050 – 1150 K at the coil outlet [4]. The thermal energy required for the endothermic cracking reactions is supplied by gas-fired floor burners and/or side wall burners. A typical value for the thermal efficiency of the radiant section is about 40 – 45%, the heat taken away by hot flue gas leaving the radiant section is recovered by preheating the feedstock mixture and by generating high pressure steam for utility system. Upon leaving the radiant section, the process gas enters the transfer line exchanger (TLE) and is quenched to around 630 K by vaporization of high-pressure boiler feed water. This rapid quenching is required to suppress the secondary reactions which decrease the selectivity towards light olefins. After this, the effluent is further cooled by heavy oil and water to remove any high-boiling components. After compression in the cracked gas compressor, the process gas enters the cold section where a complex sequence of distillation columns separates and purifies the valuable components.

One of the main problems in steam cracking is the formation of a carbonaceous deposit, namely coke, on the inner wall of the reactor coils (see Figure 1-3). The growth of the coke layer has several adverse effects on the process. On one hand, it hampers the heat transfer from the furnace to the process gas due to its low thermal conductivity. Hence more power has to be generated in the radiant section by increasing the fuel feed rate to maintain the same feedstock conversion or cracking severity. The side effect of the higher firing rate is a rise in tube metal temperature (TMT) over time, which leads to weakening of the alloy and can

eventually cause mechanical failure [5]. On the other hand, the reduced cross sectional area gives rise to an increase in pressure drop. To retain the coil outlet pressure (COP) at a constant level, which is required by the operating conditions of the cracked gas compressor, a higher coil inlet pressure (CIP) should be applied. Additionally, the higher overall pressure in the reactor favors bimolecular reactions compared to monomolecular reactions and hence decreases the selectivity towards the valuable light olefins. As a consequence of this coke formation, the furnace must be periodically taken out of production to remove the coke when either the tube metal temperature or the coil inlet pressure reaches a certain threshold value. The decoking process is carried out by feeding an air/steam mixture in a controlled way to the reactor coils to remove the coke via gasification with H_2O or O_2. A typical run length for industrial cracking furnaces, i.e. the time between two subsequent decoking operations, usually varies from 30 to 80 days, depending on the feedstock [6].

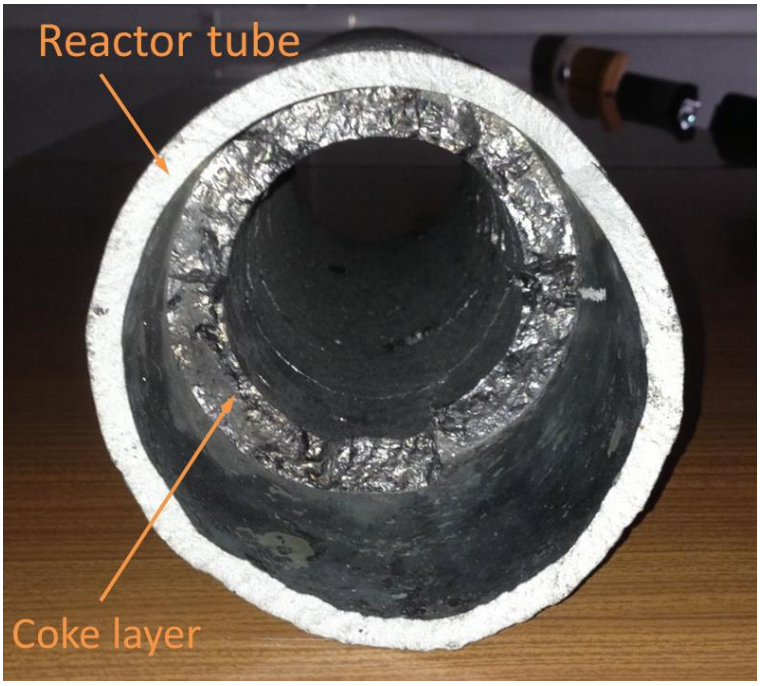

Figure 1-3: Coke layer deposited on the inner wall of an industrial cracking coil [7].

1.2 Modeling of a steam cracking furnace

It is well known that the gas-phase cracking reactions proceed through a free radical mechanism [8, 9]. In light of this, many research groups have developed their own reaction networks including a vast number of species and reactions to cover a wide range of feedstocks [10-14]. To obtain information about the detailed composition of complex hydrocarbon mixtures, molecular reconstruction based on commercial indices such as specific density, average molecular weight, distillation data or global group type analysis (PIONA) has also been widely studied [15-20]. Detailed reaction networks are combined with reactor models describing the conservation of species, global mass, energy and momentum. Due to the high Reynolds number of the process gas inside the reactor coil, the radial and azimuthal gradients of temperature and species concentration can usually be safely neglected [21]. Two commercial tools are often used in industrial practice to model a steam cracking furnace, with particular attention for the process side, i.e. COILSIM1D [22] and SPYRO [14, 23, 24]. In addition, studies of reactor design optimization have be conducted by many researchers using multi-dimensional reactor simulations [25-28].

Research on the fire side of the furnace initially focused on the radiative heat transfer modeling [29-35] using the zone method of Hottel and Sarofim [36]. With the development of computational fluid dynamics (CFD) and the drastic increase in computational power, the radiative transfer equations (RTE) can nowadays be solved together with the traditional Navier-Stokes equations in the entire flow domain. This has resulted in several studies on the fire side simulation to investigate turbulence-reaction interactions [4, 37, 38], NO_x emission [37, 39-41], radiative heat transfer [42-45], high-emissivity coatings [34, 35, 46] and thermal coupling between the furnace and the reactors [47-50].

1.3 Olefin market and challenges for steam cracking

Light olefins are nowadays considered as commodities such as cooling water and electricity. They must be produced at the lowest cost, continuously, and reliably to feed the integrated downstream units, which are the real profit centers [51]. Main derivatives of ethene are polyethylene (PE), ethylene oxide (EO), ethylene dichloride (EDC), ethylbenzene (EBZ), vinyl acetate and alpha olefins as shown in Figure 1-4 (a), among which various types of polyethylenes consume about 60% of the world ethene. The primary demand of propene by end-use is the production of polypropylene (PP), together with other derivatives including propylene oxide (PO), acrylonitrile (AN), acrylic acid, isopropanol, and cumene (CU), see Figure 1-4 (b).

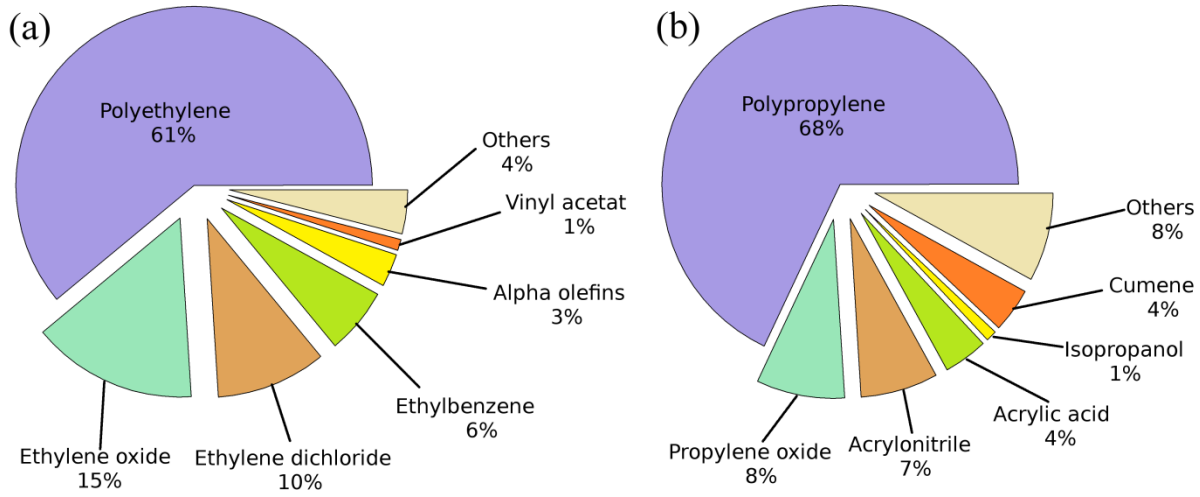

Figure 1-4: Derivatives from (a) ethene and (b) propene [52].

Global production capacities of light olefins are growing steadily due to the ever-increasing world demand of the olefin-based derivatives (polyethylene and polypropylene in particular). Estimations indicate that the nameplate annual ethene capacity has increased by 2.26 million ton per year (tpy) from 2014 to 146.02 million tpy in 2015 [53]. Figure 1-5 illustrates that the

production will further grow with an additional 50 million tpy by 2025, reaching a total annual ethene production capacity of about 200 million tpy. Even though a rapid growth of the market share by the methanol to olefins (MTO) technology [54] is anticipated over the period 2015-2025 (see Figure 1-5), ethene production by means of steam cracking of hydrocarbon feedstocks will still dominate (more than 80% of the total capacity). This means that the anticipated 50 million tpy increase in production capacity will mainly be completed by constructing new grass-roots steam crackers, especially in the Asia-Pacific region, and by debottlenecking or expanding existing sites, in particular in the US Gulf Coast region [55].

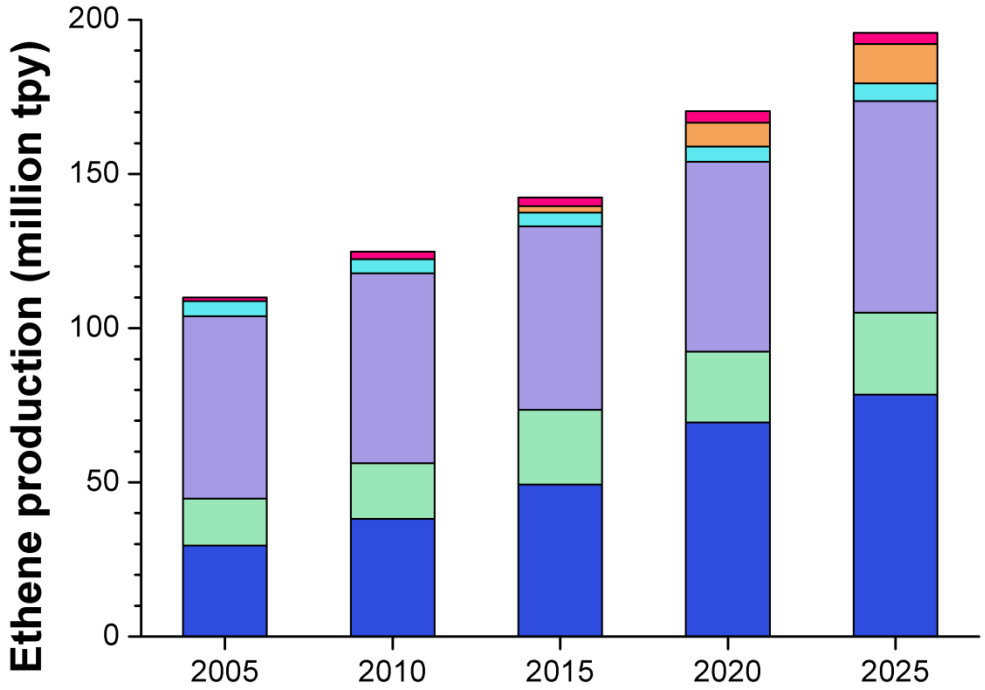

Figure 1-5: Estimated ethene production capacity by feed slate (- ethane; - LPG; - naphtha; - gas oil; - methanol; - others) [56].

One of the major concerns considered when investing in a steam cracking facility is the energy consumption per unit olefin production. It is known that a steam cracker with a larger size will greatly reduce the investment and operating costs (real estate, administration, maintenance, and financial) per ton olefin produced [51]. During the past 40 years, the capacity of a typical single train steam cracker has increased tenfold from 100,000 tpy to more than 1 million tpy, while the required energy per ton olefin produced decreased by a factor 3 [57]. However, ethene producers currently face several bottlenecks to expand the capacity of a single train facility beyond 1.4 million tpy, which is mainly due to mechanical constraints of the furnaces and the cracked gas compressor [51]. Therefore one of the current challenges is to design and operate steam cracking furnaces at higher energy efficiency. Lastly, more and more projects are carried out to minimize the environmental impact of steam cracking. Its contribution to CO_2 emissions is considerable as steam cracking globally uses approximately 8% of the sector's total primary energy [58]. Also, combustion of hydrocarbons in air at elevated temperatures substantial NO_x emissions, even though producers dedicate considerable effort to fine tuning the furnace operating conditions to minimize harmful emissions. With today's requirements of low NO_x emissions, the best available technologies allow European ethene producers to operate their furnaces at NO_x emissions levels of 80 to 100 mg/Nm^3.

1.4 Objectives and outline

In light of the fairly high energy efficiency of modern olefin plants , it is difficult to make improvements in design and operation via engineering experiences and/or empirical correlations. First principals based modeling seems to be one of few promising solutions to gain, albeit marginal, benefits for steam crackers. For the reactor side, the commercial software COILSIM1D [22] developed at the Laboratory for Chemical Technology (LCT) of

Ghent University, Belgium has proven to be superior to others in cracking reaction modeling due to an extensive and sophisticated reaction network consisting of hundreds of species and thousands of elementary reactions [59]. Although accurate reactor simulations can be performed with COILSIM1D, sufficient information is required about the reactor operating conditions, especially about the heat flux profile along the reactor. This information is not straightforward to obtain due to the strong thermal coupling of the furnace side and the reactor side. The heat flux profile can be precisely predicted only if a reliable furnace model is established, which is the main objective of this work. To this end, research has been conducted to investigate the most important aspects in advanced furnace modeling and their respective effects on the process side by means of fully coupled 3D-furnace-1D-reactor simulations combining computational fluid dynamics (CFD) and the commercial tool COILSIM1D.

In Chapter 2 the development and validation of a non-gray model describing the real radiative properties of the flue gas is presented. The results using the non-gray model are compared against the gray model commonly applied in engineering practice to show the necessity of taking into account the non-gray properties of the flue gas in steam cracking furnace modeling. The non-gray model is then modified to be computationally more efficient. In addition, it is the first time that the impacts of the shadow effects and the burner geometry on the reactor simulations performance are evaluated together.

Chapter 3 shows the design optimization of an industrial naphtha cracking furnace via feedstock flow distribution to reduce the non-uniformity of the thermal condition of different reactor coils. The influences of this design optimization on the furnace run length and production capacity are quantified by comparing the results of the run length simulations with different feedstock flow distribution schemes.

Although the CFD based furnace model can provide accurate simulation results, coupled furnace-reactor run length simulations often require too long computational times to be routinely applied for plant optimization. Therefore an alternative approach based on the incident radiative heat flux (IRHF) is proposed to reduce the computational time while retaining the accuracy. The model development and performance are discussed in Chapter 4.

In Chapter 5 the turbulence-chemistry interaction of the combustion process is studied using 2D CFD simulations. Several simplified combustion mechanisms, reduced from the detailed GRI-Mech 3.0 and 2.11 based on quasi steady state approximation (QSSA), are compared and validated against experimental data from benchmark combustion cases. The validated combustion mechanism is then used to perform a simulation of an industrial steam cracking furnace to predict NO_x emissions.

Finally, Chapter 6 provides a summary of the main conclusions of this work and the future research perspectives

References

[1] J. Conradt, Furnace Operation, in: Olefin Academy 2010, 2010.
[2] K. Van Geem, Single event microkinetic model for steam cracking of hydrocarbons, in, Ghent University, 2006.
[3] H. Zimmermann, R. Walzl, Ethylene, in: Ullmann's Encyclopedia of Industrial Chemistry, Wiley-VCH, Weinheim, Germany, 2000.
[4] G.D. Stefanidis, B. Merci, G.J. Heynderickx, G.B. Marin, CFD simulations of steam cracking furnaces using detailed combustion mechanisms, Comput Chem Eng, 30 (2006) 635-649.
[5] A. Goossens, M. Dente, E. Ranzi, Improve steam cracker operation, Hydrocarb Process, 57 (1978) 227-236.
[6] K.M. Sundaram, G.F. Froment, Kinetics of coke deposition in the thermal cracking of propane, Chem Eng Sci, 34 (1979) 635-644.
[7] A. Muñoz Gandarillas, K. Van Geem, M.-F. Reyniers, G. Marin, Assessing the influence of Alloy composition on coke formation in steam cracking reactors, in: 25th American Institute of Chemical Engineers Spring Meeting (AIChE Spring-2013), 2013.
[8] F.O. Rice, K.F. Herzfeld, The thermal decomposition of organic compounds from the standpoint of free radicals. VI. The mechanism of some chain reactions, J Am Chem Soc, 56 (1934) 284-289.

[9] F.O. Rice, The thermal decomposition of organic compounds from the standpoint of free radicals. I. Saturated hydrocarbons, J Am Chem Soc, 53 (1931) 1959-1972.
[10] K.M. Van Geem, M.-F. Reyniers, G.B. Marin, J. Song, W.H. Green, D.M. Matheu, Automatic reaction network generation using RMG for steam cracking of n-hexane, AIChE J, 52 (2006) 718-730.
[11] W. Sun, M. Saeys, Construction of an ab initio kinetic model for industrial ethane pyrolysis, AIChE J, 57 (2011) 2458-2471.
[12] M.K. Sabbe, K.M. Van Geem, M.-F. Reyniers, G.B. Marin, First principle-based simulation of ethane steam cracking, AIChE J, 57 (2011) 482-496.
[13] E. Ranzi, A. Frassoldati, S. Granata, T. Faravelli, Wide-Range Kinetic Modeling Study of the Pyrolysis, Partial Oxidation, and Combustion of Heavy n-Alkanes, Ind Eng Chem Res, 44 (2004) 5170-5183.
[14] M.W.M. van Goethem, F.I. Kleinendorst, C. van Leeuwen, N. van Velzen, Equation-based SPYRO® model and solver for the simulation of the steam cracking process, Comput Chem Eng, 25 (2001) 905-911.
[15] N. Charon-Revellin, H. Dulot, C. López-García, J. Jose, Kinetic Modeling of Vacuum Gas Oil Hydrotreatment using a Molecular Reconstruction Approach, Oil Gas Sci. Technol. – Rev. IFP Energies nouvelles, (2010).
[16] S.P. Pyl, K.M. Van Geem, M.-F. Reyniers, G.B. Marin, Molecular reconstruction of complex hydrocarbon mixtures: An application of principal component analysis, AIChE J, 56 (2010) 3174-3188.
[17] J.J. Verstraete, P. Schnongs, H. Dulot, D. Hudebine, Molecular reconstruction of heavy petroleum residue fractions, Chem Eng Sci, 65 (2010) 304-312.
[18] D. Hudebine, J.J. Verstraete, Molecular reconstruction of LCO gasoils from overall petroleum analyses, Chem Eng Sci, 59 (2004) 4755-4763.
[19] K.M. Van Geem, D. Hudébine, M.F. Reyniers, F. Wahl, J.J. Verstraete, G.B. Marin, Molecular reconstruction of naphtha steam cracking feedstocks based on commercial indices, Comput Chem Eng, 31 (2007) 1020-1034.
[20] J.J. Verstraete, H. Dulot, N. Revellin, D. Hudebine, Molecular Reconstruction of Vacuum Gasoils, Preprints of Papers - American Chemical Society, Division of Fuel Chemistry, 49 (2004) 20-21.
[21] T. Gál, B.G. Lakatos, Thermal cracking of recycled hydrocarbon gas-mixtures for re-pyrolysis: Operational analysis of some industrial furnaces, Appl Therm Eng, 28 (2008) 218-225.
[22] Zolo Technologies, Inc. http://zolotech.com/chemical-and-refining/ethylene-cracking-furnace-efficiency/.
[23] M. Dente, E. Ranzi, A.G. Goossens, Detailed prediction of olefin yields from hydrocarbon pyrolysis through a fundamental simulation model (SPYRO), Comput Chem Eng, 3 (1979) 61-75.
[24] E. Ranzi, M. Dente, S. Pierucci, G. Biardi, Initial product distributions from pyrolysis of normal and branched paraffins, Industrial & Engineering Chemistry Fundamentals, 22 (1983) 132-139.
[25] D.J. Van Cauwenberge, C.M. Schietekat, J. Floré, K.M. Van Geem, G.B. Marin, CFD-based design of 3D pyrolysis reactors: RANS vs. LES, Chem Eng J, 282 (2015) 66-76.
[26] C.M. Schietekat, D.J. Van Cauwenberge, K.M. Van Geem, G.B. Marin, Computational fluid dynamics-based design of finned steam cracking reactors, AIChE J, 60 (2014) 794-808.

[27] P.A. Reyniers, C.M. Schietekat, D.J. Van Cauwenberge, L.A. Vandewalle, K.M. Van Geem, G.B. Marin, Necessity and Feasibility of 3D Simulations of Steam Cracking Reactors, Ind Eng Chem Res, 54 (2015) 12270-12282.
[28] C.M. Schietekat, M.W.M. van Goethem, K.M. Van Geem, G.B. Marin, Swirl flow tube reactor technology: An experimental and computational fluid dynamics study, Chem Eng J, 238 (2014) 56-65.
[29] P.M. Plehiers, G.C. Reyniers, G.F. Froment, Simulation of the run length of an ethane cracking furnace, Ind Eng Chem Res, 29 (1990) 636-641.
[30] T. Detemmerman, G. Froment, F., Three Dimensional Coupled Simulation of Furnaces and Reactor Tubes for the Thermal Cracking of Hydrocarbons, Oil & Gas Science and Technology - Rev. IFP, 53 (1998) 181-194.
[31] G.J. Heynderickx, G.F. Froment, Simulation and Comparison of the Run Length of an Ethane Cracking Furnace with Reactor Tubes of Circular and Elliptical Cross Sections, Ind Eng Chem Res, 37 (1998) 914-922.
[32] A.J.M. Oprins, G.J. Heynderickx, G.B. Marin, Three-Dimensional Asymmetric Flow and Temperature Fields in Cracking Furnaces, Ind Eng Chem Res, 40 (2001) 5087-5094.
[33] G.J. Heynderickx, A.J.M. Oprins, G.B. Marin, E. Dick, Three-dimensional flow patterns in cracking furnaces with long-flame burners, AIChE J, 47 (2001) 388-400.
[34] G.J. Heynderickx, M. Nozawa, High-emissivity coatings on reactor tubes and furnace walls in steam cracking furnaces, Chem Eng Sci, 59 (2004) 5657-5662.
[35] G.J. Heynderickx, M. Nozawa, Banded gas and nongray surface radiation models for high-emissivity coatings, AIChE J, 51 (2005) 2721-2736.
[36] H.C. Hottel, A.F. Sarofim, Models of radiative transfer in furnaces, Journal of Engineering Physics and Thermophysics, 19 (1970) 1102-1114.
[37] G. Hassan, M. Pourkashanian, D. Ingham, L. Ma, P. Newman, A. Odedra, Predictions of CO and NOx emissions from steam cracking furnaces using GRI2.11 detailed reaction mechanism – A CFD investigation, Comput Chem Eng, 58 (2013) 68-83.
[38] H. Guihua, W. Honggang, Q. Feng, Numerical simulation on flow, combustion and heat transfer of ethylene cracking furnaces, Chem Eng Sci, 66 (2011) 1600-1611.
[39] A. Habibi, B. Merci, G.J. Heynderickx, Multiscale modeling of turbulent combustion and NOx emission in steam crackers, AIChE J, 53 (2007) 2384-2398.
[40] S. Barendregt, M. van Goethem, I. Risseeuw, F. Alessio, T. Faravelli, A.A. Cuoci, X.J. Li, The Design Of Ultra-Low NOx Critical Furnaces, in: The Eighth European Conference on Industrial Furnaces and Boilers, Portugal, 2008.
[41] Q. Tang, M. Denison, B. Adams, D. Brown, Towards comprehensive computational fluid dynamics modeling of pyrolysis furnaces with next generation low-NOx burners using finite-rate chemistry, Proceedings of the Combustion Institute, 32 (2009) 2649-2657.
[42] G.D. Stefanidis, B. Merci, G.J. Heynderickx, G.B. Marin, Gray/nongray gas radiation modeling in steam cracker CFD calculations, AIChE J, 53 (2007) 1658-1669.
[43] A. Habibi, B. Merci, G.J. Heynderickx, Impact of radiation models in CFD simulations of steam cracking furnaces, Comput Chem Eng, 31 (2007) 1389-1406.
[44] Y. Zhang, F. Qian, C.M. Schietekat, K.M. Van Geem, G.B. Marin, Impact of flue gas radiative properties and burner geometry in furnace simulations, AIChE J, 61 (2015) 936-954.
[45] G. Hu, C.M. Schietekat, Y. Zhang, F. Qian, G.J. Heynderickx, K.M. Van Geem, G.B. Marin, Impact of Radiation Models in Coupled Simulations of Steam Cracking Furnaces and Reactors, Ind Eng Chem Res, 54 (2015) 2453-2465.

[46] G.D. Stefanidis, K.M. Van Geem, G.J. Heynderickx, G.B. Marin, Evaluation of high-emissivity coatings in steam cracking furnaces using a non-grey gas radiation model, Chem Eng J, 137 (2008) 411-421.
[47] A.J.M. Oprins, G.J. Heynderickx, Calculation of three-dimensional flow and pressure fields in cracking furnaces, Chem Eng Sci, 58 (2003) 4883-4893.
[48] X. Lan, J. Gao, C. Xu, H. Zhang, Numerical Simulation of Transfer and Reaction Processes in Ethylene Furnaces, Chemical Engineering Research and Design, 85 (2007) 1565-1579.
[49] G. Hu, H. Wang, F. Qian, Y. Zhang, J. Li, K.M. Van Geem, G.B. Marin, Comprehensive CFD Simulation of Product Yields and Coking Rates for a Floor- and Wall-Fired Naphtha Cracking Furnace, Ind Eng Chem Res, 50 (2011) 13672-13685.
[50] G. Hu, H. Wang, F. Qian, K.M. Van Geem, C.M. Schietekat, G.B. Marin, Coupled simulation of an industrial naphtha cracking furnace equipped with long-flame and radiation burners, Comput Chem Eng, 38 (2012) 24-34.
[51] M. Buffenoir, J. Aubry, X. Hurstel, Large ethylene plants present unique design, construction challenges, Oil Gas J, 102 (2004) 60-65.
[52] T. Potter, The Great Energy Price Deflation and the Impacton Feedstock Markets and Petrochemicals, in: Asia Petrochemical Industry Conference, 2015.
[53] OSJ Subscriber Survey. http://www.ogj.com/ogj-survey-downloads.html.
[54] P. Tian, Y. Wei, M. Ye, Z. Liu, Methanol to Olefins (MTO): From Fundamentals to Commercialization, ACS Catalysis, 5 (2015) 1922-1938.
[55] L. Nichols, What is next for the US downstream projects market?, in: Hydrocarb Process, 2016.
[56] S. Halliday, Global Energy Outlook: Implications for Petrochemical Feedstocks, in, Wood Mackenzie, Dubai, 2015.
[57] D. Cole, Olefin economics impacts of the technology supplier, in: Proceedings of the 8th Ethylene Producers' Conference, New York, NY (United States), 1996.
[58] T. Ren, M. Patel, K. Blok, Olefins from conventional and heavy feedstocks: Energy use in steam cracking and alternative processes, Energy, 31 (2006) 425-451.
[59] K.M. Van Geem, M.F. Reyniers, G.B. Marin, Challenges of modeling steam cracking of heavy feedstocks, Oil & Gas Science and Technology - Rev. IFP, 63 (2008) 79-94.

Chapter 2: Impact of flue gas radiative properties in furnace simulations

This chapter is based on the following paper:

Zhang, Y.; Qian, F.; Schietekat, C. M.; Van Geem, K. M.; Marin, G. B., Impact of flue gas radiative properties and burner geometry in furnace simulations. AlChE Journal 2015, 61 (3): 936-954.

Abstract

Three fully coupled Computational Fluid Dynamics (CFD) simulations of a complete industrial steam cracking furnace equipped with floor burners are performed. The influence of the flue gas radiative properties and burner geometry on the flame front in the firebox, the heat transfer to the coils and the product selectivities has been investigated. A nine-band model developed from the Exponential Wide Band Model (EWBM) is used as non-gray gas radiation model to compare with the gray gas implementation of Weighted Sum of Gray Gas Model for the evaluation of the flue gas radiative properties. The gray gas radiation model predicts a flue gas outlet temperature that is 70 K lower than the temperature obtained with the non-gray gas radiation model, resulting in a 3.6% higher thermal efficiency and 44 K higher average Coil Outlet Temperature (COT). Important differences between the 22 reactors in the furnace are seen because of shadow effects with and without accounting for the detailed burner geometry. The maximum difference between the COT of different reactors in the furnace caused by shadow effects is about 29 K which corresponds to a propene-over-ethene difference of 0.1. Full furnace CFD simulations prove thus to be essential in design and during debottlenecking, when aiming for a more uniform COT distribution to the reactors by feed or fuel distribution.

Keywords: steam cracking, computational fluid dynamics, heat transfer, gas radiative properties, shadow effect

2.1 Introduction

Steam cracking of hydrocarbons is the main petrochemical process for the production of light olefins such as ethene and propene, which are key base chemicals for the chemical industry. The cracking chemistry mainly proceeds through a free-radical mechanism. As most reactions are highly endothermic, the process is carried out in tubular reactors with a high aspect ratio suspended in a large furnace. The energy required for heating of the process gas and the heat of reaction is supplied by combustion of a fuel from burners in the furnace floor and/or side walls. Downstream this so-called hot side, a complex separation section, i.e. the cold side, separates the reactor effluent into the main product streams.

The process is very energy-intensive using about 8% of the chemical industry's primary energy consumption. Furthermore in naphtha steam crackers, about 65% of the total process energy is consumed by the hot side [1]. In order to improve the energy efficiency and the process selectivity, a lot of efforts have been made towards the development of detailed reaction networks describing the pyrolysis reactions [2-5], which can be implemented into one-, two- or three-dimensional reactor simulations [6-10]. The implementation of a coking model in these reactor simulations allows to predict run lengths [11, 12]. Accurate results can be obtained by these reactor simulations, provided that the heat flux profile to the reactors is precisely defined. In other words, the quality of the reactor simulation depends on the accuracy of the simulation of the combustion and the heat transfer inside the furnace.

Over the past decades, significant progress has been made in the modeling of steam cracking furnaces. Coupled simulations of furnace and reactor coils were first performed using a combination of a CFD model for the fluid dynamics and the Hottel's zone method [13] for the radiative heat transfer [14, 15]. In this zone method the computational domain is divided into several isothermal regions and the view factors between every two zones and surfaces are

calculated. Since the computational cost for the calculation of view factors increases exponentially with the number of zones, it is infeasible to use as many zones as are used in the fluid dynamics simulation. Hence, two different grids were used for the fluid dynamics and the radiative heat transfer calculation, with the former being much finer than the latter. With progress in radiation modeling and drastic increase in computational power, the Radiative Transfer Equation (RTE) can nowadays be solved in each cell of the flow domain to perform the fluid dynamics and radiative heat transfer calculation on the same grid. The six-flux radiation model was the first to be used [16, 17], followed by a comparison of several radiation models by Habibi et al. [18]. More recently, a number of coupled furnace-reactor simulations of naphtha steam cracking furnaces were conducted using the commercial CFD software ANSYS Fluent [19-23]. Notwithstanding the great progress over the last decades in steam cracking furnace modeling, most of the reported previous work have three important shortcomings.

First of all, the flue gas radiative properties are typically described by the gray gas implementation of the Weighted Sum of Gray Gases Model (WSGGM), which is reported to yield unsatisfactory results in three-dimensional enclosures [24]. Moreover, as stated by Edwards, the “gray gas myth”, shows that treating the flue gas as a gray gas in combustion systems may lead to temperature underpredictions of 100 K or more [25]. This was also confirmed by comparing gray and non-gray gas models in steam cracking furnace simulations [26, 27]. However, no coupled furnace-reactor simulations were performed in most of these works, which means that the influence on the product yields and coking rates of the radiative properties has not been evaluated. Furthermore, a uniform composition of the flue gas over the entire furnace was assumed in these works as the simulated furnaces only had radiation wall burners. However, the flue gas composition changes drastically in most steam cracking

furnaces as floor burners or a combination of floor and wall burners is typically used. Hence, the effect of changing composition on the non-gray gas model has to be considered.

Moreover many reactors are suspended in a single furnace, with some closer to the burners and projecting shadows on other adjacent reactors reducing heat transfer to these reactors. This so-called "shadow effect" [28] causes non-uniformities in cracking severity over the different reactors and is not considered in most furnace-reactor simulations as only a single reactor is typically simulated.

Besides providing an accurate heat flux profile for reactor simulations, environmental concerns are another reason for the simulation of the fire side of steam cracking furnaces. The main pollutants from a furnace are carbon and nitrogen oxides. Detailed reaction networks result in high computational costs because of the vast number of species and reactions and the large grid size of the computational domain of the furnace. To save computational time, detailed reaction networks are often reduced before implementation in the furnace simulation [29, 30] or the calculation of NOx formation is performed in a post-processing step [31-33]. It is well known that the details of the burner geometry, such as burner tips and stages, influence the formation of NOx. Although these burner details are typically accounted for in the simulation of small test furnaces [34], they are omitted in most industrial furnace simulations to reduce the grid size [17, 19]. Therefore, the effect of simplifying the burner geometry in an industrial furnace simulation is assessed here.

In this chapter, three cases were studied for the investigation of the influence of flue gas radiative properties and burner geometry on the combustion and radiative heat transfer in an industrial naphtha cracking furnace equipped with floor burners. In all cases, shadow effects were evaluated by simulating all the reactors suspended in the furnace. Two furnace configurations were established, one with the detailed burner geometry and the other with a

simplified burner geometry. A nine-band and a five-band non-gray gas model were developed based on the Exponential Wide Band Model (EWBM). The latter is a simplification of the nine-band model for the purpose of computational cost reduction. Both non-gray models were validated using benchmark solutions of 5 radiative heat transfer problems in two-dimensional enclosure. The non-gray model was then compared with the gray gas implementation of the Weighted Sum of Gray Gases Model (WSGGM) in the three furnace simulation cases. All simulations were performed using the commercial CFD software ANSYS Fluent 14.0 with the non-gray gas radiative properties model implemented in a User Defined Function (UDF). The reactor simulations were performed with COILSIM1D [35] developed at the Laboratory for Chemical Technology (LCT) of Ghent University.

2.2 Flue Gas Radiative Properties

2.2.1 Model selection

Solving the RTE for an absorbing-emitting gas mixture contained by opaque walls requires the knowledge of the gas radiative properties in terms of the absorption coefficient κ, which consists of millions of narrow spectral lines arising mainly from rotational and vibrational level transitions of the gas species of the mixture. To perform heat transfer calculations using these spectral lines, a great number of spectral evaluations of the RTE are required along with high resolution spectroscopic databases such as HITRAN and HITEMP [36, 37]. These so-called Line-By-Line Radiative Transfer Models (LBLRTM) are computationally so expensive that even with today's powerful computing facilities, they can only be used as benchmarks for validation of more approximate models.

Spectral band models divide the wavelength spectrum into a number of spectral intervals in which the actual absorption coefficient is replaced by a smoothened average value. They can

be further classified into narrow band models and wide band models based on the spectral resolution. Most of the narrow band models were developed about 60 years ago, among which there are two extremes in considering the overlapping of spectral lines. The Elsasser model assumes equally spaced lines of equal intensity, while the statistical model randomly distributes both line space and intensity [38]. The narrow band databases RADCAL [39] and EM2C [40], established from spectroscopic measurements and the HITRAN database respectively, are used in narrow band models to yield very accurate band transmittances and absorption coefficients.

Despite their high accuracy and efficiency, narrow band models still require too many bands to be used in the simulation of industrial furnaces as the grid size is too large, i.e. in the order of millions of cells. As the blackbody intensity does not vary substantially across an entire vibration-rotation band, wide band models calculate the total absorption or emission for an entire band. The most successful wide band model is the Exponential Wide Band Model (EWBM) proposed by Edwards [41]. Apart from the wide band model, k-distribution models are also quite often used in dealing with non-gray radiative properties of gas mixture. As the Planck function can be considered as constant over a small spectral interval of few tens of wavenumbers, the intensity is a function of solely absorption coefficient, which varies wildly even across this narrow spectrum and attains the same value many times. In order to avoid wasteful calculations, k-distribution models reorder the absorption coefficients into a monotonically increasing function, assuring that the intensity calculation is carried out only once. Research works on development and evaluation of the k-distribution models can be found in literatures [40, 42-44]. Another type of non-gray treatment uses total emissivity data of a gas mixture to estimate the heat transfer. The Weighted Sum of Gray Gases Model

(WSGGM), first developed by Hottel and Sarofim within the framework of the zone method [13], is the most widely used model in this category.

A less sophisticated, but more practical engineering treatment is to solve the RTE over the entire spectrum. This so-called gray gas modeling requires much less computational power and is usually sufficient to evaluate the radiative properties of an absorbing-emitting gas mixture. However for radiative heat transfer problems in multi-dimensional large-scale enclosures, the gray gas modeling can give poor results [24] and thus non-gray modeling becomes necessary. In this chapter, gray and non-gray gas simulations based on WSGGM and EWBM respectively were used for the simulation of an industrial scale steam cracking furnace. The model details are given in the next paragraphs.

2.2.2 Weighted sum of gray gases model

This model replaces a non-gray gas by a number of fictitious gray gases N, each of them having a constant absorption coefficient κ_i and a temperature dependent weight factor a_i. Hence, the total emissivity over a path length L can be expressed as:

$$\varepsilon = \sum_{i=0}^{N-1} a_i(T)(1 - e^{-\kappa_i L}) \tag{2.1}$$

Since the total emissivity should have unity as limit as L tends to infinity, the sum of weight factors should also be unity. However, a single-component gas usually has spectral bands in which it would take a very large path length for the emissivity to be close to unity. To take this so-called spectral window into account, the absorption coefficient for the first fictitious gas $i = 0$ is assigned to zero so the weight factor for $i = 0$ is evaluated using the following expression making sure the total emissivity has unity as limit.

$$a_0 = 1 - \sum_{i=1}^{N-1} a_i \tag{2.2}$$

It is common to approximate the temperature dependence of a_i by a polynomial:

$$a_i = \sum_{j=1}^{M} b_{i,j} T^{j-1} \tag{2.3}$$

Values of $b_{i,j}$ and κ_i can be found by fitting equation (2.1) to the experimental total emissivity curve at different partial pressure ratios of the absorbing species, i.e. H_2O and CO_2. The coefficients used in ANSYS Fluent are taken from Smith and coworkers [45] for the temperature range usually encountered in combustion applications, i.e. between 600 and 2400 K and from Coppalle and Vervisch [46] for higher temperatures, both at a total pressure of 1 atm. Scaling rules suggested by Edwards [47] are employed to correct κ_i in case of combustion under non-atmospheric pressure. However, it is important to note that WSGGM can also be applied in a non-gray implementation by calculating an emissivity for each 'virtual' band using equation (2.1) per band. However, only the gray gas implementation of WSGGM is compatible with the radiation models in ANSYS Fluent [48]. Therefore the WSGGM was used as a gray gas model in this chapter.

2.2.3 Exponential wide band model

The EWBM was developed based on the assumption that the line intensity decreases exponentially in the band wings far away from the band center. There are three types of wide band shapes according to the location of the band center, i.e. bands with an upper limit head, bands with a lower limit head and symmetric bands. For each absorption band included in the EWBM, the band absorption coefficient κ is evaluated from Beer's law [27] with the band emissivity $\varepsilon = 1 - \tau$:

$$\kappa = \frac{1}{L}\ln\left(\frac{1}{1-\varepsilon}\right) \tag{2.4}$$

where τ is the band transmittance and is calculated by:

$$\tau = \frac{\tau_0}{A^*}\frac{dA^*}{d\tau_0} \tag{2.5}$$

Edwards provided a four region expression [41] summarized in Table 2-1 to describe the dimensionless band absorptance A^* in equation (2.5) as function of the band strength parameter α, the line overlapping parameter β and the band width parameter ω. The temperature and pressure dependence of the parameters α, β, and ω are given below:

$$\alpha(T) = \alpha_0\frac{\Psi(T)}{\Psi(T_0)} \tag{2.6}$$

$$\beta(T) = \beta_0^*\sqrt{\frac{T_0}{T}}\frac{\Phi(T)}{\Phi(T_0)}P_e \tag{2.7}$$

$$\omega(T) = \omega_0\sqrt{\frac{T}{T_0}} \tag{2.8}$$

$$P_e = \left[\frac{p}{p_0}\left(1+(b-1)\frac{p_i}{p}\right)\right]^n \tag{2.9}$$

where α_0, β_0^*, and ω_0 are reference parameters, b and n are pressure parameters. The values of all parameters for 6 different species included in EWBM, i.e. H_2O, CO_2, CO, CH_4, NO, and SO_2 can be found in literature [38]. $p_0 = 101325\ Pa$ and $T_0 = 100\ K$ are the reference pressure and temperature respectively. The EWBM parameters for the H_2O and CO_2, which are the main participating gas species in the present work, are listed in Table 2-2.

Table 2-1: Exponential Wide band correlation for an isothermal gas [38].

$\beta \leq 1$	$0 \leq \tau_0 \leq \beta$	$A^* = \tau_0$	Linear regime
	$\beta \leq \tau_0 \leq 1/\beta$	$A^* = 2\sqrt{\tau_0 \beta} - \beta$	Square root regime
	$1/\beta \leq \tau_0 \leq \infty$	$A^* = \ln(\tau_0 \beta) + 2 - \beta$	Logarithmic regime
$\beta \geq 1$	$0 \leq \tau_0 \leq 1$	$A^* = \tau_0$	Linear regime
	$1 \leq \tau_0 \leq \infty$	$A^* = \ln\tau_0 + 1$	Logarithmic regime

$\tau_0 = \alpha X/\omega$ is the optical thickness at the band center, where $X = \rho L$ is the density path length.
$A^* = A/\omega$ is the dimensionless band absorptance

Table 2-2: Exponential Wide band model parameters for H_2O and CO_2 [38].

Band location	Vibration quantum step	Pressure parameter		Correlation Parameters		
		n	b	α_0 [cm^{-1}/(g/m^2)]	β_0^*	ω_0 [cm^{-1}]
H_2O						
71 μm	(0,0,0)	1	$8.6\sqrt{T/T_0 + 0.5}$	5.455	0.143	69.3
6.3 μm	(0,1,0)	1	$8.6\sqrt{T/T_0 + 0.5}$	41.2	0.094	56.4
	(0,2,0)			0.2		
2.7 μm	(1,0,0)	1	$8.6\sqrt{T/T_0 + 0.5}$	2.3	0.132	60.0
	(0,0,1)			23.4		
1.87 μm	(0,1,1)	1	$8.6\sqrt{T/T_0 + 0.5}$	3.0	0.082	43.1
1.38 μm	(1,0,1)	1	$8.6\sqrt{T/T_0 + 0.5}$	2.5	0.116	32.0
CO_2						
15 μm	(0,1,0)	0.7	1.3	19.0	0.062	12.7
10.4 μm	(-1,0,1)	0.8	1.3	2.47×10^{-9}	0.040	13.4
9.4 μm	(0,-2,1)	0.8	1.3	2.48×10^{-9}	0.119	10.1
4.3 μm	(0,0,1)	0.8	1.3	110.0	0.247	11.2
2.7 μm	(1,0,1)	0.65	1.3	4.0	0.133	23.5
2.0 μm	(2,0,1)	0.65	1.3	0.060	0.393	34.5

2.2.4 Non-gray radiation model development

For most combustion processes in furnaces, the main absorbing gaseous species are H_2O and CO_2. EWBM contains nine absorption bands for these two species [38], however, some of

these bands are far less important than the others at the temperature range which is usually encountered in combustion systems, i.e 1100 K – 1900 K [27]. Thus only five absorption bands were suggested by Stefanidis et al. [27] for modeling the gas radiative properties in a steam cracking furnace, which also has a similar flue gas composition as that of the present work. These bands are:

- H_2O: 6.3 μm, 2.7 μm
- CO_2: 15 μm, 4.3 μm, 2.7 μm

As the absorption bands of H_2O and CO_2 overlap at a wavelength of 2.7 μm, they were combined into one band.

To calculate band transmittance and therefore the absorption coefficient of each of the remaining four absorption bands in the considered non-gray radiative properties model, equations (2.6) - (2.9) need be solved. However, the numerator and denominator of $\Psi(T)$ and $\Phi(T)$ consist of complicated series expressions which are computationally rather expensive. Lallemant and Weber [49] developed a more efficient method to calculate $\Psi(T)$ and $\Phi(T)$ using exact analytical expression and fourth-order polynomial correlations respectively. They showed that the computational time for calculating the total emissivity of H_2O and CO_2 were 28 and 98 times faster by this approach with maximum relative errors less than 1% compared to calculation by equation (2.6) and (2.7). Hence, the method of Lallemant and Weber [49] was adopted.

For non-gray implementation of the EWBM, the absorption coefficient should be determined for each wide band. First, the bandwidth is calculated using the following equation:

$$\Delta\eta = \frac{A}{1-\tau} \tag{2.10}$$

τ can be described as a function of τ_0 and β by substituting the expressions in Table 2-1 into equation (2.5).

One problem with equation (2.10) is that the band transmittance will be equal to 1 in the linear regime of Table 2-1, which is usually encountered at very small path lengths. This results in an infinite bandwidth. Therefore, Edwards suggested an upper limit of 0.9 for the calculation of band transmittance [50]. Ströhle and Coelho pointed out that an arbitrary imposed upper limit may introduce serious errors if the recurrence relation is employed due to a strong dependence on the grid resolution [51]. One way to remedy this is to define a fixed bandwidth $\Delta\eta_{fix}$ from the flue gas temperature and concentrations averaged over the entire domain first. Then the band limits can be determined using the following equations:

$$\eta_u = \eta_c + \Delta\eta_{fix}/2 \quad and \quad \eta_l = \eta_c - \Delta\eta_{fix}/2 \tag{2.11}$$

$$\eta_u - \eta_l = \Delta\eta_{fix} \tag{2.12}$$

where $\eta = 1/\lambda$ is the wavenumber which has the same units as the band absorptance. For a symmetric band, equation (2.11) is used to determine the upper and lower limits from a specified band center η_c. In the case of an asymmetric band, either the upper or the lower limit is known, so the other limit can be obtained by equation (2.12).

The band transmittance is then recalculated from the band absorptance A obtained from Table 2-1 by the following expression:

$$\tau = 1 - \frac{A}{\Delta\eta_{fix}} \tag{2.13}$$

When calculating band transmittance for two overlapping bands, an effective band absorptance A_{eff} is used to replace the band absorptance A in equation (2.13) which can be calculated as [52]:

$$A_{eff} = A_1 + A_2 - \frac{A_1}{\Delta\eta_1}\frac{A_2}{\Delta\eta_2}\Delta\eta_{eff} \quad (2.14)$$

where $\Delta\eta_{eff}$ is the effective bandwidth of the overlapping band, with its two limits chosen as the largest of the two overlapping bands' lower limits and the smallest of their upper limits.

Including the five spectral windows in-between the four absorption bands, a nine-band model was developed based on the EWBM as summarized in Table 2-3. The absorption coefficients of the spectral windows were set to zero. The averaged bandwidths over the temperature range from 300-2200 K were determined before the CFD simulation. The absorption coefficients can be calculated on-the-fly, i.e. as a function of temperature, pressure and H_2O and CO_2 concentrations in each cell during each iteration. To cover the entire wavelength spectrum with the nine-band model, the maximum wavelength, i.e. the upper limit of the last band is computed as $\lambda_{max}T_{min} \geq 50000$ as recommended by ANSYS Fluent [48], where T_{min} is the minimum temperature in the furnace.

Table 2-3: Bands information of the nine-band model derived from the EWBM.

Band No.	Lower limit, (μm)	Upper limit, (μm)	Absorption coefficient, (m^{-1})
1	0	2.50	0
2	2.50	2.84	EWBM
3	2.84	4.15	0
4	4.15	4.69	EWBM
5	4.69	5.48	0
6	5.48	7.27	EWBM
7	7.27	12.42	0
8	12.42	18.92	EWBM
9	18.92	150.00	0

It is important to note that all the absorption coefficient in the spectral windows, i.e. band No. 1, 3, 5, 7 and 9, is set to zero. This means that these spectral windows can be considered as one region although they are discrete in wavelength. The benefit of this treatment is that the

RTE only needs to be solved once in this combined region instead of 5 times when dealing with these spectral windows separately. As usually several millions of cells are required to cover the computational domain of the furnace, combining the five spectral bands has the potential to considerably reduce the cost in terms of both computational power and disk space. Therefore, by combining the five spectral windows into one, the nine-band model was reduced to a 'five-band model', in which the absorption band NO. 2, 4, 6 and 8 were kept but all the other spectral windows were combined as one band. The validity and performance of this model will be demonstrated together with the nine-band model in the next sections.

2.3 Validation of non-gray radiation model

Because six absorption bands of the full EWBM were omitted, the validity of the nine-band model and the five-band model under steam cracking furnace operating conditions needs to be verified. In this section, the two non-gray models are compared with full EWBM in total emissivity calculation and with the commonly used gray implementation of WSGGM in 2D radiative heat transfer calculation cases.

2.3.1 Total emissivity calculation

As the chosen absorption bands in the nine-band model and in the five-band model are identical, the two models show no difference for the calculated total emissivity. Hence only the nine-band model is discussed. The total emissivities of H_2O and CO_2 calculated by the nine-band model and the full EWBM were compared with those calculated from a correlation developed by Leckner [53] based on spectrally integrated emissivities. For the nine-band model, the band energy approximation method [49] was adopted to evaluate the emissivity of each absorption band:

$$\varepsilon_i = f(n\lambda_u T) - f(n\lambda_l T) \tag{2.15}$$

where λ_u and λ_l are the upper and lower limits of the band and can be computed by replacing the $\Delta\eta_{fix}$ in equation (2.11) and (2.12) by band absorptance A. The emissivity of each species ε is then calculated by summing the emissivities of all bands. $f(n\lambda T)$ is the fractional emissive power of a black body and can be described as follows:

$$f(n\lambda T) = \frac{15}{\pi^4}\sum_{m=1}^{\infty}\frac{e^{-m\zeta}}{m^4}[6 + 6(m\zeta) + 3(m\zeta)^2 + (m\zeta)^3],\ \ \zeta = \frac{C_2}{n\lambda T} \tag{2.16}$$

where C_2 is the Planck constant.

If two or more bands of the a certain species are overlapping, the total emissivity of this species will be smaller than the sum of individual band contributions. Hottel and Sarofim [13] dealt with this problem in an approximate way, assuming that the transmissivities of the two bands are independent from each other. Hence the total transmissivity is expressed as follows.

$$\tau_{i+j} = \tau_i \tau_j \tag{2.17}$$

As $\varepsilon = 1 - \tau$, the total emissivity of the species with two overlapping bands can be calculated by the following equation.

$$\varepsilon_{i+j} = \varepsilon_i + \varepsilon_j - \varepsilon_{ij} \tag{2.18}$$

It is worth noting that equation (2.18) is accurate only if both bands fully overlap with each other. While for partial overlapping band, the correction term ε_{ij} should be calculated based on the fractions of band emissivity in the overlap region. As this information is not available in band energy approximation method [49], equation (2.18) was used in emissivity calculation for both fully and partially overlapping bands.

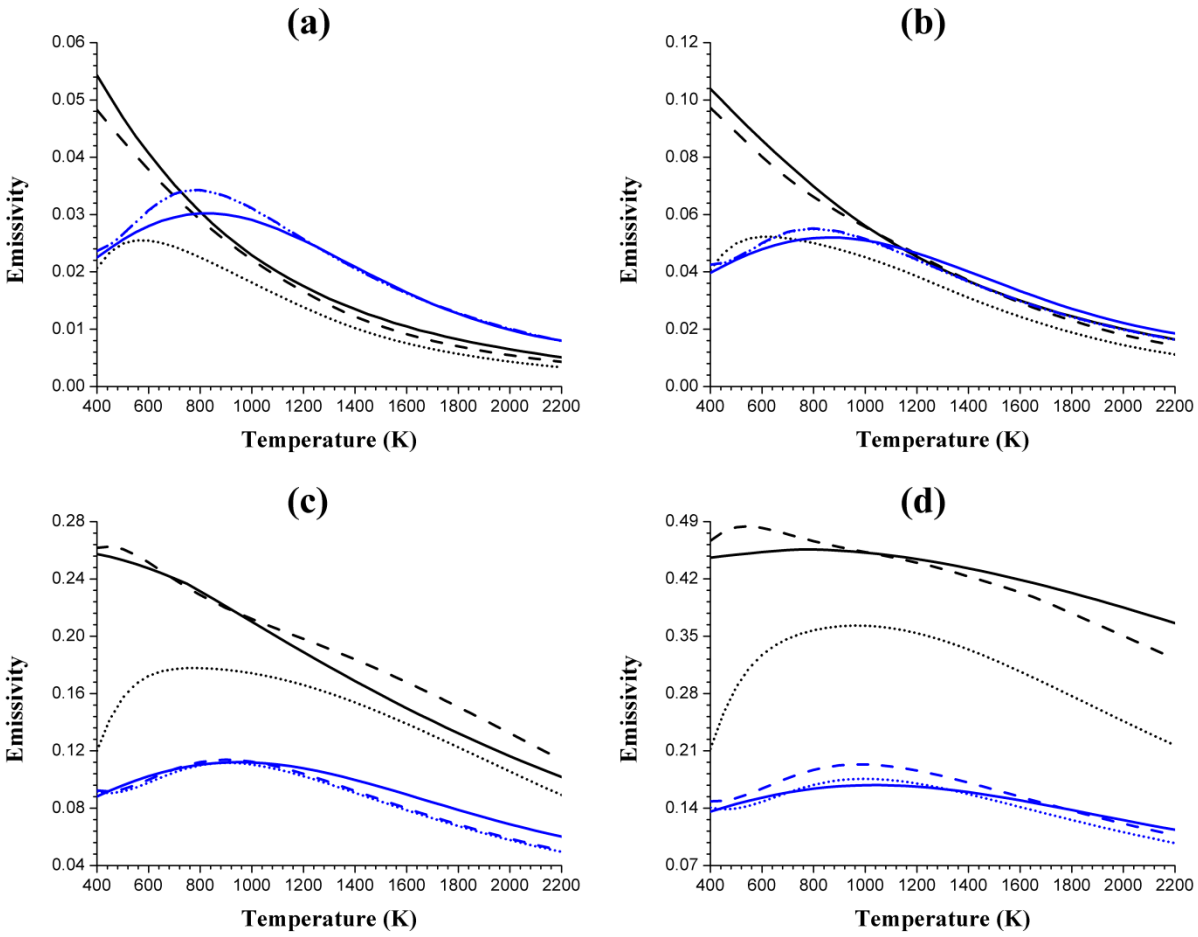

Figure 2-1: Emissivities of H_2O and CO_2 (——— – H_2O Leckner's; - - - – H_2O EWBM; ····· – H_2O nine-band model; ——— – CO_2 Leckner's; - - - – CO_2 EWBM; ····· – CO_2 nine-band model) as a function of temperature (K) at different path lengths L: (a) $L = 0.03\ m$; (b) $L = 0.1\ m$; (c) $L = 1\ m$; (d) $L = 10\ m$. (total pressure $p = 101325\ Pa$; mole fraction $x_{H_2O} = 0.18$, $x_{CO_2} = 0.09$).

Figure 2-1 shows the H_2O and CO_2 emissivities calculated by the nine-band model, the EWBM and Leckner's correlation for different path lengths at typical conditions in the furnace, i.e. a total pressure of $101325\ Pa$ and a mole fraction of H_2O and CO_2 equal to 0.18 and 0.09 respectively. Figure 2-1 (a) shows the results using a path length of 3 10^{-2} m, i.e. the path length averaged over all cells of the computational domain. The path length of a cell is calculated as $L = 3.6\,V/A$ [38], where V and A are the volume and the surface area of the cell

respectively. Good agreement between Leckner's correlation and EWBM is observed for both H_2O and CO_2 for most of the temperature range, but the errors tend to increase with increasing path length as shown in Figure 2-1 (b-d). This can mainly be attributed to the band absorptance increasing at larger path length, leading to more overlap of bands. As the way of dealing with overlapping bands in the EWBM using equation (2.18) is rather approximate, the emissivities calculated by the EWBM at larger path length are less accurate. However, it should be stressed that for the path length of the simulated furnace, i.e. $3\ 10^{-2}$ m, the agreement between EWBM and Leckner's correlation is satisfactory.

Agreement between the EWBM and the nine-band model for CO_2 is good besides for the largest path length. The difference between the two models for H_2O is larger than for CO_2, especially at lower temperature and larger path lengths. The deviations are a result of omitting some absorption bands in the nine-band model compared to the full EWBM. To demonstrate this, the contribution of each band to the total emissivities of H_2O and CO_2 at a path length of $3\ 10^{-2}$ m is shown in Figure 2-2. The results at larger path lengths show similar trends and are therefore not depicted. Six bands of the EWBM are not included in the nine-band model, i.e.71 μm, 1.87 μm, 1.38 μm for H_2O; and 10.4 μm, 9.4 μm, 2.0 μm for CO_2. The CO_2 bands at 10.4 μm and 9.4 μm contribute less than 0.1% to the total CO_2 emissivity at all temperatures used in Figure 2-1 and are therefore not depicted in Figure 2-2. The 2.0 μm band of CO_2 accounts for about 0.25% of the total CO_2 emissivity at a path length of $3\ 10^{-2}$ m. However, the contribution of the three omitted CO_2 bands increases with increasing path length and reaches a maximum value of 6% at 10 m, resulting in the underprediction of the total CO_2 emissivity by the nine-band model in Figure 2-1 (d). Hence, for large path length simulations, these bands could be important. The contribution of the omitted rotational band of H_2O at 71 μm to the total H_2O emissivity is almost 60% at 400 K but decreases rapidly

with increasing temperature to about 10% at 2200 K. This band becomes less important when temperature is above 1200 K. The effect of the two excluded hot bands at 1.87 μm and 1.38 μm becomes more important at higher temperature. Consequently, the nine-band model underpredicts the H_2O emissivity at both low and high temperatures due to the omission of the rotational band and the hot bands, particularly for large path lengths, as shown in Figure 2-1.

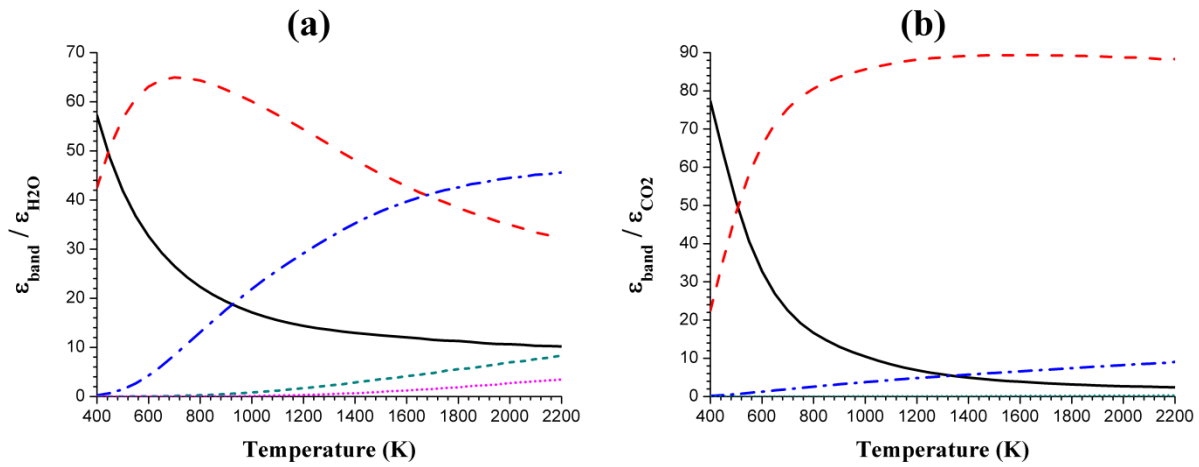

Figure 2-2: The ratio of band emissivity to the total emissivity (%) calculated using the EWBM as a function of temperature (K) at path length $L = 0.03\ m$: (a) ——— – H_2O 71 μm band; – – – – H_2O 6.3 μm band (incl.); – • – – H_2O 2.7 μm band (incl.); – – – – H_2O 1.87 μm band; ‥‥‥‥ – H_2O 1.38 μm band; (b) ——— – CO_2 15 μm band (incl.); – – – – CO_2 4.3 μm band (incl.); – • – – CO_2 2.7 μm band (incl.); ‥‥‥‥ – CO_2 2.0 μm band. (total pressure $p = 101325\ Pa$; mole fraction $x_{H_2O} = 0.18$, $x_{CO_2} = 0.09$; incl. indicates that the absorption band is included in the nine-band model).

For the path length used in the present furnace simulations, the nine-band model is only inaccurate at temperatures below 1200 K. However, H_2O and CO_2 are only formed at higher temperatures in the furnace. Hence, the effect of the inaccurate emissivity at lower

temperatures on the simulation results is quite limited. This statement is corroborated by Figure 2-3, showing the average heat flux profile to all reactor coils in a small test furnace with a simplified coil geometry. The gray implementation of the EWBM and the nine-band model were used to calculate the gas radiative properties respectively. The results using the nine-band model and the EWBM are almost identical, which means that the total emissivity calculation of the nine-band model is a good approximation under typical operating conditions in industrial steam cracking furnaces.

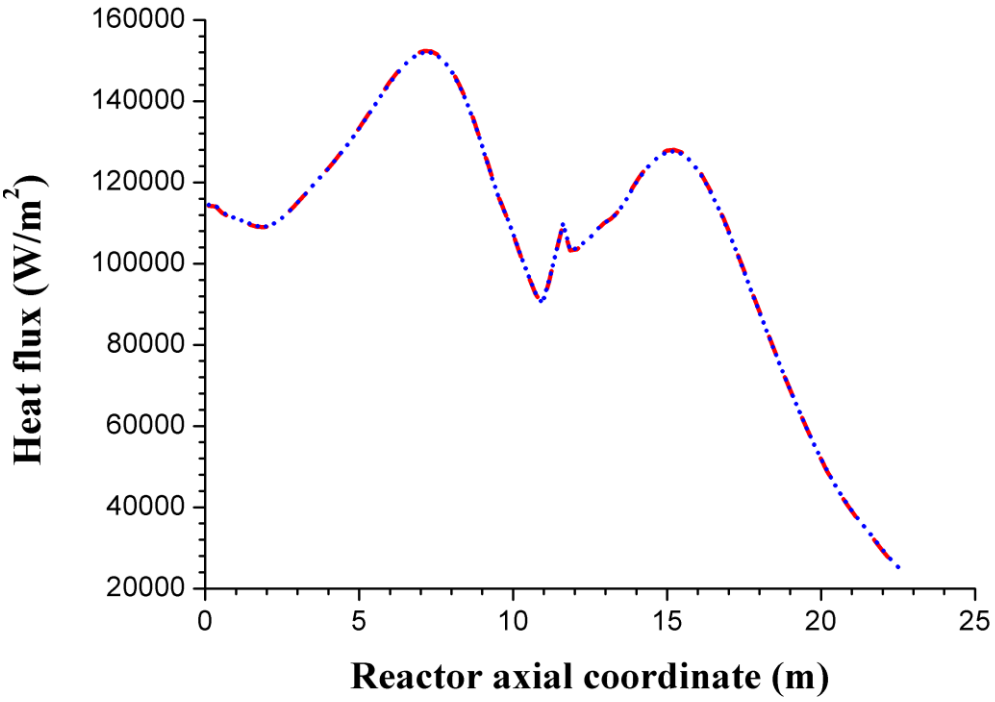

Figure 2-3: Averaged heat flux (W/m²) over all reactors in the test furnace as a function of the reactor axial coordinate (m): – – – – EWBM; ····· – nine-band model.

2.3.2 Radiative heat transfer in 2D enclosure

2.3.2.1 Description of the test cases

To verify the non-gray implementation of the nine-band and the five-band models, radiative heat transfer problems in a 2D rectangular enclosure of 1.0 m by 0.5 m were simulated (see Figure 2-4). Five test cases were previously studied by Goutiere et al [54] with benchmark solutions using the statistical narrow band (SNB) model. In all five cases, the wall surfaces were considered as ideal black bodies at 0 K and the gas medium was at a uniform pressure of 101325 Pa. The gas mixture consists of H_2O and CO_2 as absorbing-emitting species and N_2 as non-participating species. The temperature and the concentration field of the participating gas for the five cases are listed in Table 2-4.

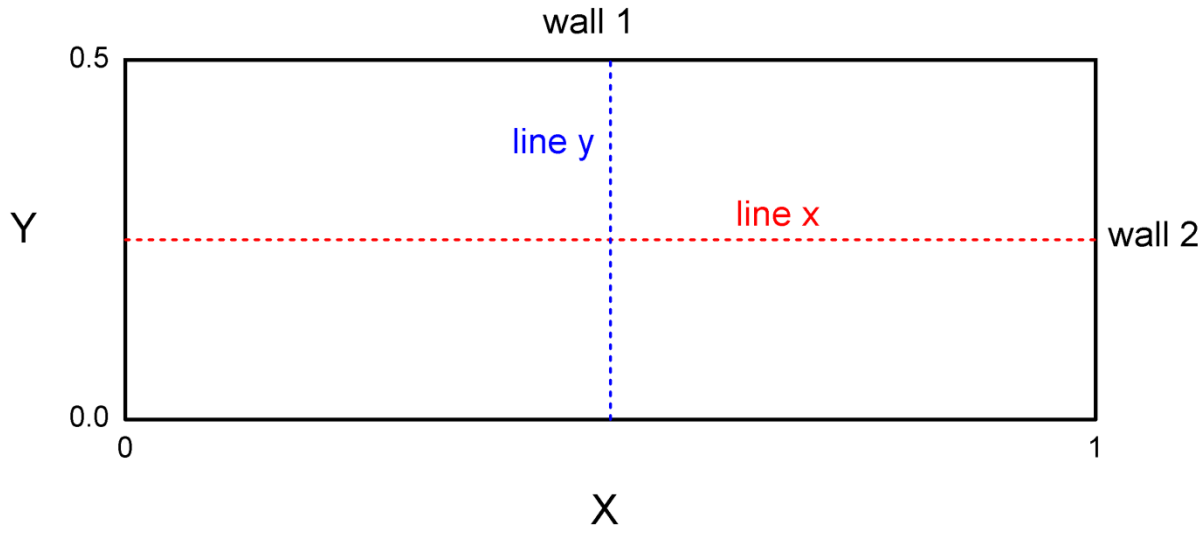

Figure 2-4: 2D rectangular enclosure.

For the two non-isothermal and inhomogeneous cases, i.e. Case 2 and 4, the distribution of the temperature and species concentration are given as follows [54].

$$T(x,y) = T_0[0.3333(1-2|x-0.5|)(1-4|y-0.25|)+1] \quad (2.19)$$

$$c(x,y) = c_0[4(1-2|x-0.5|)(1-4|y-0.25|)+1] \tag{2.20}$$

where T_0 is 1200 K and c_0 is 0.02 for CO_2 and 0.04 for H_2O. Case 5 is more representative of gas combustion process in a furnace with uniform concentrations of the participating species and a temperature field of a typical flame as described below.

$$\begin{aligned} &for\ x \le 0.1, \qquad T(x,y) = (14000x - 400)(1 - 3y_0^2 + 2y_0^3) + 800 \\ &for\ x \ge 0.1, \qquad T(x,y) = -\frac{10000}{9}(x-1)(1 - 3y_0^2 + 2y_0^3) + 800 \end{aligned} \tag{2.21}$$

where $y_0 = |0.25 - y|/0.25$.

Table 2-4: Temperature and concentration field of the five test cases.

Case	Participating gas	Temperature (K)	Mole fraction
1	CO_2	Isothermal: 1000	Homogeneous: 10%
2	CO_2	Non-isothermal: Eq. (2.19)	Inhomogeneous: Eq. (2.20)
3	H_2O	Isothermal: 1000	Homogeneous: 20%
4	H_2O	Non-isothermal: Eq. (2.19)	Inhomogeneous: Eq. (2.20)
5	CO_2 + H_2O	Non-isothermal: Eq. (2.21)	Homogeneous: 10% CO_2 + 20% H_2O

2.3.2.2 Comparison of the gas radiative models

The five test cases were studied by performing radiative heat transfer simulations using the nine-band model, the five-band model and the gray implementation of the WSGGM of Smith et al. [45]. The aim was to validate the two non-gray gas models developed in section 2.2.4 on the one hand, and to quantitative show the advantages of the non-gray gas models over the gray gas model in radiative heat transfer calculations on the other hand. A uniform grid of 100 × 50 was found to be sufficiently accurately to discretize the 2D enclosure according to a grid independence study and was therefore used in all cases. The distribution of the radiative source term along line x and line y (see Figure 2-4) as well as the heat flux profile along wall

1 and wall 2 (see Figure 2-4) are shown in Figure 2-5 to Figure 2-9 for each of the five cases. The benchmark solutions calculated by Goutiere et al [54] using the SNB model are compared with those computed by the non-gray and gray gas models discussed previously.

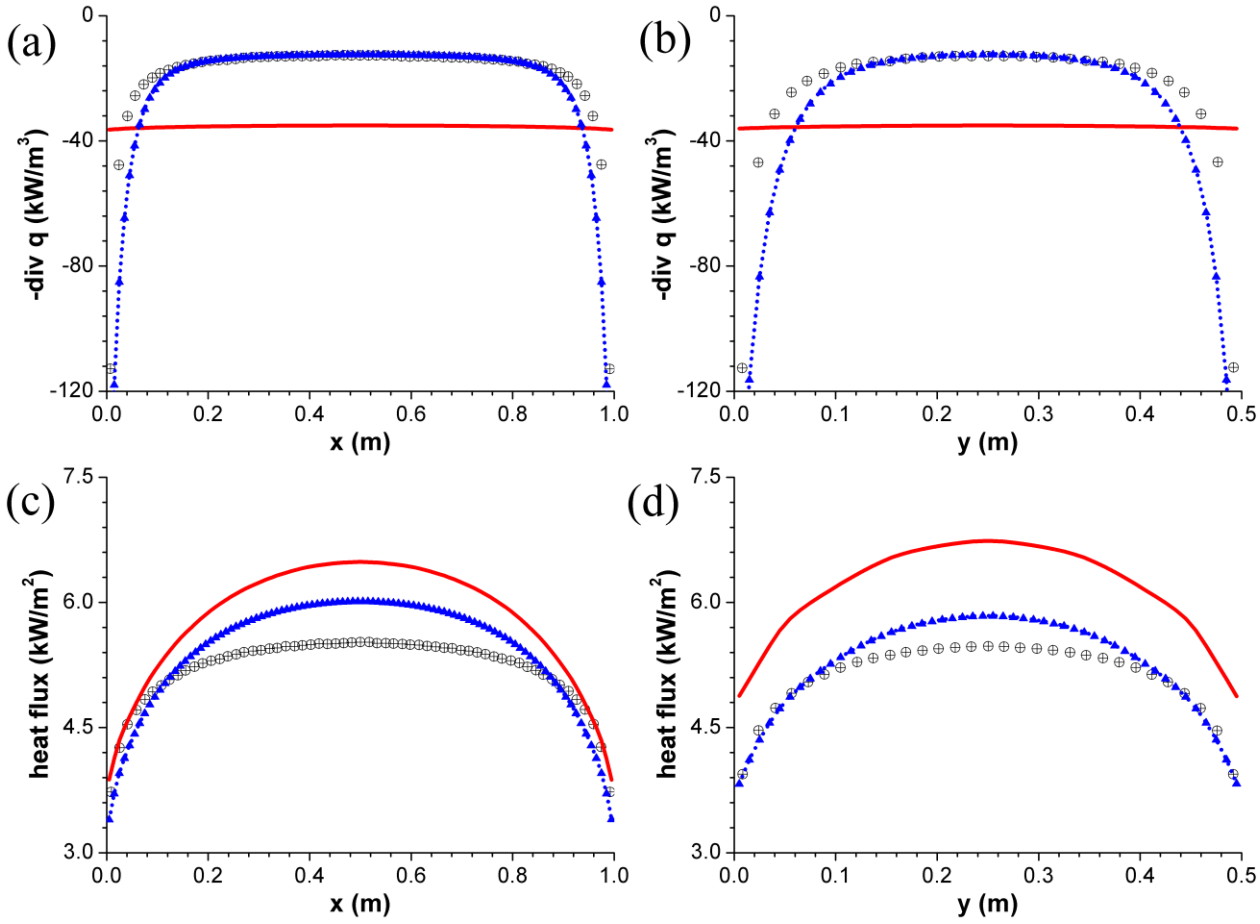

Figure 2-5: Evolution of (a) radiative source term along line x; (b) radiative source term along line y; (c) heat flux along wall 1; (d) heat flux along wall 2 for Case 1. ⊕ - SNB model; ——— - WSGGM; ••••• - nine-band model; ▲ - five-band model.

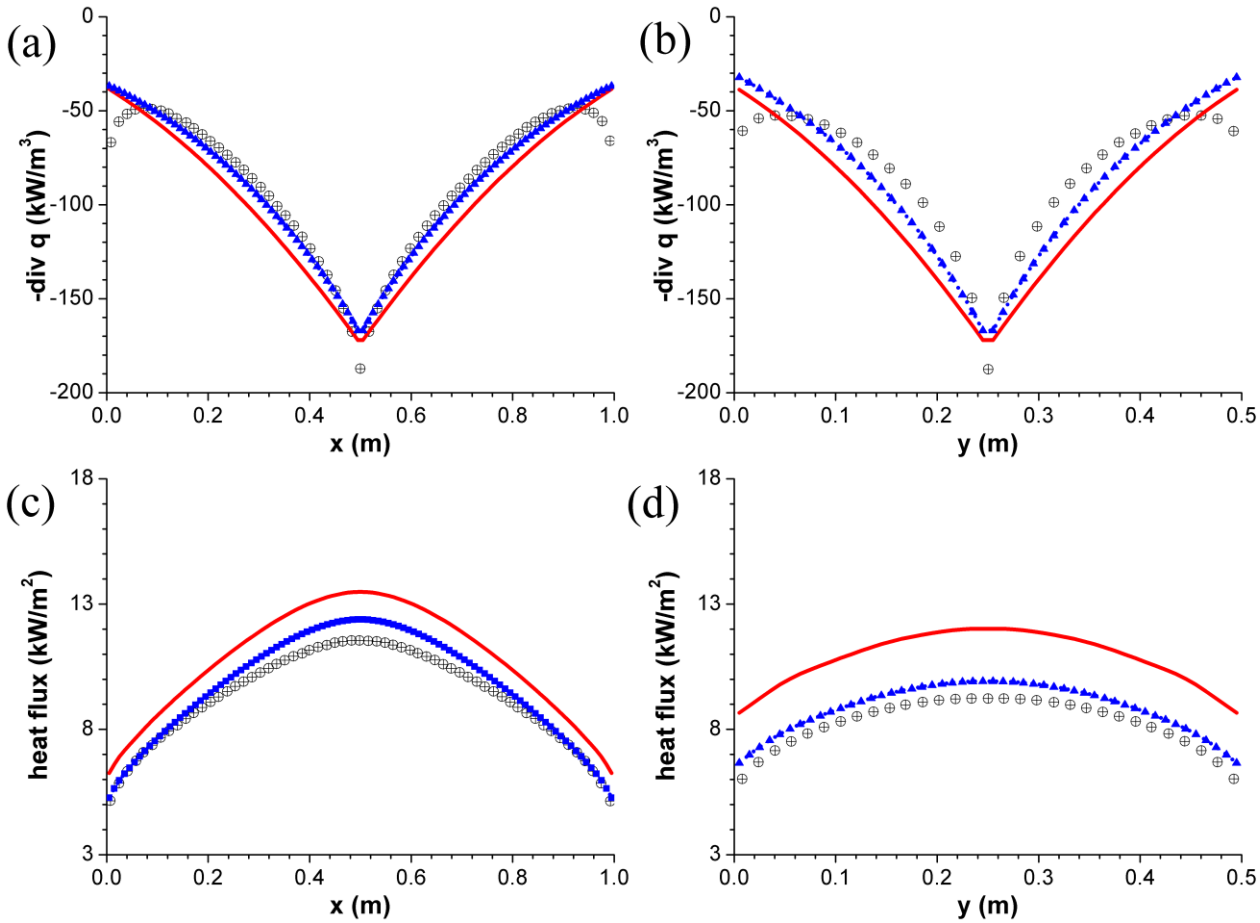

Figure 2-6: Evolution of (a) radiative source term along line x; (b) radiative source term along line y; (c) heat flux along wall 1; (d) heat flux along wall 2 for Case 2. ⊕ - SNB model; ——— - WSGGM; ••••••- nine-band model; ▲ - five-band model.

First of all, it can be observed in all figures that the nine-band model and the five-band model provide exactly the same results, which is just as expected. This means that combining all spectral windows in non-gray gas model is a successful way to reduce the number of bands and hence the computational cost. As the two non-gray models are identical, the nine-band model will be taken as the representative to compare with the gray gas model, i.e. the WSGGM, in the subsequent discussion.

Figure 2-5 (a) and (b) shows that the gray gas model (WSGGM) is incapable of capturing the reversed U-shape of the radiative source term in both x and y directions. Instead, nearly

constant values are predicted. It is interesting that the same trend can also be found in Figure 2-7 (a) and (b). As the temperature and species concentration fields in both Case 1 and Case 3 are constant, it seems that the gray treatment fails in this scenario. Besides, the wall heat fluxes are overpredicted by the WSGGM, even though the results for H_2O as participating gas (Case 3) are somewhat better than those for CO_2 as participating gas (Case 1). However, the sharp decrease of the radiative source term near the wall is well predicted in both cases by the nine-band model in spite of the overprediction at the center of line x and line y for Case 3. This may be caused by omitting the 71 μm rotational band of H_2O in the nine-band model, which plays an important role in the radiative heat transfer calculation at a temperature of 1000 K in Case 3, as previously illustrated in Figure 2-2. Nevertheless, the results of the nine-band model are generally a lot better than those of the WSGGM. In addition, the wall heat flux is less overpredicted by the nine-band model as well.

For the non-isothermal and inhomogeneous cases, i.e. Case 2 and Case 4, all models yield reasonable results, with the nine-band model again being better than the WSGGM in terms of the radiative source term calculation. However, the wall heat flux profiles predicted by the WSGGM are still too high compared to the benchmark solutions while good agreement between the nine-band model and the SNB model is observed in both CO_2 and H_2O case. It is worth to note that the nine-band model becomes somewhat less accurate in calculating the radiative source term near the walls. This is probably due to the relatively lower participating species concentration and the higher temperature close to the walls in these two cases, leading to a very small band absorptance which is in the linear regime of the EWBM calculation and thus causes serious problems in radiative heat transfer calculation. Although the fixed bandwidth method, described in section 2.2.4, was designed to remedy this, it will still bring some errors when the band absorptance becomes very small, which is usually encountered at

conditions of high temperature and low participating species concentrations. Fortunately, in combustion systems, high temperature is always accompanied by exhausted gas mixtures in which the concentration of H_2O and CO_2 is normally high, which decreases the probability that the calculated band absorptance is in the linear regime of the EWBM.

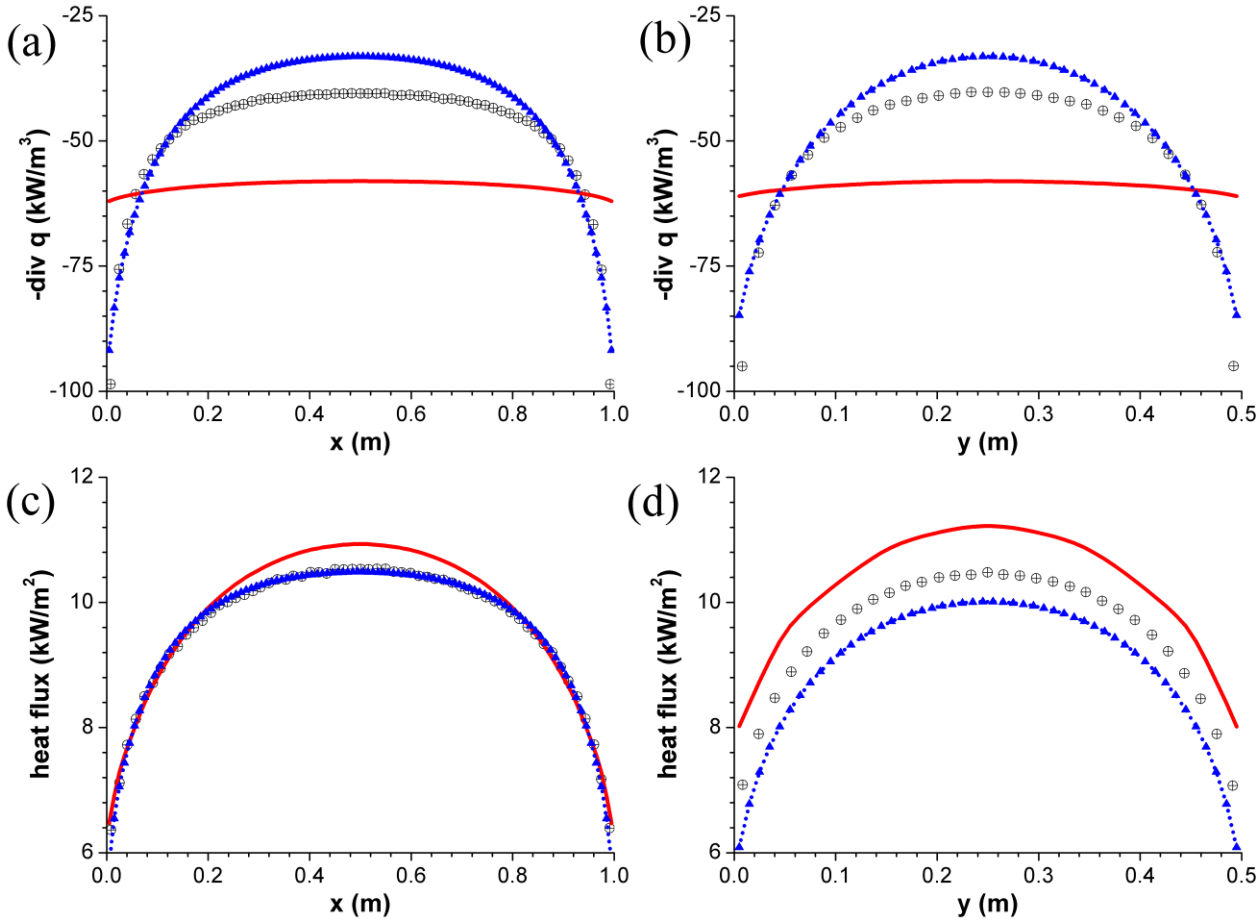

Figure 2-7: Evolution of (a) radiative source term along line x; (b) radiative source term along line y; (c) heat flux along wall 1; (d) heat flux along wall 2 for Case 3. ⊕ - SNB model; ▬ - WSGGM; ••••••- nine-band model; ▲ - five-band model.

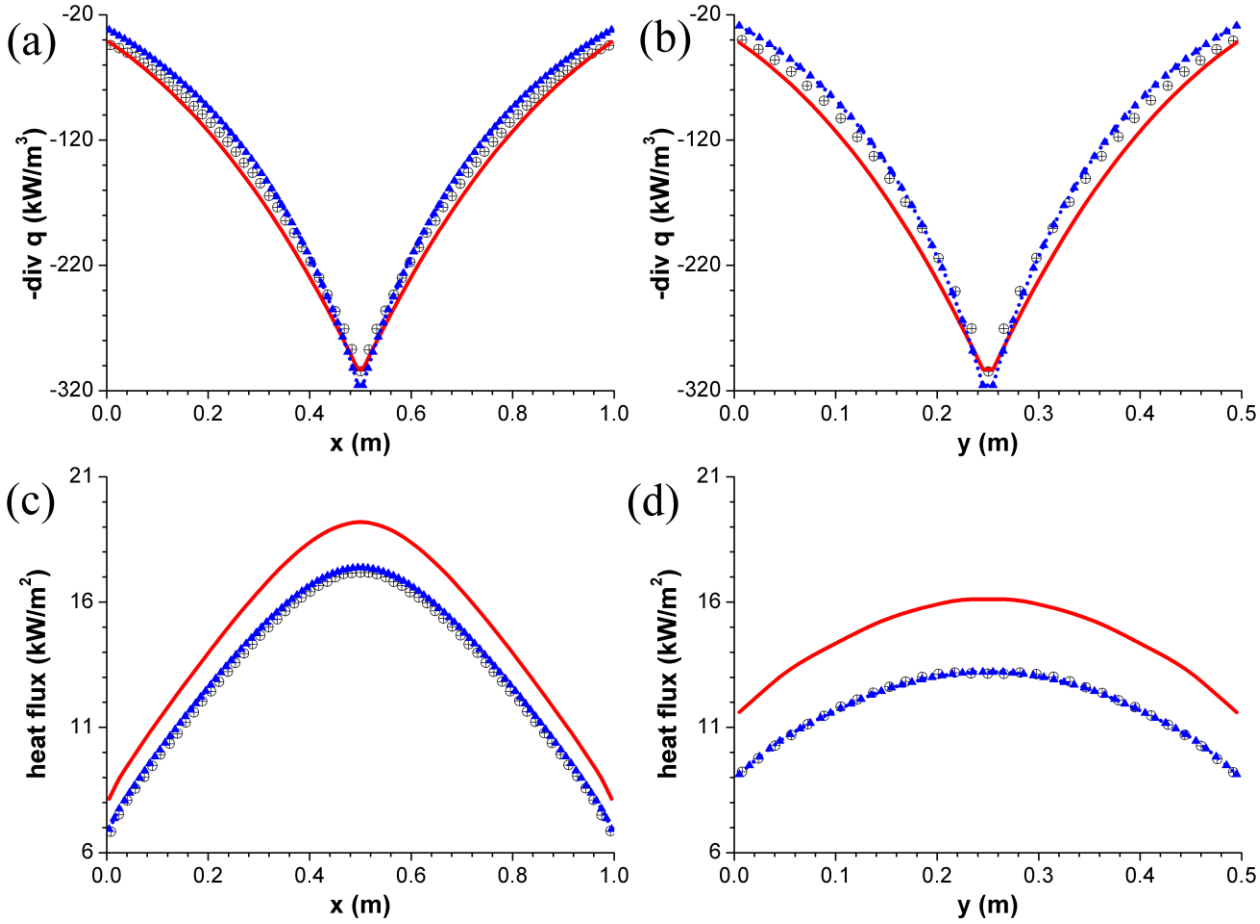

Figure 2-8: Evolution of (a) radiative source term along line x; (b) radiative source term along line y; (c) heat flux along wall 1; (d) heat flux along wall 2 for Case 4. ⊕ - SNB model; ——— - WSGGM; ••••••• - nine-band model; ▲ - five-band model.

Figure 2-9 shows the results of Case 5, which is representative of the gas combustion in a furnace. It can be observed that the nine-band model provides accurate predictions except for the heat flux profiles along the right wall (wall 2) as depicted in Figure 2-15 (d). This is again due to the omitted 71 μm rotational band of H_2O. The gas temperature near wall 2 is only about 800 K, at which the rotational band acts like an absorbing medium and reabsorbs more than 60% of the radiation emitted from the hot flame. While the lack of this band in the model leads to overprediction the heat flux reaching wall 2. However, it is worth noting that in

industrial furnaces the flue gas temperature remains at around 1100 K, hence the H_2O rotational band can be safely omitted as shown in Figure 2-3.

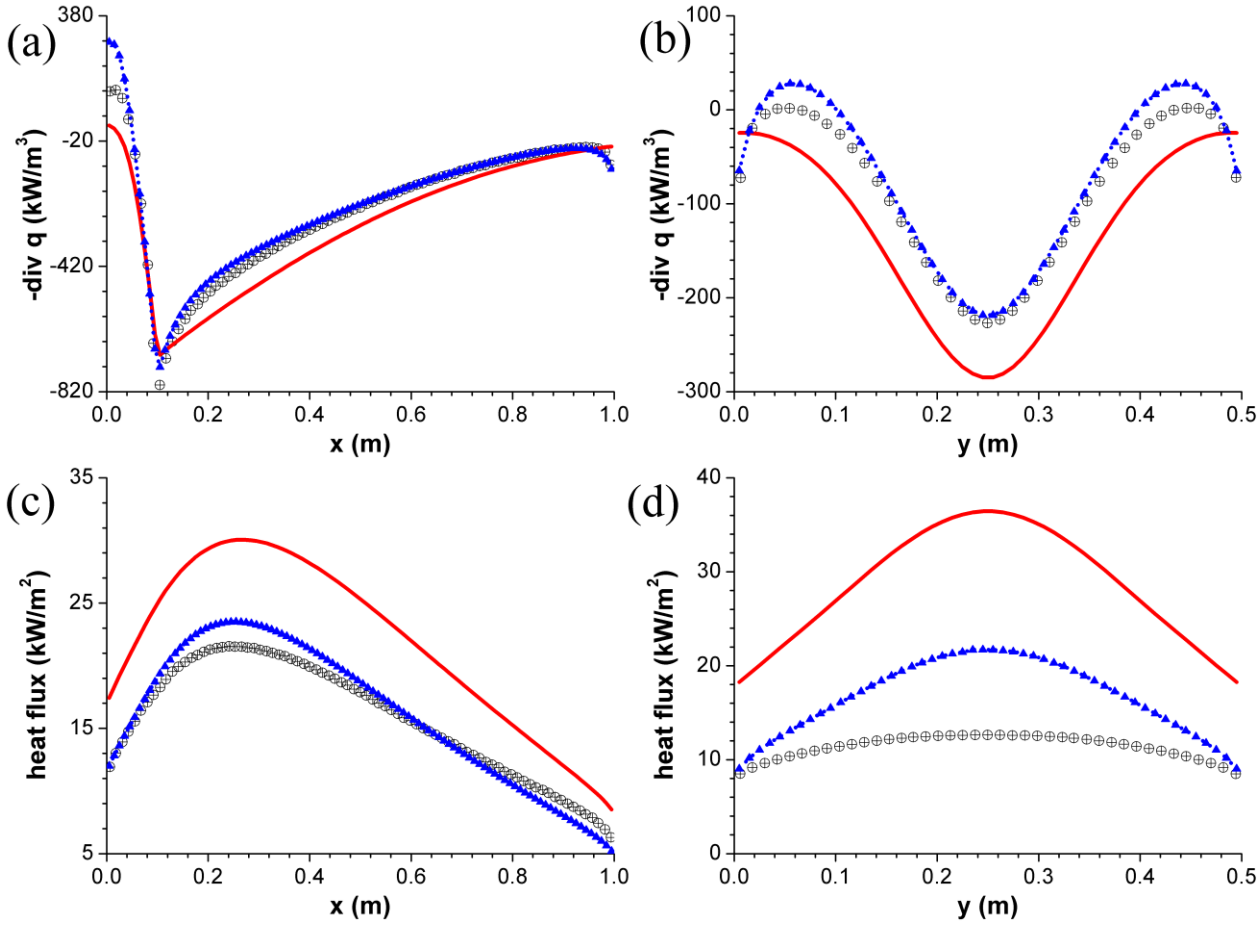

Figure 2-9: Evolution of (a) radiative source term along line x; (b) radiative source term along line y; (c) heat flux along wall 1; (d) heat flux along wall 2 for Case 5. ⊕ - SNB model; ——— - WSGGM; ••••• - nine-band model; ▲ - five-band model.

The foregoing case studies have demonstrated that the nine-band model generally performs significantly better than the gray implementation of the WSGGM and is therefore suitable for the simulation of furnaces.

2.4 Reactor and Furnace Models

2.4.1 Reactor model

For a one-dimensional plug flow reactor at steady-state, the species, momentum and energy conservation equations form a set of ordinary differential equations:

$$\frac{dF_i}{dz} = \frac{\pi d_i^2}{4} R_i \tag{2.22}$$

$$-\frac{dp}{dz} = \left(\frac{2f}{d_i} + \frac{\zeta}{\pi r_b}\right)\rho u^2 + \rho u \frac{du}{dz} \tag{2.23}$$

$$\sum_{i=1}^{N_s} F_i c_{p_i} \frac{dT}{dz} = \pi d_i q_i + \frac{\pi d^2}{4} \sum_{j=1}^{N_R} r_j \left(-\Delta H_j\right) \tag{2.24}$$

The first term at the right-hand side of equation (2.24) represents the heat flux to the reactors which is obtained from the furnace simulations. The second term accounts for the heat generation/consumption by the reactions. Based on the process gas temperature T_{gas} computed from equation (2.24), the internal tube metal temperature $T_{w,i}$ and external tube metal temperature $T_{w,o}$ can be calculated by the following equations:

$$\mathrm{q}_i = h_c\left(T_{w,i} - T_{gas}\right) \tag{2.25}$$

$$\mathrm{q}_i = \frac{2\lambda_w\left(T_{w,o} - T_{w,i}\right)}{d_i \ln\frac{d_o}{d_i}} \tag{2.26}$$

where the convective heat transfer coefficient h_c is obtained from Dittus-Boelter correlation and λ_w is the thermal conductivity of the reactor tube alloy. This external tube metal temperature profile $T_{w,o}$ is then used in the furnace simulation.

The equations above are embodied in the COILSIM1D software package. An extensive reaction network with more than 750 components and thousands of elementary reactions is used to describe the gas-phase cracking chemistry [55].

The detailed molecular composition of the feedstock is necessary because a boundary condition at the reactor inlet is needed for each species transport equation in the reactor simulation. For a complex feedstock like naphtha, only a limited number of so-called commercial indices are typically available such as specific density, average molecular mass, PIONA analysis, etc. Molecular reconstruction provides a detailed composition of the feedstock from these commercial indices [56]. The software package SIMCO is adopted here. It uses the Shannon entropy maximization method or an Artificial Neutral Network (ANN) for the molecular reconstruction of naphtha [56, 57].

2.4.2 Furnace model

2.4.2.1 Governing equations

The mass, momentum and energy conservation equations for the flow of a three-dimensional, steady-state, compressible, reactive fluid are given by:

$$\nabla \cdot (\rho \vec{u}) = 0 \tag{2.27}$$

$$\nabla \cdot (\rho \vec{u}\vec{u}) = -\nabla p + \nabla \cdot (\bar{\bar{\tau}}) + S_M \tag{2.28}$$

$$\nabla \cdot \left(\vec{u}(\rho E + p)\right) = \nabla \cdot \left(k_{eff} \nabla \mathrm{T} - \sum_i h_i \vec{J}_i + \left(\bar{\bar{\tau}}_{eff} \cdot \vec{u}\right) \right) + S_E \tag{2.29}$$

where S_M is the source term of the momentum equation which includes the contributions due to any possible body forces. Only gravity is considered in the z-coordinate, i.e. $S_{M,x} = S_{M,y} =$

0, $S_{M,z} = -\rho g . \vec{J}_i$ in the energy governing equation represents the diffusive flux of species i. The source term in the energy equation S_E is the net volumetric heat release due to radiation and reactions.

2.4.2.2 Turbulence model

The governing equations are transformed to the Reynolds Averaged Navier Stokes (RANS) equations. The Boussinesq hypothesis [58], relating the Reynolds stresses to the mean velocity gradients is used to close the Reynolds stresses. The Renormalization Group (RNG) k-ε model [59] is adopted to calculate the turbulent viscosity by solving two additional transport equations for the turbulent kinetic energy k and its dissipation rate ε:

$$\nabla \cdot (\rho \vec{u} k) = \nabla \cdot (\alpha_k (\mu + \mu_t) \cdot \nabla k) + P_k - \rho \varepsilon \tag{2.30}$$

$$\nabla \cdot (\rho \vec{u} \varepsilon) = \nabla \cdot (\alpha_\varepsilon (\mu + \mu_t) \cdot \nabla \varepsilon) + C_{1\varepsilon} \frac{\varepsilon}{k} P_k - C_{2\varepsilon}^* \rho \frac{\varepsilon^2}{k} \tag{2.31}$$

where $\mu_t = C_\mu \rho \, k^2/\varepsilon$ is the turbulent viscosity. $P_k = \mu_t S^2$ represents the production of turbulent kinetic energy, with S the modulus of the mean strain rate defined as $S_{ij} = \frac{1}{2}\left(\frac{\partial u_i}{\partial x_j} + \frac{\partial u_j}{\partial x_i}\right)$. $C_{2\varepsilon}^* = C_{2\varepsilon} + \frac{C_\mu \eta^3 (1-\eta/\eta_0)}{1+\beta\eta^3}$, $\eta = Sk/\varepsilon$. α_k, α_ε, $C_{1\varepsilon}$, $C_{2\varepsilon}$, C_μ, η_0 and β in the above-mentioned expressions are the model constants.

Since the k-ε models are primarily valid for turbulent core flows and turbulent flows are significantly affected by the presence of a wall, it is important to represent the flow in the near wall region accurately. Two approaches of modeling near-wall region are provided, being wall functions and near-wall models. The large scale of the furnace leads to a drastic increase of the computational cost if a near-wall model is used. Furthermore, the influence of the reactor and furnace walls on the flow pattern in the furnace is limited due to the vast volume compared to the rather small wall surface area. Hence, the widely used standard wall function

based on the work of Launder and Spalding [60] is adopted to account for the near-wall behavior.

This model deals with convective heat transfer on the reactor and refractory walls based on the Reynolds' analogy between momentum and energy transport, where the dimensionless temperature $T^* = \frac{(T_w - T_p)\rho c_p C_\mu^{1/4} k_P^{1/2}}{q_{conv}}$ and dimensionless distance from the wall $y^* = \frac{\rho y_p C_\mu^{1/4} k_P^{1/2}}{\mu}$ follow a linear relationship for the thermal conduction sublayer and a logarithmic law for the turbulent region. y_p T_p, and k_p represent the distance from the wall to the first near-wall node P, its temperature and its turbulence kinetic energy. All the expressions for heat transfer are well documented in the ANSYS Fluent User Guide [48] and will not be duplicated here. As the reactor external wall temperature $T_{w,o}$ is imposed, the convective heat flux q_{conv} can be calculated.

2.4.2.3 Combustion model

For a turbulent, non-premixed, combusting flow, the mole fraction Y_i of species i is calculated by solving the following species transport equations:

$$\nabla \cdot \left(\frac{\vec{u} Y_i}{V_m}\right) = -\nabla \cdot \vec{J}_i + R_i \tag{2.32}$$

where V_m is the molar volume and R_i is the net rate of production of species i, given by the following sum over the N_R reactions in which species i participates:

$$R_i = \sum_{j=1}^{N_R} \left(\upsilon''_{i,j} - \upsilon'_{i,j}\right) r_j \tag{2.33}$$

With $\upsilon''_{i,j} - \upsilon'_{i,j}$ the net stoichiometric coefficient of species i in reaction j and $r_{i,j}$ the reaction rate of reaction j. A simplified two-step global reaction network derived by

Westbrook and Dryer [61] is employed to describe the combustion process of the hydrocarbons. In this reaction network, hydrocarbons are converted to carbon monoxide and steam by partial oxidation in the first step. Carbon monoxide then reacts with oxygen to yield carbon dioxide:

$$CH_4 + 1.5O_2 \rightarrow CO + 2H_2O \tag{2.34}$$

$$C_2H_4 + 2O_2 \rightarrow 2CO + 2H_2O \tag{2.35}$$

$$CO + 0.5O_2 \rightarrow CO_2 \tag{2.36}$$

$$H_2 + 0.5O_2 \rightarrow H_2O \tag{2.37}$$

With the following reaction rate expressions:

$$r_{CH_4} = 1.5 \times 10^7 e^{-125580/RT} C_{CH_4}^{-0.3} C_{O_2}^{1.3} \tag{2.38}$$

$$r_{C_2H_4} = 7.589 \times 10^7 e^{-125580/RT} C_{C_2H_4}^{0.1} C_{O_2}^{1.65} \tag{2.39}$$

$$r_{CO} = 1.259 \times 10^{10} e^{-167430/RT} C_{CO} C_{O_2}^{0.25} C_{H_2O}^{0.5} \tag{2.40}$$

$$r_{H_2} = 10^4 C_{H_2} C_{O_2}^{0.25} \tag{2.41}$$

For the combustion of hydrogen, the kinetic parameters in equation (2.41) are taken from Stefanidis et al. [17].

To account for the effect of turbulent mixing on the reaction rates, the Eddy-Dissipation Model (EDM) is adopted. The EDM, first developed by Magnussen and Hjertager [62], assumes that the reactions taking place in the smallest turbulent structures are quite fast. Hence, the rate of combustion is determined by the rate of mixing of reactants contained in the molecular scale eddies, i.e. the dissipation rate of the eddies. Consequently, the eddy

dissipation rate, as well as the combustion rate, can be expressed to be proportional to the reciprocal of the eddy mixing time scale $\tau = k/\varepsilon$, leading to the following equations:

$$R_{i,j} = \frac{\nu'_{i,j}}{V_m} A \frac{\varepsilon}{k} \min\left(\frac{Y_R}{\nu'_{R,j}}\right) \tag{2.42}$$

$$R_{i,j} = \frac{\nu'_{i,j}}{V_m} AB \frac{\varepsilon}{k} \frac{\sum_P Y_P}{\sum_P^N \nu''_{P,j}} \tag{2.43}$$

where A and B are empirical constants equal to 4.0 and 0.5 respectively. Equation (2.42) represents the reaction rate calculated with the mole fraction of the limiting reactant involved in reaction *j*, while equation (2.43) is the rate limited by the presence of all the hot products. The net production of species *i* due to reaction *j* is then determined by the smaller of these two equations. One assumption of EDM is that the time scale of combustion rate is much smaller that of the turbulent mixing in diffusion flame. However, infinitely fast chemistry is not valid in regions with strong turbulence and low temperature. To account for the effect of finite rate of combustion, EDM is adopted here in an extended form, introducing the Arrhenius reaction rate in equation (2.33) as a "switch" for combustion kinetics governed flame region [63]. This so-called finite-rate/eddy-dissipation model takes the minimum of the Arrhenius and eddy-dissipation reaction rates as the net reaction rate.

2.4.2.4 Radiation model

The Discrete Ordinates (DO) model [64, 65] is adopted to solve the RTE for a finite number of discrete solid angles, each associated with a vector direction $\vec{s}$, leading to the following equation:

$$\nabla \cdot (I(\vec{r},\vec{s})\vec{s}) + (\kappa + \sigma_s) I(\vec{r},\vec{s}) = \kappa n^2 \frac{\sigma T^4}{\pi} + \frac{\sigma_s}{4\pi} \int_0^{4\pi} I(\vec{r},\vec{s}\,')\Phi(\vec{s},\vec{s}\,')d\Omega' \tag{2.44}$$

The first term on the left-hand side represents radiative intensity changes along a path in direction $\vec{s}$. The decrease of intensity due to absorption and scattering away from direction $\vec{s}$ by the participating gases is modeled by the second term. On the right-hand side, the two terms account for the increase of intensity by emission from the hot gases and by the radiation scattered from other directions $\vec{s}'$ to $\vec{s}$, respectively.

ANSYS Fluent also provides a non-gray implementation of the DO model solving the RTE for the spectral intensity I_i of each wavelength band separately, turning equation (2.44) into:

$$\nabla \cdot (I_i(\vec{r},\vec{s})\vec{s}) + (\kappa_i + \sigma_s) I_i(\vec{r},\vec{s}) = \kappa_i I_{b,i} + \frac{\sigma_s}{4\pi}\int_0^{4\pi} I_i(\vec{r},\vec{s}')\Phi(\vec{s},\vec{s}')d\Omega' \qquad (2.45)$$

where κ_i is the spectral absorption coefficient. The refractive index n, scattering coefficient σ_s and scattering phase function Φ are assumed to be wavelength independent. $I_{b,i}$ is the spectral black body intensity for the i-th band calculated by Planck's law:

$$I_{b,i} = \left[f\left(n\lambda_{u,i}T\right) - f\left(n\lambda_{l,i}T\right)\right]n^2\frac{\sigma T^4}{\pi} \qquad (2.46)$$

where $\lambda_{u,i}$ and $\lambda_{l,i}$ are the upper and lower wavelength limits of the band, $\Delta\lambda_i = \lambda_{u,i} - \lambda_{l,i}$ is the width of band i. The total intensity over all bands is then calculated from:

$$I(\vec{r},\vec{s}) = \sum_i I_i(\vec{r},\vec{s})\,\Delta\lambda_i \qquad (2.47)$$

Furnace refractory and reactor coils are always treated as opaque, diffuse walls when modeling the surface radiative heat transfer. In the case of gray gas radiation, the incident radiative heat flux on the wall is given by:

$$q_{in} = \int_{\vec{s}\cdot\vec{n}>0} I_{in}\vec{s}\cdot\vec{n}d\Omega \qquad (2.48)$$

The radiative heat flux leaving a surface is:

$$q_{out} = (1 - \varepsilon_w) q_{in} + n^2 \varepsilon_w \sigma T_w^4 \tag{2.49}$$

where ε_w is the emissivity of the gray wall. On the other hand, if the flue gas is considered as non-gray, the radiative heat flux at the surface is calculated on the basis of each band using the following equations:

$$q_{in,i} = \Delta\lambda_i \int_{\vec{s}\cdot\vec{n}>0} I_{in,i} \vec{s} \cdot \vec{n} d\Omega \tag{2.50}$$

$$q_{out,i} = \left(1 - \varepsilon_{w,i}\right) q_{in,i} + \varepsilon_{w,i} \left[f\left(n\lambda_{u,i} T_w\right) - f\left(n\lambda_{l,i} T_w\right) \right] n^2 \sigma T_w^4 \tag{2.51}$$

where $\varepsilon_{w,i}$ is the wall emissivity within band i with an interval width $\Delta\lambda_i$. The net radiative wall heat flux q_{rad} is then calculated by $q_{rad} = q_{out} - q_{in}$ for gray gas radiation and $q_{rad} = \sum_i \left(q_{out,i} - q_{in,i}\right)$ for non-gray gas radiation.

For most combustion processes in furnaces, the main absorbing gaseous species are H_2O, CO and CO_2 and scattering can be safely neglected ($\sigma_s = 0$) [66]. In this case, the only unknown variable for solving the RTE is the absorption coefficient of the flue gas, which is accounted for by the non-gray gas models developed in the section 2.2.4.

2.5 Simulation Methodology

2.5.1 Furnace geometry and operating conditions

The radiation section of an Ultra Selective Conversion (USC) furnace was studied in this chapter. Only one-fourth of the furnace, as depicted in Figure 2-10, was simulated to reduce the computational cost. Two sets of eleven U-coil reactors, are suspended in the center line of the furnace. Every U-coil has two passes, i.e. an inlet and outlet leg connected by a return bend and a joint where the diameter gradually expands from the inlet leg diameter to the outlet leg diameter. Eight floor burners positioned against the furnace refractory side walls

supply the heat for the endothermic cracking reactions. The burners are grouped in four sets of two burners at opposite sides of the reactors. Each burner has primary and staged fuel inlets reducing the non-premixed flame temperature and, hence the NO_x formation. The dimensions of the furnace and reactors, the fuel and feedstock composition and the operating conditions are summarized in Table 2-5.

Two furnace configurations were considered to investigate the effect of accounting for the burner details on the furnace simulation. In the first configuration, the geometrical details of the burners such as stages and tips were modeled, while in the second configuration the burners were modeled as a rectangular hole in the furnace floor as done in some previous work [14, 17]. The fuel and air inlets in both configurations were extended upstream to ensure fully developed turbulent flow entering the furnace. A mixed meshing scheme was used to discretize the furnace domain. Hexahedral cells were used in the upper part of the furnace where the reactor tubes are straight. Tetrahedral cells were first generated near the burners and the return bends due to the geometrical complexity. The tetrahedral cells were then converted to polyhedral cells to reduce the number of cells and improve the numerical stability of the solver [48]. The mesh was refined until no significant changes of the flow variables at the furnace stack were simulated. The total number of cells of the furnace with detailed and simplified burners was about 6.39 and 7.24 million respectively.

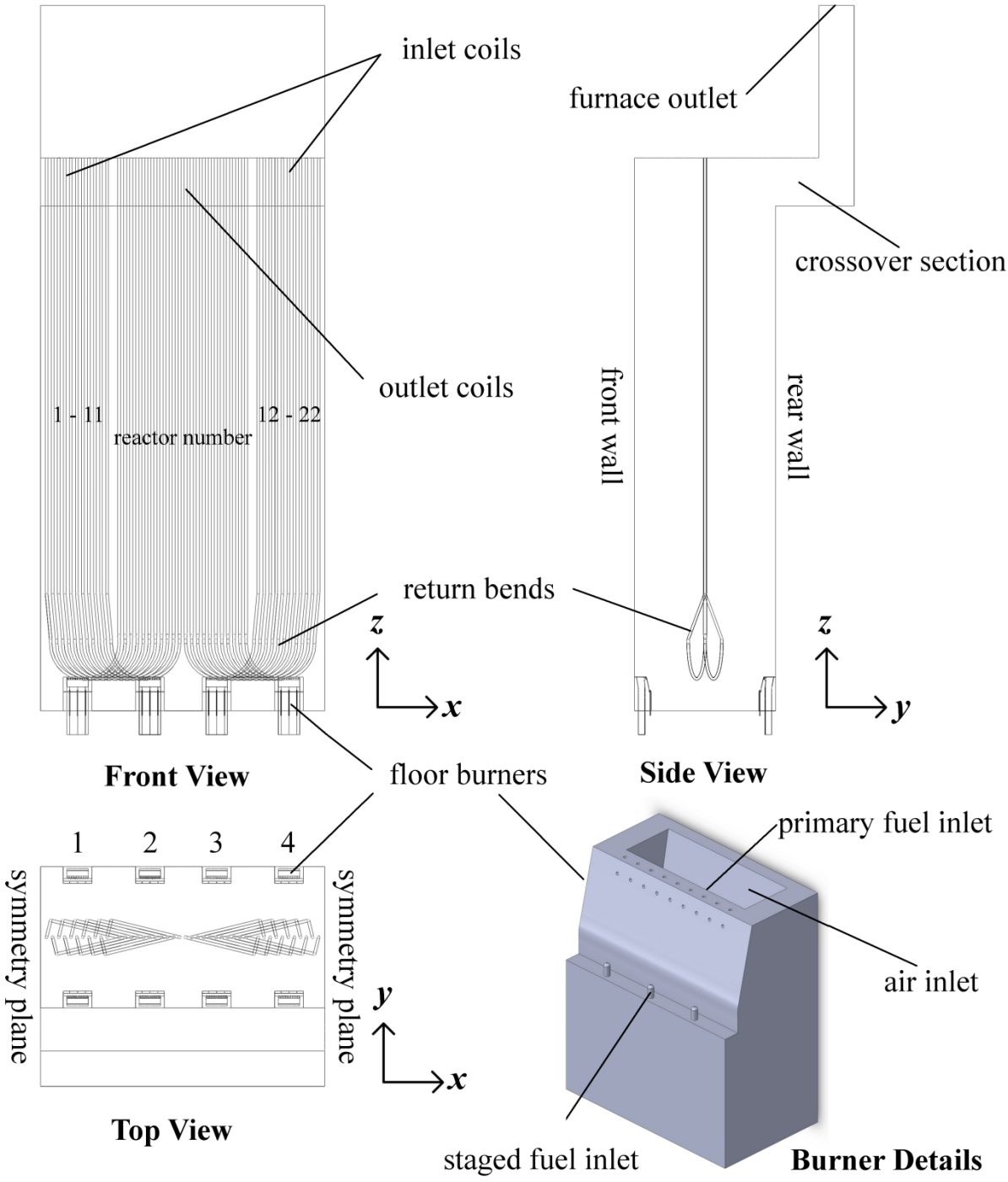

Figure 2-10: Schematic representation of the simulated furnace segment and detailed burner geometry.

Table 2-5: Furnace dimensions and operating conditions.

Simulated furnace segment	
Length x-direction (m)	5.969
Width y-direction (m)	2.964
Height z-direction (m)	11.609
Number of burners	8
Firing condition	
Fuel gas flow rate (kg/s)	0.2777
Air equivalence ratio	1.2
Fuel gas inlet temperature (K)	288.75
Furnace outlet pressure (Pa)	101300
Fuel composition (mol%)	
CH_4	88.55
H_2	11.14
CO	0.17
C_2H_4	0.14
Reactor coils	
Number of coils	22
Reactor coil length (m)	22.792
Number of passes	2
Inlet leg external diameter (m)	0.0566
Inlet leg thickness (m)	0.0058
Outlet leg external diameter (m)	0.0666
Outlet leg thickness (m)	0.0078
Coil operating condition	
Feedstock flow rate of single coil (kg/s)	0.0914
Steam dilution ratio (kg/kg)	0.5
Coil inlet temperature (K)	853.15
Coil inlet pressure (Pa)	236325
Feedstock PIONA (wt%)	
n-Paraffins	29.25
i-Paraffins	29.25
Naphthenes	31.50
Aromatics	10.00
Material properties	
Furnace refractory emissivity	0.75
Reactor tube skin emissivity	0.85

2.5.2 Solution procedures

All the governing equations for the furnace simulation are discretized using the finite volume method and solved with a segregated solver. The convection operators are discretized by a

second-order upwind scheme. The Semi-Implicit Method for Pressure-Linked Equations (SIMPLE) is employed for pressure-velocity coupling. The commercial CFD software ANSYS Fluent 14.0 is applied.

Three coupled furnace-reactor simulations were performed to evaluate the influence of flue gas radiative properties and burner geometry on the flow, combustion and heat transfer in the furnace. Gray and non-gray gas radiation models were compared in the furnace configuration with detailed burner geometry. The default WSGGM implemented in ANSYS Fluent described above was used for the gray gas simulation since it was often used in previous work [18-20, 22, 23]. In the non-gray simulations, the flue gas absorption coefficient was calculated by the above described nine-band model implemented in a user-defined function. The furnace refractory wall and reactor tubes were treated as gray diffusive walls in all three cases, in other words, the wall emissivity of all bands in the non-gray simulations is constant and specified in Table 2-5. The heat loss through the furnace refractory walls was calculated from a heat balance over the industrial unit and accounts for about 1% of the total heat of combustion. This value is set as a uniform heat flux boundary condition at the furnace walls.

The reason for performing coupled furnace-reactor simulations is to investigate the interaction between the fire side and process gas side for all three cases. Similar as in the work by Hu et al. [20], solution procedure of the coupled simulation is described as follows. First a furnace simulation is performed using an initial guess for the external Tube Metal Temperature (TMT) profiles as thermal boundary condition on the reactor outer walls. When the residuals of all the transport equations are lower than 10^{-4} (for energy equation is 10^{-6}) and the changes of the flow variables such as stack outlet temperature and O_2 mole fraction over 500 iterations are below 0.1 K and 0.05% respectively, the simulation is considered as converged. The tube external heat flux q_o which consists of q_{rad} and q_{conv} is then obtained by the models and

expressions discussed previously in the turbulence model and the radiation model sections. Afterwards q_o is converted to the heat flux based on the internal tube area, q_i, by the following expression $\frac{q_o}{q_i} = \frac{d_i}{d_o}$. By solving equation (2.24) - (2.26) for each of the 22 reactors, updated external TMT profiles for all reactors are generated. This process is repeated until the maximum differences between the previous and the updated TMTs for every reactors are less than 1 K. All 22 reactors were simulated using updated heat flux profiles obtained from the furnace simulation, whereas in previous coupled simulations [19, 20, 22, 23, 67] only one reactor was simulated. The total flow rate was uniformly distributed over all reactors to enable an easy evaluation of the variation in cracking severity over the different reactors due to shadow effects. The industrial unit is also operated with a uniform mass flow rate distribution.

The furnace simulations were performed on two 32-core computing nodes with AMD Magny-Cours Opteron 6136 processors and required about 15 h and 20 h wall time for gray and non-gray cases respectively. The CPU time of the reactor simulations is negligible, requiring less than 2 minutes for 22 reactor simulations. In total 5 furnace-reactor iterations were required for each of the three cases to be converged. It thus takes approximately 75 h and 100 h to finish a gray or a non-gray case on two 32-core machines respectively, as shown in Table 2-6. The 4π angular space at each spatial location was discretized into 32 solid angles in DO model, which corresponds to a discrete number of 2×2 for the polar angle θ and the azimuth angle φ respectively in each octant. Although it has been demonstrated in Appendix A that the θ×φ = 4×4 is just sufficient to eliminate the ray effect in DO model and to obtain heat flux results which are independent of the discrete number, the data file is unacceptably large as 72 GB in this case. Therefore a compromise between the computational cost and the discrete number was made and 2×2 was eventually used in the current simulation. This means the

radiative intensities in all 32 solid angles need be stored for every cell for the gray gas simulation. In a non-gray simulation, the number increases to 9×32 since the RTE is solved for all 9 bands. This results in very large disk space requirements, i.e. about 3.7 GB and 21.8 GB for one gray and non-gray data file respectively. As the RTE is solved once every 10 flow iterations, only around 10% of the total computational cost is spent on radiative heat transfer calculation. This explains why the total clock time does not differ very much for the gray and the non-gray cases.

Table 2-6: Comparison of simulation results of all three cases with the industrial design data.

	Gray Detailed	Non-gray Detailed	Non-Gray Simplified	Industrial design data
Flue gas outlet temperature (K)	1298.5	1367.0	1370.4	1364.2
Total heat transfer to the process (kW)	6994.66	6485.71	6453.50	6425
Furnace thermal efficiency (%)	49.41	45.81	45.58	45.48
COT range (K)	1108.7-1206.0	1135.9-1165.0	1136.8-1161.4	1161.2
Ethene yield range (wt%)	30.30-30.71	28.33-29.82	28.43-29.65	28.1
Propene yield range (wt%)	9.28-12.16	13.80-15.93	14.15-15.85	n.a.
P/E ratio range (wt%/wt%)	0.30-0.40	0.46-0.56	0.48-0.56	n.a.
Total clock time on two 32-core machines (h)	75.85	96.65	98.90	n.a.

2.6 Results and Discussion

2.6.1 Flow variables in the furnace

Three cases were studied: a ‘gray gas radiation model and detailed burner geometry’ case, a ‘non-gray gas radiation model and detailed burner geometry’ case and a ‘non-gray gas radiation model and simplified burner geometry’ case. They are referred to as “gray detailed”, “non-gray detailed” and “non-gray simplified” respectively.

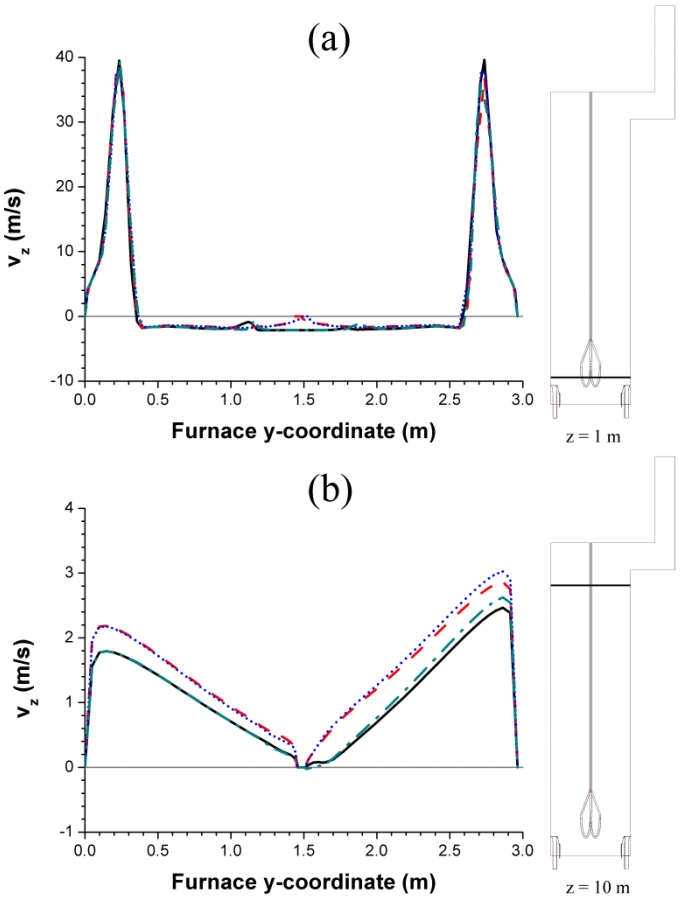

Figure 2-11: Flue gas velocity z-component (m/s) for the gray detailed case as a function of furnace y-coordinate (m) at the center of different burner sets at (a) height = 1 m; (b) height = 10 m: ——— – burner set 1; – – – – burner set 2; ····· – burner set 3; – · – – burner set 4.

As shown in the top view in Figure 2-10, four burner sets are positioned in the furnace, each consisting of two burners at opposite sides of the reactors. The flue gas velocity profiles along the width of the furnace at the x-coordinate of the center of the different burner sets for the gray detailed case are depicted in Figure 2-11. For z = 1 m, the velocity difference between the burner sets is less pronounced compared to the profiles at z = 10 m. The only exception is at the center of the furnace where burner set 1 and 4 show a higher downward velocity compared to burner set 2 and 3 in Figure 2-11 (a). The start of the return bends are located near burner set 1 and 4, creating more space between the reactors for the flue gas to pass.

However, near burner set 2 and 3 the end of the returns bends are located, creating very little space between the reactors. This observation explains the velocity difference in the furnace center between the four burner sets. At z = 10 m in Figure 2-11 (b), the flue gas velocity is higher above burner set 2 and 3. The temperature above these burners is slightly higher compared to burner set 1 and 4 because here the outlet tubes are located which absorb less heat. This higher temperature leads to a lower gas density and resulting higher velocity above these burners. As similar results are obtained for the non-gray detailed case and the non-gray simplified case, comparison between the different cases will be done at the x-coordinate of burner set 1, i.e. x = 0.778 m.

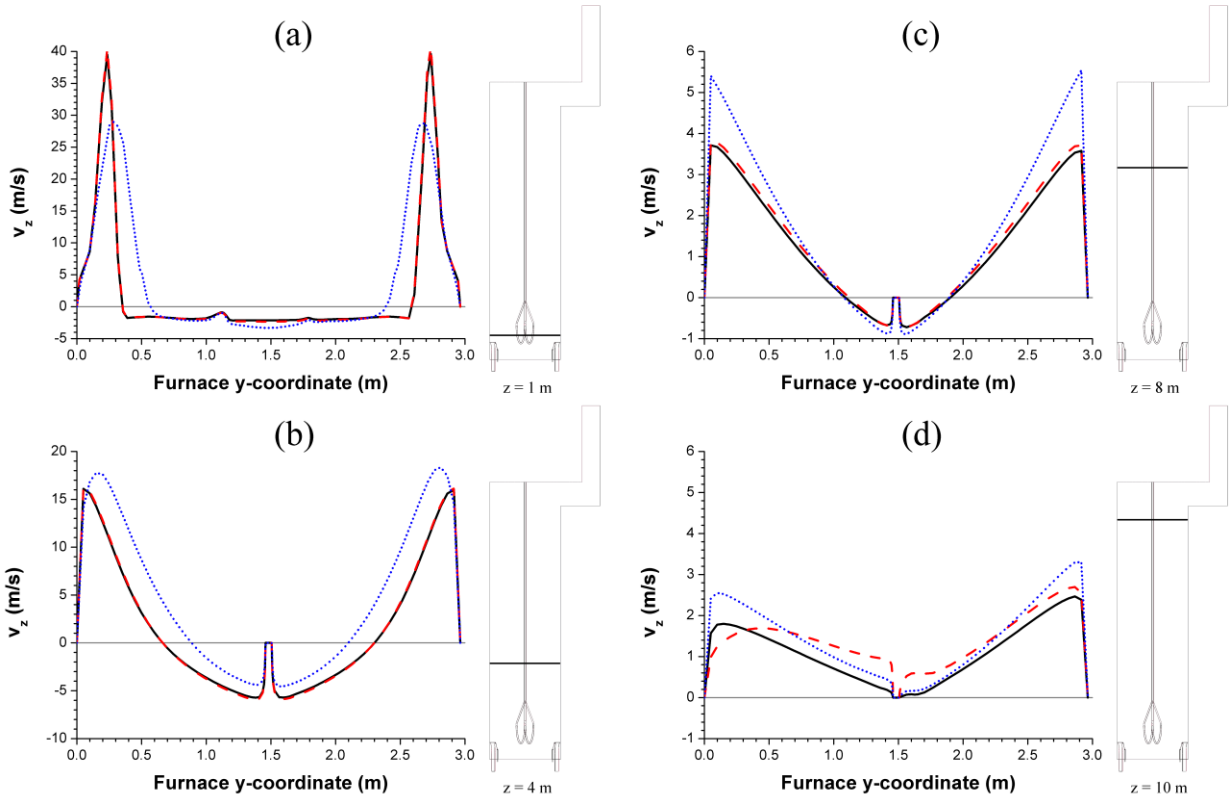

Figure 2-12: Flue gas velocity (m/s) as a function of furnace y-coordinate (m) at different heights above the center of the burner set 1, i.e. at x = 0.778 m: (a) height = 1 m; (b) height = 4 m; (c) height = 8 m; (d) height = 10 m: ——— – gray detailed case; – – – – non-gray detailed case; ····· – non-gray

simplified case.

Figure 2-12 compares the flue gas velocity profiles along the furnace width in the vertical plane x = 0.778 m at different heights for the three cases. The gas radiative properties have very limited effect on the flue gas velocity profiles, especially at the lower heights in the furnace. The velocity difference between the gray detailed and non-gray detailed cases only becomes distinguishable near the furnace ceiling. Slightly higher velocities are predicted in the non-gray detailed case compared to the gray detailed case. The upward velocity is driven by two phenomena: the pressure difference between the burner inlet and the furnace outlet and buoyancy force due to temperature differences of the flue gas. The effect of the former is overwhelming at heights near the burners, while the latter starts to have some influence when the effect of the high velocity near the burners has faded out. As higher flue gas temperatures are predicted by the non-gray detailed simulation near the furnace top as shown in Figure 2-13, the upward velocity is higher compared to the gray detailed case. On the other hand, the velocity difference between the non-gray detailed and non-gray simplified simulations is more pronounced as seen in Figure 2-12. Because of the detailed tip structure of the nozzle, the fuel gas flows out of the burner towards the furnace refractory. This causes a velocity distribution of the non-gray detailed case which is narrower and closer to the front and rear wall than that of the non-gray simplified case. Higher velocity at the burner outlet leads to stronger recirculation in the furnace as indicated by the higher absolute value of the downward flue gas velocity close to the center of the furnace calculated from the non-gray detailed simulation. With the increase of the height near the bottom of the furnace, the velocity predicted by the non-gray detailed case decreases rapidly as a result of the friction

with the wall. Thus the flue gas velocity for the non-gray detailed case is first higher than that of the simplified one and becomes lower at around z = 4 m.

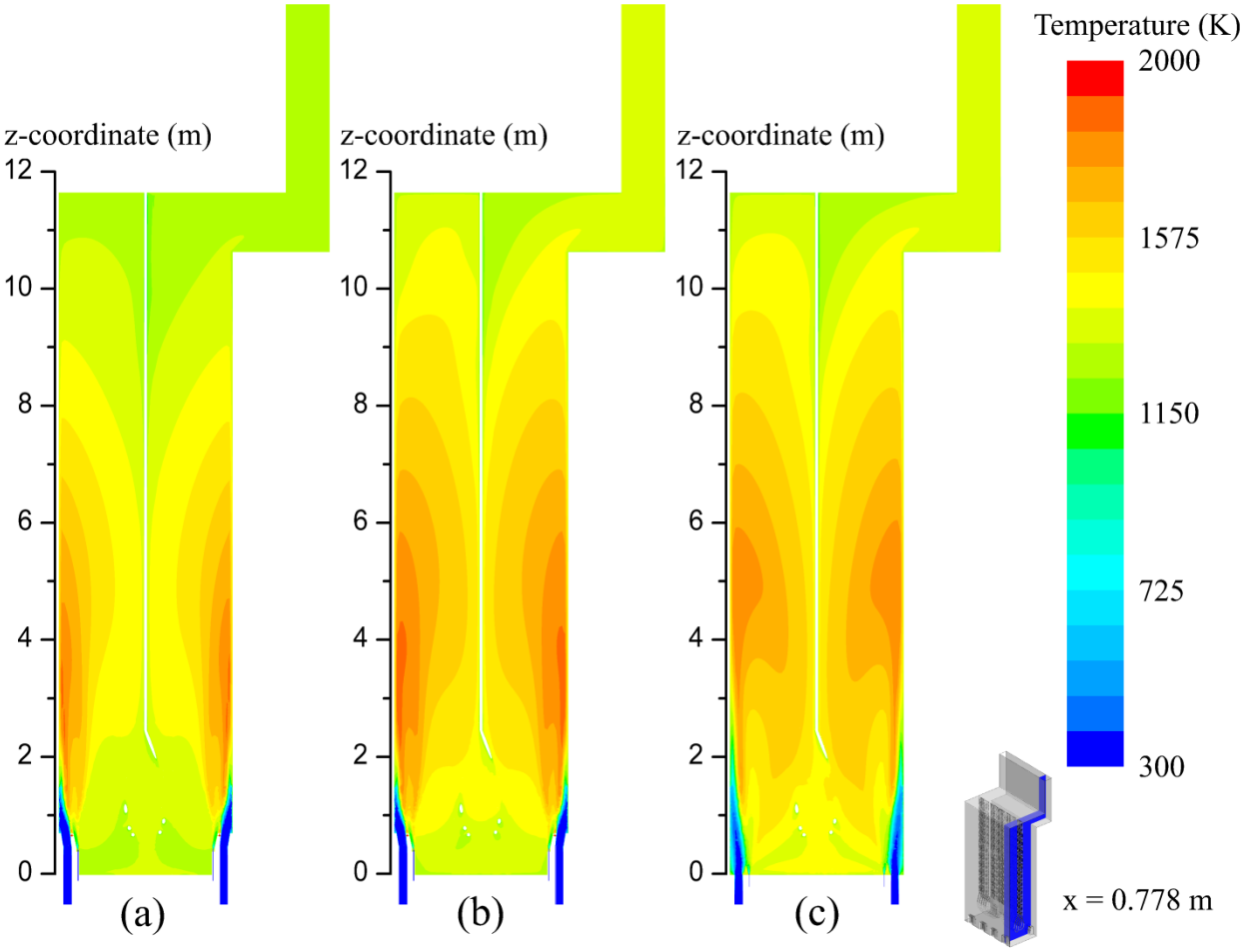

Figure 2-13: Temperature (K) field in a vertical cross section at the center of the burner set 1, i.e. at x = 0.778 m: (a) gray detailed case; (b) non-gray detailed case; (c) non-gray simplified case.

The flue gas temperature contours of a vertical cross section at x = 0.778 m are depicted in Figure 2-13. Higher flame temperatures are simulated when using non-gray gas radiative properties, which is consistent with the work of Wang et al. [68] and Stefanidis et al. [27]. Although the flue gas temperature differs a lot between the gray detailed and non-gray detailed cases, the flame shapes of the two cases are very similar. However, simplification of

the burner geometry gives a different temperature distribution with a much wider flame and a shift of the temperature maximum to higher positions. This suggests that the radiative properties mainly determine the mean flue gas temperature while the burner details determine the temperature distribution. Figure 2-14 (a) shows the mixing-cup averaged flue gas temperature as a function of height. Below 2 m, the burner geometry determines the temperature as the non-gray simplified case shows a higher temperature than the gray detailed and non-gray detailed cases. The temperature in the non-gray simplified case is higher because the fuel and air inlet is lower compared to the detailed cases, i.e. at z = 0 m instead of at z = 0.7 m because of the burner geometry. The influence of the radiative properties is small because only a minor amount of CO_2 and H_2O has been formed at these heights. In the detailed burner cases, fuel is forced towards the air by the burner tip, enhancing turbulent mixing and increasing the consumption rates. This results in a rapid temperature rise in both the detailed burner cases. Above 5 m, the radiative properties determine the temperature as the effect of the burner has faded out and radiation dominates the flue gas temperature instead of reaction and convection.

Figure 2-15 (a) and (b) show the mole fraction and consumption rate of methane in the vertical plane at x = 0.778 m respectively. As the fuel consists of 90 mol% methane, most heat is released from the combustion of CH_4. These two variables are very similar for the two detailed burner simulations, which is in agreement with the similar temperatures near the burners of these simulations. Methane flows out of the nozzle in the direction of the refractory wall to better mix with the air, resulting in a narrow flame close to the wall. Two regions with high methane consumption rate corresponding to the primary and staged fuel inlets are observed in Figure 2-15 (b). In the non-gray simplified case, the primary and staged fuel inlets are both placed in the furnace floor. Hence, the two methane flows meet and a single

region with high methane consumption is simulated. As the flame is wider, the average velocity of the flame is lower compared to the detailed burner cases. Less turbulence is therefore created leading to lower consumption rates and a shift upwards of the temperature maximum of about 0.5 m.

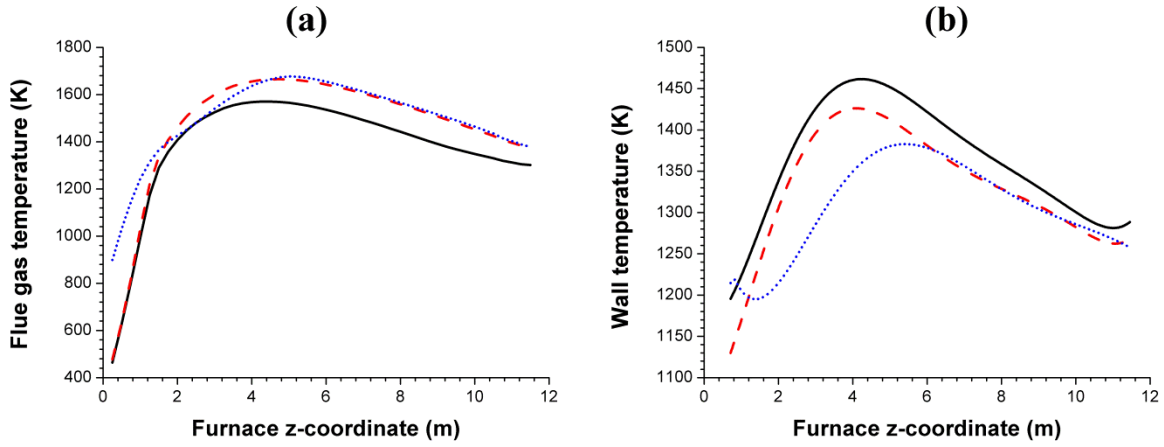

Figure 2-14: (a) Mixing-cup averaged flue gas temperature (K) and (b) area-averaged furnace refractory wall temperature (K) as a function of furnace z-coordinate (m) above the burner at x = 0.778 m: ——— – gray detailed case; – – – – non-gray detailed case; ····· – non-gray simplified case.

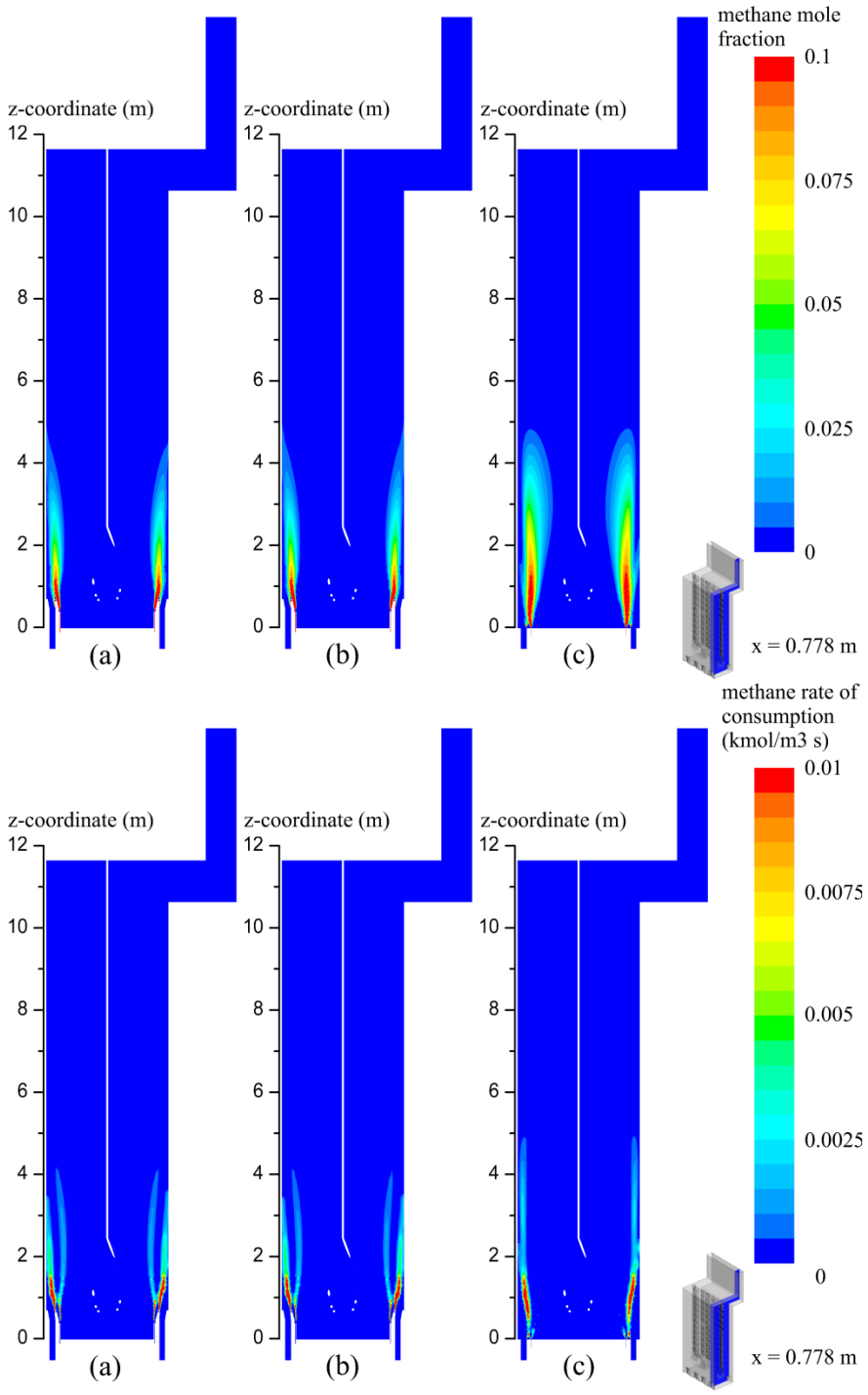

Figure 2-15: Methane mole fraction (top) and methane rate of consumption (kmol/m³/s) (bottom) field in a vertical cross section at the center of burner set 1, i.e. at x = 0.778 m: (a) gray detailed case; (b) non-gray detailed case; (c) non-gray simplified case.

2.6.2 Gas radiative properties

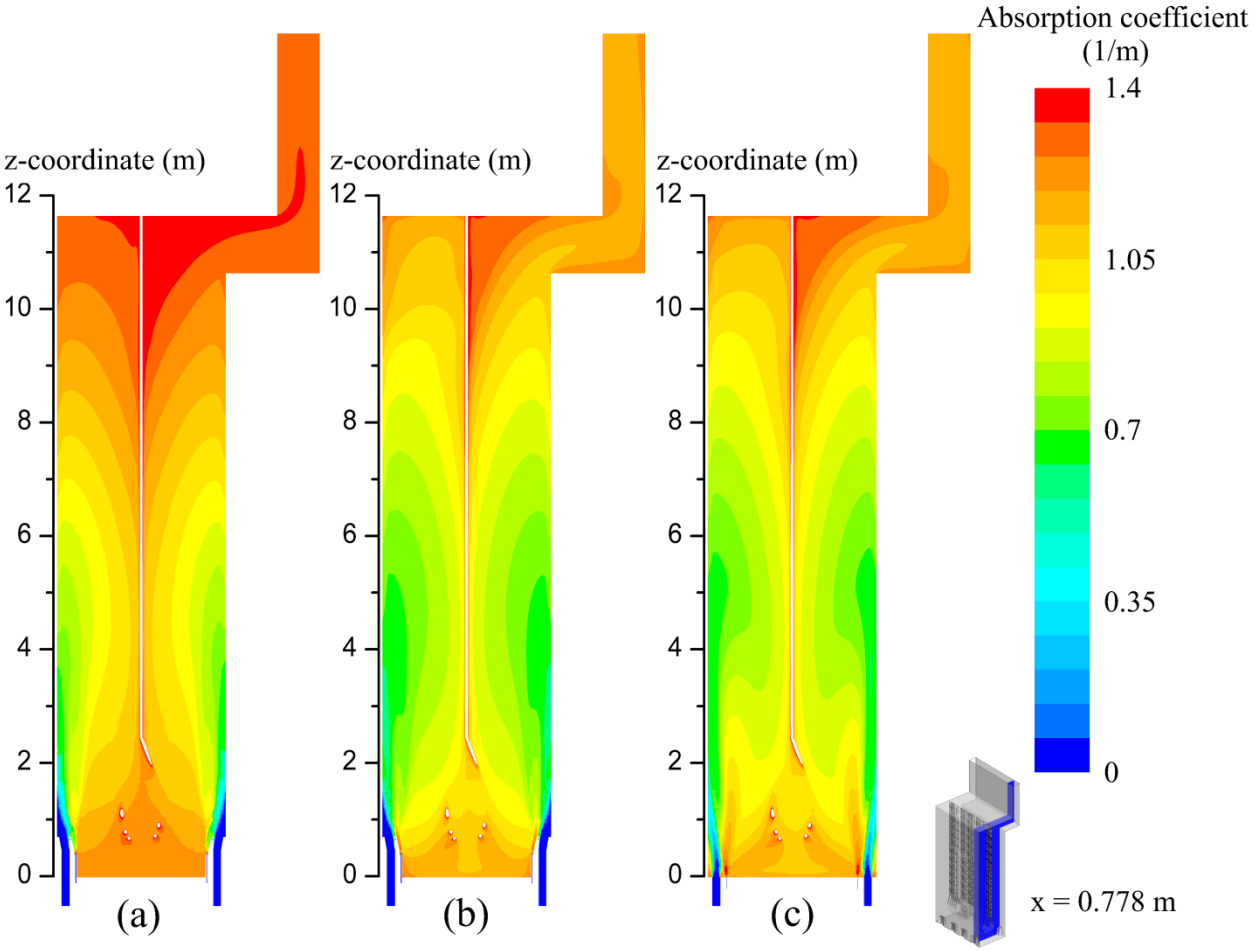

Figure 2-16: Total absorption coefficient κ (1/m) field in a vertical cross section at the center of burner set 1, i.e. at x = 0.778 m: (a) gray detailed case; (b) non-gray detailed case; (c) non-gray simplified case.

The absorption coefficient of the flue gas mixture in the vertical plane x = 0.778 is depicted in Figure 2-16. For the non-gray gas cases, the total emissivity is calculated by summing the emissivities of all absorption bands to obtain the absorption coefficient of the flue gas mixture based on Beer's law. The absorption coefficient shows an inverse dependency on temperature, i.e. lower values occur at higher temperatures, which is in agreement with Figure 2-1 (a) at the temperatures prevailing in the furnace. Only near the burner inlets do low temperatures

and low absorption coefficients coexist as fuel conversion is low here and no absorbing species, i.e. H_2O or CO_2 are present.

It would be expected that the calculated furnace thermal efficiency, i.e. the ratio of the heat transferred to the reactors to the total heat release, using a non-gray gas radiation model is higher as the flame temperature is higher, which means more heat is emitted from the flame. However, the opposite is observed. The bands in a non-gray model can be divided into two main band categories: the spectral windows and the absorbing/emitting bands. Radiation emitted by the refractory walls with wavelengths in the spectral windows travel directly to the reactor coils without interference of the flue gas. Radiation with wavelengths in the other bands experiences an absorbing and re-emitting process by the flue gas before reaching the reactors. Figure 2-17 shows the contribution of the nine bands to the total incident radiation on the reactors for the non-gray detailed and non-gray simplified cases. As very similar results are obtained for the two cases, only the non-gray detailed case is discussed here. About 68% of the total incident radiation on the reactor coils is emitted through the spectral windows, i.e. summation over bands 1, 3, 5, 7 and 9 in Figure 2-17. As in the spectral windows, radiation is determined by the walls, the incident radiation on the reactors depends much more on the refractory wall temperature than on the flue gas temperature. It can be observed in Figure 2-14 (b) that the gray details case gives more than 50 K higher furnace refractory wall temperature than the non-gray detailed case, which results in more energy emitted from the refractory and increases the incident radiation on the reactors. Thus the furnace thermal efficiency is much higher in the gray detailed case due to its higher refractory wall temperature and radiative energy emission.

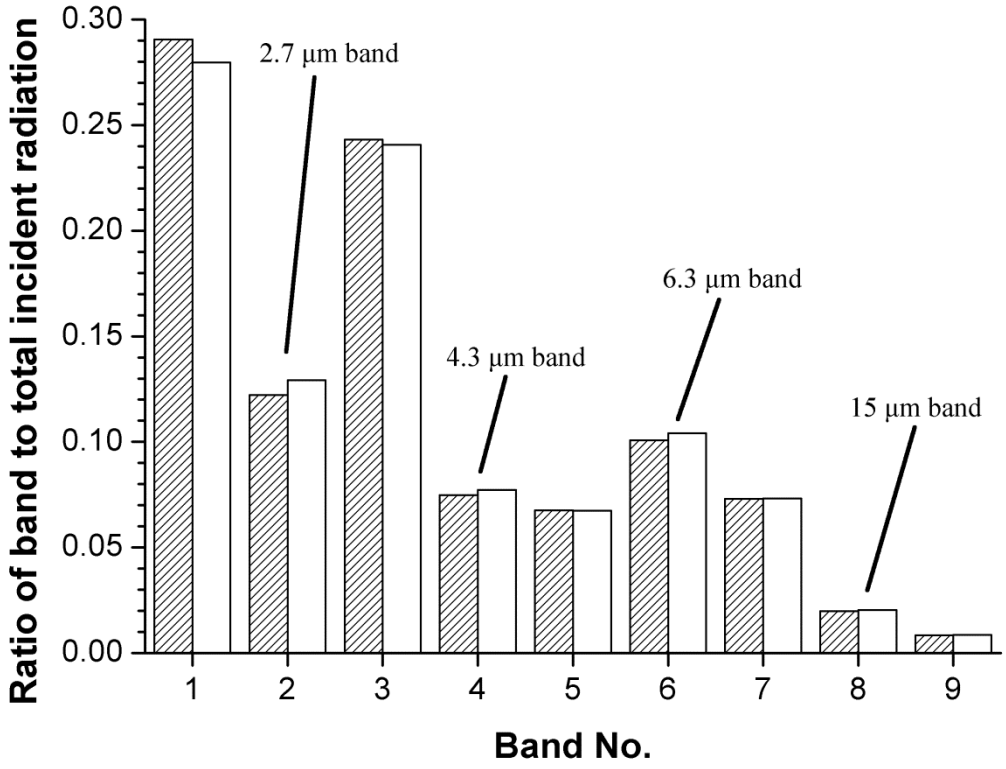

Figure 2-17: The ratio of the band incident radiation to the total incident radiation on the reactors: ▨ – non-gray detailed case; □ – non-gray simplified case where band 2, 4, 6, 8 represent the 2.7 μm, 4.3 μm, 6.3 μm, and 15 μm absorption bands respectively and band 1, 3, 5, 7, 9 represent the spectral windows.

Figure 2-18 shows the band incident radiation in the first spectral window, in the 2.7 μm band and the incident radiation over the entire spectrum for the non-gray detailed case in the horizontal plane z = 4.5 m. These bands are chosen as they contribute the most to the total incident radiation of all bands in their band category. The incident radiation of the other bands is very similar to that of the depicted band of their band category. In the spectral window, the incident radiation is determined by the wall and reactor outer wall temperature and the relative position of the surfaces to one another, i.e. the view factors. In Figure 2-18 (a) the

maximum radiation intensity is located just above the burners because the wall temperature is maximal at this height. The reactor tubes in-between two burners receive most radiation in the spectral windows, while the reactors in front of a burner receive the least amount of incident radiation. The configuration of the burners and reactors in the furnace makes that the view factor from the high temperature wall zones, i.e. above the burners, is higher to the reactor tubes in-between two burners. A completely different incident radiation distribution is observed for the 2.7 μm absorption band, where the maximum is found about 0.2 m away from the refractory and the incident radiation over the different reactor tubes is more uniform. The latter indicates that the radiation emitted from the refractory is absorbed and redistributed by the flue gas. The change in radiative intensity when it travels through the flue gas is determined by the flue gas absorption coefficient and the temperature as seen in equation (2.45) and (2.46). However, the emitted radiation intensity is proportional to the fourth power of the flue gas temperature, while the absorbed radiation intensity, which is proportional to the flue gas absorption coefficient, decreases almost linearly with the temperature in the range of 1000-1900 K. Hence, a large amount of the intensity emitted by the high temperature flame flue gas and furnace refractory walls is absorbed by the flue gas at lower temperature near the reactor coils. This results in a more uniform flue gas temperature and incident radiation. The total incident radiation distribution depicted in Figure 2-18 (c) is a combination of the incident radiation of the spectral windows and the absorption bands.

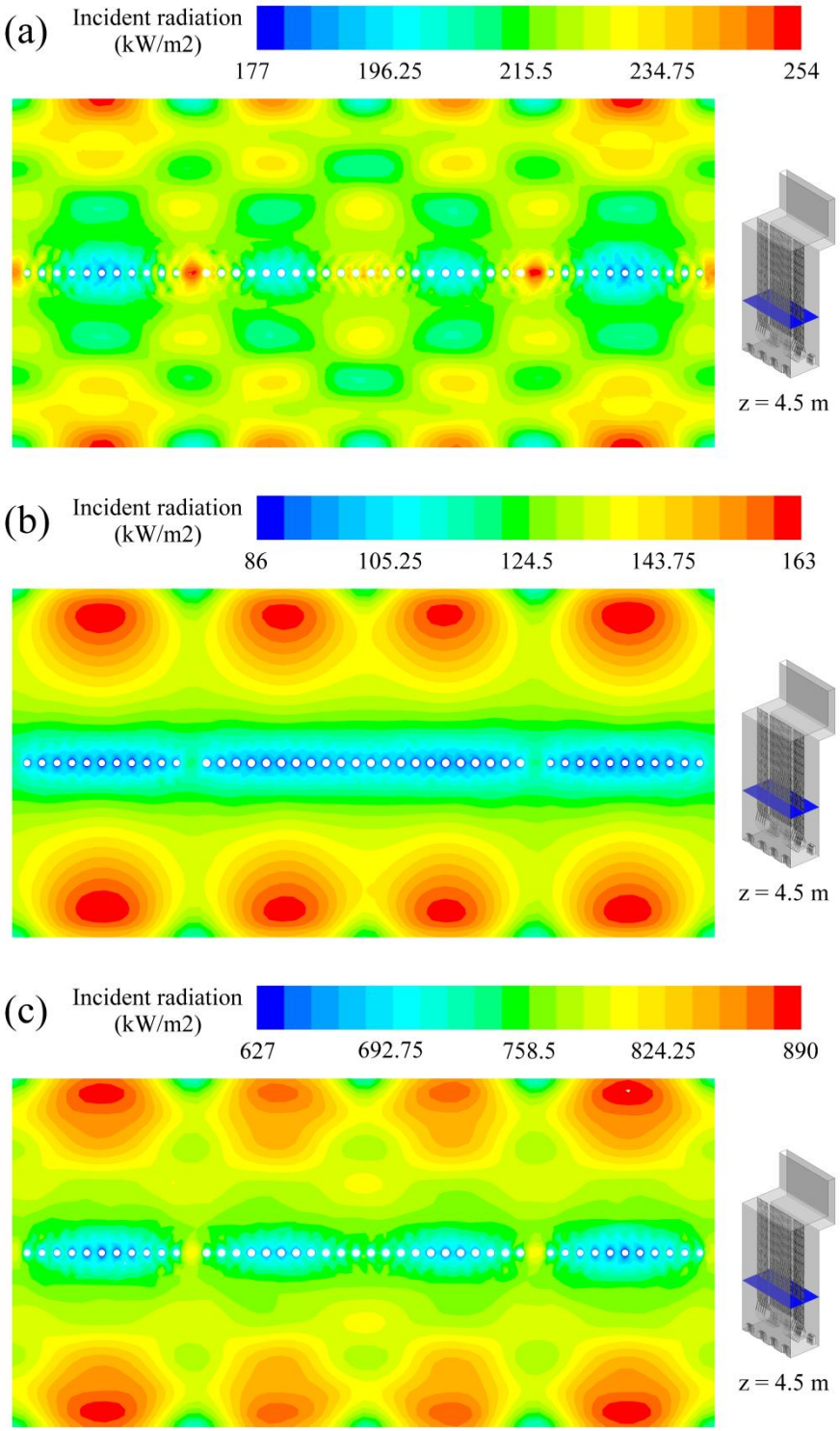

Figure 2-18: Incident radiation (kW/m²) field for the non-gray detailed case in a horizontal plane at z = 4.5 m in the: (a) first spectral window (band 1); (b) 2.7 µm band (band 2); (c) entire spectrum.

2.6.3 Shadow effects and reactor simulations

As a reactor simulation is performed for all 22 reactors individually, the variation of heat transfer to the different reactors and the resulting distribution of coil outlet temperatures (COT) can be studied. Figure 2-19 shows the radiative heat flux and the absorbed radiative heat of all the reactor coils within the first spectral window and the 2.7 μm band, where the absorbed radiative heat is defined as the integration of the radiative heat flux absorbed by the reactor over the entire coil surface. Similar results as for the incident radiation are seen, i.e. the radiative heat flux distribution is more uniform for the absorption band than for the spectral window.

Figure 2-20 shows the transferred thermal power by radiation and convection, COT, maximum TMT, and propene-to-ethene (P/E) ratio of the different reactors. It is clearly observed from Figure 2-20 (a) that in all three cases, radiation plays a more important role in the variation of the total transferred thermal power to the reactors than convection. For the gray gas case a lower contribution of convective heat transfer to the reactors is observed. This can be attributed to the lower flue gas temperature near the tube wall for the gray gas simulation. A similar average value of the sum of transferred thermal power by radiation and convection of the two non-gray cases suggests that the thermal efficiency of these two cases is almost the same. The average heat transfer predicted in the gray detailed simulation is higher compared to the non-gray cases, while the profile shape is very similar to the non-gray detailed case. The radiation properties strongly affect the flue gas and wall average temperature, as shown previously in Figure 2-14. Hence, it mainly determines the average heat transfer to the reactors. On the other hand, the burner details mainly affect the temperature distribution in the furnace as shown previously in Figure 2-13. Accordingly, the burner details determine the distribution of heat transfer over the reactors. The TMT

maximum, COTs, and P/E ratios depicted in Figure 2-20 are a direct consequence of the heat transfer. The average COT and P/E ratio in the gray detailed simulation differs about 45 K and 0.16 from than the non-gray detailed simulation values. Accounting for the non-gray character of the flue gas mixture is therefore necessary to perform reliable reactor simulations. The maximum COT difference between the reactors is 25.2 K, 29.1 K and 24.6 K for the gray detailed, non-gray detailed and non-gray simplified case respectively. A reduction of the non-uniformity of the heat transfer to the reactors could be obtained by e.g. altering the distribution of the fuel over the different burners or the mass flow rate over the different reactors. The TMT maximum for the non-gray simplified case are lower than those of the non-gray detailed case in spite of the higher thermal power received by some reactors in the simplified burner case. For example reactors 16 to 19 receive more thermal power in the simplified burner case compared to the non-gray detailed case but their TMTs are lower. This is a result of the more uniform heat flux along the reactor axial coordinate in the simplified burner case as shown in Figure 2-21 (a). Hence, to perform runlength predictions the effect of burner details on the heat flux profile should be taken into account.

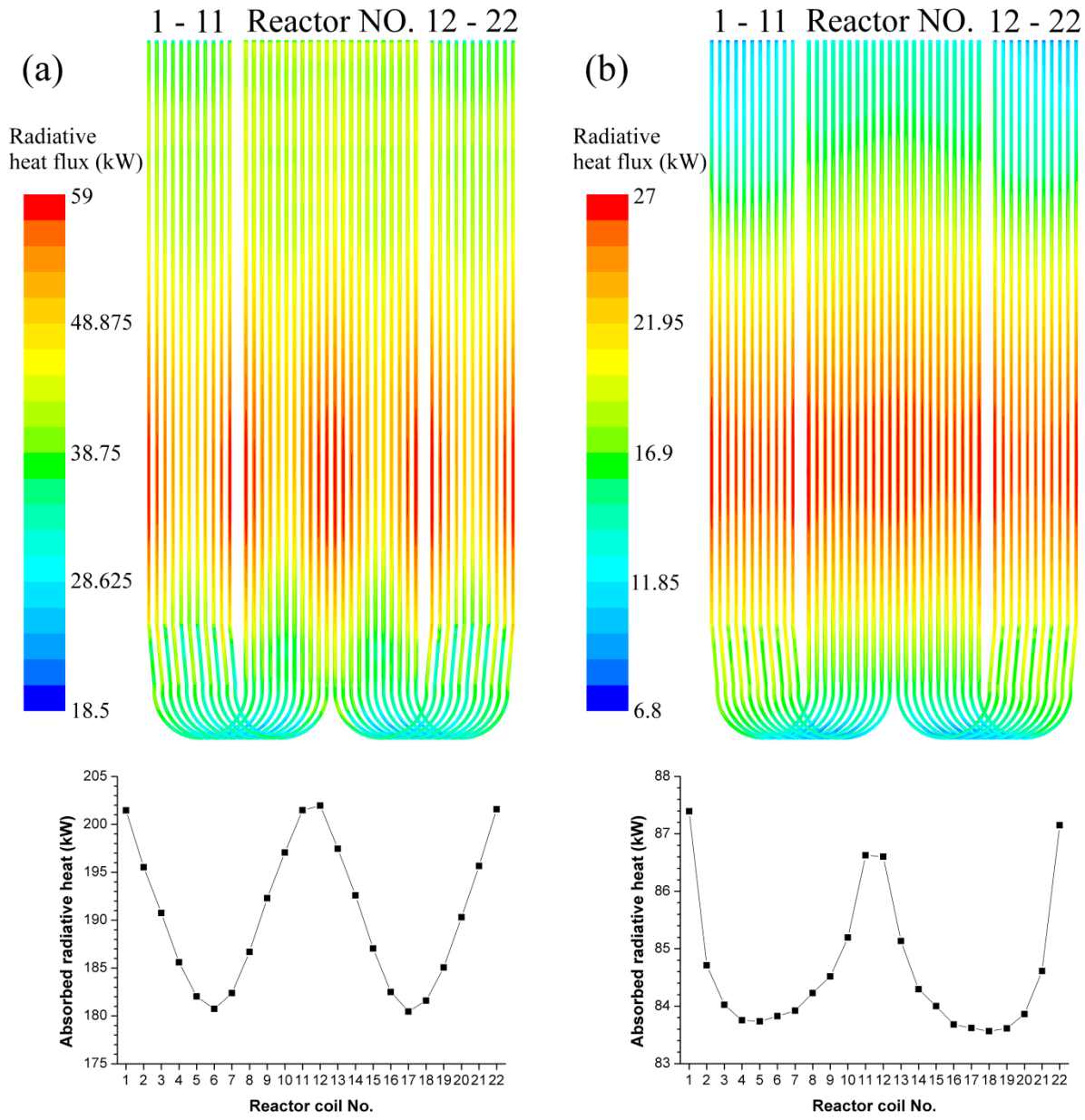

Figure 2-19: Radiative heat flux (kW) (top) and absorbed radiative heat (kW) (bottom) of all 22 reactors in the: (a) first spectral window (band 1); (b) 2.7 µm band (band 2).

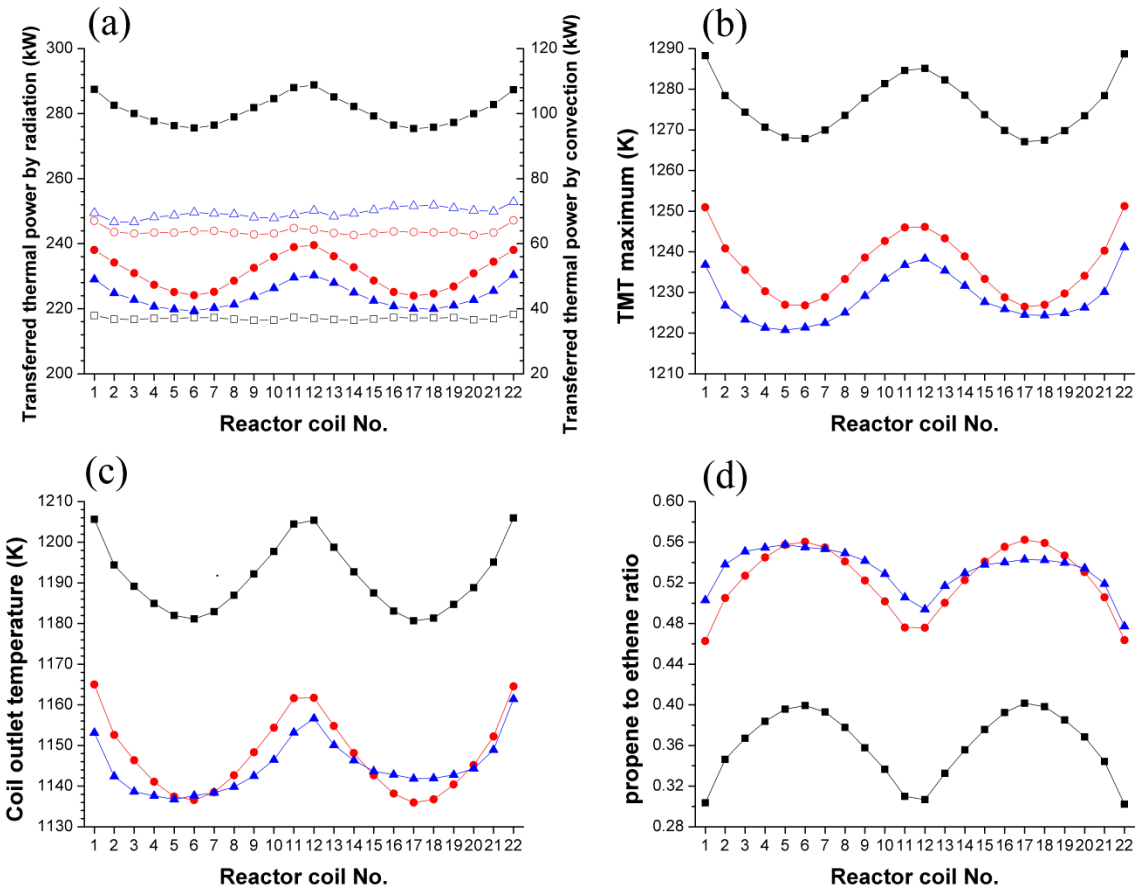

Figure 2-20: The distribution of (a) transferred thermal power by radiation (solid symbols) and by convection (open symbols) (kW), (b) maximum external tube metal temperature (K), (c) coil outlet temperature (K) and (d) propene-to-ethene ratio (wt%/wt%) over all 22 reactors: —■— —□— – gray detailed case; —●— —○— – non-gray detailed case; —▲— —△— – non-gray simplified case.

Figure 2-21 shows the heat flux, TMT, process gas temperature and ethene and propene yield profiles as a function of axial position for reactor 1. Clearly the non-gray simplified case simulates a more uniform heat flux profile than the non-gray detailed case, resulting in a lower TMT maximum. The heat flux, TMT and process gas temperature are greatly overpredicted by the gray gas radiation model, leading to an overprediction of the propene consumption near the reactor outlet.

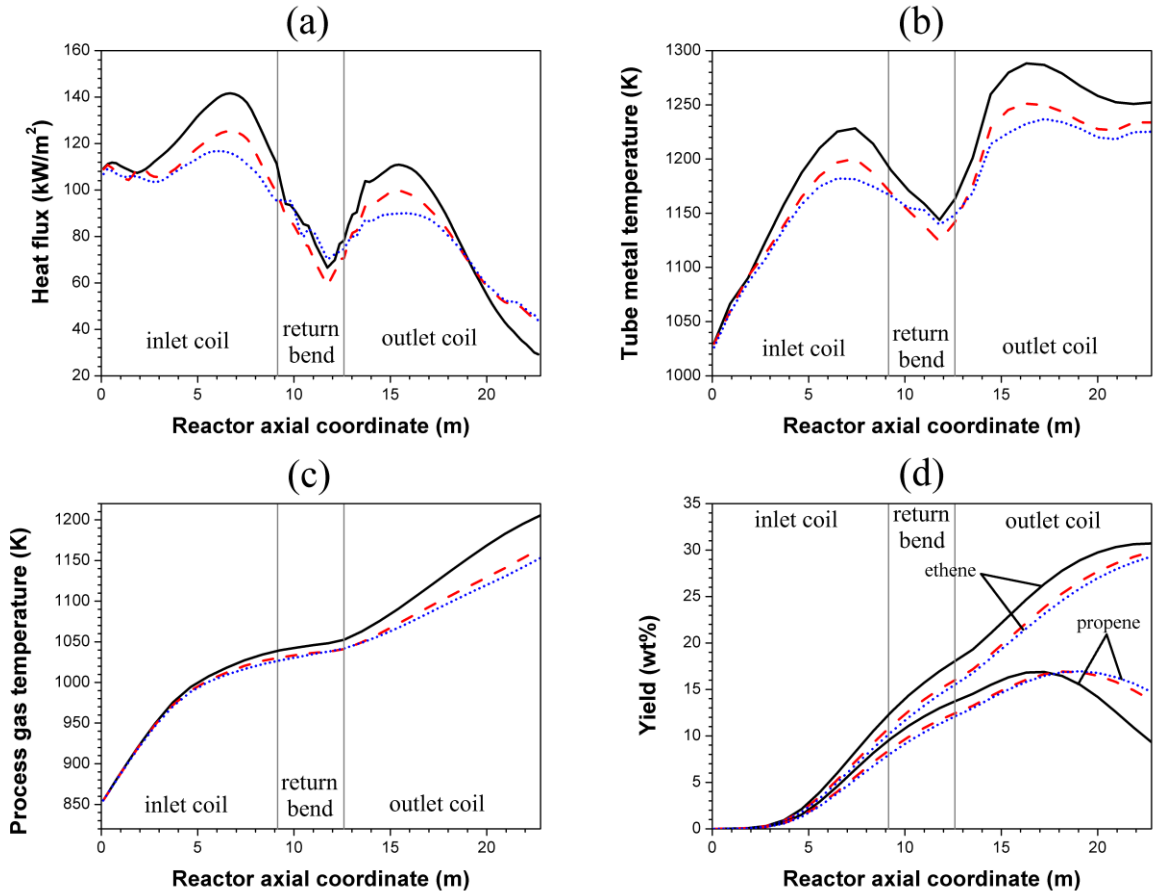

Figure 2-21: (a) Heat flux (kW/m²); (b) external tube metal temperature (K); (c) process gas temperature (K); (d) ethene and propene yields (wt%) as a function of the reactor axial coordinate (m) for reactor 1: ——— – gray detailed case; – – – – non-gray detailed case; ····· – non-gray simplified case.

Finally, in Table 2-6 the results of the three cases are compared to industrial design data. The heat transfer to the reactors when using a non-gray gas model is about 500 kW lower compared to the gray gas case and quite close to the industrial design data. Consequently, the thermal efficiency and flue gas outlet temperature are also in good agreement with the industrial data. The necessity of using a non-gray gas radiation model to accurately predict the heat transfer process in the cracking furnace is evident from these results. Since the non-gray detailed and non-gray simplified burner cases give similar results in terms of total transferred thermal power and thermal efficiency, it is reasonable to omit the detailed burner geometry to

reduce meshing effort for some industrial applications where only the total transferred heat and thermal efficiency are of interest. However, the shape of the heat flux profile to the reactors can be substantially different when using a simplified burner geometry, and hence, the resulting TMT's and runlength of the furnace are unreliable when using simplified burner geometries. The COT and olefin yields differ significantly between the different cases and the industrial data. Measuring the COT for all reactors in a furnace accurately remains one of the challenges of the industry [69]. Moreover, the use of a detailed single-event microkinetic model that has been validated over a broad range of conditions is essential to predict accurately the product yields [55].

2.6.4 Comparison of nine-band model and five-band model

As discussed in section 2.3.2, the five-band model provides identical results as the nine-band model in all five radiative heat transfer benchmark cases. But obviously the five-band model is less computational expensive. To evaluate the impact of the proposed band reduction, coupled simulations of the USC furnace were performed using the five-band model. The calculated heat flux, TMT, process gas temperature and ethene and propene yield profiles as function of the reactor axial coordinate for rector 5 are plotted together with those computed by the nine-band model in Figure 2-22. Again, the results of these two models perfectly agree.

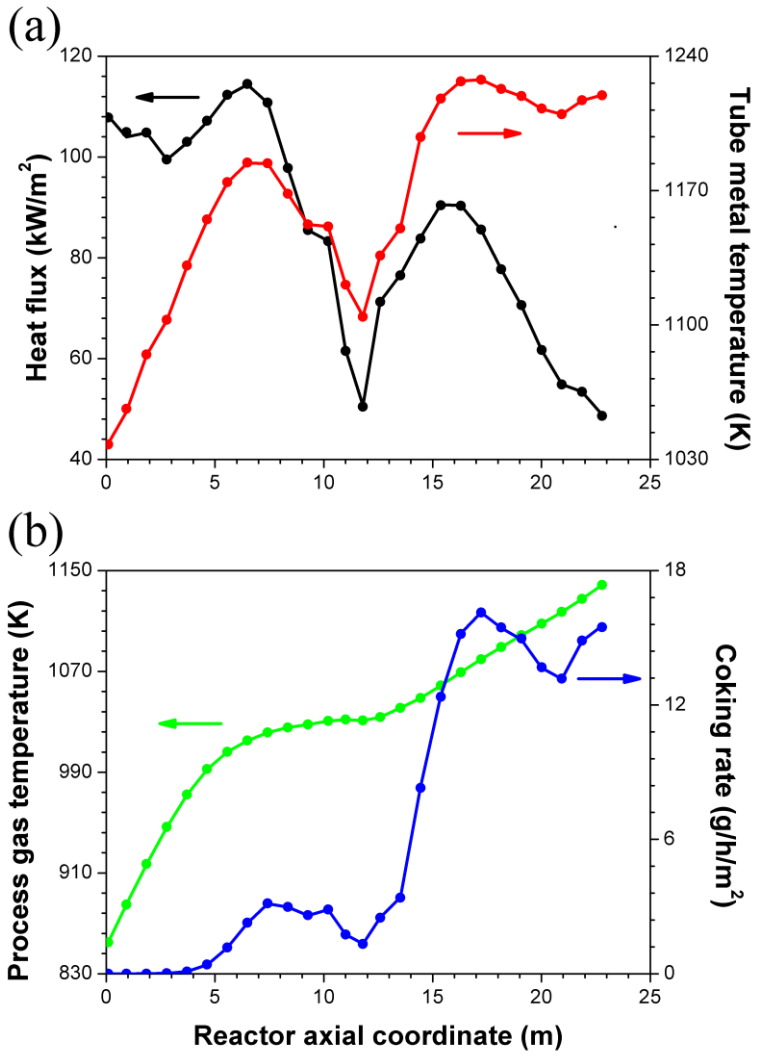

Figure 2-22: (a) Heat flux (black) and external tube metal temperature (red); (b) process gas temperature (green) and coking rate (blue) as a function of the reactor axial coordinate reactor 7 calculated by the nine-band model (lines) and the five-band model (symbols).

Table 2-7: Comparison of simulation results of the nine-band model and the five-band model.

	Nine-band model	Five-band model
Flue gas outlet temperature (K)	1367.0	1367.3
Total heat transfer to the process (kW)	6485.71	6483.55
Furnace thermal efficiency (%)	45.81	45.80
Total clock time on two 32-core machines (h)	96.65	89.50
Size of the data file (GB)	21.84	12.84

Finally, some of the global results and the required computational resources are compared in Table 2-7 for the two non-gray gas models. It can be seen that using the five-band model helps to reduce the total clock time by nearly 8%. Moreover, the benefit of disc space reduction is even more pronounced since the size of the data file is almost half of the nine-band model, making the five-band model a better choice for radiative heat transfer simulation of industrial cracking furnaces.

2.7 Conclusions

Fully coupled simulations of an industrial steam cracking furnace equipped with floor burners were performed and the influences of flue gas radiative properties, burner geometry and shadow effects were evaluated. Two non-gray gas radiation models which take four main H_2O and CO_2 absorption bands into account were developed from the EWBM. They were proven to give identical results, however, the five-band model is superior to the nine-band model due to its lower computational cost. The WSGGM embodied in ANSYS Fluent was used as gray gas radiation model. The simulation shows that the gray gas radiation model underpredicts the flue gas outlet temperature by about 70 K compared to the non-gray gas radiation model, resulting in a 3.6% higher thermal efficiency. This is quite significant as it results in a 44 K higher average COT. The non-gray gas radiation model provides much better results for the radiative heat transfer in the furnace with flue gas outlet temperature and thermal efficiency very close to the industrial design data. Similar total transferred thermal power are obtained in the non-gray detailed and non-gray simplified burner cases. However, the shape of the heat flux profile to the individual reactors can be substantially different when using a simplified burner geometry. Shadow effects further complicate interpretation. For the USC furnace simulated in this chapter, shadow effects cause a maximum difference in COT of 29 K and a difference in propene-over-ethene of 0.1 between two different U-coils in the furnace. In

order to obtain more uniform COTs and olefin yields for the individual reactors, the cracking feedstock could be unevenly distributed over the latter. During the design of a new unit, a combination of floor and wall burners could further improve the heat flux uniformity to the reactors. As wall burners can be regulated separately, they can make up for the non-uniformities induced by the floor burners.

References

[1] T. Ren, M. Patel, K. Blok, Olefins from conventional and heavy feedstocks: Energy use in steam cracking and alternative processes, Energy, 31 (2006) 425-451.
[2] K.M. Van Geem, M.-F. Reyniers, G.B. Marin, J. Song, W.H. Green, D.M. Matheu, Automatic reaction network generation using RMG for steam cracking of n-hexane, AIChE J, 52 (2006) 718-730.
[3] W. Sun, M. Saeys, Construction of an ab initio kinetic model for industrial ethane pyrolysis, AIChE J, 57 (2011) 2458-2471.
[4] M.K. Sabbe, K.M. Van Geem, M.-F. Reyniers, G.B. Marin, First principle-based simulation of ethane steam cracking, AIChE J, 57 (2011) 482-496.
[5] E. Ranzi, A. Frassoldati, S. Granata, T. Faravelli, Wide-Range Kinetic Modeling Study of the Pyrolysis, Partial Oxidation, and Combustion of Heavy n-Alkanes, Ind Eng Chem Res, 44 (2004) 5170-5183.
[6] C.M. Schietekat, D.J. Van Cauwenberge, K.M. Van Geem, G.B. Marin, Computational fluid dynamics-based design of finned steam cracking reactors, AIChE J, 60 (2014) 794-808.
[7] K.M. Van Geem, R. Žajdlík, M.-F. Reyniers, G.B. Marin, Dimensional analysis for scaling up and down steam cracking coils, Chem Eng J, 134 (2007) 3-10.
[8] K.M. Van Geem, G.J. Heynderickx, G.B. Marin, Effect of radial temperature profiles on yields in steam cracking, AIChE J, 50 (2004) 173-183.
[9] M. Berreni, M. Wang, Modelling and dynamic optimization of thermal cracking of propane for ethylene manufacturing, Comput Chem Eng, 35 (2011) 2876-2885.
[10] S.M. Sadrameli, A.E.S. Green, Systematics and modeling representations of naphtha thermal cracking for olefin production, J Anal Appl Pyrol, 73 (2005) 305-313.
[11] G.J. Heynderickx, G.F. Froment, Simulation and Comparison of the Run Length of an Ethane Cracking Furnace with Reactor Tubes of Circular and Elliptical Cross Sections, Ind Eng Chem Res, 37 (1998) 914-922.
[12] P.M. Plehiers, G.C. Reyniers, G.F. Froment, Simulation of the run length of an ethane cracking furnace, Ind Eng Chem Res, 29 (1990) 636-641.
[13] H.C. Hottel, A.F. Sarofim, Radiative transfer, McGraw-Hill, New York, 1967.
[14] A.J.M. Oprins, G.J. Heynderickx, G.B. Marin, Three-Dimensional Asymmetric Flow and Temperature Fields in Cracking Furnaces, Ind Eng Chem Res, 40 (2001) 5087-5094.
[15] G.J. Heynderickx, A.J.M. Oprins, G.B. Marin, E. Dick, Three-dimensional flow patterns in cracking furnaces with long-flame burners, AIChE J, 47 (2001) 388-400.
[16] A.J.M. Oprins, G.J. Heynderickx, Calculation of three-dimensional flow and pressure fields in cracking furnaces, Chem Eng Sci, 58 (2003) 4883-4893.

[17] G.D. Stefanidis, B. Merci, G.J. Heynderickx, G.B. Marin, CFD simulations of steam cracking furnaces using detailed combustion mechanisms, Comput Chem Eng, 30 (2006) 635-649.
[18] A. Habibi, B. Merci, G.J. Heynderickx, Impact of radiation models in CFD simulations of steam cracking furnaces, Comput Chem Eng, 31 (2007) 1389-1406.
[19] G. Hu, H. Wang, F. Qian, Y. Zhang, J. Li, K.M. Van Geem, G.B. Marin, Comprehensive CFD Simulation of Product Yields and Coking Rates for a Floor- and Wall-Fired Naphtha Cracking Furnace, Ind Eng Chem Res, 50 (2011) 13672-13685.
[20] G. Hu, H. Wang, F. Qian, K.M. Van Geem, C.M. Schietekat, G.B. Marin, Coupled simulation of an industrial naphtha cracking furnace equipped with long-flame and radiation burners, Comput Chem Eng, 38 (2012) 24-34.
[21] G.D. Stefanidis, K.M. Van Geem, G.J. Heynderickx, G.B. Marin, Evaluation of high-emissivity coatings in steam cracking furnaces using a non-grey gas radiation model, Chem Eng J, 137 (2008) 411-421.
[22] X. Lan, J. Gao, C. Xu, H. Zhang, Numerical Simulation of Transfer and Reaction Processes in Ethylene Furnaces, Chemical Engineering Research and Design, 85 (2007) 1565-1579.
[23] H. Guihua, W. Honggang, Q. Feng, Numerical simulation on flow, combustion and heat transfer of ethylene cracking furnaces, Chem Eng Sci, 66 (2011) 1600-1611.
[24] P.J. Coelho, Numerical simulation of radiative heat transfer from non-gray gases in three-dimensional enclosures, Journal of Quantitative Spectroscopy and Radiative Transfer, 74 (2002) 307-328.
[25] M.F. Modest, The Treatment of Nongray Properties in Radiative Heat Transfer: From Past to Present, Journal of Heat Transfer, 135 (2013) 061801-061801.
[26] G.J. Heynderickx, M. Nozawa, Banded gas and nongray surface radiation models for high-emissivity coatings, AIChE J, 51 (2005) 2721-2736.
[27] G.D. Stefanidis, B. Merci, G.J. Heynderickx, G.B. Marin, Gray/nongray gas radiation modeling in steam cracker CFD calculations, AIChE J, 53 (2007) 1658-1669.
[28] G.J. Heynderickx, G.G. Cornelis, G.F. Froment, Circumferential tube skin temperature profiles in thermal cracking coils, AIChE J, 38 (1992) 1905-1912.
[29] G.D. Stefanidis, G.J. Heynderickx, G.B. Marin, Development of Reduced Combustion Mechanisms for Premixed Flame Modeling in Steam Cracking Furnaces with Emphasis on NO Emission, Energ Fuel, 20 (2006) 103-113.
[30] R.W. Bilger, S.H. Stårner, R.J. Kee, On reduced mechanisms for methane-air combustion in nonpremixed flames, Combust Flame, 80 (1990) 135-149.
[31] A. Stagni, A. Cuoci, A. Frassoldati, T. Faravelli, E. Ranzi, A fully coupled, parallel approach for the post-processing of CFD data through reactor network analysis, Comput Chem Eng, 60 (2014) 197-212.
[32] A. Habibi, B. Merci, G.J. Heynderickx, Multiscale modeling of turbulent combustion and NOx emission in steam crackers, AIChE J, 53 (2007) 2384-2398.
[33] A. Cuoci, A. Frassoldati, A. Stagni, T. Faravelli, E. Ranzi, G. Buzzi-Ferraris, Numerical Modeling of NOx Formation in Turbulent Flames Using a Kinetic Post-processing Technique, Energ Fuel, 27 (2012) 1104-1122.
[34] G. Hassan, M. Pourkashanian, D. Ingham, L. Ma, P. Newman, A. Odedra, Predictions of CO and NOx emissions from steam cracking furnaces using GRI2.11 detailed reaction mechanism – A CFD investigation, Comput Chem Eng, 58 (2013) 68-83.
[35] COILSIM1D. http://www.avgi.be/.

[36] L.S. Rothman, I.E. Gordon, R.J. Barber, H. Dothe, R.R. Gamache, A. Goldman, V.I. Perevalov, S.A. Tashkun, J. Tennyson, HITEMP, the high-temperature molecular spectroscopic database, Journal of Quantitative Spectroscopy and Radiative Transfer, 111 (2010) 2139-2150.
[37] L.S. Rothman, I.E. Gordon, A. Barbe, D.C. Benner, P.F. Bernath, M. Birk, V. Boudon, L.R. Brown, A. Campargue, J.P. Champion, K. Chance, L.H. Coudert, V. Dana, V.M. Devi, S. Fally, J.M. Flaud, R.R. Gamache, A. Goldman, D. Jacquemart, I. Kleiner, N. Lacome, W.J. Lafferty, J.Y. Mandin, S.T. Massie, S.N. Mikhailenko, C.E. Miller, N. Moazzen-Ahmadi, O.V. Naumenko, A.V. Nikitin, J. Orphal, V.I. Perevalov, A. Perrin, A. Predoi-Cross, C.P. Rinsland, M. Rotger, M. Šimečková, M.A.H. Smith, K. Sung, S.A. Tashkun, J. Tennyson, R.A. Toth, A.C. Vandaele, J. Vander Auwera, The HITRAN 2008 molecular spectroscopic database, Journal of Quantitative Spectroscopy and Radiative Transfer, 110 (2009) 533-572.
[38] M.F. Modest, Radiative Heat Transfer (Third Edition), Elsevier Science, 2013.
[39] W.L. Grosshandler, RADCAL: A Narrow-Band Model for Radiation Calculations in a Combustion Environment, in, National Institute of Standards and Technology, 1993.
[40] A. Soufiani, J. Taine, High temperature gas radiative property parameters of statistical narrow-band model for H2O, CO2 and CO, and correlated-K model for H2O and CO2, Int J Heat Mass Tran, 40 (1997) 987-991.
[41] D.K. Edwards, A. Balakrishnan, Thermal radiation by combustion gases, Int J Heat Mass Tran, 16 (1973) 25-40.
[42] F. Liu, G.J. Smallwood, An efficient approach for the implementation of the SNB based correlated-k method and its evaluation, Journal of Quantitative Spectroscopy and Radiative Transfer, 84 (2004) 465-475.
[43] F. Liu, G.J. Smallwood, Ö.L. Gülder, Application of the statistical narrow-band correlated-k method to non-grey gas radiation in CO2–H2O mixtures: approximate treatments of overlapping bands, Journal of Quantitative Spectroscopy and Radiative Transfer, 68 (2001) 401-417.
[44] S. Mazumder, M.F. Modest, Application of the full spectrum correlated-k distribution approach to modeling non-gray radiation in combustion gases, Combust Flame, 129 (2002) 416-438.
[45] T.F. Smith, Z.F. Shen, J.N. Friedman, Evaluation of coefficients for the weighted sum of gray gases model Journal of Heat Transfer, 104 (1982) 602-608.
[46] A. Coppalle, P. Vervisch, The total emissivities of high-temperature flames, Combust Flame, 49 (1983) 101-108.
[47] D.K. Edwards, R. Matavosian, Scaling Rules for Total Absorptivity and Emissivity of Gases, Journal of Heat Transfer, 106 (1984) 684-689.
[48] ANSYS, ANSYS FLUENT User's Guide. Release 14.0, in, ANSYS, Inc, 2011.
[49] N. Lallemant, R. Weber, A computationally efficient procedure for calculating gas radiative properties using the exponential wide band model, Int J Heat Mass Tran, 39 (1996) 3273-3286.
[50] D.K. Edwards, Molecular Gas Band Radiation, in: F.I. Thomas, P.H. James (Eds.) Advances in Heat Transfer, Elsevier, 1976, pp. 115-193.
[51] J. Ströhle, P.J. Coelho, On the application of the exponential wide band model to the calculation of radiative heat transfer in one- and two-dimensional enclosures, Int J Heat Mass Tran, 45 (2002) 2129-2139.
[52] Q. Brewster, Thermal Radiative Transfer and Properties, Wiley, New York, 1992.
[53] B. Leckner, Spectral and total emissivity of water vapor and carbon dioxide, Combust Flame, 19 (1972) 33-48.

[54] V. Goutiere, F. Liu, A. Charette, An assessment of real-gas modelling in 2D enclosures, Journal of Quantitative Spectroscopy and Radiative Transfer, 64 (2000) 299-326.
[55] K.M. Van Geem, M.F. Reyniers, G.B. Marin, Challenges of modeling steam cracking of heavy feedstocks, Oil & Gas Science and Technology - Rev. IFP, 63 (2008) 79-94.
[56] S.P. Pyl, K.M. Van Geem, M.-F. Reyniers, G.B. Marin, Molecular reconstruction of complex hydrocarbon mixtures: An application of principal component analysis, AIChE J, 56 (2010) 3174-3188.
[57] K.M. Van Geem, D. Hudébine, M.F. Reyniers, F. Wahl, J.J. Verstraete, G.B. Marin, Molecular reconstruction of naphtha steam cracking feedstocks based on commercial indices, Comput Chem Eng, 31 (2007) 1020-1034.
[58] H.K. Versteeg, W. Malalasekera, An Introduction to Computational Fluid Dynamics: The Finite Volume Method, Longman Group Ltd, Harlow, 1995.
[59] V. Yakhot, S.A. Orszag, S. Thangam, T.B. Gatski, C.G. Speziale, Development of turbulence models for shear flows by a double expansion technique, Physics of Fluids A: Fluid Dynamics (1989-1993), 4 (1992) 1510-1520.
[60] B.E. Launder, D.B. Spalding, The numerical computation of turbulent flows, Comput Method Appl M, 3 (1974) 269-289.
[61] C.K. Westbrook, F.L. Dryer, Simplified Reaction Mechanisms for the Oxidation of Hydrocarbon Fuels in Flames, Combust Sci Technol, 27 (1981) 31-43.
[62] B.F. Magnussen, B.H. Hjertager, On mathematical modeling of turbulent combustion with special emphasis on soot formation and combustion, Symposium (International) on Combustion, 16 (1977) 719-729.
[63] G.H. Yeoh, K.K. Yuen, Computational Fluid Dynamics in Fire Engineering: Theory, Modelling and Practice, Butterworth-Heinemann, Burlington, 2009.
[64] E.H. Chui, G.D. Raithby, Computation of Radiant Heat Transfer on a Non-Orthogonal Mesh Using the Finite-Volume Method, Numerical Heat Transfer, Part B: Fundamentals, 23 (1993) 269-288.
[65] J.Y. Murthy, S.R. Mathur, Finite Volume Method for Radiative Heat Transfer Using Unstructured Meshes, J Thermophys Heat Tr, 12 (1998) 313-321.
[66] C.E. Baukal, V. Gershtein, X.J. Li, Computational Fluid Dynamics in Industrial Combustion, CRC Press, Boca Raton, 2000.
[67] Y.L. Han, R. Xiao, M.Y. Zhang, Combustion and Pyrolysis Reactions in a Naphtha Cracking Furnace, Chem Eng Technol, 30 (2007) 112-120.
[68] L. Wang, M.F. Modest, D.C. Haworth, S.R. Turns, Modelling nongrey gas-phase and soot radiation in luminous turbulent nonpremixed jet flames, Combust Theor Model, 9 (2005) 479-498.
[69] D.J. Brown, M.A. Cremer, P.J. Smith, R.T. Waibel, Fireside modeling in cracking furnaces, in: 9th Ethylene Producers' Conference, Proceedings, Amer Inst Chemical Engineers, New York, 1997, pp. 158-193.

Chapter 3: Furnace optimization using feedstock flow distribution

This chapter is based on the following paper:

Zhang, Y.; Reyniers, P. A.; Schietekat, C. M.; Du, W.; Van Geem, K. M.; Marin, G. B., Computational fluid dynamics-based steam cracking furnace optimization using feedstock flow distribution. (Published online in AlChE Journal, DOI: 10.1002/aic.15669)

Abstract

Nonuniform temperature fields in steam cracking furnaces caused by geometry factors such as burner positions, shadow effects and asymmetry of the reactor coil layout are detrimental for product yields and run lengths. The techniques of adjusting burner firing (zone firing) and feedstock mass flow rate (pass balancing) have been practiced industrially to mitigate these effects but could only reduce the nonuniformities between the so-called modules (a group of many coils). An extension of the pass balancing methodology is presented to further minimize the intra-module nonuniformities, i.e. variation between the coils within a module, in floor fired furnaces. Coupled furnace-reactor CFD-based simulations of an industrial ultra-selective conversion (USC) furnace were performed to evaluate four different feedstock flow distribution schemes, realizing equal values for coil outlet temperature (COT), propene/ethene mass ratio (P/E), maximum coking rate and maximum tube metal temperature (TMT) respectively over all the reactor coils. It is shown that feedstock flow distribution creates a larger operating window and extends the run length. Out of the four cases, the coking rate as criterion leads to the highest yearly production capacity for ethene and propene. Uniform maximum coking rates boost the annual production capacity of the USC furnace with a nameplate ethene capacity of 130 10^3 metric tons per year with 1000 metric tons for ethene and 730 metric tons for propene. For industrial application, achieving uniform maximum TMT is more practical due to its measurability by advanced laser based techniques. Most steam cracking furnaces can be retrofitted by optimizing the dimensions of venturi nozzles that regulate the feedstock flow to the coils.

Keywords: computational fluid dynamics, steam cracking, optimization, flow rate distribution, economics

3.1 Introduction

The primary objective of a steam cracking furnace is to maximize the annual production of valuable light olefins ethene and propene. To improve the process performance, extensive studies by means of numerical simulation have been conducted on the design and optimization of steam crackers. Simulations are required as the complexity associated with steam cracking of hydrocarbons prohibits that experimental results obtained at lab scale to be directly applied to full scale industrial units [1]. The results obtained at pilot plants at a semi-industrial scale, such as the ones available at the Laboratory for Chemical Technology of Ghent University [2] and at Tarbiat Modares University [3, 4], still require careful scale-up to ensure unchanged product distribution for a given feedstock [5, 6], which gives rise to some uncertainty when translating data from scale to another. Additionally, the cost of running and maintaining a pilot plant is high as a result of the harsh operating conditions characteristic for steam cracking. On the other hand, numerical simulations allow to observe the industrial furnace at its full scale, thus avoiding the use of scale-up rules. For the purpose of studying the effect of operating conditions on the product yields, numerical modeling has the advantage over experiments of a wider operating range, which allows to find the theoretical optimum as guidance for practical optimization [7].

Coupled numerical simulations of steam cracking furnaces have already been used extensively for design and optimization purposes. One aspect of the optimization is to increase the yields for the valuable light olefins. Van Damme et al. concluded that the process gas temperature, instead of the residence time, determines the product yield in steam cracking [8]. This reoriented the optimization work towards finding the optimal temperature profile in the tubular reactor to maximize the olefins yield for different feedstocks. Later on, Plehiers and Froment showed that a linear temperature profile is superior for ethene selectivity

compared to the conventional convex temperature profile, which provided the basis for a new coil design, i.e. the reversed split reactor [9, 10]. Similar conclusions were drawn by Van Goethem et al. who developed a conceptual distributive reaction-mixing model (d-RMix) to investigate the theoretical optimal conditions [11]. Disregarding any practical constraints, the optimal process temperature profile was found to be linear or concave to obtain maximum ethene yield or maximum ethene plus propene yield respectively [12]. It was also reported that a higher coil outlet temperature (COT) increases the ethene yield.

Another aspect that needs to be taken into account in steam cracking design and optimization is coke formation. As the rate of coke deposition on the inner wall of the reactor coil increases with increasing tube inner wall temperature, the furnace has to be shut down more frequently for decoking when it is operated at a higher COT for maximizing the ethene yield. Therefore, for the operational optimization of steam crackers, a tradeoff between ethene yield and on-stream time has to be made. The objective function of the optimization not only includes the revenue from selling the products but also includes the incurred cost for decoking [13-15] and the fuel cost for the furnace. Efforts have been made towards extending the run length of a steam cracker by means of 3D reactor technology which improves the radial mixing, and hence, decreases the inner wall temperature and consequently the rate of coke deposition [16].

Despite the remarkable progress in finding the optimal temperature profile and COT set point, achieving these ideal conditions for all reactor coils in an industrial furnace is not straightforward. This is because of the uneven distribution of thermal power over the different reactor coils as a result of their different spatial locations, their position relative to the burners, the asymmetry of the coil layout and the shadow effects caused by projections of adjacent coils. As typically the feedstock flow rate to each of the reactors is set to a constant and identical value by venturi nozzles, this uneven distribution of thermal power results in

large COT variations over the reactor coils. Zhang et al. [17] have shown that for an industrial ultra-selective conversion (USC) cracking furnace the difference between the highest and lowest COT over 22 reactor coils can be as much as 29 K, which means that even if the optimal temperature profile and COT can be achieved for this furnace, not all coils will be operated at these desired conditions. Additionally, coke formation on the inner wall hampers the on-stream time and compels the operators to decoke the furnace every 30-80 days [3]. The decoking procedure is initiated when the maximum allowed value for either of the following two process parameters has been reached: the pressure drop over the reactor coil or the tube metal temperature (TMT). A too high pressure drop causes loss of criticality across the venturis, which means that the flow is no longer choked. While a too high tube metal temperature accelerates the aging process of the reactor coil and hence decreases its lifetime. Both decoking criteria are directly related to the thickness of the coke layer. Therefore in the majority of the cases, the coil which receives the highest thermal power, reaches one of the decoking criteria first, making this coil the limiting factor for the run length of the entire furnace.

The foregoing discussion clearly shows that it is desirable to reduce the nonuniformities in an industrial steam cracking furnace. The zone firing and pass balancing techniques described amongst others by Brown et al. [18, 19] to mitigate this effect between modules, i.e. a group of several coils, have been applied industrially for years. However, the intra-module nonuniformities remain to be reduced, especially for the U-coil configuration where many reactor coils are grouped in one module. In this chapter an extension of the pass balancing technique is proposed to maximize the potential of all reactors in a furnace by altering the feedstock flow rate to each coil within a module according to their respective heat input. Different flow distribution approaches were evaluated and optimized via coupled furnace-

reactor simulations. Run length simulations were performed based on the calculated heat flux profiles to determine the potential benefit of feedstock flow distribution on the annual ethene and propene production. Finally, the possibility and difficulty in achieving the uniformity for real life industrial cracking furnaces was also discussed.

3.2 Mathematical models

Recent work has shown significant progress in the modeling of steam cracking reactors in terms of describing the complex steam cracking chemistry for various feedstocks [20-22] and its implementations in multi-dimensional reactor simulations [16, 23-26]. Additionally, molecular reconstruction, which simulates the detailed composition of a complex hydrocarbon feedstock based on commercial indices like PIONA mass fractions, specific density, average molecular weight and boiling point curve, has proven its benefit [27-30]. This is essential for complex naphtha and heavier feedstocks whose exact composition is not readily available, but which is needed for reactor simulations using detail kinetic mechanisms. Firebox modeling, on the other hand, has evolved from solving flue gas flow and radiation on two different grids via turbulence model and Hottel's zone method respectively [31, 32], to the use of comprehensive computational fluid dynamic (CFD) simulations dedicated models for flow field and turbulence-chemistry interaction by Oprins et al and Stefanidis et al [33, 34], coupling effect of the furnace and reactor by Hu et al. [35-37], and NOx emission by Brown et al. and Tang et al.[38-40].

3.2.1 Reactor model

The process gas flow in a tubular steam cracking reactor is highly turbulent because of the high velocity and hence short residence time applied to suppress secondary reactions which decrease the light olefins yield. As most of the industrial cracking reactor coils have a high

length to inner diameter ratio, it is commonly assumed that the flow approximates the one-dimensional plug flow regime, neglecting any radial or azimuthal gradients, which greatly simplifies numerical simulations. The effect of neglecting the radial gradient of temperature and product concentrations on product yield was studied by Van Geem et al. [5, 41]. It was reported that the absolute differences in ethane conversion and ethene yield between 1D and 2D simulations are 1.9% and 0.4% respectively. For the other major products, the differences are also relatively small, ranging from 0.1% to 0.3%. Considering the scale of an industrial steam cracking furnace the differences are quite pronounced, however, the bias introduced by the 1D assumption exists in all the reactor coil simulations and therefore does not affect the aim of the present work, i.e. evaluating feedstock flow rate distribution. Hence it was sufficient to use the computationally less expensive 1D model in COILSIM1D in this study. The core of COILSIM1D [42] is an extensive reaction network consisting of hundreds of species and thousands of elementary reactions [30]. The detailed composition of complex feedstocks is estimated based on the commercial indices of the feed via the molecular reconstruction [27]. The conservation equations for species, momentum and energy are given in equations (3.1), (3.2) and (3.3) respectively.

$$\frac{dF_i}{dz} = \frac{\pi d^2}{4} R_i \tag{3.1}$$

$$-\frac{dp}{dz} = \left(\frac{2f}{d} + \frac{\zeta}{\pi r_b}\right)\rho u^2 + \rho u \frac{du}{dz} \tag{3.2}$$

$$\sum_{i=1}^{N_s} F_i c_{p_i} \frac{dT}{dz} = \pi d q + \frac{\pi d^2}{4} \sum_{j=1}^{N_R} r_j \left(-\Delta H_j\right) \tag{3.3}$$

Semi-empirical models were used to calculate the rate of coke formation on the inner wall of the reactor coil, the coking rate was computed based on a modified version of the model of Plehiers [26].

3.2.2 Furnace model

3.2.2.1 Governing equations

The three-dimensional steady-state conservation equations for mass, momentum, energy and species in a compressible reactive flow are given in equations (3.4) – (3.7).

$$\nabla \cdot (\rho \vec{u}) = 0 \tag{3.4}$$

$$\nabla \cdot (\rho \vec{u}\vec{u}) = -\nabla p + \nabla \cdot (\bar{\bar{\tau}}) + S_M \tag{3.5}$$

$$\nabla \cdot \left(\vec{u}(\rho E + p)\right) = \nabla \cdot \left(k_{eff} \nabla \mathrm{T} - \sum_i h_i \vec{J}_i + \left(\bar{\bar{\tau}}_{eff} \cdot \vec{u}\right) \right) + S_E \tag{3.6}$$

$$\nabla \cdot \left(\frac{\vec{u} Y_i}{V_m}\right) = -\nabla \cdot \vec{J}_i + R_i \tag{3.7}$$

As the typical radiant box height for an industrial furnace is often in the range of 10 – 13 meters, buoyancy effects are important and hence gravitational force was taken into account in the momentum equation, i.e. $S_{M,z} = -\rho g$. Applying Reynolds-averaging to the Navier-Stokes equations replaces the instantaneous quantities in the governing equations by a time-averaged component and a fluctuating component. The Renormalization Group (RNG) k-ε model [43] was used to approximate the resulting Reynolds stress terms by solving two additional equations for the turbulent kinetic energy k and the turbulent dissipation rate ε.

3.2.2.2 Combustion model

The two-step methane and hydrogen combustion scheme proposed by Westbrook and Dryer [44] was adopted, see equations (3.8) – (3.11). The kinetic parameters for all reactions involved are found in the work of Stefanidis et al. [34].

$$CH_4 + 1.5O_2 \rightarrow CO + 2H_2O \tag{3.8}$$

$$C_2H_4 + 2O_2 \rightarrow 2CO + 2H_2O \tag{3.9}$$

$$CO + 0.5O_2 \rightarrow CO_2 \tag{3.10}$$

$$H_2 + 0.5O_2 \rightarrow H_2O \tag{3.11}$$

The turbulent chemistry interaction was accounted for via the Eddy-Dissipation Model (EDM) [45], which expresses the rate of combustion reactions to be proportional to the reciprocal of the eddy mixing time scale $\tau = k/\varepsilon$. The actual rate of reaction is determined as the minimum of equations (3.12) and (3.13).

$$R_{i,j} = \frac{\nu'_{i,j}}{V_m} A \frac{\varepsilon}{k} \min\left(\frac{Y_R}{\nu'_{R,j}}\right) \tag{3.12}$$

$$R_{i,j} = \frac{\nu'_{i,j}}{V_m} AB \frac{\varepsilon}{k} \frac{\sum_P Y_P}{\sum_P^N \nu''_{P,j}} \tag{3.13}$$

However, the combustion rate in equation (3.12) and (3.13) is a function of turbulence properties and species concentration but does not depend explicitly on temperature. The EDM assumes that in diffusion flames the rate of chemical reactions is much faster than the rate of dissipation of eddies. However in regions with strong turbulence and low temperature, e.g. the inlet regions for fuel and air, this assumption is generally not valid. The finite rate of the combustion kinetics was accounted for by combining the EDM with the model of Stefanidis

et al. [34] in order to prevent an overestimation of the rate of combustion in the regions where the assumption of infinitely fast chemistry was not valid [46].

3.2.2.3 Radiation model

As investigated by Habibi et al. [47] and Hu et al. [37], the Discrete Ordinates (DO) model has the best performance in dealing with radiative heat transfer in full scale industrial furnace simulations where neither of the limiting cases, i.e. optically thick or optically thin, is valid. In this chapter, the non-gray implementation of the DO model was used to solve the Radiative Transfer Equation (RTE) for spectral radiation intensity I_i in a number of wavelength bands, see equation (3.14).

$$\nabla \cdot (I_i(\vec{r},\vec{s})\vec{s}) + (\kappa_i + \sigma_s)I_i(\vec{r},\vec{s}) = \kappa_i I_{b,i} + \frac{\sigma_s}{4\pi}\int_0^{4\pi} I_i(\vec{r},\vec{s}')\Phi(\vec{s},\vec{s}')d\Omega' \qquad (3.14)$$

The entire spectrum was divided into nine spectral bands consisting of four absorption bands and five spectral windows to account for the non-gray radiative properties of the flue gas. The spectral absorption coefficient κ_i in each of the nine bands was described as a function of temperature and mass fraction of H_2O and CO_2 using the Exponential Wide Band Model (EWBM) [48]. Details on the development and validation of the EWBM based nine-band model are available in the work of Zhang et al. [17].

The furnace refractory and reactor coils were treated as opaque and gray, i.e. their emissivity is the same in all bands. The radiative heat flux reaching and leaving the surfaces was calculated via equations (3.15) and (3.16).

$$q_{in,i} = \Delta\lambda_i \int_{\vec{s}\cdot\vec{n}>0} I_{in,i}\vec{s}\cdot\vec{n}d\Omega \qquad (3.15)$$

$$q_{out,i} = \left(1-\varepsilon_{w,i}\right)q_{in,i} + \varepsilon_{w,i}\left[f\left(n\lambda_{u,i}T_w\right) - f\left(n\lambda_{l,i}T_w\right)\right]n^2\sigma T_w^4 \qquad (3.16)$$

where $f(n\lambda T)$ is the fractional emissive power of a black body.

$$f(n\lambda T) = \frac{15}{\pi^4}\sum_{m=1}^{\infty}\frac{e^{-m\zeta}}{m^4}[6 + 6(m\zeta) + 3(m\zeta)^2 + (m\zeta)^3],\ \ \zeta = \frac{C_2}{n\lambda T} \qquad (3.17)$$

3.3 Simulation setup

3.3.1 Furnace geometry and operating conditions

The industrial naphtha steam cracking furnace modeled in this chapter consists of two identical radiant sections, both are connected to the same convection section. To reduce the computational cost, only one fourth of one radiant section was simulated as shown in Figure 3-1, making use of the internal symmetry along the x-coordinate. The simulated section of the furnace contains 22 ultra-selective (USC) U-coils. There are 11 inlet legs on both sides of the modeled section, which are connected to 22 outlet legs located in the center of the section. Eight fuel staging low NOx floor burners are located in the simulated section. The two boundaries of the simulated furnace section along the x-coordinate were set as symmetry plane. Table 3-1 summarizes the dimensions of the radiant section and the reactor coil, PIONA values of the hydrocarbon feedstock and the operating conditions for the radiant section and the reactors.

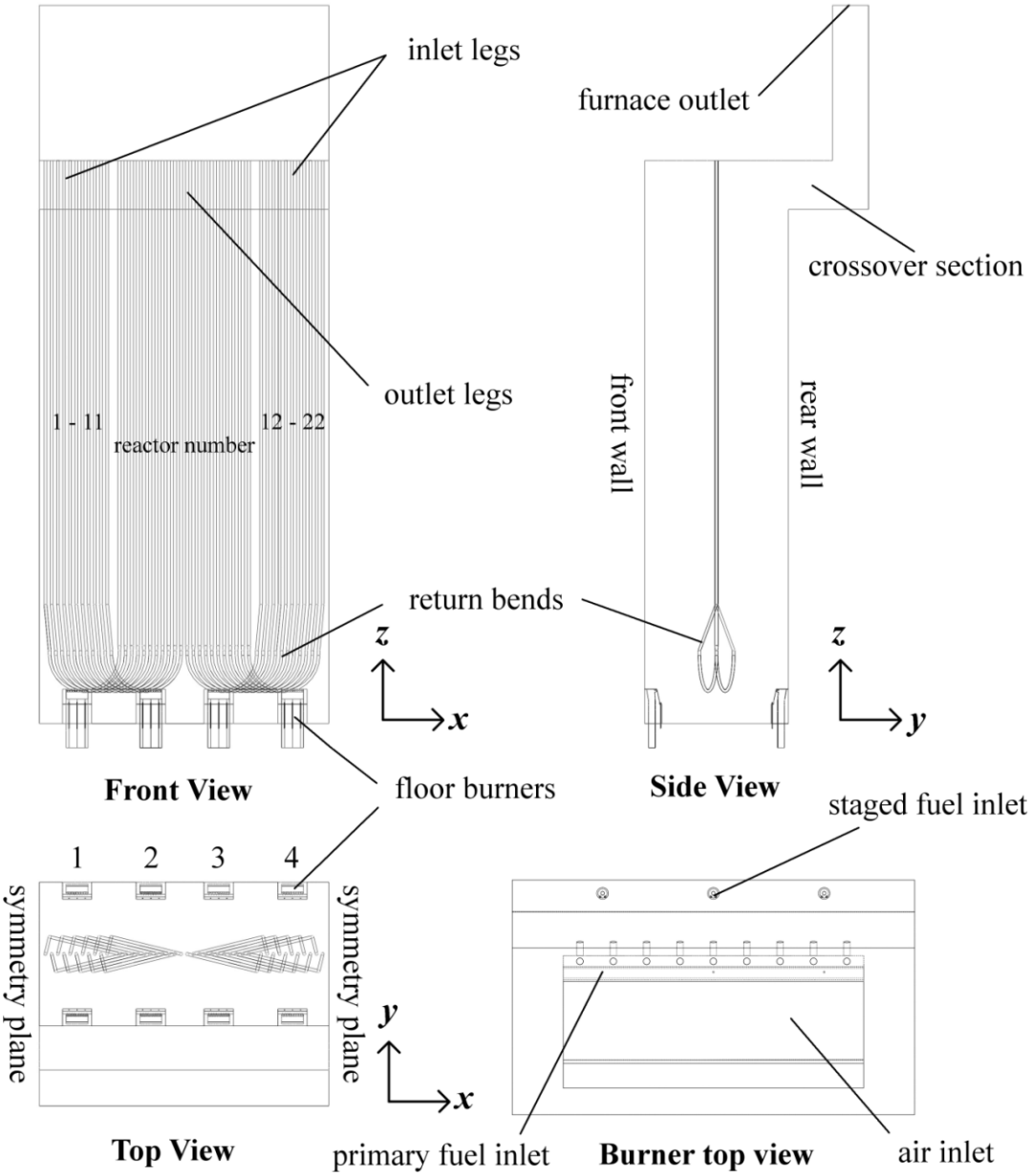

Figure 3-1: Schematic representation of the simulated furnace segment.

Table 3-1: Furnace dimensions and operating conditions.

Simulated furnace segment	
Length x-direction (m)	5.969
Width y-direction (m)	2.964
Height z-direction (m)	11.609
Number of burners	8

Firing condition	
Fuel gas flow rate (kg/s)	0.2777
Air equivalence ratio	1.1
Fuel gas inlet temperature (K)	289
Furnace outlet pressure (Pa)	101300
Fuel composition (mol%)	
CH_4	88.55
H_2	11.14
CO	0.17
C_2H_4	0.14
Reactor coils	
Number of coils	22
Reactor coil length (m)	22.792
Number of passes	2
Inlet leg external diameter (m)	0.0566
Inlet leg thickness (m)	0.0058
Outlet leg external diameter (m)	0.0666
Outlet leg thickness (m)	0.0078
Coil operating condition	
Feedstock flow rate of single coil for base case (kg/s)	0.0914
Steam dilution ratio (kg/kg)	0.5
Coil inlet temperature (K)	853
Coil inlet pressure (Pa)	236325
Feedstock PIONA (wt%)	
n-Paraffins	29.25
i-Paraffins	29.25
Olefins	0.00
Naphthenes	31.50
Aromatics	10.00
Material properties	
Furnace refractory emissivity	0.75
Reactor tube skin emissivity	0.85

3.3.2 Numerical scheme and coupling procedures

A hybrid meshing strategy was adopted to divide the simulated section in computational cells. In the upper part of the furnace, hexahedral cells were used. Near the burners and around the return bends, initially tetrahedral cells were used which were subsequently combined to polyhedral cells to reduce the number of cells and increase the numerical stability. Further mesh refinement was carried out based on the local gradients of temperature, pressure and

species concentration until the flow variables at the furnace stack stabilized. The final number of cells amounted to 6.39 million. The set of partial differential equations was discretized via the finite volume method, available in the commercial CFD software ANSYS FLUENT 14.5. The EWBM calculations for the spectral absorption coefficients required in the nine-band model were implemented as a user-defined function. The heat loss through the furnace refractory walls was calculated by imposing a convection heat transfer boundary condition with an ambient temperature of 298 K. The convective heat transfer coefficient was set to 0.625 W m^{-2} K^{-1} to match a total heat loss through the refractory wall equal to 1% of the total heat of combustion, conforming to previously calculated heat balances of the furnace [17] and literature [49].

Due to the strong interaction between the process side and the fire side of a steam cracking unit, it was necessary to couple both sides in the simulation. The coupling procedure started from the furnace simulation using initial estimated external TMT profiles as boundary condition for the reactor coils. The furnace simulation was run to convergence, i.e. the scaled residuals for all governing equations were lower than 10^{-4} and the changes of flue gas outlet temperature and O_2 mole fraction were below 0.1 K and 0.05%, respectively. The heat flux profiles for all 22 reactor coils were exported from the furnace simulation and used for the reactor simulations. Updated TMT profiles for the reactor coils were obtained and used as boundary condition in the next iteration of the furnace simulation. This procedure was repeated until for each reactor the difference between the maximum TMT value in the old and new furnace simulation was less than 1 K.

3.3.3 Feedstock flow distribution strategies

Four cases were studied and compared with the ‘base case’ in which the hydrocarbon feedstock is uniformly distributed over all 22 reactor coils. The coupling procedure was

applied to each of these four alternatives separately to obtain a distribution of the hydrocarbon feedstock over the reactor coils that resulted in uniform values for the following variables over all reactor coils:

- coil outlet temperature (COT)
- propene/ethene mass ratio at the reactor outlet (P/E)
- maximum coking rate on reactor inner surface (coking rate)
- maximum tube metal temperature (TMT)

Accordingly, the four cases are referred to as ‘COT case’, ‘P/E case’, ‘coking rate case’ and ‘TMT case’. To allow a fair comparison between the cases, the total hydrocarbon feedstock mass flow rate and the total fuel flow rate to the burners were kept constant and equal to the values in the ‘base case’. The aim of this work was to investigate qualitatively and quantitatively the benefit for a steam cracker by applying a certain distribution of the hydrocarbon feedstock over the reactor coils.

3.4 Results and discussion

3.4.1 Yield effect

First feedstock flow distribution was assessed at start-of-run conditions, i.e. no coke was present yet on the inner wall of the reactor coils, focusing on the impact on product yields and selectivities. The results of the coupled furnace-reactor simulations reported in Figure 3-2 show that there is indeed a substantial difference in the mass flow rate distribution over the 22 reactor coils in the four different cases. The corresponding profiles of COT, P/E, maximum coking rate and maximum TMT as function of the reactor coil number in the different cases are depicted in Figure 3-3. It can be observed that feedstock flow distribution reduces the nonuniformity of COT, P/E, maximum coking rate and maximum TMT. This is especially

true for the maximum coking rate and TMT, both of which significantly affect the run length of a steam cracking furnace.

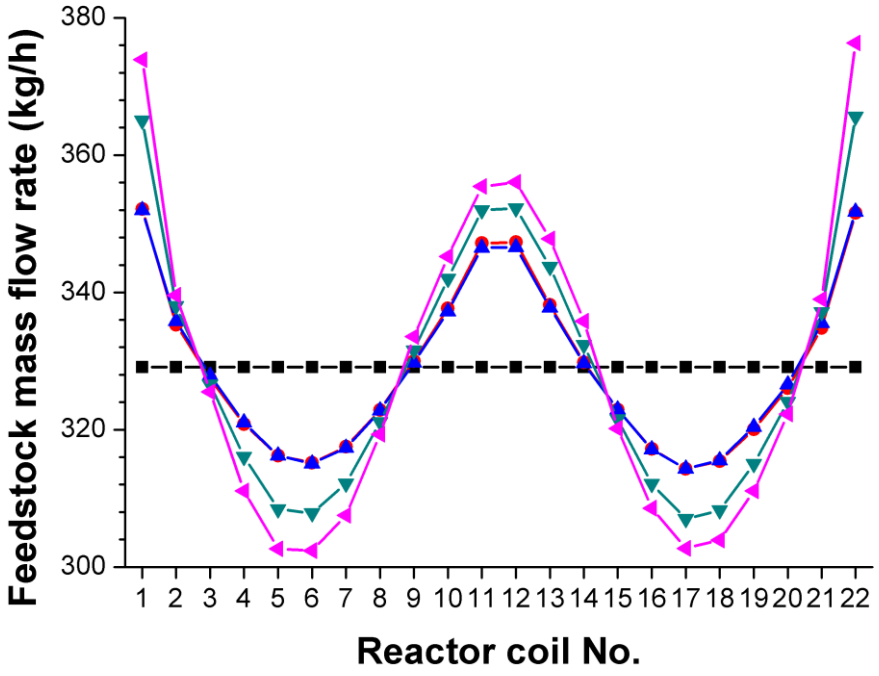

Figure 3-2: Feedstock mass flow rate per reactor coil for the 22 reactor coils: ■ – base case; ● – COT case; ▲ – P/E case; ▼ – coking rate case; ◀ – TMT case.

The W-shape of the COT profile, maximum coking rate profile and maximum TMT profile in the base case is due to the higher heat flux to the reactor coils located at the extremities and in the middle of the furnace. This higher heat flux is a consequence of geometry effects, that is the proximity to the burners, the shadow effect of adjacent coils, and the asymmetry of the coil layout within the module. It is worth noting that the last effect, which results in the adjacent hotter outlet legs emitting energy towards each other, is considered as the dominant mechanism for the nonuniform heat flux. On the other hand, the P/E profile exhibits an inverse, M-shaped profile because the propene yield decreases and ethene yield increases with

increasing cracking severity, i.e. increasing coil outlet temperature at the observed conversion range. Since COT, maximum coking rate and maximum TMT are higher with an increased heat flux, a W-shaped feedstock flow distribution profile is needed to compensate for this effect and create uniform distribution of the set variables, as is observed in Figure 3-2. The required corrections on the mass flow rate distribution were smallest in the P/E case and the COT case, followed by the coking rate case. The largest corrections were needed in the TMT case.

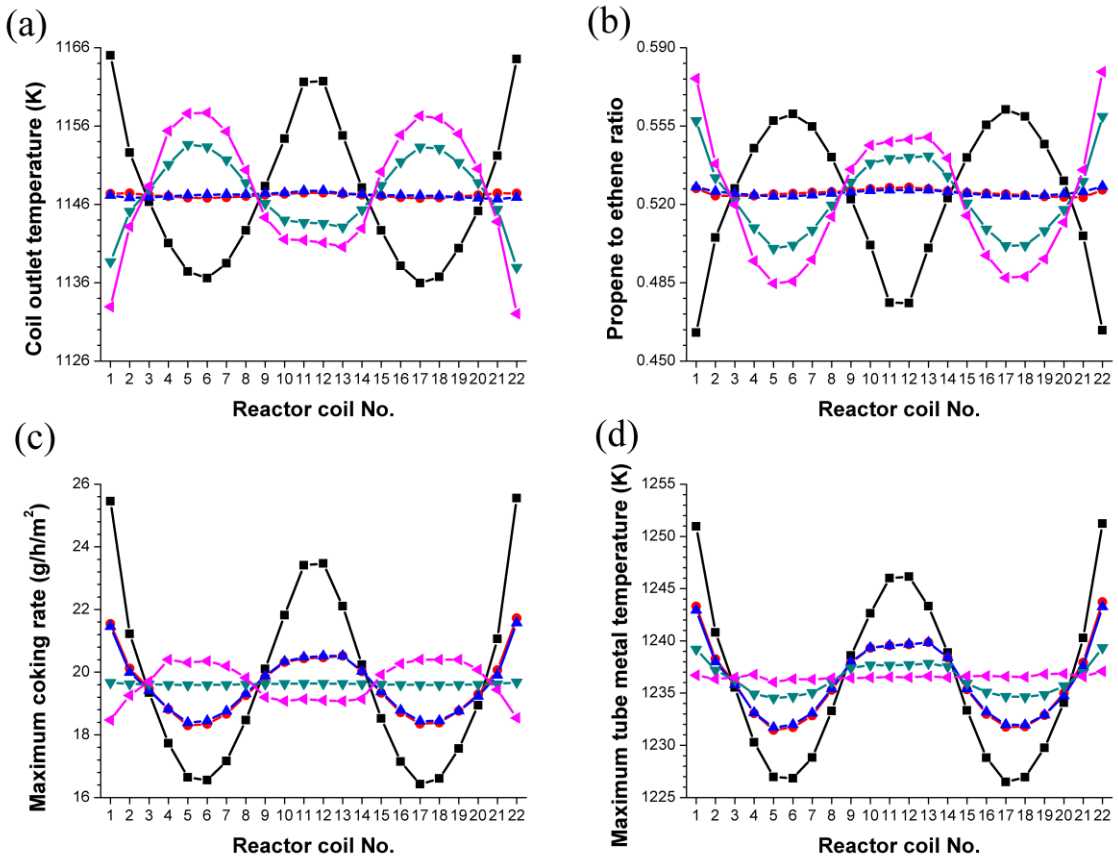

Figure 3-3: Profiles of different variables for the 22 reactor coils. (a) COT; (b) P/E; (c) maximum coking rate; (d) maximum TMT: ■ – base case; ● – COT case; ▲ – P/E case; ▼ – coking rate case; ◀ – TMT case.

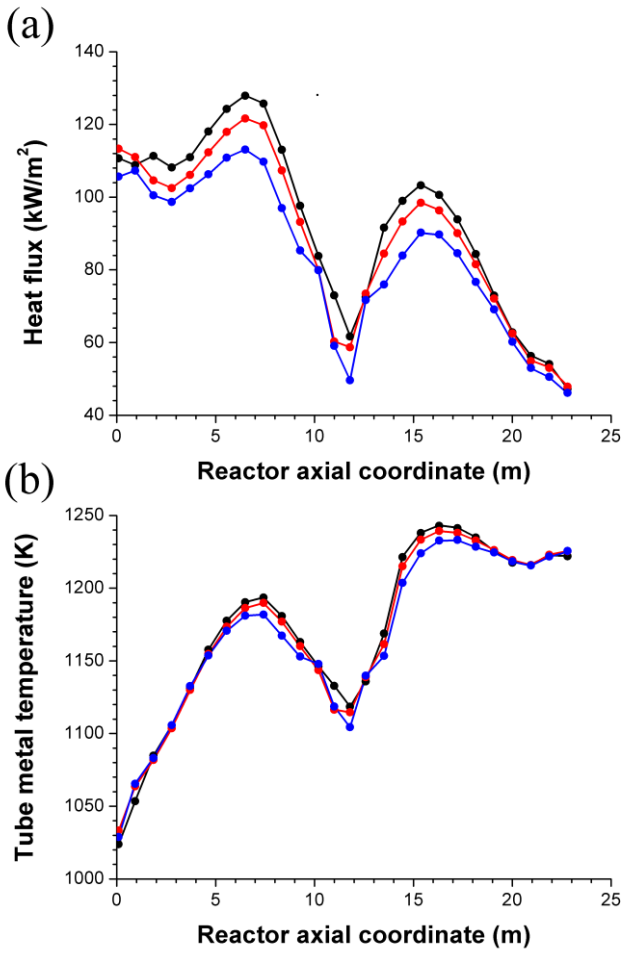

Figure 3-4: Profile of (a) heat flux; (b) TMT as a function of the reactor axial coordinate of reactor coil No.1 (black), No.10 (red) and No.18 (blue) for the COT case (lines) and the P/E case (symbols).

It is interesting to see that among the four cases, the distributions in Figure 3-3 for the COT case and the P/E case are nearly identical. This is confirmed by the profiles of heat flux and tube metal temperature as function of the axial coordinate for the COT case and the P/E case, given in Figure 3-4. For the sake of clarity, the values for only 3 out of the 22 reactors are plotted, however the conclusion that the results for the COT case and the P/E agree very well is generally valid. Despite the significant difference between the shape of the heat flux profile along different reactor coils, a more uniform COT still results in nearly uniform P/E in the COT case, and uniform P/E results in nearly uniform COT in the P/E case. Since the

residence time of the process gas differs from one reactor coil to anther for the flow rate distribution case, this strong dependence between COT and P/E indicates that the effect of residence time on the product distribution is negligible as long as the temperature levels in different reactor coils are the same. Similar conclusion was previously drawn by Van Damme et al. [8] as well. As the results of the COT case and the P/E case show very little difference, only the COT case will be compared to other cases in the following discussion.

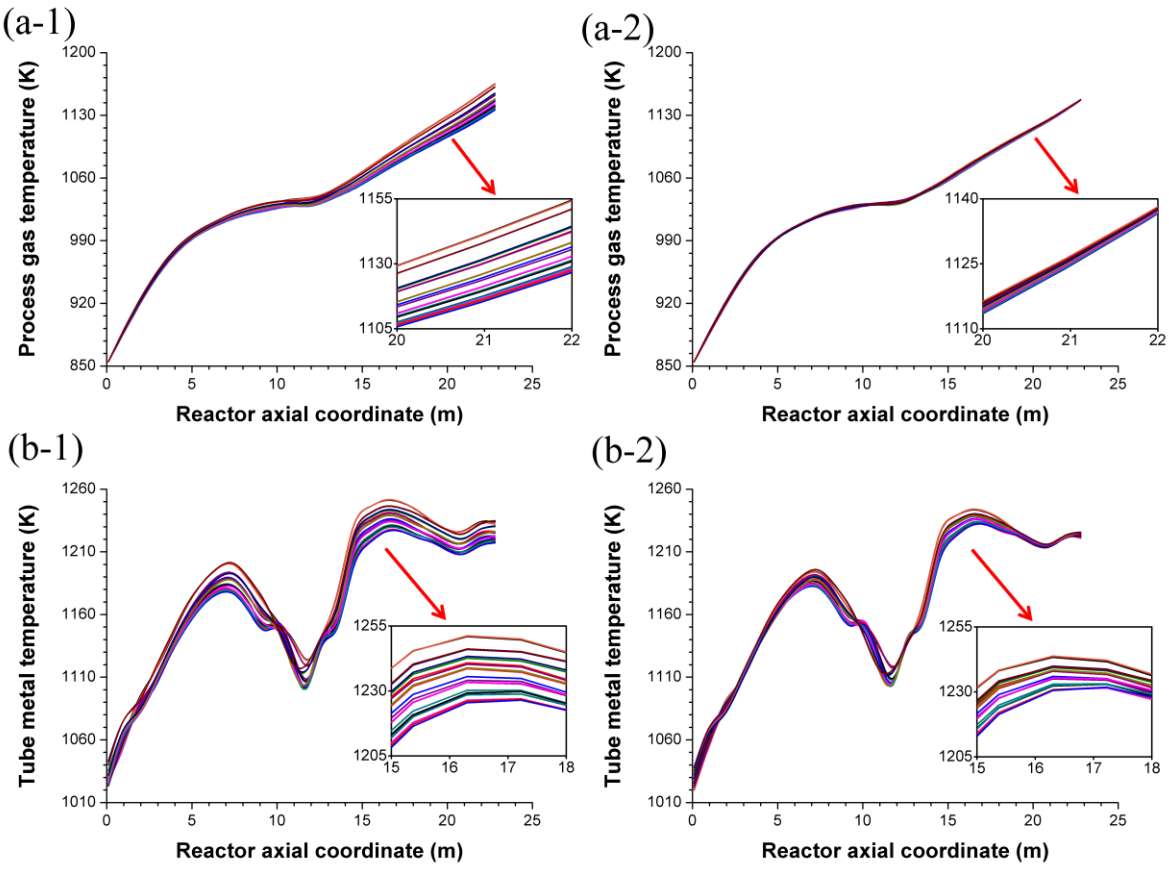

Figure 3-5: (a) process gas temperature and (b) TMT as a function of reactor axial coordinate of all 22 reactor coils in (1) the base case and (2) the COT case.

Although it seems that feedstock flow distribution is a good attempt to achieve uniformity in the simulated furnace, so far the displayed results have been limited to zero-dimensional

values such as COT and P/E at the reactor coil outlet or maximum tube metal temperature. To have a better understanding of the effect of feedstock flow distribution, in principle, simulation results at each axial position along the reactor coil have to be examined. The profiles of the process gas temperature and the tube metal temperature for all reactor coils in the base case and the COT case are compared in Figure 3-5. The variation on the process temperature and the tube metal temperature in the COT case is clearly less than in the base case, meaning that feedstock flow distribution reduces nonuniformities of the distributed variables not only at a single point but over the full length of the reactor. This provides three clear benefits for this type of steam cracking furnaces. Firstly, it allows to apply the optimal process gas temperature profile found in literatures [8, 12, 15] to every reactor coil in the furnace as the process gas temperature profiles are nearly identical for all reactor coils in the COT case. Moreover, reducing TMT variations creates more room for furnace control and operation, providing the possibility of operating the furnace at a higher overall temperature, obtaining a higher ethene yield, at the cost of a lower propene yield. Finally, the run length can be extended when the tube metal temperature is the limiting criterion of the furnace run length as feedstock flow distribution generally reduces the overall maximum TMT.

Apart from the COT case and the P/E case, Figure 3-3 also shows the relation between the coking rate case and the TMT case. The rate of coke formation is dependent on the inner wall surface temperature of the reactor coil, which is directly related to the TMT. However, the rate of coke formation is also a function of the concentration of coke precursors. Hence the position along the reactor axial coordinate with the maximum TMT does not necessarily coincide with the reactor position along the axial coordinate with the maximum rate of coke formation. This is confirmed by the small shift of the position for the two respective maximums as shown in Figure 3-6. It can be seen that the profile of both tube metal

temperature and coking rate exhibit two maxima, which occur at the positions corresponding to the flame peak temperature for inlet and outlet legs of the reactor coil respectively. As a consequence of lower tube metal temperature and concentration of coke precursors (unsaturated hydrocarbons such as ethene, propene and so on), the maximum coking rate in the inlet leg is much lower than that of the outlet leg. Since the rate of coke formation is not exclusively determined by the temperature, the agreement between the results of the coking rate case and the TMT case is poorer compared to that between the COT case and the P/E case. Figure 3-7 plots the tube metal temperature and rate of coke formation as a function of the axial coordinate in reactor coil No.1 for different flow distribution cases. It is observed that by applying feedstock flow distribution, the profiles of coking rate and TMT do not change in shape but are only scaled.

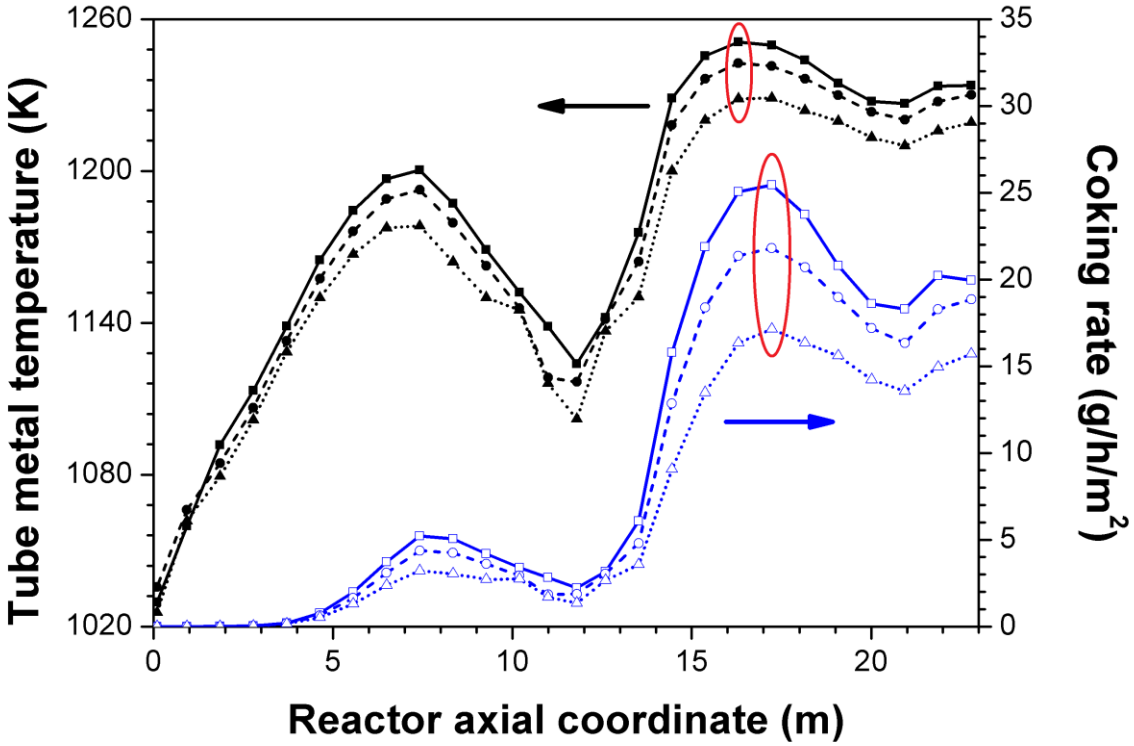

Figure 3-6: Tube metal temperature profiles (left axis, black) and coking rate profiles (right axis, blue) as a function of the reactor axial coordinate of reactor coil No.1 (squares, solid lines), No.10 (circles, dashed lines) and No.18 (triangles, dotted lines) for the base case.

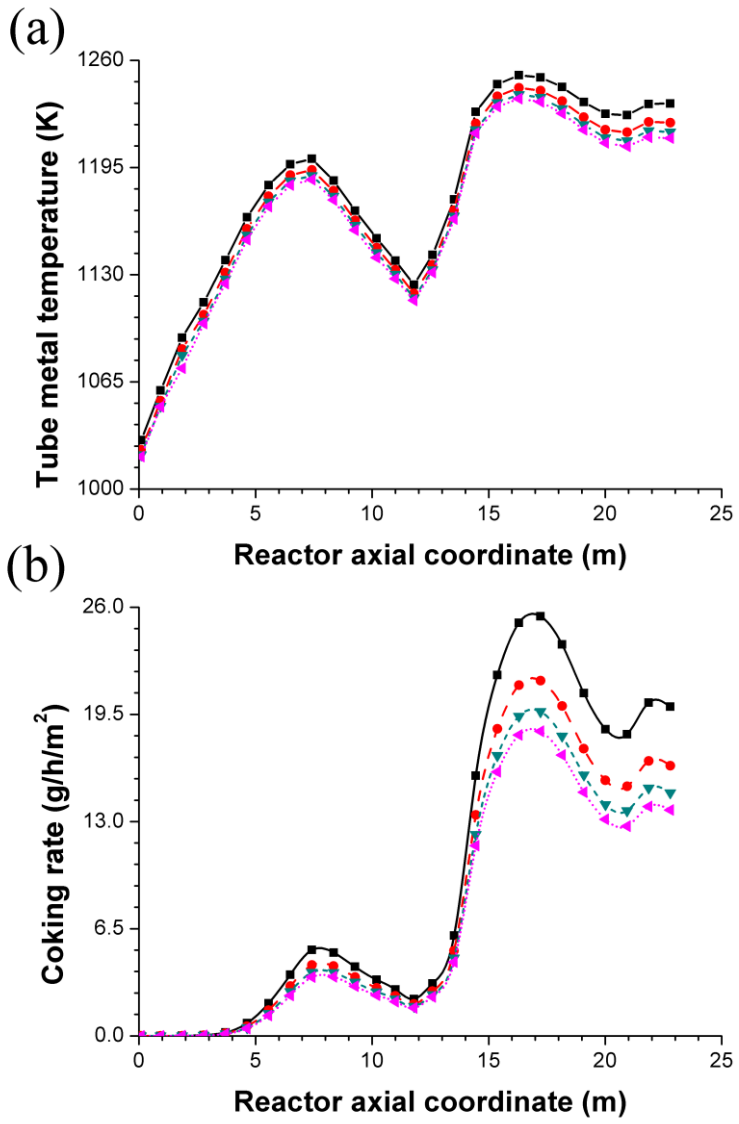

Figure 3-7: (a) Tube metal temperature and (b) coking rate profiles at start-of-run conditions as a function of the reactor axial coordinate of reactor coil No.1 for different feedstock flow distribution cases: ■ – base case; ● – COT case; ▼ – coking rate case; ◀ – TMT case.

So far only the uniformity of some important process variables has been discussed. However, for the purpose of furnace optimization, the overall light olefins yield should be compared to evaluate if feedstock flow distribution also increases the product yield of the furnace. To this end, the ethene and propene production rates at start-of-run for the four flow distribution cases were calculated and compared with those of the base case. As the feedstock mass flow rate through a coil changes, the product yields per reactor cannot be compared directly. Instead, the amounts of ethene and propene produced per unit of time were calculated as the sum of the respective product dry mass fraction at the reactor outlet multiplied with the mass flow rate of hydrocarbons through that reactor, see equations (3.18) and (3.19)for ethene and propene respectively:

$$E_{prod} = \sum_{i=1}^{n} F_i Y_{C_2H_4,i} \tag{3.18}$$

$$P_{prod} = \sum_{i=1}^{n} F_i Y_{C_3H_6,i} \tag{3.19}$$

where E_{prod} and P_{prod} represent the amounts of ethene and propene produced per unit of time, F_i is the hydrocarbon mass flow rate through reactor coil i. $Y_{C_2H_4,i}$, and $Y_{C_3H_6,i}$ are the ethene yield and propene dry mass fractions at the outlet of reactor coil i. The summation range parameter n equals the number of reactor coils in the modeled part of the radiant section, which is in this case 22 coils. The calculated E_{prod} and P_{prod} were multiplied by 8 to determine the production rate of ethene and propene for the entire furnace as the total number of reactor coils of the USC furnace is 176. The results plotted in Figure 3-8 show that there is a very small increase in the amounts of ethene and propene produced per unit of time at start-of-run conditions in the feedstock flow distribution cases compared to that of the base case,

except for the amount of ethene produced per unit of time in the TMT case. Taking the best flow distribution case, i.e. the COT case as an example, the increased amounts of ethene and propene produced is of 0.007 t/h and 0.041 t/h respectively. This means a relative increase in ethene and propene production rate of 0.04% and 0.47%, which can hardly be considered significant for a steam cracker. Furthermore, the TMT case even produces less ethene than the base case. Applying feedstock flow distribution hence provides little benefit to the yields at start-of-run conditions. Although feedstock flow distribution shows a limited effect on the amounts of valuable light olefins produced per unit of time, it reduces the nonuniformity and creates a wider operating window for the cracking furnace. Therefore, this has been studied more extensively because the start-of-run simulation results indicate that a longer run length could be expected in combination with an increase in annual light olefin production because of increased on-stream time.

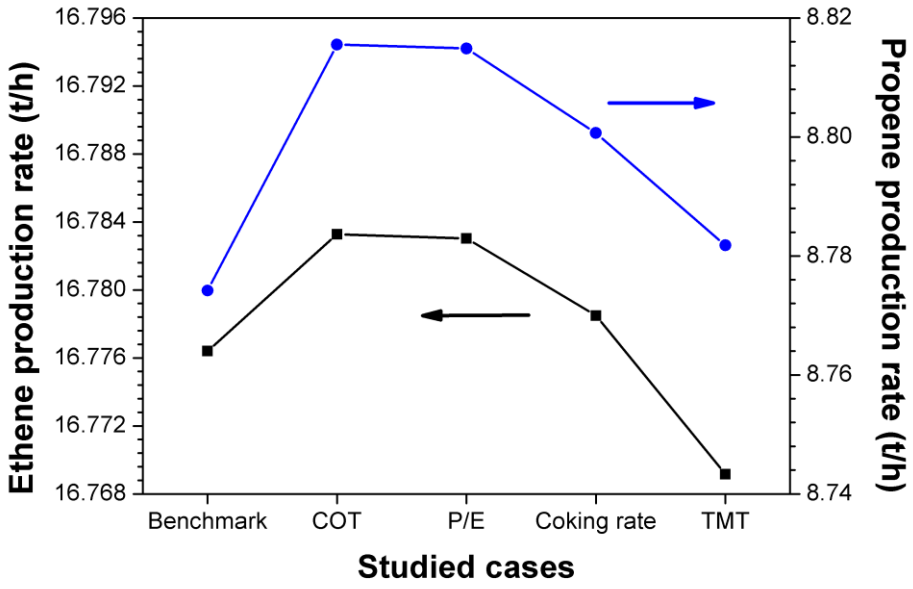

Figure 3-8: Rate of production of ethene (left axis, black) and propene (right axis, blue) at start-of-run in the base case and all flow distribution cases.

3.4.2 Run length improvement

In the majority of the cases, the run length of a steam cracker is controlled by one of two criteria, namely the tube metal temperature (TMT) or the coil inlet pressure (CIP). Both the TMT and CIP increase with increasing coke layer thickness; the TMT is mainly determined by the local coke layer thickness while the pressure drop is determined by the average coke layer thickness throughout the tube. When either the TMT or the CIP reaches the maximum allowed value, the production in the steam cracking furnace has to be interrupted for decoking. With increasing on-stream time, the coke layer grows thicker, resulting in an increased thermal resistance for heat transfer to the process gas due to the insulating properties of the coke. To maintain the same cracking severity over the furnace run length, the fuel flow rate should be gradually increased to compensate for the increased thermal resistance over the growing coke layer. As the heat flux profile along the reactor is affected, reactor calculations have to be executed at each time step of the run length simulation. The typical run length for the USC furnace is in the range of 30 to 60 days, depending on the feedstock. Because the difference in time scales between the gas phase reactions (product yields) and the surface reactions (coke formation) is significant, it can be assumed that coke formation does not directly affect the primary reactions in a steam cracker. Therefore it is acceptable to use discrete time steps in the numerical simulation of the coke layer growth, which is inherently a continuous process. In this work, a time step of 100 h was deemed appropriate [50] based on the characteristic time scale for coke formation. The rate of coke formation was assumed to be constant during each time step: the thickness of the coke layer was updated after each step based on the prevailing conditions of species concentration and coke-gas interface temperature. Subsequently, the heat flux profile was adapted to maintain the desired cracking severity. Two sets of run length simulations were performed for each of the four feedstock

flow distribution cases using a maximum TMT of 1373 K and a maximum CIP of 3.46 atm (corresponding to 1.7 atm pressure drop over the coil) as the stopping criterion respectively.

The profiles of the maximum TMT per reactor coil as a function of the on-stream time are shown in Figure 3-9. The run length simulation implemented a maximum TMT of 1373 K as stopping criterion. When the first reactor reaches the TMT criterion, the furnace operation has to be interrupted for decoking, accordingly, the simulation were stopped when this criterion was reached. It is clear from Figure 3-9 that as the on-stream time increases, the spread on the maximum TMT values for all reactors in one flow distribution case increases, i.e. the maximum TMT profiles diverge. In all flow distribution cases, the reactors at the extremities (No.1 and No.22) reach the limiting TMT criterion first and hence trigger the interruption in the furnace operation for decoking. The explanation is based on the results in Figure 3-3: reactor coils No.1 and No.22 receive the highest heat flux and exhibit the highest values for maximum coking rate and maximum TMT in the base case. From the spread of the maximum TMT values at start-of-run conditions, it is expected that the run length will increase successively in the base case, the COT case, the coking rate case and the TMT case in case the TMT is the limiting criterion. This trend is indeed confirmed by the simulated run lengths for all flow distribution cases summarized in Table 3-2. In the COT case and the P/E, the run length increases by about 8 days compared to the base case with TMT as limiting criterion. The run length in the coking rate case and in the TMT case are nearly 13 days longer than the base case. The run length of the TMT case is the longest but the difference of 0.3 day with the coking rate case is rather small.

Table 3-2: Run length simulation results for all feedstock flow distribution cases.

	Base case	COT case	P/E case	Coking rate case	TMT case
	TMT criterion				
Run length (days)	46.5	54.3	54.7	59.5	59.8
Ethene production (kt/a)	137.42	138.49	138.51	138.90	138.60
Propene production (kt/a)	71.84	72.70	72.73	72.84	72.70
	CIP criterion				
Run length (days)	43.1	46.8	47.2	48.9	48.9
Ethene production (kt/a)	136.83	137.57	137.59	137.83	137.77
Propene production (kt/a)	71.52	72.21	72.23	72.25	72.11
Furnace thermal efficiency (%)	45.814	45.811	45.814	45.810	45.789

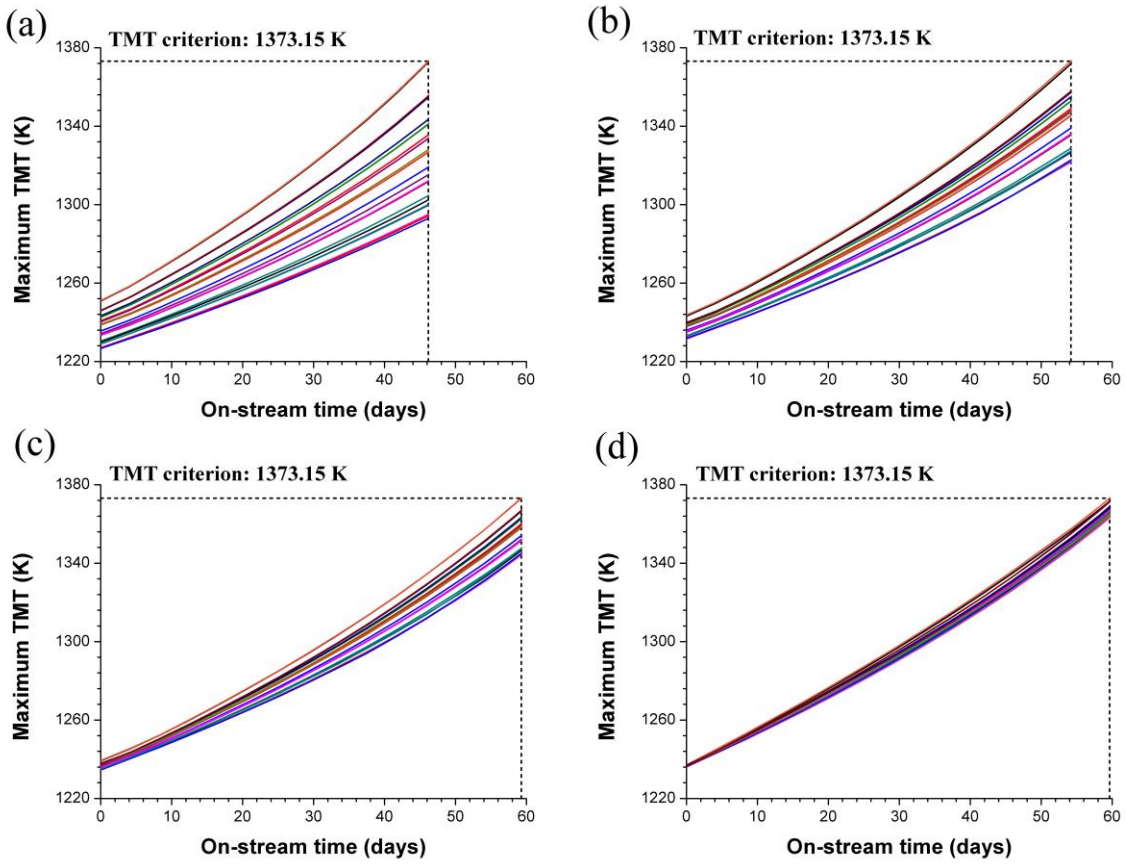

Figure 3-9: Maximum TMT for all 22 reactor coils as a function of the on-stream time in (a) base case; (b) COT case; (c) coking rate case; (d) TMT case.

A drawback of the feedstock flow distribution is that the pressure drop at start-of-run conditions of the reactor coils with an increased feedstock flow rate becomes higher. The

start-of-run CIP is higher so the operating window is smaller for pressure drop limited reactor coils. Therefore, run length simulations using a maximum CIP of 3.46 atm (corresponding to a pressure drop of 1.7 atm) as limiting criterion were performed to evaluate the effect of pressure limitation as well. The profiles of pressure drop in all 22 reactor coils as function of the on-stream time are plotted in Figure 3-10. In contrast with the maximum TMT profiles, applying flow distribution increases the spread on the pressure drop at start-of-run conditions. Although the higher feedstock mass flow rates to the reactor coils receiving a higher heat flux increases their initial pressure drop, the average coke layer thickness of these coils is reduced and hence the increase of the pressure drop with increasing on-stream time becomes slower. On the other hand, reactor coils which receive a lower heat flux experience the opposite: a lower feedstock flow rate leads to a higher coking rate and a faster pressure drop increase. Consequently, the divergence at start-of-run helps to reduce the pressure drop spread at end-of-run. However, less CIP divergence at end-of-run does not mean a longer run length.

The run lengths of all feedstock flow distribution cases with CIP as limiting criterion are also compared in Table 3-2. It is clear that the benefit of feedstock flow distribution in terms of run length is smaller when CIP is the limiting criterion compared to when TMT is the limiting criterion. The run length only increases by 4 days in the COT and P/E cases and by 6 days in the coking rate and TMT cases compared to the base case. The explanation for this can be found by simulations performed to study the on-stream time of a single reactor coil limited by TMT and CIP respectively as function of the feedstock flow rate. As illustrated in Figure 3-11, the run length increases monotonically when TMT is the limiting factor, which is obvious since increasing feedstock flow rate through a reactor coil reduces its maximum TMT and therefore creates always longer the run lengths. Whereas if the reactor coil is limited by CIP, the run length exhibits a maximum due to the double effect of increasing feedstock flow rate.

On the one hand, the coke formation rate is reduced due to the lower tube inner wall temperatures. On the other hand, the velocity and hence the pressure drop increase, resulting in a higher CIP at start-of-run conditions. Whether the run length is increased or decreased under CIP limitation is dependent on which of the two effects is more pronounced. Therefore, the TMT case which exhibits the longest run length when TMT is the limiting criterion for decoking is no longer the optimal case when CIP is the limiting criterion as compared in Table 3-2, because the high mass flow rates through some of the reactors limit the operating window.

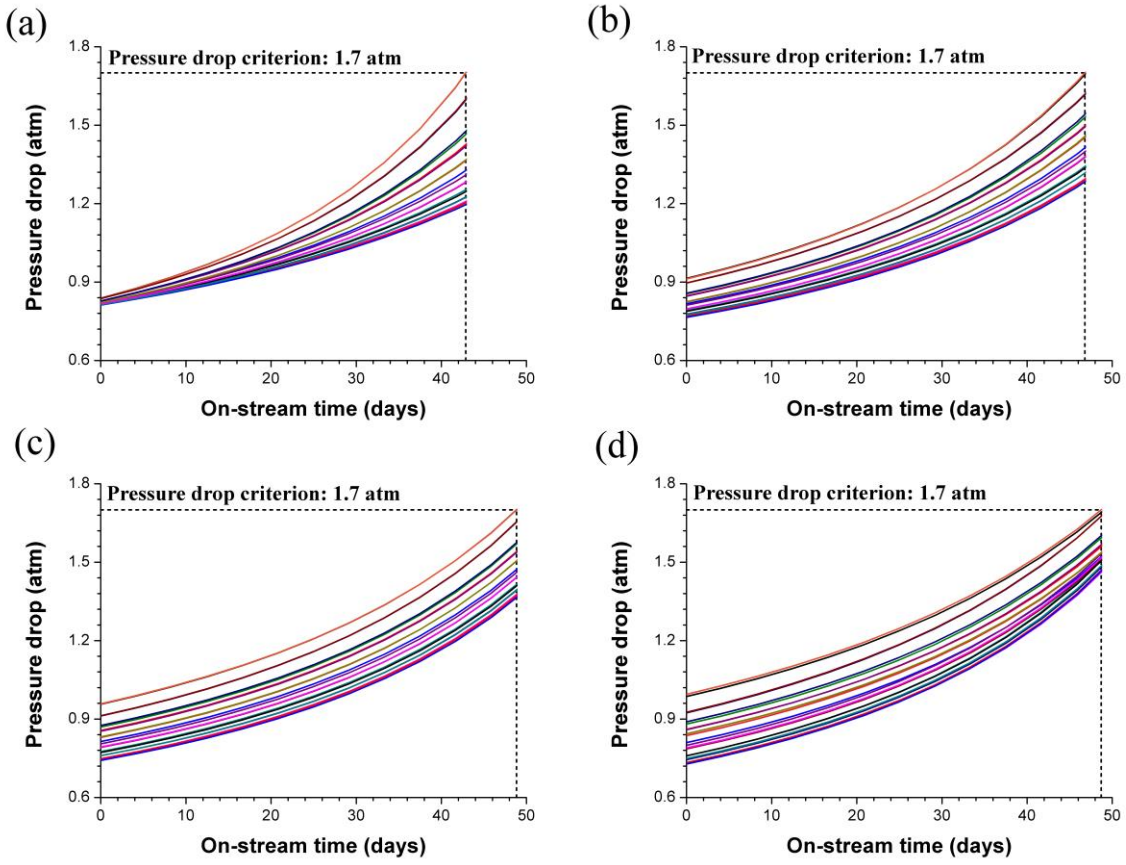

Figure 3-10: Profiles of pressure drop for all 22 reactor coils as a function of the on-stream time in (a) base case; (b) COT case; (c) coking rate case; (d) TMT case.

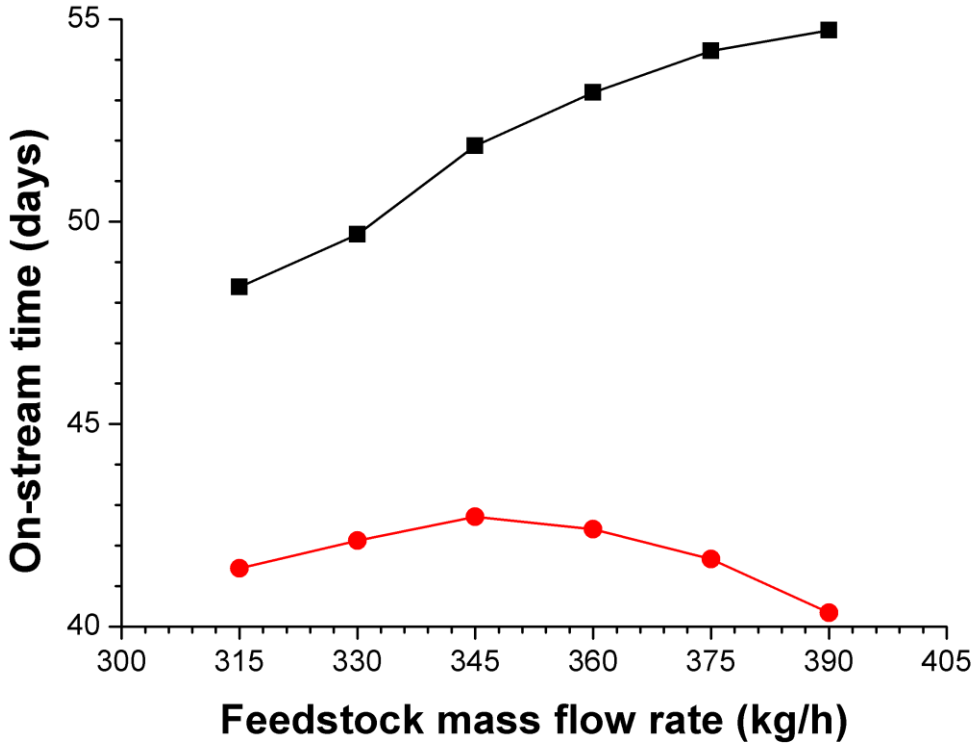

Figure 3-11: Single reactor coil on-stream time as a function of feedstock mass flow rate for ■ – TMT limiting criterion; ● – CIP limiting criterion.

Generally speaking, a longer run length increases the total annual light olefin production However, the ethene and propene yields change slightly as the on-stream time increases because the cracking severity (P/E) is maintained constant. To achieve this, the COT increases slightly with increasing on-stream time to have a higher conversion. This in turn leads to a change in ethene and propene yields in different time steps. Therefore, the production capacity for ethene and propene should be calculated by taking the sum over the discrete time intervals of the run length simulation, , see equations (3.20) and (3.21) for ethene and propene respectively.

$$C_{ethene} = \sum_{j}^{t_n} E_{prod,j} \Big/ (t_r t_n + t_d) \tag{3.20}$$

$$C_{propene} = \sum_{j}^{t_n} P_{prod,j} \Big/ (t_r t_n + t_d) \tag{3.21}$$

where $E_{prod,j}$ and $P_{prod,j}$ are the yields of ethene and propene at time step j respectively, t_r is the time step size, t_n is the number of time steps taken in a certain flow distribution case and t_d is the decoking time which is taken as 72 h [49]. The resulting annual production volumes for ethene and propene in the USC furnace are given in Table 3-2. In contrast to the conclusions drawn based on the run length, the coking rate case provides the highest annual production of ethene and propene for both decoking criteria. As the olefin yield decreases towards the end of the run, it is not necessarily beneficial to operate the furnace until its longest possible run length is reached. For the TMT case in particular, it would be beneficial to stop the furnace before the run length criterion is reached to be able to initiate decoking. The olefin yield from the extended run length cannot compensate for the olefin yield at renewed start-of-run conditions after decoking, even when taking the production loss due to decoking into account. Additionally, the difference in olefin capacities between the TMT as limiting criterion and CIP as limiting criterion is small. For the current USC cracking furnace which is limited by the CIP criterion, the coking rate case as the optimal feedstock flow distribution case annually increases the ethene production by 1000 metric tons and the propene production by 730 metric tons. The relative increase of ethene and propene productions in the coking rate case are 0.73% and 1.02% respectively. Note that, although the extended run length by flow distribution for the TMT criterion limited furnace is about 2 times longer than that for the CIP criterion limited one, the increase of the ethene and propene

productions for both limiting criterion are basically the same. In the case of TMT as limiting criterion, the annual increase of ethene and propene productions are 1480 metric tons and 1000 metric tons respectively. However, the relative increase of the ethene and propene productions are 1.08% and 1.39% when TMT is the limiting criterion, which is only 0.35% higher than that when CIP is the limiting criterion. Generally, steam cracking furnaces whose run length is often limited by a TMT criterion could benefit more from feedstock flow distribution compared to those furnaces whose run length is often limited by a CIP criterion.

Finally, as shown in Table 3-2, the furnace thermal efficiency is almost identical in all cases. Hence, feedstock flow distribution has a negligible influence on the fire side of the furnace and on the operation of the convection section. This allows to apply the different feedstock flow distribution schemes to industrial steam crackers with similar configurations as the USC furnace since there is no need to adjust the fuel flow distribution on the fire side.

3.4.3 Practical implementation

As demonstrated in the foregoing discussion, the coking rate case is the optimal one for the USC cracking furnace, hence the flow distribution scheme should aim at achieving a uniform distribution of the maximum coke rate. However, from an operational point of view, this is implausible because the feedstock mass flow rate is typically based on real-time measurements instead of on simulated data and on-line measurements of the maximum coking rate in an industrial coil are not possible. Considering that the goal of industrially practiced pass balancing and zone firing is also to reduce the nonuniform coking rate in order to extend the run length, the distribution of maximum TMT over all reactor coils, which is stronger correlated to the coking rate distribution than the COT distribution, is suggested as the best indicator for the flow distribution (pass balancing) between and/or within modules. The tube

metal temperature can nowadays be measured using advanced laser based techniques or via weld-on thermocouples in strategic locations.

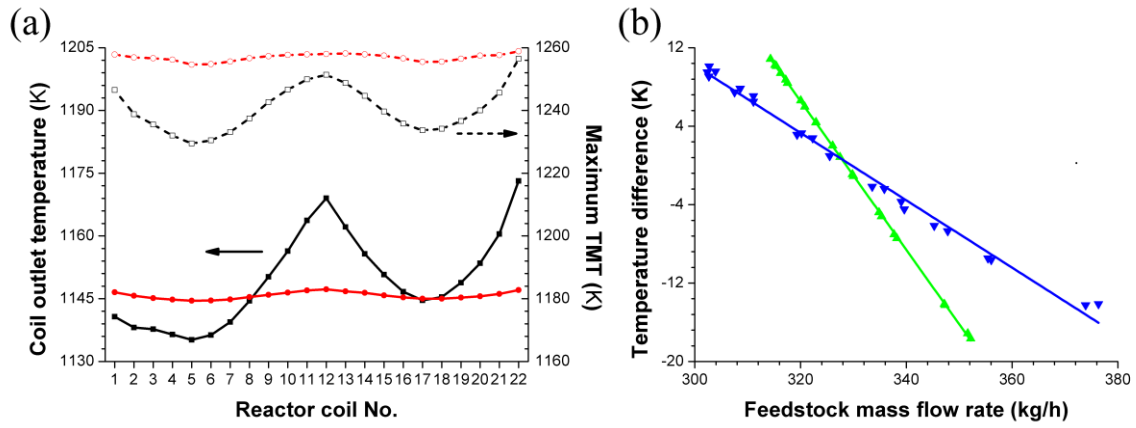

Figure 3-12: (a) Profile of COT (solid line, solid symbols) and maximum TMT (dashed line, open symbols) for the 22 reactor coils in the external quarter case (black) and the propane feedstock case (red). (b) Temperature change as a function of feedstock flow rate: ▲ - COT; ▼ - maximum TMT.

In the present study, only the internal quarter was simulated due to the high computational cost for coupled CFD simulations. But for the external quarter, an additional cold surface is present in the form of the furnace side wall, which has a considerable impact on the nonuniformity and leads to a lower COT and a lower maximum TMT in the coils closest to the end wall [19]. This phenomena is also observed in one additional coupled simulation, denoted as "external quarter case", where the left boundary along the x-coordinate was set to solid wall instead of symmetry plane. As shown in Figure 3-12 (a), the lower heat input to coils NO. 1 – 11 is clearly reflected by the COT and the maximum TMT variations. In light of this, half of the furnace should be taken into account in the simulation so as to obtain a complete flow distribution scheme for the entire furnace as studied by Brown et al. [18, 19], but the concept will be the same as presented in the previous sections.

The present approach requires that the feedstock flow rate per reactor coil is modified individually, i.e. a separate mass flow controller should be present per coil, installed between the convection section and the radiant section. As this is not realistic for reasons of cost and valve longevity, another solution is proposed. A so called fixed heterogeneous distribution can be achieved by modifying the diameter of the venturi nozzles between the convection section and the radiant section based on CFD calculations in the design stage or when retubing the complete furnace. As the flow rate through a venturi nozzle depends linearly on the cross sectional area in the nozzle throat in the choked regime, assuming the fluid can be described as an ideal gas, as indicated in equation (3.22), the diameter of the venturi nozzle is a degree of freedom in the design stage that can be used to instate the desired feedstock flow distribution over the coils.

$$F_{feed} = \frac{\Omega p_t}{\sqrt{T_t}} \sqrt{\frac{\gamma}{R}} \left(\frac{\gamma + 1}{2}\right)^{-\frac{\gamma+1}{2(\gamma-1)}} \tag{3.22}$$

F_{feed} is the feedstock mass flow rate at choked condition; Ω is the cross sectional area in the nozzle throat; p_t, T_t, and γ are the terminal pressure, terminal temperature and specific heat capacity ratio respectively.

There is one minor downside to this approach: once set, the distribution is fixed so it cannot be changed anymore in between complete furnace shutdowns. As this typically is done every 5 years it means that this fixed distribution will be used for this period. The question could be raised whether the flow distribution is still valid when other feedstocks are used during this period. To evaluate the generality of the flow distribution method, a set of coupled simulations were performed with previously obtained flow distribution schemes for realizing uniform COT, P/E, maximum coking rate and maximum TMT, while using propane as a new feedstock. Although this change is unlikely in practice due to the significant difference in heat

balance, especially in the convection section, it can act as a worst case scenario to verify the generality of the method. The simulations here are hence only meant to analyze the sensitivity of the flow distribution method to feedstock change. It is shown in Figure 3-12 (a) that the COT and maximum TMT are still quite uniformly distributed in the propane feedstock case, indicating the generality of the flow distribution method.

Finally, considering the large uncertainty in determining the mass flow rate distribution based solely on calculation in practical application, it is suggested to utilize a combination of historically measured COT and/or maximum TMT variations of a similar existing furnace and detailed CFD simulation to determine the mass flow distribution scheme for furnace design or retrofit. As applying flow distribution in a real life furnace may also require some simpler rules which can be verified by real measurements, plots of the changes in COT and maximum TMT as a function of feedstock mass flow rate are depicted in Figure 3-12 (b). It can be seen that the changes of COT and maximum TMT vary almost linearly with feedstock mass flow rate, which is to be used as a rule of thumb for determining the magnitude and trend based on real measurements. However there are still many factors with regard to installation and operation such as imperfect coil alignment, variations in tip drilling size and orientation from burner to burner, and variations in draft along the box, which can have big impact on the furnace nonuniformity. With respect to the measurement, the normal methods of using skin thermocouple and hand held IR pyrometer for COT and TMT respectively, still have large uncertainties. Additionally, some other factors such as the cooling effect of having a peep door open, the angle of inclination of the device to the tube, etc. in the course of measuring cannot be easily controlled. Therefore, extreme care should be taken that the design of the venturi nozzles provides a globally optimal distribution for different feedstocks and operating

conditions, which have to be based on the combination of detailed CFD calculation and historical measurement.

3.5 Conclusions

Feedstock flow distribution allows to reduce nonuniformities between multiple reactor coils in steam cracking furnaces. It extends the total production and run length. This was demonstrated via coupled numerical simulation combining computational fluid dynamics and COILSIM1D for an industrial USC furnace. Four feedstock flow distribution cases, aiming at a uniform COT, P/E, maximum coking rate and maximum TMT over all coils, were studied and compared with a base case without feedstock flow distribution. Although the results of the four cases at start-of-run conditions show no significant improvement of ethene and propene production rate as a result of feedstock flow distribution, the run length simulations of the four cases indicate that feedstock flow distribution increases the run length and therefore decreases the decoking frequency. As the annual olefin production capacity increases with increasing run length, the feedstock flow distribution results in a higher annual olefin production capacity. The only minor drawback of flow distribution is the increased pressure drop at start-of-run conditions for the reactor coils with an increased feedstock flow rate. Hence feedstock flow distribution, which can be straight forwardly implemented in furnaces equipped with venturis, provides a potential benefit for furnaces where run length is often limited by a maximum tube metal temperature. The potential benefit for furnaces where run length is often limited by the pressure drop is smaller. A feedstock flow distribution leading to a uniform maximum coking rate over all the coils is identified as the optimal case. The annual production capacity increases by 1000 metric tons for ethene and 730 metric tons for propene compared to the base case for an ultra-selective conversion furnace with a nameplate production capacity for ethene of 130 kt/a.

For practical consideration, uniform maximum TMT is more beneficial than uniform COT as this is found to be the best indicator for the coking behavior of an individual coil. As confirmation, it is suggested to also consider historical data to determine the flow distribution scheme and to complement the detailed CFD calculations.

References

[1] P.S. Van Damme, G.F. Froment, W.B. Balthasar, Scaling up of naphtha cracking coils, Industrial & Engineering Chemistry Process Design and Development, 20 (1981) 366-376.
[2] G.F. Froment, Kinetics and reactor design in the thermal cracking for olefins production, Chem Eng Sci, 47 (1992) 2163-2177.
[3] M.E. Masoumi, S.M. Sadrameli, J. Towfighi, A. Niaei, Simulation, optimization and control of a thermal cracking furnace, Energy, 31 (2006) 516-527.
[4] S.M. Sadrameli, Thermal/catalytic cracking of hydrocarbons for the production of olefins: A state-of-the-art review I: Thermal cracking review, Fuel, 140 (2015) 102-115.
[5] K.M. Van Geem, R. Žajdlík, M.-F. Reyniers, G.B. Marin, Dimensional analysis for scaling up and down steam cracking coils, Chem Eng J, 134 (2007) 3-10.
[6] K.M. Van Geem, M.-F. Reyniers, G.B. Marin, Two Severity Indices for Scale-Up of Steam Cracking Coils, Ind Eng Chem Res, 44 (2005) 3402-3411.
[7] Zolo Technologies, Inc. http://zolotech.com/chemical-and-refining/ethylene-cracking-furnace-efficiency/.
[8] P. Van Damme, P. Willems, G. Froment, Temperature, not time, controls steam cracking yields, Oil Gas J, 82 (1984) 68-73.
[9] P. Plehiers, G. Froment, Reversed split coil improves ethylene yields, Oil Gas J.;(United States), 85 (1987) 41-49.
[10] P.M. Plehiers, G.F. Froment, The Uno-Quattro coil: high severities for increased ethylene selectivity, Ind Eng Chem Res, 30 (1991) 1081-1086.
[11] M.W.M. Van Goethem, S. Barendregt, J. Grievink, J.A. Moulijn, P.J.T. Verheijen, Towards synthesis of an optimal thermal cracking reactor, Chemical Engineering Research and Design, 86 (2008) 703-712.
[12] M.W.M. van Goethem, S. Barendregt, J. Grievink, J.A. Moulijn, P.J.T. Verheijen, Model-based, thermo-physical optimisation for high olefin yield in steam cracking reactors, Chemical Engineering Research and Design, 88 (2010) 1305-1319.
[13] M. Ghashghaee, R. Karimzadeh, Multivariable optimization of thermal cracking severity, Chemical Engineering Research and Design, 89 (2011) 1067-1077.
[14] G.Y. Gao, M. Wang, C. Ramshaw, X.G. Li, H. Yeung, Optimal operation of tubular reactors for naphtha cracking by numerical simulation, Asia-Pacific Journal of Chemical Engineering, 4 (2009) 885-892.
[15] M. Shahrokhi, A. Nejati, Optimal Temperature Control of a Propane Thermal Cracking Reactor, Ind Eng Chem Res, 41 (2002) 6572-6578.
[16] D.J. Van Cauwenberge, C.M. Schietekat, J. Floré, K.M. Van Geem, G.B. Marin, CFD-based design of 3D pyrolysis reactors: RANS vs. LES, Chem Eng J, 282 (2015) 66-76.
[17] Y. Zhang, F. Qian, C.M. Schietekat, K.M. Van Geem, G.B. Marin, Impact of flue gas radiative properties and burner geometry in furnace simulations, AIChE J, 61 (2015) 936-954.

[18] D. Brown, P. Smith, B. Adams, Cracking furnace fireside modeling advances, in: Proceedings of the 6th Ethylene Producers' Conference, Atlanta, GA (United States), 1994.
[19] D.J. Brown, M.A. Cremer, P.J. Smith, R.T. Waibel, Fireside modeling in cracking furnaces, in: Proceedings of the 9th Ethylene Producers' Conference, Houston, TX (United States), 1997, pp. 159-193.
[20] K.M. Van Geem, M.-F. Reyniers, G.B. Marin, J. Song, W.H. Green, D.M. Matheu, Automatic reaction network generation using RMG for steam cracking of n-hexane, AIChE J, 52 (2006) 718-730.
[21] W. Sun, M. Saeys, Construction of an ab initio kinetic model for industrial ethane pyrolysis, AIChE J, 57 (2011) 2458-2471.
[22] M.K. Sabbe, K.M. Van Geem, M.-F. Reyniers, G.B. Marin, First principle-based simulation of ethane steam cracking, AIChE J, 57 (2011) 482-496.
[23] C.M. Schietekat, D.J. Van Cauwenberge, K.M. Van Geem, G.B. Marin, Computational fluid dynamics-based design of finned steam cracking reactors, AIChE J, 60 (2014) 794-808.
[24] P.A. Reyniers, C.M. Schietekat, D.J. Van Cauwenberge, L.A. Vandewalle, K.M. Van Geem, G.B. Marin, Necessity and Feasibility of 3D Simulations of Steam Cracking Reactors, Ind Eng Chem Res, 54 (2015) 12270-12282.
[25] G.J. Heynderickx, G.F. Froment, Simulation and Comparison of the Run Length of an Ethane Cracking Furnace with Reactor Tubes of Circular and Elliptical Cross Sections, Ind Eng Chem Res, 37 (1998) 914-922.
[26] P.M. Plehiers, G.C. Reyniers, G.F. Froment, Simulation of the run length of an ethane cracking furnace, Ind Eng Chem Res, 29 (1990) 636-641.
[27] S.P. Pyl, K.M. Van Geem, M.-F. Reyniers, G.B. Marin, Molecular reconstruction of complex hydrocarbon mixtures: An application of principal component analysis, AIChE J, 56 (2010) 3174-3188.
[28] J.J. Verstraete, P. Schnongs, H. Dulot, D. Hudebine, Molecular reconstruction of heavy petroleum residue fractions, Chem Eng Sci, 65 (2010) 304-312.
[29] K.M. Van Geem, D. Hudébine, M.F. Reyniers, F. Wahl, J.J. Verstraete, G.B. Marin, Molecular reconstruction of naphtha steam cracking feedstocks based on commercial indices, Comput Chem Eng, 31 (2007) 1020-1034.
[30] K.M. Van Geem, M.F. Reyniers, G.B. Marin, Challenges of modeling steam cracking of heavy feedstocks, Oil & Gas Science and Technology - Rev. IFP, 63 (2008) 79-94.
[31] A.J.M. Oprins, G.J. Heynderickx, G.B. Marin, Three-Dimensional Asymmetric Flow and Temperature Fields in Cracking Furnaces, Ind Eng Chem Res, 40 (2001) 5087-5094.
[32] G.J. Heynderickx, A.J.M. Oprins, G.B. Marin, E. Dick, Three-dimensional flow patterns in cracking furnaces with long-flame burners, AIChE J, 47 (2001) 388-400.
[33] A.J.M. Oprins, G.J. Heynderickx, Calculation of three-dimensional flow and pressure fields in cracking furnaces, Chem Eng Sci, 58 (2003) 4883-4893.
[34] G.D. Stefanidis, B. Merci, G.J. Heynderickx, G.B. Marin, CFD simulations of steam cracking furnaces using detailed combustion mechanisms, Comput Chem Eng, 30 (2006) 635-649.
[35] G. Hu, H. Wang, F. Qian, Y. Zhang, J. Li, K.M. Van Geem, G.B. Marin, Comprehensive CFD Simulation of Product Yields and Coking Rates for a Floor- and Wall-Fired Naphtha Cracking Furnace, Ind Eng Chem Res, 50 (2011) 13672-13685.
[36] G. Hu, H. Wang, F. Qian, K.M. Van Geem, C.M. Schietekat, G.B. Marin, Coupled simulation of an industrial naphtha cracking furnace equipped with long-flame and radiation burners, Comput Chem Eng, 38 (2012) 24-34.

[37] G. Hu, C.M. Schietekat, Y. Zhang, F. Qian, G.J. Heynderickx, K.M. Van Geem, G.B. Marin, Impact of Radiation Models in Coupled Simulations of Steam Cracking Furnaces and Reactors, Ind Eng Chem Res, 54 (2015) 2453-2465.
[38] Q. Tang, M. Denison, B. Adams, D. Brown, Towards comprehensive computational fluid dynamics modeling of pyrolysis furnaces with next generation low-NOx burners using finite-rate chemistry, Proceedings of the Combustion Institute, 32 (2009) 2649-2657.
[39] D.J. Brown, J. Ma, B.R. Adams, Development of an improved prediction model for chemical process furnaces, in: AIChE Spring National Meeting, New Orleans, LA (United States), 2003.
[40] Q. Tang, B. Adams, M. Bockelie, M. Cremer, M. Denison, C. Montgomery, A. Sarofim, D. Brown, Towards comprehensive CFD modeling of lean premixed ultra-low NOx burners in process heaters, in: Proceedings of the 17th Ethylene Producers' Conference, Atlanta, GA (United States), 2005, pp. 594-619.
[41] K.M. Van Geem, G.J. Heynderickx, G.B. Marin, Effect of radial temperature profiles on yields in steam cracking, AIChE J, 50 (2004) 173-183.
[42] COILSIM1D. http://www.avgi.be/.
[43] V. Yakhot, S.A. Orszag, S. Thangam, T.B. Gatski, C.G. Speziale, Development of turbulence models for shear flows by a double expansion technique, Physics of Fluids A: Fluid Dynamics (1989-1993), 4 (1992) 1510-1520.
[44] C.K. Westbrook, F.L. Dryer, Simplified Reaction Mechanisms for the Oxidation of Hydrocarbon Fuels in Flames, Combust Sci Technol, 27 (1981) 31-43.
[45] B.F. Magnussen, B.H. Hjertager, On mathematical modeling of turbulent combustion with special emphasis on soot formation and combustion, Symposium (International) on Combustion, 16 (1977) 719-729.
[46] G.H. Yeoh, K.K. Yuen, Computational Fluid Dynamics in Fire Engineering: Theory, Modelling and Practice, Butterworth-Heinemann, Burlington, 2009.
[47] A. Habibi, B. Merci, G.J. Heynderickx, Impact of radiation models in CFD simulations of steam cracking furnaces, Comput Chem Eng, 31 (2007) 1389-1406.
[48] D.K. Edwards, A. Balakrishnan, Thermal radiation by combustion gases, Int J Heat Mass Tran, 16 (1973) 25-40.
[49] H. Zimmermann, R. Walzl, Ethylene, in: Ullmann's Encyclopedia of Industrial Chemistry, Wiley-VCH, Weinheim, Germany, 2000.
[50] K. Van Geem, Z. Zhou, M.-F. Reyniers, G.B. Marin, Effect of process conditions and feedstock composition on run lengths of steam cracking coils, in: 2009 AIChE Spring National meeting; 5th Global Congress on Process Safety, New York, NY (United States), 2009.

Chapter 4: Incident radiative heat flux based furnace run length simulation

This chapter is based on the following paper:

Zhang, Y.; Reyniers, P. A.; Du, W.; Van Geem, K. M.; Marin, G. B., Incident radiative heat flux based method for the coupled run length simulation of steam cracking furnaces. Industrial & Engineering Chemistry Research, 2017, 56 (14): 4156-4172.

Abstract

Due to the significant economic penalty associated to decoking steam cracking furnaces accurate run length predictions are crucial for assessing their techno-economic performance. Therefore, for the first time a full coupled run length simulation of an industrial naphtha steam cracking furnace was performed using detailed computational fluid dynamics simulations for the furnace side. The results show that the unevenly deposited coke layer within the reactors results in a redistribution of the thermal power over the time on stream, which is beneficial for the uniformity of the coke growth in the reactor. These effects were not observed in traditional standalone run length simulations, which justifies the high computational cost. However, the high computational cost of these CFD iterations can be overcome by using a novel method which correlates the incident radiative heat flux (IRHF) to the flue gas bridge wall temperature obtained from an overall zero-dimensional heat balance. This so-called IRHF based method provides similar accuracy as the CFD coupled method but at a fraction of the computational cost. The CPU time was decreased by a factor over 2000, allowing to move these calculations from a high-performance computing environment to a personal computer. The generality of this method for changing operating conditions or feedstock compositions was also demonstrated by comparing with CFD coupled run length simulations of a set of new cases. With relative errors well below 1%, the novel IRHF based method is recommended for coupled run length simulations of steam cracking units.

Keywords: computational fluid dynamics, steam cracking, run length simulation, incident radiative heat flux, furnaces

4.1 Introduction

Steam cracking of hydrocarbon feedstock to produce light olefins such as ethene and propene is accompanied by the formation of carbonaceous deposits on the inner surface of the cracking reactor coils, referred to as coke. This coke layer hampers the heat transfer from the fired furnace to the process gas, hence the heat input from the fire side has to be increased over time to maintain the same feedstock conversion and cracking severity, leading to a rise in tube metal temperature (TMT). In addition, the pressure drop gradually increases since the growing coke layer reduces the cross sectional area for flow. This results in a higher overall pressure in the reactor which favors bimolecular reactions and decreases the selectivity towards the desired light olefins. To mitigate these adverse effects, the furnace is periodically shut down for decoking when either the tube metal temperature (TMT) or the coil inlet pressure (CIP) reaches a certain threshold value.

This decoking procedure has a significant economic penalty as production is halted, and as resources such as thermal and mechanical energy are consumed. To minimize the economic penalty, the period between subsequent decoking operations should be prolonged, i.e. the decoking frequency should be kept as low as possible. However, at the end of the run length, the selectivity towards valuable components decreases considerably due to the higher pressure drop over the reactor, sometimes to such an extent that further production is economically unjustified since the product selectivity becomes too low. Hence there is a trade-off between loss of selectivity and decoking cost, resulting in an optimal run length maximizing the economic gain.

Many studies on steady-state and dynamic optimization of steam cracking furnaces to maximize the total olefin production [1-5] are available in the literature. The accuracy of such studies is entirely dependent on a meticulous description of the furnace as function of the time

on stream. Erroneous values for the run length or the olefin selectivity significantly skew the results of the economic calculations.

The most important factor affecting the run length simulation is the heat flux to the reactor, however, it should be stressed that there are actually two different concepts of heat flux often used in literatures with the same term as "heat flux". To avoid any confusion, two distinct terminologies are used to refer to these two concepts in the present paper. The first is referred to as the *total heat flux*, which is defined as the local *net* thermal power received by the external surface of the reactor coils per unit surface area. The total heat flux profile along the axial reactor coordinate changes over time as a consequence of the coke deposited on the inner reactor wall. The second is the *incident radiative heat flux*, defined as radiative power reaching the external surface of the reactor coils. The incident radiative heat flux is determined by the firing conditions in the furnace and thus independent of thermal conditions of the reactor coils.

Three types of methods have been developed to update this total heat flux profile during the furnace time on stream, and are listed here in the order of increasing complexity and computational cost. In the first type, only the reactor side is considered in the run length simulations. Since no information on the furnace side is available, the process gas temperature profile is kept constant over time and the required total heat flux profile is back-calculated from this imposed temperature profile [1, 2]. Despite the easy implementation and low computational cost, this type of run length simulation does not account for the increasing process gas temperature profile and coil outlet temperature (COT) over time to maintain the same conversion or cracking severity. In the second type, the total heat flux profile obtained from a coupled furnace-reactor simulation at start-of-run conditions is utilized. In this so-called standalone run length simulation, the total heat flux profile at start of run is uniformly

scaled up over time to keep the conversion or cracking severity constant at a predefined value until either of the two stopping conditions is reached. [4, 6, 7]. This scaling procedure only affects the absolute values of the total heat flux profile but maintains its shape. However, the nonuniform coke layer thickness along the reactor coil will affect the total heat flux profile shape. The third type of run length simulation fully accounts for the thermal interaction between furnace and reactor coils, referred to as coupled run length simulations [8, 9]. A clear change in the shape of the total heat flux profile was observed, indicating that it should be updated over time using coupled run length simulations.

The coupled run length simulations available in the literature to date [8, 9] implemented the zone method [10] to model the furnace side. The lack of computational resources at that time made that the number of (isothermal) zones in these simulations was rather small, and hence that the accuracy of the resulting total heat flux profile shape can be considered as questionable. With the rapidly increased availability of computational resources in recent years, researches switched to computational fluid dynamic (CFD) simulations as the new state-of-the-art method to simulate the furnace side and process side of steam cracking units. The higher level of detail and accuracy on velocity, temperature and species concentrations clearly outweigh the increased computational cost. CFD research has been focused on specific aspects of the steam cracking process such as 3D reactor technologies [11-14], turbulence-reaction interactions [15-19], NO_x and soot emission [15, 20-24] , radiative heat transfer [7, 25-28], and high-emissivity coating [29-31]. However, in all of the aforementioned CFD studies, the thermal interaction between the furnace side and the process side was only taken into account at start-of-run conditions, i.e. in the absence of a coke layer. In this chapter, coupled run length simulations were performed using CFD to describe the furnace side of an industrial ultra-selective conversion (USC) furnace. The results are compared with those of

standalone run length simulations and the relative errors are quantified. Two types of thermal interaction between furnace and reactor coils with on stream time, i.e. intra-coil and inter-coil thermal redistribution, are observed. The former is the shift of the transferred thermal power along the axial coordinate of each reactor coil, while the latter is the thermal power redistributed over different reactor coils in the furnace. As CFD calculations of the furnace still have a considerable computational cost, the time required to perform the coupled run length simulation becomes prohibitively long to be routinely used, e.g. for optimization purposes. Therefore, a novel method based on the *incident* radiative heat flux, defined as radiative power reaching the external surface of the reactor coils, rather than the total heat flux was proposed. The effectiveness of this method in reducing the computational time and retaining the accuracy comparing to the CFD coupled run length simulations was shown. Coupled start-of-run and run length simulations at different operating conditions indicated its general nature.

4.2 Mathematical models

4.2.1 Furnace model

4.2.1.1 Governing equations

As previous research has shown that Reynolds-averaged Navier-Stokes (RANS) simulations with two-equation turbulence model can provide satisfactory results for important characteristics such as flame temperature, flame height and NO_x emission predictions in industrial furnaces [15, 27, 32], RANS was adopted in the present work as well. The governing equations for global mass, momentum, energy and species transport in three-dimensional steady-state compressible turbulent flow are given by equations (4.1) – (4.4) respectively.

$$\nabla \cdot (\rho \vec{u}) = 0 \tag{4.1}$$

$$\nabla \cdot (\rho \vec{u}\vec{u}) = -\nabla p + \nabla \cdot (\bar{\bar{\tau}}) + S_M \tag{4.2}$$

$$\nabla \cdot \left(\vec{u}(\rho E + p)\right) = \nabla \cdot \left(k_{eff} \nabla \mathrm{T} - \sum_i h_i \vec{J}_i \right) + S_E \tag{4.3}$$

$$\nabla \cdot \left(\frac{\vec{u} Y_i}{V_m} \right) = -\nabla \cdot \vec{J}_i + R_i \tag{4.4}$$

The contribution of the gravitational force in the z-coordinate is considered in the momentum source term S_M, that is, $S_{M,z} = -\rho g$. The Reynolds stresses in equation (4.2) are modeled by introducing turbulent viscosity, which is assumed to be isotropic and approximated using the ReNormalization Group k-ε model [33]. The first two terms on the right-hand side of equation (4.3) represent energy transfer via conduction and species diffusion respectively. The diffusion flux of species $\vec{J}_i$ can be expressed by equation (4.5).

$$\vec{J}_i = -\left(D_{i,m} + \frac{\mu_t}{\rho Sc_t} \right) \nabla \left(\frac{x_i}{V_m} \right) - \frac{D_{T,i}}{\rho} \frac{\nabla \mathrm{T}}{T} \tag{4.5}$$

where $D_{i,m}$ is the mass diffusion coefficient of species i, Sc_t is the turbulent Schmidt number, and $D_{T,i}$ is the thermal diffusion coefficient. As steam cracking furnace is usually operated at high temperatures up to 2200 K and atmospheric pressure, the ideal gas law was used as equation of state for the flue gas.

4.2.1.2 Combustion model

The fuel gas used by this furnace has a composition of mainly methane (88.55%) and hydrogen (11.14%). A simplified two-step combustion mechanism was used [34]. In this mechanism, methane is converted to carbon monoxide and water in the first step by partial oxidation, followed by the complete combustion of carbon monoxide with oxygen to form

carbon dioxide. The reaction equations and the corresponding kinetic parameters can be found elsewhere [27]. The reasons for using this simplified combustion mechanism is to keep the computational cost as low as possible since a fully coupled CFD-based run length simulation will require a large number of iterations. Moreover, this mechanism was already applied in previous coupled CFD simulation at start-of-run conditions in which good agreement with industrial data was observed [27]. To account for the turbulence-chemistry interaction, the Eddy-Dissipation Model (EDM) [35] was adopted. This model assumes that the rate of the combustion reactions is controlled by the mixing of the reactants in the turbulent eddies. Hence the rate of the combustion is proportional to the reciprocal of the eddy mixing time scale $\tau = k/\varepsilon$. As infinitely fast chemistry is not always valid, the EDM was combined with the Arrhenius rate expressions of the foregoing two-step combustion mechanism to form the so-called finite-rate/eddy-dissipation model, in which the minimum of the Arrhenius reaction rate and the eddy-dissipation reaction rate is taken as the final reaction rate [36].

4.2.1.3 Radiation model

As demonstrated in literature [7, 26], the Discrete Ordinates (DO) model is superior in modeling radiative heat transfer in steam cracking furnaces for a wide range of optical thicknesses [7, 26, 27]. Therefore the non-gray implementation of the model was used to solve the Radiative Transfer Equation (RTE) for spectral radiation intensity I_i as expressed by equation (4.6).

$$\nabla \cdot (I_i(\vec{r},\vec{s})\vec{s}) + (\kappa_i + \sigma_s) I_i(\vec{r},\vec{s}) = \kappa_i I_{b,i} + \frac{\sigma_s}{4\pi} \int_0^{4\pi} I_i(\vec{r},\vec{s}\,') \Phi(\vec{s},\vec{s}\,') d\Omega' \qquad (4.6)$$

In the discrete ordinates model, each octant of the angular space 4π is discretized into $N_\theta \times N_\varphi$ solid angles, where N_θ and N_φ represent the discretize number of the polar angle θ and the azimuth angle φ respectively. This results in the total number of $8N_\theta N_\varphi$ directions for

three-dimensional flow domain. A discrete number independent study was carried out in the present paper as well (see Appendix A for details). It was shown that four N_θ and four N_φ divisions are adequate for modeling radiative transfer in an industrial steam cracking furnace, which in in consistent with the conclusion drawn by Stefanidis et al. [25]. However, the actual divisions used in this study were two N_θ and two N_φ to make a compromise between the computational cost and the model accuracy.

The non-gray properties of the flue gas were described by dividing the spectrum into nine consecutive regions including four absorption bands and five transparent bands. In each of the absorption bands, the spectral absorption coefficient κ_i was expressed as a function of temperature and concentration of the participating species, i.e. H_2O and CO_2. While in the transparent bands, the spectral absorption coefficient κ_i was zero. The details regarding the development and validation of the nine-band model are discussed by Zhang et al. [27]. The furnace refractory and reactor coils were treated as gray and opaque surfaces, having a constant value for the emissivity in all considered bands of 0.75 and 0.85 respectively [27].

4.2.2 Reactor model

For tubular reactors with a large length to inner diameter ratio, the process gas flow inside the reactor coils can be assumed as ideal plug flow. For reasons of computational cost reduction, this is broadly accepted in simulations of industrial steam cracking reactor simulations and therefore adopted in the present work, although work on two-dimensional [37, 38] or three-dimensional [11-14, 17] reactor models is already available in literature. The steady-state conservation equations for species, momentum and energy are given by equations (4.7) – (4.9).

$$\frac{dF_i}{dz} = \frac{\pi(d_i - 2\delta_{coke})^2}{4} R_i \tag{4.7}$$

$$-\frac{dp}{dz} = \left(\frac{2f}{d_i - 2\delta_{coke}} + \frac{\zeta}{\pi r_b}\right)\rho u^2 + \rho u \frac{du}{dz} \tag{4.8}$$

$$\sum_{i=1}^{N_r} F_i c_{p_i} \frac{dT_g}{dz} = \pi(d_i - 2\delta_{coke}) q_i + \frac{\pi(d_i - 2\delta_{coke})^2}{4} \sum_{j=1}^{N_R} r_j \left(-\Delta H_j\right) \tag{4.9}$$

where d_i, δ_{coke}, and R_i in equation (4.7) represent the inner diameter of reactor coil, coke thickness and molar reaction rate of species i, respectively. The first term on the right hand side of equation (4.8) is the pressure drop caused by friction of straight tube and bend, while the second term stands for pressure drop due to velocity gradient. In equation(4.9), the change in process gas temperature T_g due to the energy transferred from the furnace and energy consumed by endothermic reactions are shown. q_i represents the total heat flux on the internal surface of the reactor coil. It is calculated from the total heat flux q_{flux} (on the external surface of the rector coil) obtained via furnace simulation, by the following expression $\frac{q_i}{q_{flux}} = \frac{d_o}{d_i}$. Based on the process gas temperature, the tube metal temperature T_w needed for furnace simulation can be calculated by equation(4.10).

$$q_i = \frac{T_w - T_g}{\frac{d_i}{2\lambda_w}\ln\frac{d_o}{d_i} + \frac{d_i}{2\lambda_{coke}}\ln\frac{d_i}{d_i - 2\delta_{coke}} + \frac{d_i}{h_c(d_i - 2\delta_{coke})}} \tag{4.10}$$

where d_o is the outer diameter of reactor coil. λ_w and λ_{coke} are the thermal conductivity of tube metal and coke respectively. h_c is the convective heat transfer coefficient.

With a certain q_i provided by the furnace simulation, an updated tube metal temperature (TMT) profile can be obtained from the reactor simulation using equations (4.7)-(4.10), which in turn affect the furnace simulation. Hence the thermal coupling is accounted for by

exchanging the total heat flux and the tube metal temperature between furnace and rector coils. This is repeated until convergence of the thermal boundary conditions is reached, which will be discussed in detail in section 3.3.1.

Molecular reconstruction based on the commercial indices PIONA mass fraction, average molecular weight, density and boiling point curve was carried out to obtain an estimate of the detailed composition of the heavy naphtha feedstock. All the calculations for the reactor side were carried out using the commercial software package COILSIM1D [39]. The software is well validated and has an extensive reaction network comprising hundreds of species and thousands of elementary reactions [40, 41] and its molecular reconstruction module SIMCO [42-44]. A modified version of the semi-empirical models developed by Plehiers [9] was adopted to calculate the coking rate on the reactor inner wall. At each time step, the coke thickness can be computed from the following equation.

$$\delta_{coke} = \frac{R_{coke}\Delta t}{\rho_{coke}} \tag{4.11}$$

where R_{coke} is the coking rate. Δt represents the size of time step. ρ_{coke} is the density of coke, which is assumed as a constant of 1600 kg m^{-3} in the present work.

For cracking reactions, the propene to ethene mass ratio (P/E) at the outlet is taken as severity indicator for an individual reactor coil. The averaged cracking severity over a group of coils is referred to as the mixing-cup averaged P/E, that is, the weighted average of the P/E values by the mass flow rate through each of the coils as expressed in equation (4.12).

$$PE_{mixing} = \frac{\sum_{i=1}^{22} F_{m,i} PE_i}{\sum_{i=1}^{22} F_{m,i}} \tag{4.12}$$

where PE_{mixing} stands for the mixing-cup averaged P/E, PE_i represents the P/E at the outlet of reactor coil i, and $F_{m,i}$ is the mass flow rate of process gas in reactor coil i. The total number of reactor coils in the simulated section is 22.

4.3 Simulation setup

4.3.1 Furnace configuration

An industrial USC furnace, comprising of two radiant sections and a common convection section, was studied. Because of symmetry, it was sufficient to model one fourth of one radiant section by setting two boundaries along the x-coordinate as symmetry plane. As depicted in Figure 4-1, 22 U-coils suspended in the middle of the radiant section are heated by 8 floor burners positioned against the furnace refractory, 4 on either side of the tube set. Detailed information on the dimensions of the radiant section, PIONA values of the two types of naphtha feedstocks and operating conditions can be found in Table 4-1, Table 4-2 and Table 4-3.

Table 4-1: Furnace dimensions and operating conditions.

Simulated furnace segment	
Length x-direction (m)	5.969
Width y-direction (m)	2.964
Height z-direction (m)	11.609
Number of burners	8
Firing condition	
Fuel gas flow rate (kg/s)	0.2777
Air equivalence ratio	1.1
Fuel gas inlet temperature (K)	289
Furnace outlet pressure (Pa)	101300
Fuel composition (mol%)	
CH_4	88.55
H_2	11.14
CO	0.17
C_2H_4	0.14
Reactor coils	
Number of coils	22
Reactor coil length (m)	22.792
Number of passes	2
Inlet leg external diameter (m)	0.0566
Inlet leg thickness (m)	0.0058
Outlet leg external diameter (m)	0.0666
Outlet leg thickness (m)	0.0078
Coil operating condition	
Feedstock flow rate of single coil for base case (kg/s)	0.0914

Steam dilution ratio (kg/kg)	0.5
Coil inlet temperature (K)	853
Coil inlet pressure (Pa)	236325
Material properties	
Furnace refractory emissivity	0.75
Reactor tube skin emissivity	0.85

4.3.2 Numerical schemes

For CFD modeling, a hybrid meshing scheme was used to discretize the flow domain of the radiant section. Hexahedral cells, which are better in terms of accuracy in CFD calculations, were applied in the upper part of the furnace where the geometry is simple and a structured mesh can be used. While for regions with complex details such as those adjacent to the burners and the return band of the reactor coils, tetrahedral cells were used. To reduce the number of cells in the domain, the tetrahedral cells were combined to form polyhedral cells, resulting in a mesh of 6.39 million cells.

Table 4-2: PIONA, density and boiling point curve of heavy naphtha feedstock.

Item		Value
Density at 20 ºC (kg/m^3)		734.9
ASTM distillation range (ºC)	IBP	96.4
	10 vol%	101.5
	30 vol%	115.8
	50 vol%	129.4
	70 vol%	143.6
	90 vol%	158.0
	FBP	169.4
PIONA (wt%)	n-Paraffins	29.25
	i-Paraffins	29.25
	Olefins	0
	Naphthenes	31.5
	Aromatics	10

Table 4-3: PIONA, density and boiling point curve of light naphtha feedstock.

Item		Value
Density at 20 ºC (kg/m^3)		642.7
ASTM distillation range (ºC)	IBP	34.0
	10 vol%	38.5
	30 vol%	N.A.
	50 vol%	44.3
	70 vol%	N.A.
	90 vol%	74.3
	FBP	93.3
PIONA (wt%)	n-Paraffins	45.14
	i-Paraffins	46.83
	Olefins	0.41
	Naphthenes	5.64
	Aromatics	1.99

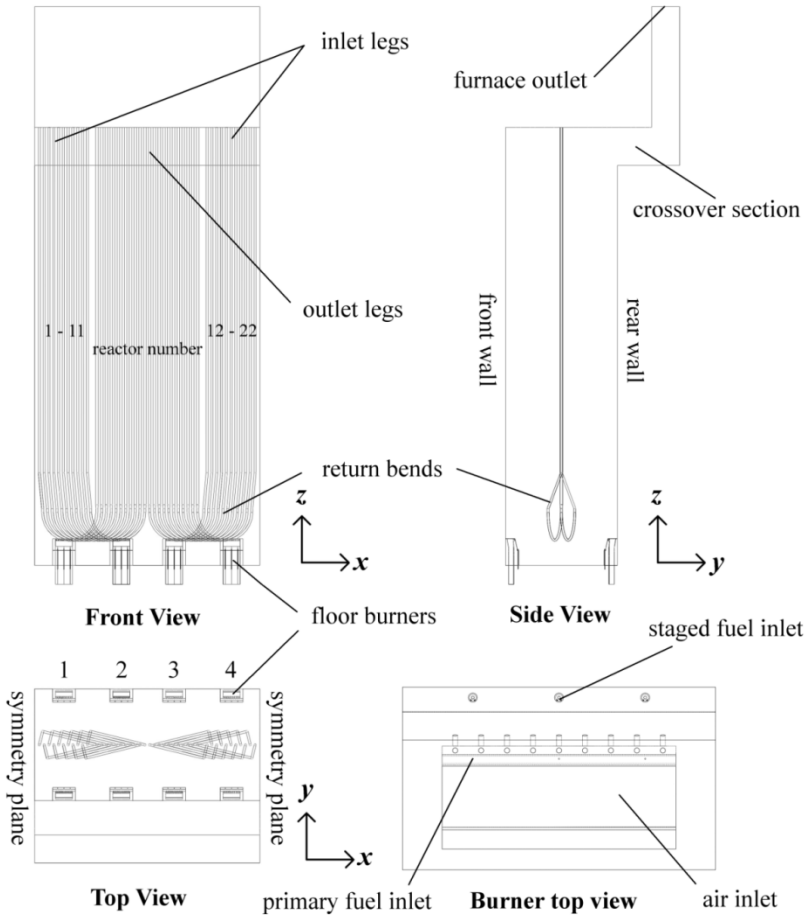

Figure 4-1: Schematic representation of the simulated furnace segment.

The governing equations were discretized by the finite volume method and solved in the commercial CFD software ANSYS Fluent 14.5. The Semi-Implicit Method for Pressure-Linked Equations (SIMPLE) was used for pressure-velocity coupling. Second-order upwind schemes were applied for convection operators. The calculations of flue gas non-gray radiative properties in the nine-band model were programmed and implemented as a user-defined function. Uniform heat loss through the furnace refractory walls equaling 1% of the total heat release, was assumed [45].

4.3.3 Run length simulation methods

As the difference in time scales between the gas-phase steam cracking reactions and the coke layer growth is significant, the dynamic behavior of the furnace during the run length can be described by means of a series of steady-state simulations at discrete time steps. A time step independence study was carried out by performing run length simulations with time interval of 50 h and 200 h, respectively. The maximum TMT of all 22 reactors and the heat flux profiles of reactor coils NO.1 at different time steps are compared in Figure 4-2. Excellent agreement between the two simulation cases at every time step can be observed, indicating that a 200 h time interval is sufficiently small to obtain results that are unaffected by the time step size. In the following section, three methods to perform coupled run length simulations are introduced and compared, where the time interval of 200 h was used in all three coupled run length simulations.

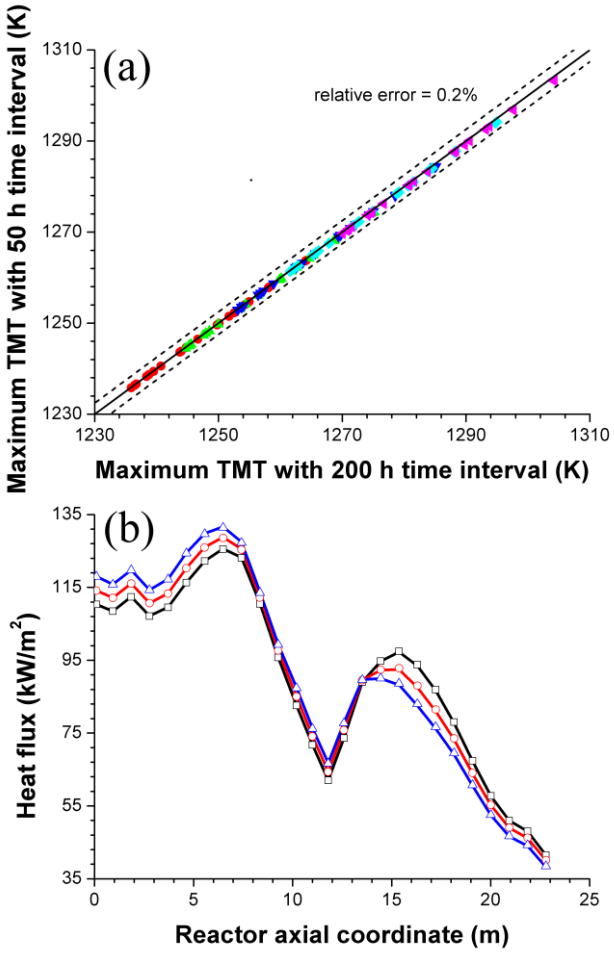

Figure 4-2: (a) Comparison of maximum TMTs between the run length simulation cases with time interval of 200 and 50 at different time steps. ● - time step = 200 h; ▲ - time step = 400 h; ▼ - time step = 600 h; ◆ - time step = 800 h; ◀ - time step = 1000 h. (b) Profiles of heat flux as a function of reactor axial coordinate for reactor coil NO.1 at different time steps in the run length simulation cases with time interval of 200 h(symbols) and of 50 h (lines): time step = 200 h (black); time step = 600 h (red); time step = 1000 h (blue).

4.3.3.1 CFD coupled run length method

Figure 4-3 depicts the flow diagrams of the CFD coupled run length simulations. The coupling is made up of three nested loops. The inner one (TMT loop, green) is a coupled furnace-reactor simulation loop, which is initiated at start-of-run based on initial TMT

profiles in the absence of a coke layer. The furnace simulation was considered as converged when the scaled residuals for all CFD equations were lower than 10^{-4} and the changes of flue gas outlet temperature and O_2 mole fraction were below 0.1 K and 0.05%, respectively. The calculated total heat flux profiles were used in COILSIM1D to perform a reactor simulation for each of the 22 coils, yielding an update of the TMT profiles which were applied as a new boundary condition in the CFD simulation. This procedure was repeated until the difference of the maximum TMT value between the old and new reactor simulations was less than 1 K for every coil. When the inner loop was completed, the mixing-cup averaged P/E of all reactor coils was calculated and compared with the value at start-of-run conditions. The middle one (P/E loop, orange) adjusted the fuel mass flow rate uniformly over all burners to match the cracking severity to that at start-of-run conditions, i.e. until the relative difference between the two P/E values was smaller than 0.01%. Once the middle loop was converged, the decoking criteria were evaluated by the outer loop (time step loop, yellow) and in case they were not yet reached, the coke profile thickness was updated and the calculations for the next time step were started. The stopping criteria of the USC furnace were taken to be 1398 K and 0.35 MPa for TMT and CIP respectively, the latter being equivalent with a maximum pressure drop over the reactor coils of 0.17 MPa.

4.3.3.2 Standalone run length method

In the standalone run length simulations the number of nested loops is reduced to two, see Figure 4-4. Here, CFD coupled furnace-reactor simulations only need to be performed at the start-of-run conditions to obtain the total heat flux profiles for all 22 reactor coils. As the total heat flux profile shape at start-of-run conditions is reused at later time steps, the TMT profiles can be determined without carrying out additional CFD furnace simulations and thus the TMT loop in the coupled run length simulation (green loop in Figure 4-3) is not required. For the

P/E loop, the total heat flux profiles were scaled with a factor which is constant for all axial positions in the coil in such a way that the relative difference of the mixing-cup averaged P/E in the run length simulation was smaller than a threshold of 0.01% compared to start-of-run conditions. The time step loop in this method is the same as that of the CFD coupled run length simulation with stopping criteria taken to be 1398 K and 0.35 MPa for TMT and CIP respectively.

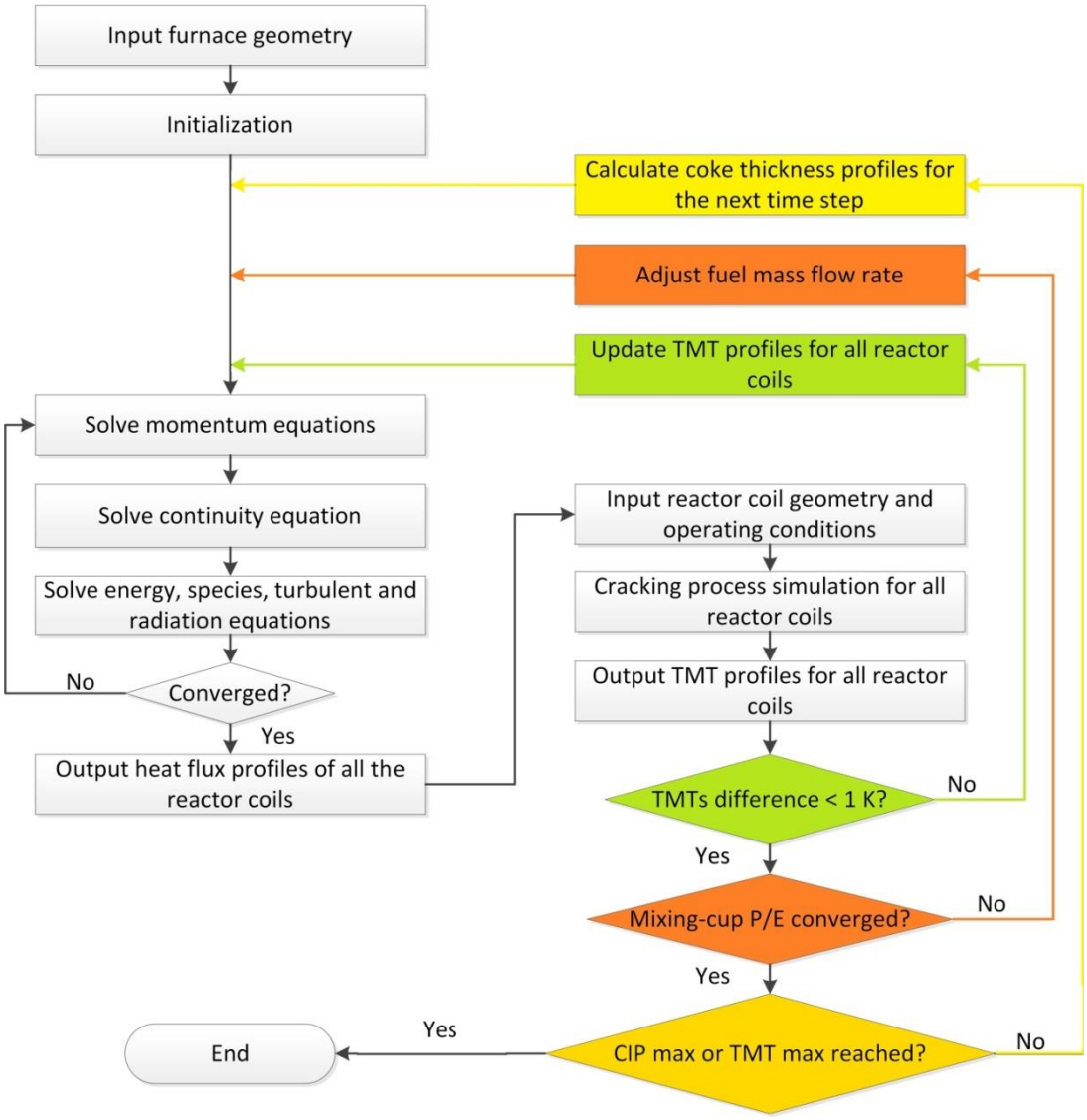

Figure 4-3: Procedure for CFD coupled run length simulations.

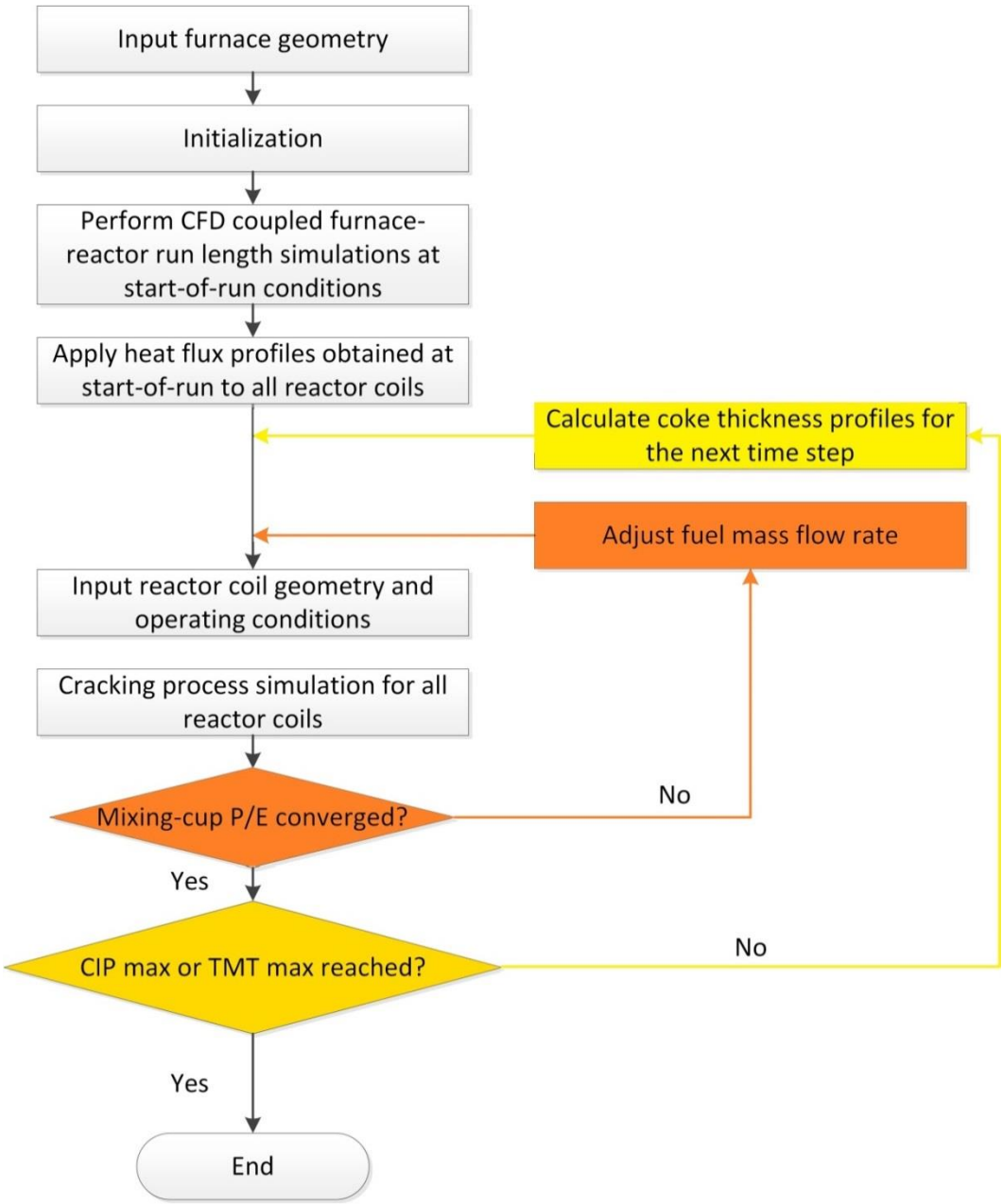

Figure 4-4: Procedure for standalone run length simulations.

4.3.3.3 Incident radiative heat flux (IRHF) based coupled simulation

Development of IRHF based method

The goal of the method is to perform a coupled run length simulation, with regular updates of the total heat flux profile shape to account for the thermal redistribution, at a fraction of the computational cost compared to CFD coupled run length simulations.

First, the individual contributions to the total heat flux on the reactor wall are analyzed. The heat balance of the reactor coil at a given axial coordinate is expressed by equation (4.13):

$$q_{flux} = q_{inci} - q_{re} - q_{emit} + q_{conv} \tag{4.13}$$

where q_{flux} and q_{inci} are the total heat flux and the incident radiative heat flux respectively. q_{re} represents the portion of the incident radiative heat flux reflected back by the surface of the reactor coil. q_{emit} stands for the radiative power emitted from the surface of the reactor coil. The latter two are calculated via the following equations:

$$q_{re} = (1 - \varepsilon_w) q_{inci} \tag{4.14}$$

$$q_{emit} = \varepsilon_w \sigma T_w^4 \tag{4.15}$$

where ε_w is the emissivity of the reactor coil surface, T_w is the TMT. The first three terms on the right hand side of equation (4.13) represent the net radiative heat flux, while q_{conv} is the convective heat flux.

Second, assuming that a CFD coupled furnace-reactor simulation at start-of-run conditions is available, performing run length simulation using a simple model to capture the thermal redistribution will require a variable which is independent of the thermal conditions of the reactor coils. The incident radiative heat flux can fulfill this requirement. Moreover, this variable should be proportional to the total heat release from the combusted fuel, i.e. the shape

of the profile should not change over time but should only be scaled. This feature allows it to be uniformly scaled up/down and thus be correlated to the furnace firing rate. Colannino [46] found a linear relationship between the total heat release and the incident radiative heat flux q_{inci}. Figure 4-5 (a) shows the profiles of the incident radiative heat flux q_{inci} at different time steps in the CFD coupled run length simulation and indeed confirms a constant profile shape. The incident radiative heat flux can thus be considered as the part of the total heat flux on the reactor wall which is not affected by thermal redistribution. Consequently, once the incident radiative heat flux profile is known from a coupled furnace-reactor simulation at start-of-run conditions, it can be updated at subsequent time steps by multiplying the incident radiative heat flux values along the axial coordinate with a time-dependent scaling factor α. This also gives the definition of the scaling factor α as the incident radiative heat flux ratio at the new and the original operating conditions.

The final step only consists of calculating the remaining parts of the total heat flux based on the scaled incident radiative heat flux profile. As heat transfer in steam cracking furnaces is mainly accomplished by radiation, it is assumed that the convective contribution to the total heat flux can be calculated as a fixed fraction of the net radiative heat flux, i.e. a constant factor β relates the convective heat flux to the net radiative heat flux:

$$q_{conv} = \beta(q_{inci} - q_{re} - q_{emit}) \tag{4.16}$$

Combining equations (4.13) to (4.16) gives the final equation for the heat flux:

$$q_{flux} = (\varepsilon_w q_{inci} - \varepsilon_w \sigma T_w^4)(1 + \beta) \tag{4.17}$$

From the CFD coupled run length simulation at start-of-run conditions, a profile of β averaged over all the reactor coils was extracted. The profile is assumed constant in time and has values ranging between 0.24 - 0.33 along the axial coordinate. Figure 4-5 (b) shows β as a

function of the reactor axial coordinate at the start-of-run conditions and after 1000 h operation. The maximum and average differences of β throughout the run length are 7.4% and 3.9% respectively. Since β varies only in a rather small range and since the contribution of convection to the overall heat transfer to the reactor is of secondary importance, using an averaged profile of β for all reactor coils provides sufficient accurate results in the IRHF method as will be demonstrated in the next section.

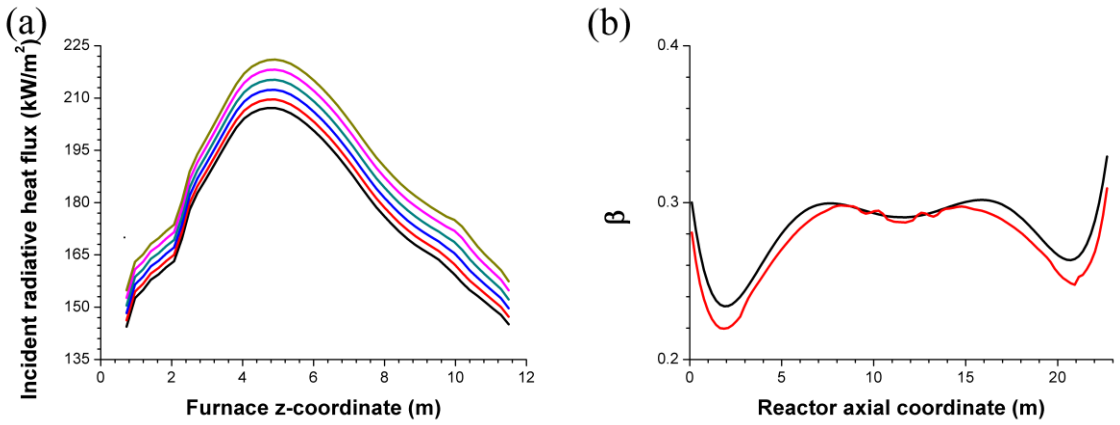

Figure 4-5: (a) Profiles of incident radiative heat flux in the CFD coupled case as a function of the furnace z-coordinate at different time steps. - start-of-run (t = 0 h); - t = 200 h; - t = 400 h; - t = 600 h; - t = 800 h; - t = 1000 h. (b) Averaged ratio of convective heat flux to the net radiative heat flux β as a function of reactor axial coordinate. . - start-of-run (t = 0 h); - t = 1000 h.

The coupling procedure for the new incident radiative heat flux (IRHF) based run length simulation is similar to that of the CFD coupled run length simulation discussed in section 4.3.3.1. The only difference is situated in calculating the updated heat flux profile: in the CFD coupled run length simulation, the total heat flux is determined via multiple CFD simulations, while in the IRHF based method, the total heat flux is calculated via equation (4.17) based on the updated start-of-run incident radiative heat flux profile with respect to time on stream.

Extension of IRHF based method

The IRHF based method is entirely dependent on an initial incident radiative heat flux profile calculated using a CFD coupled furnace-rector simulation at start-of-run conditions. However, when the operating conditions at the process side or the furnace side change, the unit will evolve to a different steady-state situation with a different incident radiative heat flux profiles on the reactor walls. This implies that the CFD coupled simulation at start-of-run conditions should be repeated every time the operating conditions change substantially, which significantly limits the general applicability of the IRHF based method.

Similar as in the IRHF based run length simulation method, one would expect to be able to scale the incident radiative heat flux profile. However, determining the scaling factor is not as straightforward when changing the operating conditions compared to when advancing in time. The reason is that at each time step of the run length simulation, the incident radiative heat flux profiles is scaled to maintain a constant cracking severity equal to that at start-of-run conditions. When simulating the furnace at modified operating conditions, the mixing-cup averaged P/E over all reactors will change but the new value cannot be determined by the current incident radiative heat flux profile. Therefore in principle a new coupled CFD furnace-reactor simulation at the modified operating conditions should be carried out to obtain a new profile of incident radiative heat flux.

To overcome the foregoing drawback, the IRHF based method was extended by calculating the scaling factor α for the incident radiative heat flux in a more general way. The scaling factor α, i.e. the incident radiative heat flux ratio at the new and the original operating conditions, should be correlated to the overall heat balance of the furnace. As the incident radiative heat flux consists of contributions of radiation from both the flue gas and the furnace refractory in all spatial locations, it is not straightforward to express it as function of any

physical temperature in the furnace. Therefore, the concept of the effective flue gas temperature used in the Lobo-Evans method [47] is introduced. The local incident radiative heat flux at different positions along the furnace z-coordinate is considered as solely emitted from a gray gas at an effective temperature T_{eff}, representing the combination of the flue gas and furnace refractory:

$$q_{inci} = A_{eff}\varepsilon_{eff}\sigma T_{eff}^4 \tag{4.18}$$

where the ε_{eff} is the effective emissivity of the gray gas. A_{eff} is the effective geometrical factor. With this assumption, the expression for the scaling factor α is given by equation(4.19).

$$\alpha = \frac{q_{inci,new}}{q_{inci,ori}} = \frac{A_{eff}\varepsilon_{eff,new}\sigma T_{eff,new}^4}{A_{eff}\varepsilon_{eff,ori}\sigma T_{eff,ori}^4} \tag{4.19}$$

The $q_{inci,new}$ and $q_{inci,ori}$ are the incident radiative heat fluxes under the new and the original operating conditions, where the latter is the CFD coupled furnace-reactor simulation case from which the incident radiative heat flux profile at start-of-run conditions is known. Equation (4.19) can be rewritten as follows:

$$\alpha = \frac{A_{eff}\varepsilon_{eff,new}\sigma\left(T_{eff,ori} + \Delta T_{eff}\right)^4}{A_{eff}\varepsilon_{eff,ori}\sigma T_{eff,ori}^4} \tag{4.20}$$

where $\Delta T_{eff} = T_{eff,new} - T_{eff,ori}$ is the difference in effective flue gas temperature between the new and the original operating conditions. A_{eff} in the numerator and the denominator of equation (4.20) are the same as changes in operating conditions have no impact on the effective geometrical factor. Due to the relatively narrow window of operation for the effective flue gas temperature, i.e. ΔT_{eff} is far smaller than T_{eff}, the difference in effective

emissivity between the new and the original operating conditions will be relatively small and is hence neglected, allowing to simplify equation (4.20) to the following:

$$\alpha = \left(1 + \frac{\Delta T_{eff}}{T_{eff,ori}}\right)^4 \tag{4.21}$$

By now, the scaling factor is still expressed as function of the effective flue gas temperature T_{eff} which cannot be directly related to the furnace thermal energy balance. The missing link is constructed by relating T_{eff} to a physical temperature in the furnace which is strongly correlated with the overall thermal energy balance. As for most applications it is acceptable to assume that the entire radiant section is isothermal, in such case the effective flue gas temperature is equivalent to the flue gas bridge wall temperature [48], which is defined as the outlet temperature of flue gas leaving the radiant section. However, it is worth to note that this assumption is only applied to calculate the overall thermal balance and the scaling factor, which are not strongly influenced by temperature gradient in the furnace. Calculation of the incident radiative heat flux profiles still requires CFD coupled simulations. Replacing the effective flue gas temperature by the flue gas bridge wall temperature in equation (4.21) leads to the final expression for the scaling factor α in the IRHF based method:

$$\alpha = \left(1 + \frac{\Delta T_{flue}}{T_{flue,ori}}\right)^4 \tag{4.22}$$

where $T_{flue,ori}$ represents the flue gas bridge wall temperature of the original case, which can be easily obtained from the CFD coupled furnace-reactor simulation at start-of-run conditions. $\Delta T_{flue} = T_{flue,new} - T_{flue,ori}$ is the difference of the flue gas bridge wall temperature at the new and the original operating conditions. The bridge wall temperature at

the new operating conditions $T_{flue,new}$ is calculated via an overall heat balance over the complete furnace, mathematically represented by equations (4.23) - (4.26).

$$Q_r = Q_{ab} + Q_{flue} + Q_{loss} \tag{4.23}$$

where the Q_r is the total heat release from the fuel combustion. Q_{ab} represents the heat absorbed by all reactor coils. Q_{flue} is the enthalpy change between the inlet fuel and air entering the furnace and the hot flue gas leaving the furnace. Q_{loss} stands for the heat loss through the furnace refractory. The total heat release Q_r and the first two terms on the right hand side of equation (4.23) can be further written as follows:

$$Q_r = F \sum_{i}^{N_r} x_i(-\Delta H_i) \tag{4.24}$$

$$Q_{ab} = \sum_{j}^{M} \int_0^z \pi d q_{flux} dz \tag{4.25}$$

$$Q_{flue} = F \sum_{k}^{N_r+N_p} x_k\left[H_k\left(T_{flue}\right) - H_k(T_{inlet})\right] \tag{4.26}$$

As the fuel is completely combusted in the furnace, the total heat release can be simply expressed as the weighted sum of the heat of combustion of all fuel components, multiplied with the fuel flow rate. Integration of the total heat flux profile along the axial coordinate for all reactor coils yields the total absorbed heat as shown in equation (4.25). Q_{flue} is mainly a function of the bridge wall temperature T_{flue} and composition of the flue gas. Under modified operating conditions, equation (4.23) is first calculated to determine the value for $T_{flue,new}$ based on the previous converged total heat flux profiles. Subsequently a new scaling factor α is computed from equation (4.22) and is used to update the total heat flux profiles to the

reactor coils. Both steps are repeated until the change in value of $T_{flue,new}$ between subsequent iterations is below a threshold of 0.1 K. To summarize, the procedure to perform a run length simulation using the IRHF based method is similar to that in the CFD coupled case, however, instead of performing a full CFD simulation of the furnace, the overall heat balance in equation (4.23) is used to determine the new total heat flux profile.

4.4 Results and discussion

4.4.1 Base case: CFD run length simulation

First, two simulation cases were executed using the CFD method and the standalone method, referred to as the "CFD coupled case" and the "standalone case". The profiles for the CIP and the maximum TMT for all reactor coils as a function of the time on stream are shown in Figure 4-6. The CIP rather than the TMT is the limiting criterion in both the CFD coupled and the standalone case. This is consistent with the conclusion of Sundaram and Froment [49] who reported that the run length of a naphtha cracking furnace is limited by the pressure drop if the internal diameter of the coils is smaller than 0.075 m. The estimated run length in the CFD coupled case (49 days) is about 6 days longer than that of the standalone case (43 days). This discrepancy in predicted run length is definitely not negligible. The latter is also reflected in the considerable difference in the maximum TMT profiles between the two cases: in the CFD coupled case, the maximum TMT increases uniformly for all reactor coils while in the standalone case, the maximum TMT increases much faster for some coils than for other coils.

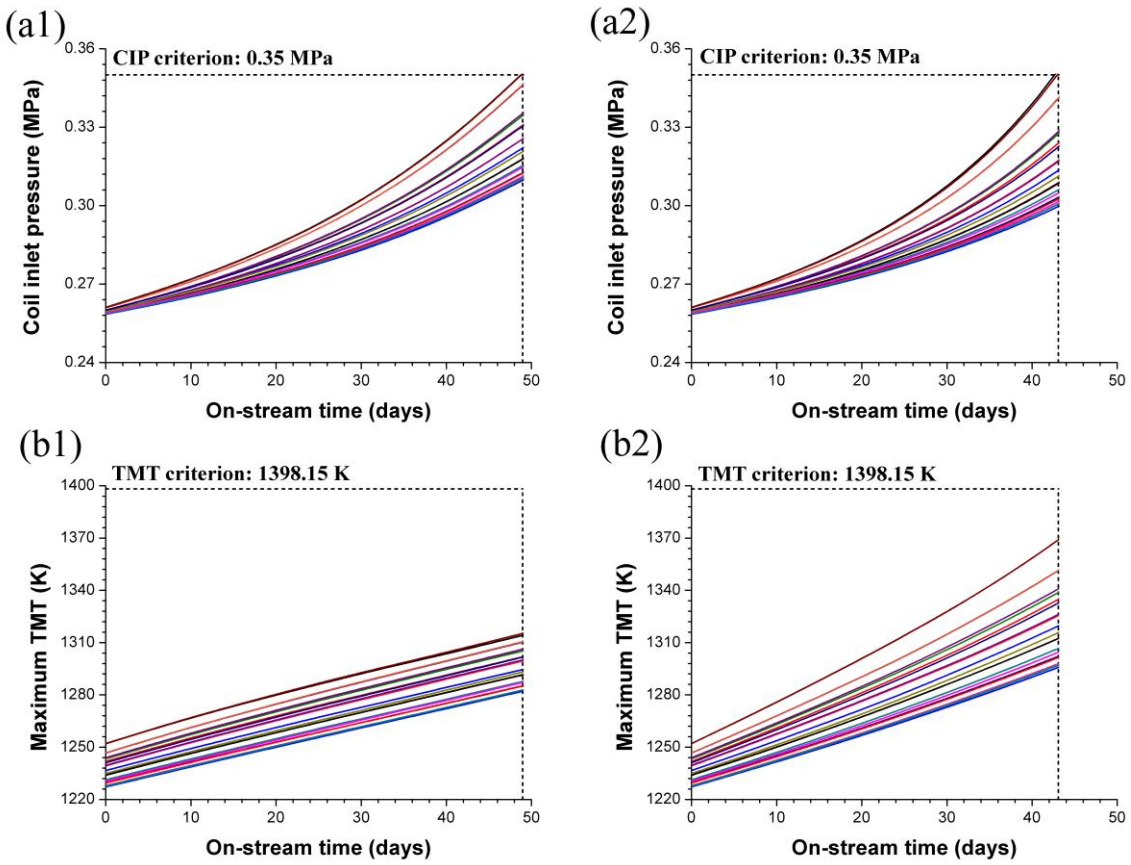

Figure 4-6: Profiles of (a) CIP and (b) maximum TMT for all reactor coils as a function of the time on stream in (1) CFD coupled case and (2) standalone case.

To understand the different maximum TMT profiles calculated in the standalone and CFD coupled run length cases, the maximum TMT (a) and maximum coking rate (b) over all 22 reactor coils at start-of-run conditions and close to end-of-run conditions (t = 1000 h) are compared in Figure 4-7. It is clear that the maximum TMT increases uniformly for every coil in the CFD coupled case, on the other hand in the standalone run length simulation, the maximum TMT increases much faster for the reactor coils located at the extremities and in the middle of the simulated furnace section.

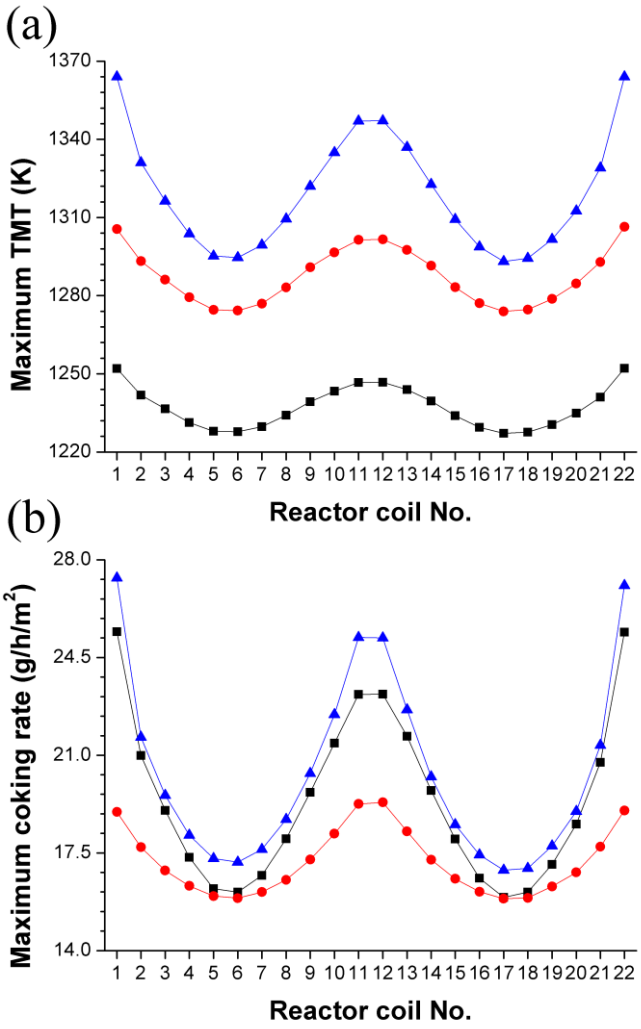

Figure 4-7: Distribution of the (a) maximum TMT and (b) maximum coking rate over all 22 reactor coils at different time steps. ■ – start-of-run (t = 0 h); ● – t = 1000 h (CFD coupled case); ▲ – t = 1000 h (standalone case).

Interestingly, although the maximum TMT increases in both simulation cases with increasing time on stream, the maximum coking rate value for each reactor does not exhibit the same trend. In the standalone case, the maximum coking rate increases over time while in the CFD coupled case, the maximum coking rate decreases over time, see Figure 4-7 (b). The explanation for this can be found in Figure 4-8 where the profiles of some important variables as function of the axial coordinate are plotted for reactor coil NO.1, both at start-of-run

conditions and close to end-of-run conditions (t = 1000 h) for the standalone and CFD coupled run length cases. The profiles of coking rate and TMT depicted in Figure 4-8 (a) and (d) are the results of CFD coupled simulation at the start-of-run conditions, based on which the standalone run length simulation and the CFD coupled run length simulation were performed. The low coking rate in the inlet leg is explained by the lower temperature and the lower concentration of unsaturated hydrocarbons, which are the main precursors for coke formation in the reactor coil. As a result, more coke is deposited on the inner wall of the outlet leg. Due to the insulating nature of the deposited coke, the heat transfer from the reactor wall to the process gas is diminished. To compensate for the reduced heat transfer coefficient and to maintain the total heat input to the process gas, the fuel flow rate to the furnace is increased. This provide a larger driving force for heat transfer towards the reactor coils. However, as the coke layer in the outlet leg is thicker, see Figure 4-8 (c), the effect of the higher firing rate will be smaller in the outlet leg compared to the inlet leg, as indeed shown in Figure 4-8 (b) for the CFD coupled case. This phenomenon is referred to as intra-coil thermal redistribution. The consequence of the intra-coil thermal redistribution is that the coking rate decreases in the outlet leg with increasing time on stream, which explains the observation in Figure 4-7 (b). Additionally, the decreased total heat flux in the outlet leg leads to a slower and more uniform increase of maximum TMT of the reactor coils in the CFD coupled case.

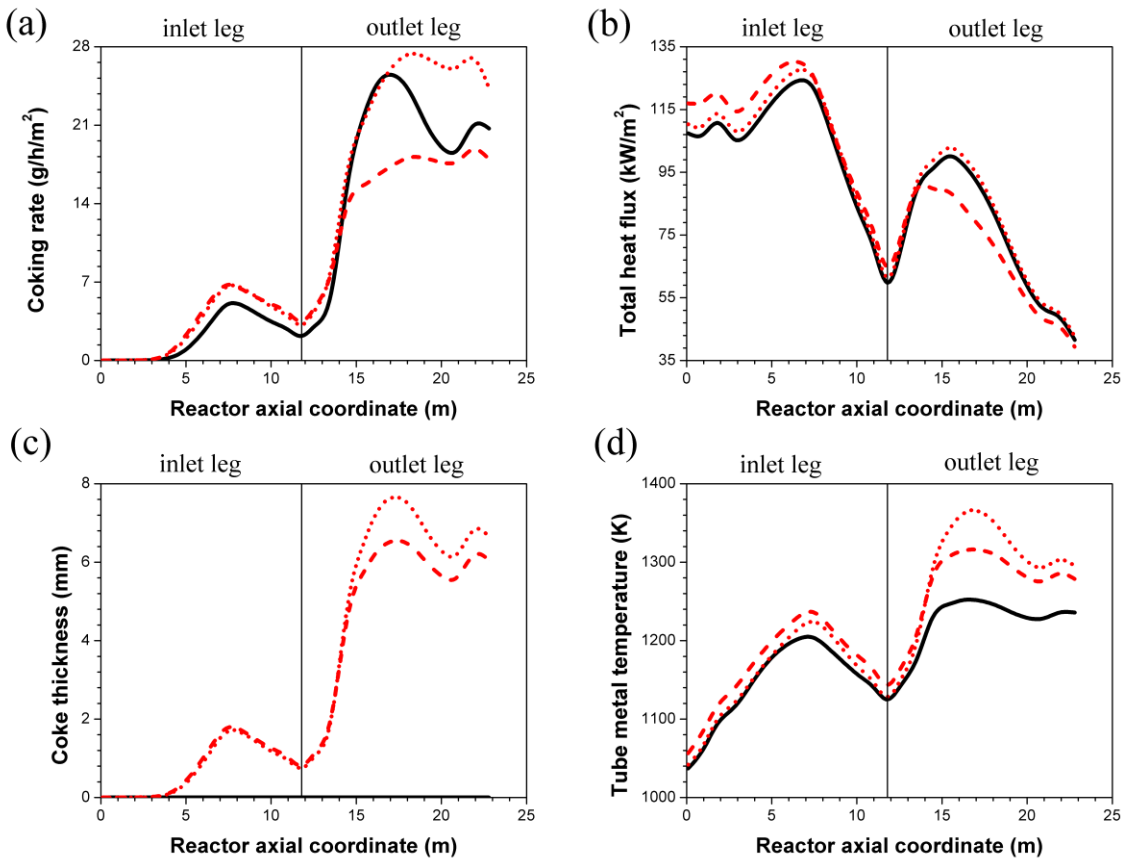

Figure 4-8: Profiles of (a) coking rate; (b) total heat flux; (c) coke thickness and (d) TMT as a function of reactor axial coordinate for reactor coil NO.1. ——— – start-of-run (t = 0 h); - - - - –t = 1000 h (CFD coupled case); ····· – t = 1000 h (standalone case).

As the total heat flux profile shape is not updated in the standalone case, the intra-coil thermal redistribution is not observed and the profile shape of the total heat flux is identical to the one at start-of-run conditions. Without taking intra-coil thermal redistribution into account, the standalone run length simulation predicted an increasing coking rate in the outlet leg with increasing time on stream Figure 4-8 (a). The calculated coke thickness is then much higher compared to the CFD coupled case, which in turn requires an ever higher total heat flux to maintain the desired cracking severity. This method results in a rapid increase in maximum TMT.

Apart from the intra-coil thermal redistribution in different passes of one reactor coil, there is also an inter-coil thermal redistribution existing in between the reactor coils located at different locations in the furnace. As presented in Figure 4-9, the difference between the maximum and the minimum of the total heat input per reactor is decreasing with the time on stream in the CFD coupled case. As a consequence, the maximum COT difference between the reactor coils is reduced from 31 K at the start-of-run to 21 K at t = 1000 h, which is beneficial from the perspective of furnace operation. The reason for this inter-coil thermal redistribution over reactor coils is similar to the discussion in the previous paragraph for a single coil. More coke will be deposited in the coils that receive higher heat input, which subsequently reduces the heat transfer to these particular coils. More heat is then transferred to the coils which initially had a lower heat input and hence a thinner coke layer. In the end, the spread on the thermal condition of the reactor coils is gradually reduced as the non-uniform deposition of coke smoothens out any differences in COT, therefore compensating for any nonuniformities amongst the coils resulting from the furnace geometry.

Although the phenomenon of intra-coil thermal redistribution was already observed in earlier work [8, 9], the underlying reason was not given and the coarse grid associated with the zoning method used to model the furnace side resulted in insufficiently accurate total heat flux profiles.

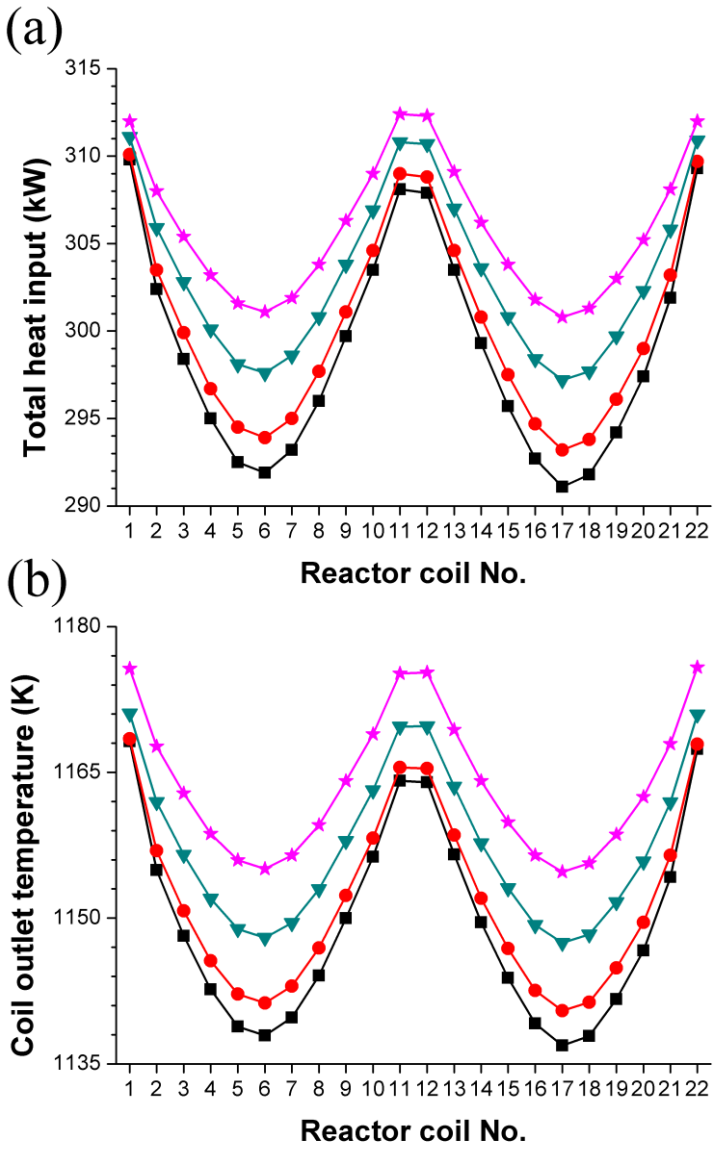

Figure 4-9: Distribution of (a) heat input; (b) COT over all 22 reactor coils at different time steps : ■ – start-of-run (t = 0 h); ● – t = 200 h; ▼ – t = 600 h; ★ – t = 1000 h.

Although several interesting effects can be studied using coupled CFD-based simulations, the obvious drawback is the huge computational cost (CPU time of 10^8 s for the coupled simulation on six 16-core compute nodes with dual Intel Xeon E5-2670 processors (2.6 GHz) versus CPU time of 10^4 s for the standalone simulation on a dual-core personal computer with Intel Core i5-3320M processor (2.6 GHz)) and the resulting long wall clock times (240 h for

the coupled simulation versus 1.6 h for the standalone simulation). It should be noted that the computational cost required to obtain the information at start-of-run conditions is not included in the foregoing calculation because it was considered as a common basis for both the standalone and the CFD coupled run length simulations. Moreover, once the total heat flux profile for is obtained from coupled CFD furnace simulation of the base case, it can be easily applied to standalone run length simulation under changed operating conditions without additional CFD simulations. As it is infeasible to use coupled CFD-based run length simulation for optimization purpose, an IRHF based method, which should reduce the computational cost while retaining the accuracy compared to the CFD base case, was developed to overcome this drawback.

4.4.2 IRHF based methods

4.4.2.1 Run length simulation

The coupled run length simulation was also carried out using the IRHF based method, further referred to as "IRHF coupled case". A parity plot of the maximum TMTs of all 22 reactor coils in the CFD coupled case and the IRHF coupled case for different time steps is given in Figure 4-10. The comparison shows that the relative error of the IRHF coupled method is consistently smaller than 0.5%., although minor maximum TMT underpredictions are observed when approaching end-of-run conditions as a result of error accumulation. Figure 4-11 depicts the profiles of total heat flux, TMT, coking rate and coke thickness as function of the axial coordinate of reactor coil NO.1 for the CFD coupled case and the IRHF coupled case at start-of-run conditions and at conditions close to end-of-run. It can be seen that all variables predicted by the two methods agree very well, again only with some minor discrepancies when approaching end-of-run conditions. In addition, the intra-coil thermal redistribution is well captured by the IRHF method as demonstrated by the change of the profiles of the total

heat flux and coking rate in Figure 4-11 (a) and (c). Similar results are observed in other reactor coils as well. Therefore, the IRHF based method is proven to be capable of replacing CFD in coupled run length simulation, given that an incident radiative heat flux profile can be obtained from a CFD coupled furnace-reactor simulation at start-of-run conditions.

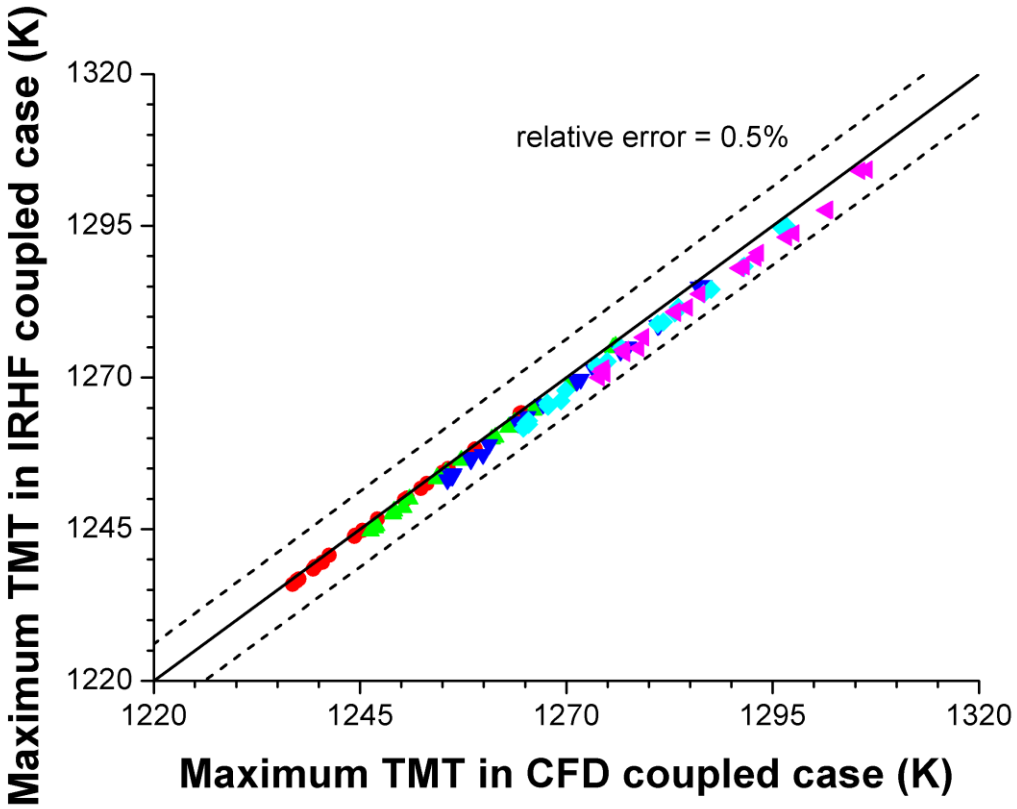

Figure 4-10: Parity plot of maximum TMTs in the CFD coupled case and the IRHF coupled case at different time steps. ● - t = 200 h; ▲ - t = 400 h; ▼ - t = 600 h; ◆ - t = 800 h; ◀ - t = 1000 h.

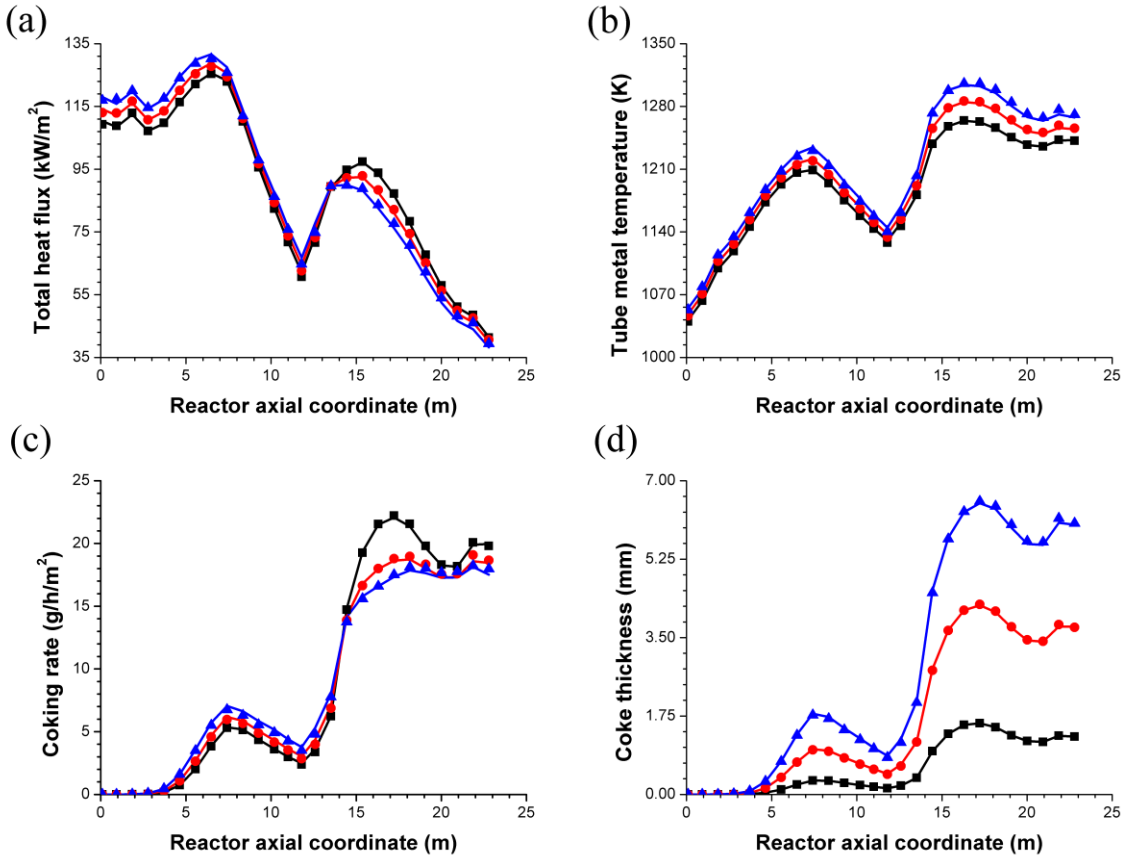

Figure 4-11: Profiles of (a) total heat flux; (b) TMT; (c) coking rate; (d) coke thickness as a function of reactor axial coordinate for reactor coil NO.1 at different time steps in the CFD coupled case (symbols) and the IRHF coupled case (lines). – t = 200 h; – t = 600 h; – t = 1000 h.

Table 4-4 summarizes the most important cracking furnace indices such as the predicted run length, olefin production capacities, furnace efficiency and flue gas bridge wall temperature. The predictions of these values in the CFD coupled case and the IRHF coupled case agree very well, with relative errors at t = 1000 h of only 0.32% and 0.5% for the thermal efficiency and the flue gas outlet temperature respectively.

Table 4-4: Comparison of the simulation results between the CFD coupled case and the IRHF coupled case under the basic operating conditions.

CFD coupled case					
Run length (days)			49.0		
Ethene production capacity (kt/a)			129.47		
Propene production capacity (kt/a)			78.87		
	T=200	T=400	T=600	T=800	T=1000
Mixing-cup ethene yield (wt%)	27.17	27.14	27.08	27.00	26.88
Mixing-cup propene yield (wt%)	16.55	16.53	16.50	16.45	16.39
Mixing-cup P/E (-)	0.6091	0.6091	0.6093	0.6093	0.6097
Total heat release (MW)	14.33	14.49	14.67	14.84	15.02
Furnace thermal efficiency (%)	46.12	45.80	45.47	45.14	44.81
Flue gas outlet temperature (K)	1375	1381	1387	1394	1400
IRHF coupled case					
Run length (days)			49.1		
Ethene production capacity (kt/a)			129.50		
Propene production capacity (kt/a)			78.89		
	T=200	T=400	T=600	T=800	T=1000
Mixing-cup ethene yield (wt%)	27.17	27.13	27.08	27.00	26.90
Mixing-cup propene yield (wt%)	16.55	16.53	16.50	16.45	16.39
Mixing-cup P/E (-)	0.6091	0.6093	0.6093	0.6093	0.6093
Total heat release (MW)	14.30	14.44	14.59	14.73	14.87
Furnace thermal efficiency (%)	46.19	45.94	45.65	45.41	45.16
Flue gas outlet temperature (K)	1374	1379	1384	1389	1394

4.4.2.2 IRHF sensitivity analysis for changing operating conditions

To test the performance of the IRHF based method under modified operating conditions at start-of-run, cases with a 10% higher and 10% lower feedstock flow rate and a 5% higher and 5% lower fuel flow rate were simulated and compared to CFD coupled furnace-reactor simulations. Figure 4-12 shows a parity plot of the COTs calculated by the two methods. The results for the changing feedstock flow rate agree very well but some discrepancies are present when changing the fuel flow rate, although the relative error still remains well below 0.5%. This is caused by the inherent overestimation of the effect of the changed fuel mass flow rate on the flue gas bridge wall temperature T_{flue} which was taken as representative for

the equivalent furnace temperature T_{eff}. The conclusion is further confirmed by Figure 4-13 (c) and (d) which indicate that the overall agreement between the two methods is acceptable but the peak values are slightly over- or underestimated in the 5% more fuel and 5% less fuel case respectively.

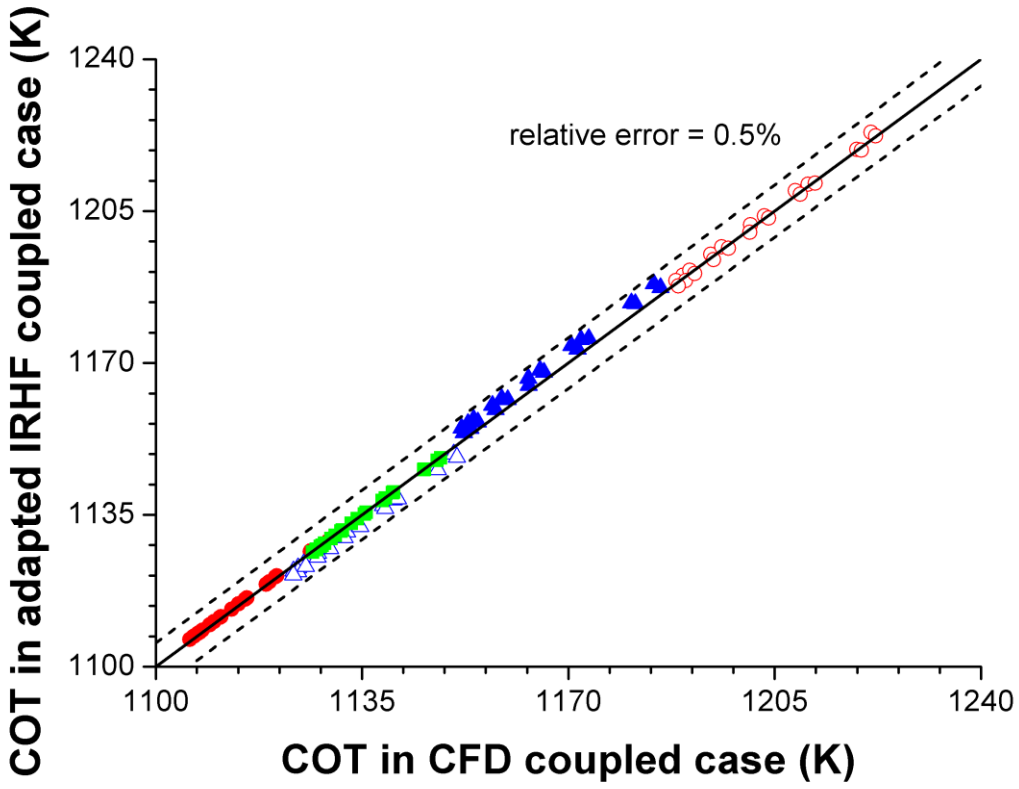

Figure 4-12: Parity plot of COTs in the CFD coupled furnace-reactor simulation and the IRHF based simulation at start-of-run (t = 0 h). ● - 10% more feedstock; ○ - 10% less feedstock; ▲ - 5% more fuel; △ - 5% less fuel; ■ - light naphtha feedstock.

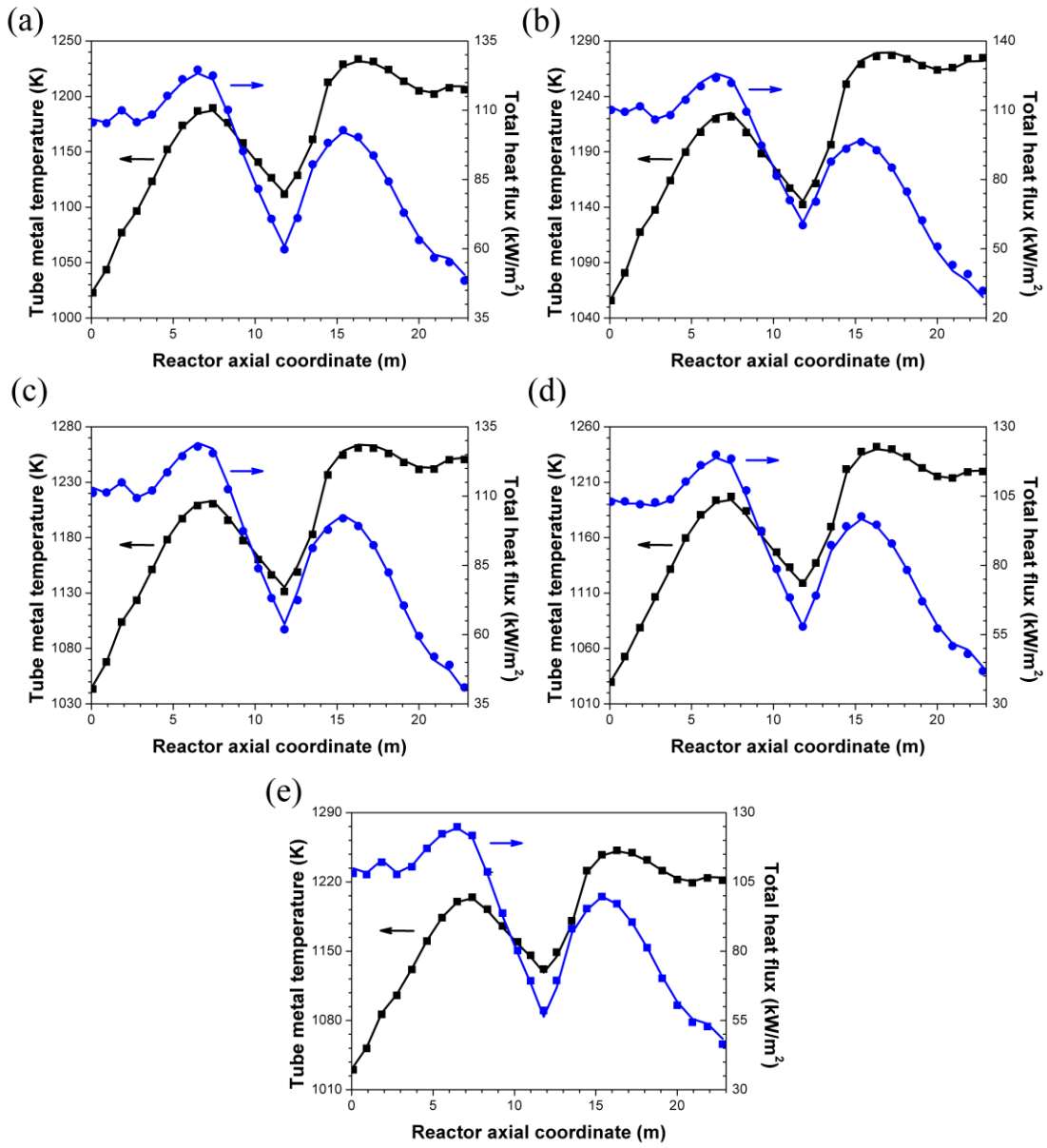

Figure 4-13: Profiles of TMT (black, left axis) and total heat flux (blue, right axis) in the CFD coupled case (solid symbols) and the IRHF coupled case (solid lines). (a) 10% more feedstock; (b) 10% less feedstock; (c) 5% more fuel; (d) 5% less fuel; (e) light naphtha feedstock.

To further test the limits of the presented methods and to verify their potential application range the feed was changed from the heavy naphtha to a light. In this study the flow rate of feedstock and fuel were the same as in the heavy naphtha cases. Comparing to the cases with different feedstock and fuel flow rates, the light naphtha case yields even smaller error in

COTs and TMT profile, see Figure 4-12 and Figure 4-13 (e). The results listed in Table 4-5 also show good agreement, especially since the changes in feedstock flow rate and fuel flow rate are quite large. In addition, the mixing-cup average P/E is well predicted even for a completely different feedstock. Therefore, the IRHF based method is able to simulate the thermal coupling of the furnace and the reactor coils with a similar accuracy as the CFD method over a wide range of operating conditions.

Table 4-5: Comparison of the simulation results between the CFD coupled case and the IRHF coupled case under adjusted operating conditions.

	Mixing-cup ethene yield (wt%)	Mixing-cup propene yield (wt%)	Mixing-cup P/E	Furnace thermal efficiency (%)	Flue gas outlet temperature (K)
10% more feedstock					
CFD	24.84	18.08	0.7287	47.00	1357
IRHF	24.81	18.09	0.7298	47.00	1357
10% less feedstock					
CFD	28.83	11.35	0.3938	45.68	1385
IRHF	28.83	11.16	0.3872	45.69	1385
5% more fuel					
CFD	27.88	15.42	0.5537	45.56	1385
IRHF	28.01	15.15	0.5416	45.79	1381
5% less fuel					
CFD	26.37	17.39	0.6599	47.35	1352
IRHF	26.21	17.50	0.6685	47.11	1356
Light naphtha feedstock					
CFD	28.55	19.53	0.6850	46.58	1366
IRHF	28.45	19.57	0.6887	46.51	1367

To assess the impact of the cracking feedstock next to calculating the starting conditions also a run length case using light naphtha was conducted. Both the CFD coupled method and the IRHF based method, referred to as the ‘CFD LNAP case’ and the ‘IRHF LNAP case’ respectively, have been carried out. Also both the feedstock and the fuel flow rate were decreased by 5%. A parity plot for the maximum TMTs of all 22 reactor coils at different time

steps are shown in Figure 4-14. The heat transfer is generally underestimated by the IRHF based method, which results in lower maximum TMTs comparing to the CFD method. Relative errors become larger with increasing time on stream and exceed 0.5% after 400 h, while the maximum relative error remains smaller than 1%, even at end-of-run conditions. Although this still means that the maximum TMT is underpredicted in the IRHF LNAP case by about 9 K.

Table 4-6 shows that the largest part of the error was introduced in the mixing-cup averaged P/E at start-of-run as a result of the significant change in feedstock and fuel mass flow rates. The start-of-run mixing-cup averaged P/E value used as shooting target in subsequent time steps was determined independently for the CFD coupled method (P/E = 0.5732) and the IRHF based method (P/E = 0.5875). Any difference in this shooting target introduces an accumulating error throughout the run length simulation which causes the large differences of more than 0.5% on the maximum TMT values at end-of-run conditions. The simulation was carried out again using the IRHF based method but with the start-of-run mixing-cup averaged P/E value from the CFD coupled method as shooting target. Results show that in this case the difference in maximum TMT between the CFD coupled case and the IRHF based method at end-of-run conditions is reduced to 4.2 K, i.e. a relative error of less than 0.5%. The error accumulation can also be observed in the profiles of some important variables as function of the reactor axial coordinate as depicted in Figure 4-15. The coking rate was affected most as a consequence of the different TMT predictions in the two cases, leading to errors in coke thickness, which in turn changes the total heat flux profile and TMT profile for the next time step.

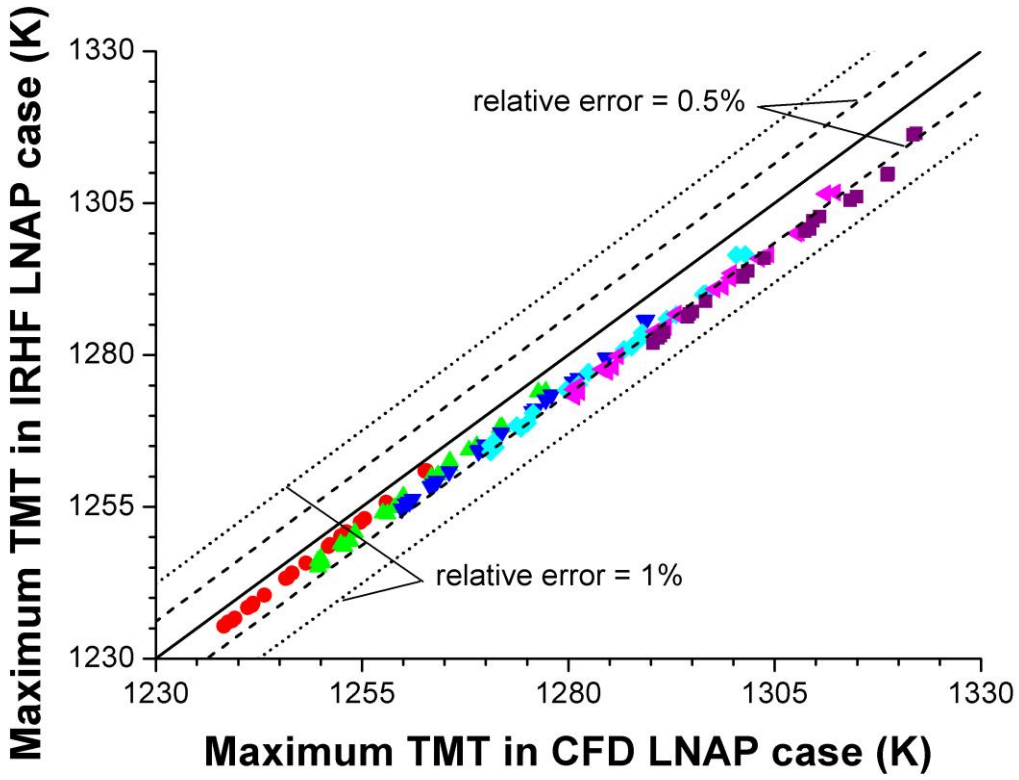

Figure 4-14: Parity plot of maximum TMTs in the CFD LNAP case and the IRHF LNAP case at different time steps. ● - start-of-run (t = 0 h); ▲ - t = 200 h; ▼ - t = 400 h; ◆ - t = 600 h; ◀ - t = 800 h; ■ - t = 1000 h.

Table 4-6: Comparison of the simulation results between the CFD LNAP case and the IRHF LNAP case.

CFD LNAP case					
Run length (days)			44.3		
Ethene production capacity (kt/a)			147.55		
Propene production capacity (kt/a)			84.49		
	T=0	T=200	T=400	T=600	T=800
Mixing-cup ethene yield (wt%)	31.00	30.97	30.92	30.84	30.72
Mixing-cup propene yield (wt%)	17.74	17.72	17.70	17.66	17.60
Mixing-cup P/E (-)	0.5722	0.5723	0.5725	0.5728	0.5730
Total heat release (MW)	13.45	13.62	13.79	13.95	14.10
Furnace thermal efficiency (%)	46.83	46.48	46.13	45.80	45.47
Flue gas outlet temperature (K)	1362	1369	1376	1382	1389

IRHF LNAP case					
Run length (days)			45.9		
Ethene production capacity (kt/a)			146.30		
Propene production capacity (kt/a)			85.86		
	T=0	T=200	T=400	T=600	T=800
Mixing-cup ethene yield (wt%)	30.72	30.69	30.65	30.58	30.49
Mixing-cup propene yield (wt%)	18.01	18.01	17.99	17.95	17.89
Mixing-cup P/E (-)	0.5864	0.5869	0.5869	0.5870	0.5869
Total heat release (MW)	13.45	13.59	13.74	13.88	14.01
Furnace thermal efficiency (%)	46.51	46.24	45.94	45.66	45.38
Flue gas outlet temperature (K)	1368	1374	1379	1385	1390

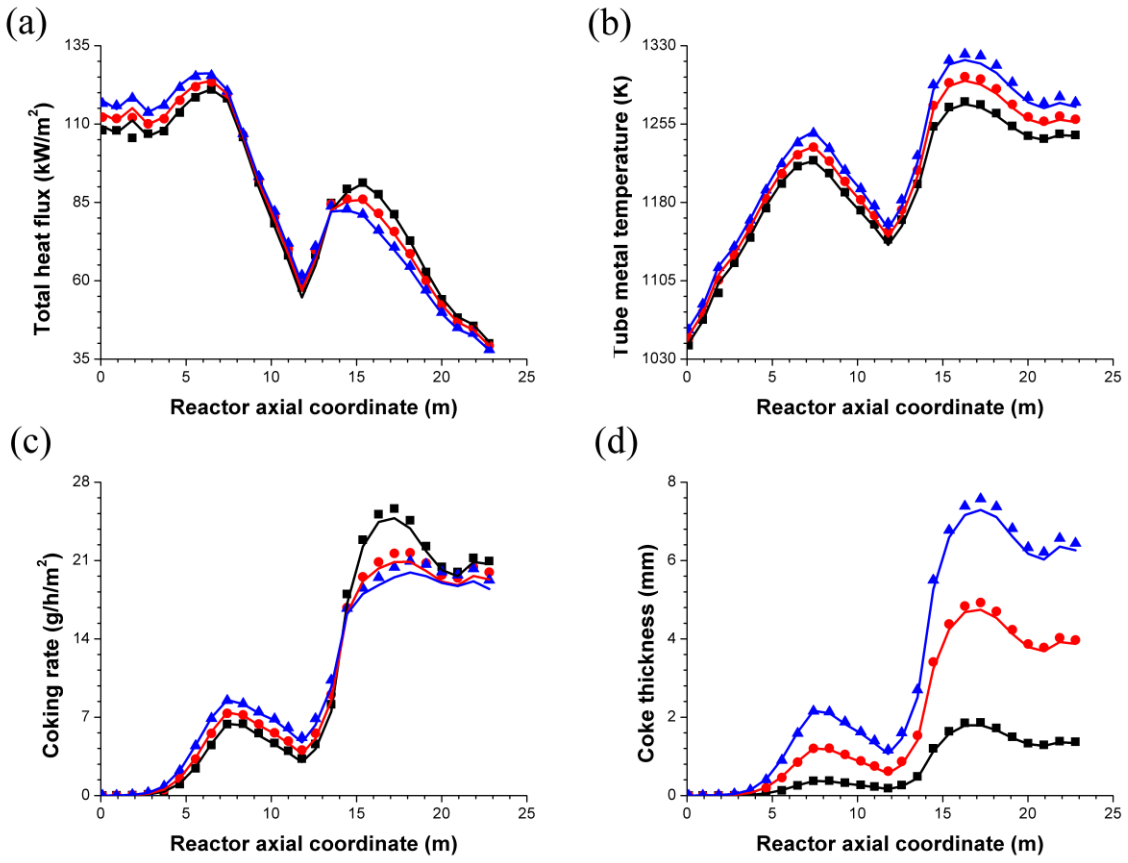

Figure 4-15: Profiles of (a) total heat flux; (b) TMT; (c) coking rate; (d) coke thickness as a function of the reactor axial coordinate for reactor coil NO.1 at different time steps in the CFD LNAP case (solid symbols) and the IRHF LNAP case (solid lines). – t = 200 h; – t = 600 h; – t = 1000 h.

4.4.3 Computational cost reduction

Table 4-7 summarizes the computational time for the CFD coupled method and the IRHF based method. The bottleneck for the simulation time switches from the furnace simulation in the CFD coupled method to the reactor simulations in the IRHF based method. Despite the fact that the IRHF based method requires more iterations per time step in the furnace-reactor convergence loop, the total wall time required for a complete run length simulation is about 5 h, which is nearly 50 times shorter than the time required for the CFD coupled method. A more fair comparison is between the required CPU time for a complete simulation rather than the required wall clock time. The reduction in computational cost for the IRHF method compared to the CFD coupled method amounts to a factor of nearly 2300. This reduction allows to move coupled run length simulations from an HPC environment to a personal computer which eliminates a major hurdle to switch from standalone to coupled run length simulations.

Table 4-7: Computational cost of the base case using the CFD coupled method and the IRHF based method (6 time steps in total)

	CFD		IRHF	
	Furnace	Reactor	Furnace	Reactor
Wall time / iteration [s]	28800	150	9	150
CPU time / iteration [s]	2764800	300	18	300
Iterations / time step [-]	5		19	
Total wall time [h]	241.25		5.04	
Total CPU time [h]	23040		10.07	

4.5 Conclusions

Coupled run length simulations of an industrial naphtha cracking furnace using computational fluid dynamics for the fire side and COILSIM1D for the reactor side were performed.

Although the concept of coupled run length simulation is not new, it was the first time that CFD was used to simulate the furnace throughout the full run length. It was shown that the total heat flux profiles of the reactor coils evolve distinctly in the inlet and the outlet legs due to intra-coil thermal redistribution caused by the non-uniformity of the coke layer deposited on the inner wall of the reactor coils. The standalone run length simulation failed to capture thermal redistribution phenomena and significantly underpredicted the run length.

Because the CFD coupled run length simulations are computationally expensive a faster method has been developed, i.e. incident radiative heat flux (IRHF) based method. In short this method utilizes the incident radiative heat flux profiles of all reactor coils obtained from coupled CFD simulations to account for intra-coil thermal redistribution that could not be captured by standalone method in run length simulations. Comparison of the run length results showed that the IRHF based method provides a comparable accuracy as the CFD coupled method with relative errors below 0.5%, i.e. the intra-coil thermal redistribution effects are well-captured. The capability of the IRHF based method to cope with modified operating conditions and feedstock compositions was further improved by introducing a correlation between the scaling factor of the incident radiative heat flux profiles and the flue gas bridge wall temperature. The performance of the method was validated by a number of simulation cases at different operating conditions in which the feedstock flow rate, fuel flow rate and feedstock composition were changed. With the relative error on the maximum TMT values consistently below than 1%, the IRHF based method was proven to be a valid alternative to the CFD method for coupled run length simulation at a fraction of the computational cost. The wall time required decreased by a factor over 50 while the required CPU time even decreased by a factor around 2300. This implies that coupled run length

simulations for a steam cracking unit do not require an HPC environment anymore and are now possible on a personal computer.

References

[1] G.Y. Gao, M. Wang, C.C. Pantelides, X.G. Li, H. Yeung, Mathematical Modeling and Optimal Operation of Industrial Tubular Reactor for Naphtha Cracking, in: C.A.O.d.N. Rita Maria de Brito Alves, B. Evaristo Chalbaud (Eds.) Computer Aided Chemical Engineering, Elsevier, 2009, pp. 501-506.
[2] M. Berreni, M. Wang, Modelling and dynamic optimization of thermal cracking of propane for ethylene manufacturing, Comput Chem Eng, 35 (2011) 2876-2885.
[3] Y. Jin, J. Li, W. Du, F. Qian, Multi-Objective Optimization of Pseudo-Dynamic Operation of Naphtha Pyrolysis by a Surrogate Model, Chem Eng Technol, 38 (2015) 900-906.
[4] M. Ghashghaee, R. Karimzadeh, Multivariable optimization of thermal cracking severity, Chemical Engineering Research and Design, 89 (2011) 1067-1077.
[5] Y. Jin, J. Li, W. Du, F. Qian, Integrated Operation and Cyclic Scheduling Optimization for an Ethylene Cracking Furnaces System, Ind Eng Chem Res, 54 (2015) 3844-3854.
[6] K. Van Geem, Z. Zhou, M.-F. Reyniers, G.B. Marin, Effect of process conditions and feedstock composition on run lengths of steam cracking coils, in: 2009 AIChE Spring National meeting; 5th Global Congress on Process Safety, New York, NY (United States), 2009.
[7] G. Hu, C.M. Schietekat, Y. Zhang, F. Qian, G.J. Heynderickx, K.M. Van Geem, G.B. Marin, Impact of Radiation Models in Coupled Simulations of Steam Cracking Furnaces and Reactors, Ind Eng Chem Res, 54 (2015) 2453-2465.
[8] G.J. Heynderickx, G.F. Froment, Simulation and Comparison of the Run Length of an Ethane Cracking Furnace with Reactor Tubes of Circular and Elliptical Cross Sections, Ind Eng Chem Res, 37 (1998) 914-922.
[9] P.M. Plehiers, G.C. Reyniers, G.F. Froment, Simulation of the run length of an ethane cracking furnace, Ind Eng Chem Res, 29 (1990) 636-641.
[10] H.C. Hottel, A.F. Sarofim, Radiative transfer, McGraw-Hill, New York, 1967.
[11] C.M. Schietekat, D.J. Van Cauwenberge, K.M. Van Geem, G.B. Marin, Computational fluid dynamics-based design of finned steam cracking reactors, AIChE J, 60 (2014) 794-808.
[12] D.J. Van Cauwenberge, C.M. Schietekat, J. Floré, K.M. Van Geem, G.B. Marin, CFD-based design of 3D pyrolysis reactors: RANS vs. LES, Chem Eng J, 282 (2015) 66-76.
[13] P.A. Reyniers, C.M. Schietekat, D.J. Van Cauwenberge, L.A. Vandewalle, K.M. Van Geem, G.B. Marin, Necessity and Feasibility of 3D Simulations of Steam Cracking Reactors, Ind Eng Chem Res, 54 (2015) 12270-12282.
[14] C.M. Schietekat, M.W.M. van Goethem, K.M. Van Geem, G.B. Marin, Swirl flow tube reactor technology: An experimental and computational fluid dynamics study, Chem Eng J, 238 (2014) 56-65.
[15] G. Hassan, M. Pourkashanian, D. Ingham, L. Ma, P. Newman, A. Odedra, Predictions of CO and NOx emissions from steam cracking furnaces using GRI2.11 detailed reaction mechanism – A CFD investigation, Comput Chem Eng, 58 (2013) 68-83.
[16] G.D. Stefanidis, B. Merci, G.J. Heynderickx, G.B. Marin, CFD simulations of steam cracking furnaces using detailed combustion mechanisms, Comput Chem Eng, 30 (2006) 635-649.

[17] G. Hu, H. Wang, F. Qian, Y. Zhang, J. Li, K.M. Van Geem, G.B. Marin, Comprehensive CFD Simulation of Product Yields and Coking Rates for a Floor- and Wall-Fired Naphtha Cracking Furnace, Ind Eng Chem Res, 50 (2011) 13672-13685.
[18] D. Brown, P. Smith, B. Adams, Cracking furnace fireside modeling advances, in: Proceedings of the 6th Ethylene Producers' Conference, Atlanta, GA (United States), 1994.
[19] D.J. Brown, M.A. Cremer, P.J. Smith, R.T. Waibel, Fireside modeling in cracking furnaces, in: Proceedings of the 9th Ethylene Producers' Conference, Houston, TX (United States), 1997, pp. 159-193.
[20] A. Habibi, B. Merci, G.J. Heynderickx, Multiscale modeling of turbulent combustion and NOx emission in steam crackers, AIChE J, 53 (2007) 2384-2398.
[21] S. Barendregt, M. van Goethem, I. Risseeuw, F. Alessio, T. Faravelli, A.A. Cuoci, X.J. Li, The Design Of Ultra-Low NOx Critical Furnaces, in: The Eighth European Conference on Industrial Furnaces and Boilers, Portugal, 2008.
[22] Q. Tang, M. Denison, B. Adams, D. Brown, Towards comprehensive computational fluid dynamics modeling of pyrolysis furnaces with next generation low-NOx burners using finite-rate chemistry, Proceedings of the Combustion Institute, 32 (2009) 2649-2657.
[23] D.J. Brown, J. Ma, B.R. Adams, Development of an improved prediction model for chemical process furnaces, in: AIChE Spring National Meeting, New Orleans, LA (United States), 2003.
[24] G. Lecocq, D. Poitou, I. Hernández, F. Duchaine, E. Riber, B. Cuenot, A Methodology for Soot Prediction Including Thermal Radiation in Complex Industrial Burners, Flow, Turbulence and Combustion, 92 (2014) 947-970.
[25] G.D. Stefanidis, B. Merci, G.J. Heynderickx, G.B. Marin, Gray/nongray gas radiation modeling in steam cracker CFD calculations, AIChE J, 53 (2007) 1658-1669.
[26] A. Habibi, B. Merci, G.J. Heynderickx, Impact of radiation models in CFD simulations of steam cracking furnaces, Comput Chem Eng, 31 (2007) 1389-1406.
[27] Y. Zhang, F. Qian, C.M. Schietekat, K.M. Van Geem, G.B. Marin, Impact of flue gas radiative properties and burner geometry in furnace simulations, AIChE J, 61 (2015) 936-954.
[28] T. Pedot, B. Cuenot, E. Riber, T. Poinsot, Coupled Heat Transfers in a Refinery Furnace in View of Fouling Prediction, Journal of Heat Transfer, 138 (2016) 072101-072101.
[29] G.J. Heynderickx, M. Nozawa, Banded gas and nongray surface radiation models for high-emissivity coatings, AIChE J, 51 (2005) 2721-2736.
[30] G.D. Stefanidis, K.M. Van Geem, G.J. Heynderickx, G.B. Marin, Evaluation of high-emissivity coatings in steam cracking furnaces using a non-grey gas radiation model, Chem Eng J, 137 (2008) 411-421.
[31] G.J. Heynderickx, M. Nozawa, High-emissivity coatings on reactor tubes and furnace walls in steam cracking furnaces, Chem Eng Sci, 59 (2004) 5657-5662.
[32] Q. Tang, B. Adams, M. Bockelie, M. Cremer, M. Denison, C. Montgomery, A. Sarofim, D. Brown, Towards comprehensive CFD modeling of lean premixed ultra-low NOx burners in process heaters, in: Proceedings of the 17th Ethylene Producers' Conference, Atlanta, GA (United States), 2005, pp. 594-619.
[33] V. Yakhot, S.A. Orszag, S. Thangam, T.B. Gatski, C.G. Speziale, Development of turbulence models for shear flows by a double expansion technique, Physics of Fluids A: Fluid Dynamics (1989-1993), 4 (1992) 1510-1520.
[34] C.K. Westbrook, F.L. Dryer, Simplified Reaction Mechanisms for the Oxidation of Hydrocarbon Fuels in Flames, Combust Sci Technol, 27 (1981) 31-43.

[35] B.F. Magnussen, B.H. Hjertager, On mathematical modeling of turbulent combustion with special emphasis on soot formation and combustion, Symposium (International) on Combustion, 16 (1977) 719-729.
[36] G.H. Yeoh, K.K. Yuen, Computational Fluid Dynamics in Fire Engineering: Theory, Modelling and Practice, Butterworth-Heinemann, Burlington, 2009.
[37] K.M. Van Geem, R. Žajdlík, M.-F. Reyniers, G.B. Marin, Dimensional analysis for scaling up and down steam cracking coils, Chem Eng J, 134 (2007) 3-10.
[38] K.M. Van Geem, G.J. Heynderickx, G.B. Marin, Effect of radial temperature profiles on yields in steam cracking, AIChE J, 50 (2004) 173-183.
[39] COILSIM1D. http://www.avgi.be/.
[40] M.K. Sabbe, K.M. Van Geem, M.-F. Reyniers, G.B. Marin, First principle-based simulation of ethane steam cracking, AIChE J, 57 (2011) 482-496.
[41] K.M. Van Geem, M.-F. Reyniers, G.B. Marin, J. Song, W.H. Green, D.M. Matheu, Automatic reaction network generation using RMG for steam cracking of n-hexane, AIChE J, 52 (2006) 718-730.
[42] S.P. Pyl, K.M. Van Geem, M.-F. Reyniers, G.B. Marin, Molecular reconstruction of complex hydrocarbon mixtures: An application of principal component analysis, AIChE J, 56 (2010) 3174-3188.
[43] K.M. Van Geem, D. Hudébine, M.F. Reyniers, F. Wahl, J.J. Verstraete, G.B. Marin, Molecular reconstruction of naphtha steam cracking feedstocks based on commercial indices, Comput Chem Eng, 31 (2007) 1020-1034.
[44] K.M. Van Geem, M.F. Reyniers, G.B. Marin, Challenges of modeling steam cracking of heavy feedstocks, Oil & Gas Science and Technology - Rev. IFP, 63 (2008) 79-94.
[45] H. Zimmermann, R. Walzl, Ethylene, in: Ullmann's Encyclopedia of Industrial Chemistry, Wiley-VCH, Weinheim, Germany, 2000.
[46] J. Colannino, Mathematical models for characterizing and predicting heat flux profiles from ethylene cracking units, in: AIChE Annual Meeting Conference Proceedings, American Institute of Chemical Engineers (AIChE) Houston, TX, 2007.
[47] W.E. Lobo, J. Evans, Heat transfer in the radiant section of petroleum heaters, Trans. Am. Inst. Chem. Engrs, 35 (1939) 748-778.
[48] H.A.-H. Ibrahim, M.M. Al-Qassimi, Calculation of Radiant Section Temperatures in Fired Process Heaters, Chemical Engineering and Science, 1 (2013) 55-61.
[49] K.M. Sundaram, G.F. Froment, Kinetics of coke deposition in the thermal cracking of propane, Chem Eng Sci, 34 (1979) 635-644.

Chapter 5: Validation of methane combustion mechanisms for NO_x prediction

This chapter is based on the following conference contribution:

Zhang, Y.; Schietekat, C. M.; Van Cauwenberge D. J.; Reyniers, P. A.; Van Geem, K. M.; Henneke, M.; Qian, F.; Marin, G. B., Numerical simulations of steam cracking test furnace using detailed combustion mechanism for CO and NO_x emission. 9^{th} International Conference on Chemical Kinetics, Proceedings 2015, 312-315.

Abstract

In industrial steam cracking furnaces floor and/or sidewall burners provide the energy necessary for attaining high temperatures via combustion of hydrocarbon fuels. Stricter emission regulations in recent years pushed the burner manufactures to design new types of ultra-low NO_x burners, which are routinely tested in pilot furnaces before being implemented in full-scale applications. However, the harsh conditions in test furnaces prohibit accurate measurements of in-flame temperature, radiative heat flux, and concentrations of major and minor species. A numerical model can complement experimental tests to provide information on the region of interest for burner design and retrofit. Non-premixed turbulent combustion in a large-scale furnace is a process in which turbulence, radiation and chemical reactions are strongly coupled. To be able to jointly model these three aspects, each of the relevant sub-models has to be carefully examined. In the present work, simulations of a propane jet into co-flowing air showed that a modified SST k-ω model was able to accurately capture the turbulence characteristics of round jet flow. Different radiation models were compared to investigate the impacts of radiative heat transfer in Sandia flame D simulations. It was demonstrated that the five-band non-gray model developed in chapter 2 gives the best performance. Four combustion mechanisms were tested for the Sandia flame D case as well. Excellent agreement between the measured and calculated NO emission was observed when using the ChenCH4 and ARM2 mechanisms. A combination of all validated sub-models can therefore be successfully applied in CFD simulations aimed at designing furnaces equipped with ultra-low NO_x burners.

Keywords: steam cracking, computational fluid dynamics, turbulence model validation, reduced combustion kinetics, radiative heat transfer, NO_x emission, Sandia flame D

5.1 Introduction

Steam cracking of hydrocarbons is the most important petrochemical process for light olefins production. The strongly endothermic cracking reactions and the high process gas temperatures in the reactor coils make that a considerable amount of thermal energy needs to be transferred from the furnace to the reactor coils, mostly via radiation. To reduce local hot spots on the reactor walls, and consequently severe coking and material deterioration, ideally a uniform heat flux is provided to the reactor coils. This is also beneficial for the run length of the furnace. Pursuing an as uniform as possible heat flux to the reactors led the furnace designers to using multiple horizontal rows of radiant wall burners above each other, in which combustion of premixed fuel and air creates small but intense flames with temperatures up to 2200 K [1]. However, the inherent downside of using a large number of wall burners is a high cost for maintenance and operation. Therefore, floor burners in which fuel and air enter separately are preferred over wall burners in recent years. These burners produce large diffusion flames which can be as high as 4-6 meters and supply most or even all the thermal power needed for the endothermic steam cracking reactions taking place inside the process tube. As the power per individual burner is typically larger for a single floor burner (1 - 4 MW) than for a single wall burner (0.08 - 1 MW), less burners are needed if the furnace is floor fired, decreasing the cost for operation and maintenance.

In recent years, increasing environmental concerns and a stricter legislation have compelled the burner manufacturers to minimize NO_x emissions, which also prompted the use of floor burners due to their more gradual combustion and hence lower flame peak temperature. To comply with the emission regulations significant effort has been dedicated to the design of ultra-low NO_x burners. NO_x is formed via three distinct chemical kinetic processes, referred to as fuel NO_x, thermal NO_x, and prompt NO_x. The fuel NO_x is due to the oxidation of

nitrogen contained in the fuel, which is usually important in combustion of coal. The thermal NO_x is formed as a result of the oxidation of nitrogen in air through a reaction path involving oxygen, hydrogen and the hydroxyl radical. This pathway becomes important when the temperature rises above 1800 K and the production NO_x increases strongly as temperatures become higher. The prompt NO_x is associated with conversion of nitrogen through a radical reaction network and therefore favored at rich conditions, i.e. when an excess of hydrocarbon fuel is present. This mechanism is less temperature dependent compared to the thermal NO_x mechanism. As the typical fuel used in steam cracking furnaces mainly consists of methane and carbon monoxide, most of the NO_x in the combustion system is formed via the thermal NO_x mechanism. Therefore it is beneficial to reduce (maximum) flame temperatures using new burner design technologies, such as staged fuel/air mixing, air preheat and flue gas recirculation [2]. The principle of the staged fuel/air technology is that it produces longer flames with more than one mixing and combustion zone to spread the heat release homogeneously over all the zones. In this case, the flame peak temperature can be effectively reduced, resulting in lower NO_x production. Validating the performance of a new burner design requires extensive testing in a test furnace. However, the extreme conditions in these furnaces make it difficult to obtain in-flame information, such as temperature and species concentrations, which are crucial for improving understanding of the flame behavior. Furthermore, even if a new design can be successfully operated in the test furnace, its application to industrial-scale furnaces should still be done with the appropriate care, considering possible pitfalls originating from the thermal coupling effect between adjacent burners and between burners and reactor coils [3]. A computational fluid dynamic (CFD) based model which accounts for the interaction between turbulence, radiative heat transfer and combustion kinetics show advantages over experimental investigation in test furnace as

its financial cost is considerably lower. Furthermore, the forgoing technologies to reduce the (maximum) flame temperature achieve their goal by optimizing the interaction between turbulent mixing and combustion kinetics, which usually requires modification of small details such as size, location, orientation and configuration of burner tips and nozzles. Such a design parametric study in a test furnace is tedious and time-consuming due to the frequent burner retrofit and reinstallation. Performing the optimization based on CFD modeling can greatly reduce both the financial cost and the time spent on the burner development and even on the manufacturing, installation and furnace start-up.

Numerous studies on CFD modeling of steam cracking furnaces were carried out since the beginning of the 1990s, leading to a comprehensive understanding of turbulence-chemistry interaction [4-8], thermal coupling effects [5, 9, 10], radiative heat transfer [11-15] and the effect of high-emissivity coatings [16-18]. However, few studies focused on predicting NO_x emissions [19-24], in particular because it requires sophisticated methane combustion mechanisms guarantee the accuracy of the results. Detailed methane combustion mechanisms including NO_x chemistry usually contain dozens of species and hundreds of reactions, e.g. there are 53 species and 325 reactions included in the widely used Gas Research Institute (GRI) natural gas combustion kinetic scheme GRI-Mech 3.0 [25]. The stiffness introduced by chemistry due to the wide range in species life time and in the time scales of the elementary reactions poses a great challenge on implementing detailed combustion kinetics in large-scale computations.

Although it is possible to overcome the abovementioned difficulties and perform furnace simulations using detailed mechanisms as in the work of Hassan et al [22], implementing elementary combustion kinetics in CFD simulations is computationally expensive in terms of CPU-time. Hence two alternative approaches are taken for NO_x predictions in large-scale

combustion systems, i.e. calculating NO_x formation during post-processing [19, 21] and reducing the detailed chemical kinetic mechanisms [20, 23]. The former method computes NO_x emission based on fixed flow, temperature, and species concentration fields obtained from a converged CFD simulation [26]. The latter implements methods such as the pseudo-steady state assumption (PSSA) which reduces the number of species conservation equations that need to be solved by calculating the concentrations of the fastest reacting species via a set of algebraic equations [27, 28]. The disadvantage of calculation NO_x emission in the post-processing step compared to using reduced kinetic mechanisms is that good NO_x prediction relies on accurate results for the temperature and species concentration fields. To obtain sufficiently accurate results for these fields, a detailed combustion mechanism is needed in any case, inherently leading to a high computational cost. Hence the method of mechanism reduction is more favorable in terms of computational cost for coupling detailed combustion kinetics with CFD calculations.

In this chapter, the effect of the turbulence model, the radiation model and the combustion kinetics on the simulation of turbulent jet flames was studied in order to develop a CFD-based model capable of assessing new designs of low-NO_x burners. 2D simulations of a mixing layer flow and a non-reacting round jet of propane into co-flowing air were performed and compared with the experimental data obtained from the NASA Langley Research Center and Sandia National Laboratories respectively for turbulence model validation. For validation of the kinetic mechanisms for combustion, a turbulent piloted methane/air diffusion flame (Sandia flame D) was calculated using several reduced combustion mechanisms. The performance of these mechanisms in terms of flame temperature and species mass fraction prediction was evaluated against experimental data. In addition, the effect of radiative heat

loss on the calculation of flame temperature and NO_x emission was also investigated by comparing different models for the flue gas radiative properties.

5.2 Validation for non-reacting flow

Although many research articles are available in which large eddy simulations (LES) were performed to study the dynamic behavior of turbulent non-premixed jet flames [29, 30], it is still infeasible to perform LES for large-scale furnaces due to the prohibitively high computational cost. On the other hand, previous research has demonstrated that Reynolds-averaged Navier-Stokes (RANS) simulations with two-equation turbulence model can provide satisfactory results for important characteristics such as flame temperature, flame height and NO_x emission predictions in industrial furnaces equipped with low-NO_x burners [19, 21, 22]. Nevertheless, validation of the two-equation turbulence models is necessary before applying them to specific turbulent flame simulations [20, 22, 23]. Therefore the performance of different turbulence models were compared against experimental data.

5.2.1 Experimental datasets

Fuel enters the furnace as a high-velocity jet through the burner nozzle and is subsequently mixed with co-flowing air, leading to a non-premixed diffusion flame. In some burner configurations, mixing of streams with different velocities occurs when staged fuel/air technology is applied. Prior to implementing detailed combustion kinetics into CFD calculations, turbulence model validation is required to ensure that the model is able to accurately capture the characteristics of the flow. To this end, two experimental datasets representing mixing layer flow and round jet flow, both relevant for industrial burner designs, are used as validation cases.

5.2.1.1 2D mixing layer flow

The experiment utilizes a splitter plate with thickness of 3 mm in a horizontal tunnel of 300 mm wide as shown in Figure 5-1. Two air streams with different velocities merge downstream at the end of the taper. The free stream velocities are 41.54 m s^{-1} and 22.40 m s^{-1} for the upper and the lower stream respectively. The experiment was carried out at a temperature of 293 K. The results demonstrated that the turbulent intensity at the velocity inlet boundary of both air streams is rather low at 0.3%. A detailed description of the experimental apparatus can be found in the work of Delville et al [31] and the measured data are summarized on the website of Turbulence Modeling Resource maintained by the NASA Langley Research Center [32], including x-velocity and specific turbulent shear stress along the y-direction at different locations downstream to the point where the mixing occurs.

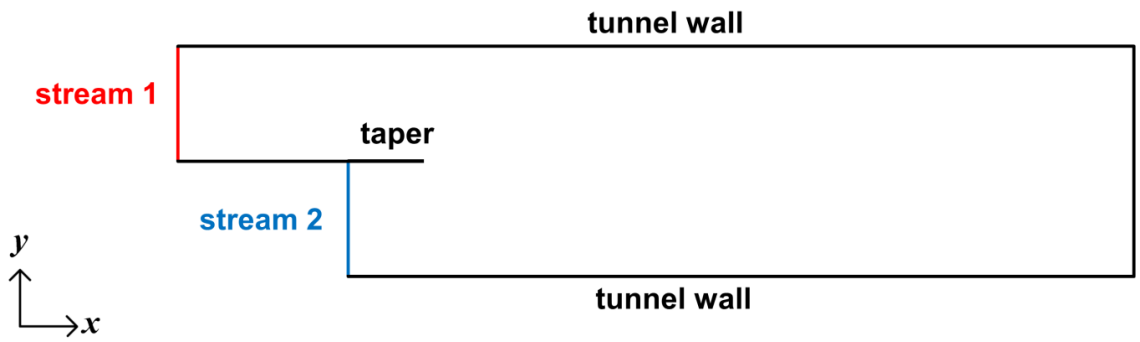

Figure 5-1: Experimental setup of shear mixing flow of two air streams.

5.2.1.2 Non-reacting propane jet flow

The non-reacting propane jet flow was experimentally investigated using the Sandia turbulent diffusion flame facility which is schematically represented in Figure 5-2. An axisymmetric fuel jet is located in the upstream center of a forced-draft vertical wind tunnel. The fully windowed tunnel has a cross-section of 0.3 m by 0.3 m and a length of 2 m. Propane flows

through the central fuel jet pipe and enters the tunnel at the jet exit with a bulk velocity of 53 m s^{-1}, and is subsequently mixed with the co-flowing air, which enters with a bulk velocity of 9.2 m s^{-1}. The most important dimensions and inlet conditions of the facility are listed in Table 5-1. A complete description of the facility and the uncertainties on the measurements are available in the work of Dibble et al. [33] and Schefer [34]. A summary of the axial and radial profiles of experimental results such as axial velocity, mixture fraction, and density can be found on the turbulent non-premixed flames (TNF) website [35].

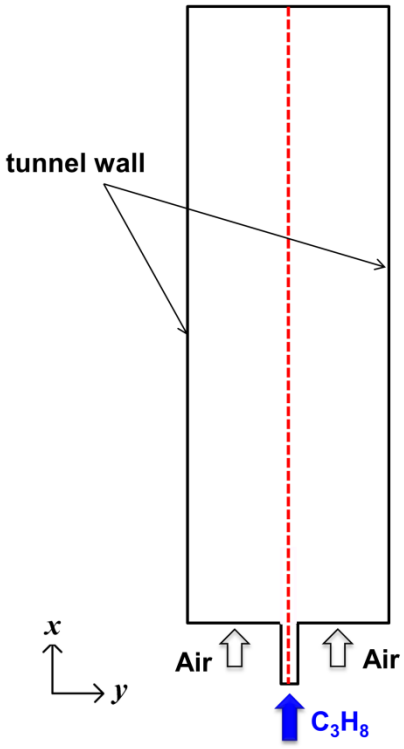

Figure 5-2: Experimental setup for non-reacting propane jet flow from Sandia National Laboratory.

Table 5-1: Dimensions and inlet conditions of the non-reacting propane jet flow facility.

Test section	
Tunnel cross section (m^2)	0.3×0.3
Tunnel length (m)	2
Jet inner diameter (10^{-3} m)	5.26
Jet outer diameter (10^{-3} m)	9.00
Inlet conditions	
Propane jet velocity (m s^{-1})	53
Propane jet temperature (K)	294
Reynolds number	68000
Co-flowing air velocity (m s^{-1})	9.2
Co-flowing air temperature (K)	294
Co-flowing air turbulent intensity	0.4%

5.2.2 Modeling approach

For the aforementioned flow situations, a two-dimensional steady-state compressible modeling approach is established, which takes into account the global mass, momentum, and energy conservation as given by the following equations.

$$\nabla \cdot (\rho \vec{u}) = 0 \tag{5.1}$$

$$\nabla \cdot (\rho \vec{u}\vec{u}) = -\nabla p + \nabla \cdot (\bar{\bar{\tau}}) + S_M \tag{5.2}$$

$$\nabla \cdot \left(\vec{u}(\rho E + p)\right) = \nabla \cdot \left(k_{eff} \nabla \mathrm{T} - \sum_i h_i \vec{J}_i + \left(\bar{\bar{\tau}}_{eff} \cdot \vec{u}\right) \right) + S_E \tag{5.3}$$

The contribution of the gravitational force in the momentum equation is not considered as its effect on gas flow at low temperature is negligible. The $\vec{J}_i$ in the energy conservation equation represents the diffusive flux of species i, which is omitted for the mixing layer flow case but is relevant in the non-reacting propane jet flow case. The energy source term S_E is zero in these simulations.

For the propane jet flow, the species conservation equation (5.4) was added to account for mixing of propane with air.

$$\nabla \cdot \left(\frac{\vec{u}Y_i}{V_m}\right) = -\nabla \cdot \vec{J}_i + R_i \tag{5.4}$$

The source term R_i representing species production/destruction due to chemical reactions is zero as the flow is non-reacting.

5.2.3 Turbulence models

Two-equation eddy-viscosity turbulence models can be divided into two groups, namely k-ε models and k-ω models. RANS equations are closed by introducing two additional conservation equations for the turbulent kinetic energy k and turbulent dissipation rate ε in the first category, and the turbulent kinetic energy k and the specific dissipation rate ω in the second category. The Renormalization Group (RNG) k-ε model [36], the Realizable k-ε model [37] and the SST k-ω model [38] are selected to be used in mixing layer flow and propane jet flow simulations. The standard k-ε model [39] and the standard k-ω model [40] are not considered as the former overpredicts the axial velocity decay of round jet flow, i.e. the so-called turbulent round-jet and plane-jet anomaly [41, 42], while the latter has a strong sensitivity to the free stream turbulent boundary conditions [38].

5.2.3.1 RNG k-ε model

The conservation equations for the turbulent kinetic energy k and the turbulent dissipation rate ε in the RNG k-ε model are the following:

$$\nabla \cdot (\rho \vec{u} k) = \nabla \cdot (\alpha_k (\mu + \mu_t) \cdot \nabla k) + P_k - \rho \varepsilon \tag{5.5}$$

$$\nabla \cdot (\rho \vec{u} \varepsilon) = \nabla \cdot (\alpha_\varepsilon (\mu + \mu_t) \cdot \nabla \varepsilon) + C_{1\varepsilon} \frac{\varepsilon}{k} P_k - C_{2\varepsilon}^* \rho \frac{\varepsilon^2}{k} \tag{5.6}$$

where $\mu_t = C_\mu \rho\, k^2/\varepsilon$ is the turbulent viscosity. $P_k = \mu_t S^2$ represents the production of turbulent kinetic energy, with S the modulus of the mean strain rate defined as $S_{ij} = \frac{1}{2}\left(\frac{\partial u_i}{\partial x_j} + \frac{\partial u_j}{\partial x_i}\right)$. $C_{2\varepsilon}^* = C_{2\varepsilon} + \frac{C_\mu \eta^3 (1-\eta/\eta_0)}{1+\beta\eta^3}$, $\eta = Sk/\varepsilon$. α_k, α_ε, $C_{1\varepsilon}$, $C_{2\varepsilon}$, C_μ, η_0 and β in equations (5.5) and (5.6) are the model constants, of which there are seven in total.

5.2.3.2 Realizable k-ε model

The Realizable k-ε model proposed by Shih et al. [37] was intended to remedy the round-jet plane-jet anomaly of the standard k- ε model, which was thought of as mainly caused by the conservation equation for the turbulent dissipation rate ε [41]. Hence the conservation equation for turbulent kinetic energy k in the Realizable k-ε model is the same as that of the RNG k-ε model, i.e. equation (5.5). The only difference is that instead of being constant, C_μ is now a function of the mean strain and rotation rates, the angular velocity of the system rotation, and the turbulence field as given in equation (5.7) and (5.8).

$$C_\mu = \frac{1}{A_0 + A_s \frac{kU^*}{\varepsilon}} \tag{5.7}$$

$$U^* = \sqrt{S_{ij}S_{ij} + \tilde{\Omega}_{ij}\tilde{\Omega}_{ij}} \tag{5.8}$$

where $\tilde{\Omega}_{ij} = \Omega_{ij} - 2\epsilon_{ijk}\omega_k$, $\Omega_{ij} = \bar{\Omega}_{ij} - \epsilon_{ijk}\omega_k$, and $\bar{\Omega}_{ij}$ is the mean rate-of-rotation tensor viewed in a rotating reference frame with the angular velocity ω_k. $A_0 = 4.04$ and $A_s = \sqrt{6}\cos\phi$ are model constants where $\phi = \frac{1}{3}\cos^{-1}\left(\sqrt{6}W\right)$ and $W = \frac{S_{ij}S_{jk}S_{ki}}{S^3}$. The other variables S, S_{ij}, and μ_t have the same expression as in the RNG k-ε model.

The conservation equation for the turbulent dissipation rate ε is given in (5.9).

$$\nabla \cdot (\rho \vec{u} \varepsilon) = \nabla \cdot (\alpha_\varepsilon (\mu + \mu_t) \cdot \nabla \varepsilon) + \rho C_1 S \varepsilon - \rho C_2 \frac{\varepsilon^2}{k + \sqrt{\frac{\mu}{\rho} \varepsilon}} \tag{5.9}$$

where $C_1 = \max\left[0.43, \frac{\eta}{\eta+5}\right]$. $\mu_t = C_\mu \rho\, k^2/\varepsilon$ is the turbulent viscosity. C_2, α_k, and α_ε are model constants. One of the major differences in the conservation equation for the turbulent dissipation rate ε between the Realizable k-ε model and the RNG k-ε model is that the equation does not include the turbulent kinetic energy production term P_k in the production term of the turbulent dissipation rate, which is to represent the spectral energy transfer in a better way. Furthermore, adding $\sqrt{\frac{\mu}{\rho} \varepsilon}$ in the third term on the right hand side of equation (5.9) also aids to avoid singularity problems when the turbulent kinetic energy k approaches zero in flow regions where turbulence is rapidly dissipated.

5.2.3.3 SST k-ω model

The shear stress transport (SST) formulation of the k-ω model developed by Menter [38] was a combination of the two best available models for the free stream and the near wall regions. It utilizes the standard k-ω model proposed by Wilcox [40] in the inner region of the boundary layer and gradually switches to the standard k-ε model when approaching the outer region of the free shear flow using blending functions. This feature allows the SST k-ω model to be used as a low Reynolds turbulence model without any extra damping functions, and avoids the problem that the standard k-ω model is too sensitive to the inlet free stream turbulent boundary conditions. The conservation equations for turbulent kinetic energy k and specific dissipation rate ω are given in (5.10) and (5.11).

$$\nabla \cdot (\rho \vec{u} k) = \nabla \cdot \left((\mu + \sigma_k \mu_t) \cdot \nabla k\right) + \tilde{P}_k - \rho \beta^* k \omega \tag{5.10}$$

$$\nabla \cdot (\rho \vec{u} \omega) = \nabla \cdot \left((\mu + \sigma_\omega \mu_t) \cdot \nabla \omega\right) + \alpha \rho S^2 - \rho \beta \omega^2 + 2(1 - F_1) \rho \frac{\sigma_{\omega 2}}{\omega} \cdot \nabla \mathrm{k} \cdot \nabla \omega \qquad (5.11)$$

where $\tilde{P}_k = \min(P_k, 10\rho\beta^* k\omega)$ represents the production of turbulent kinetic energy due to mean velocity gradients. The term P_k is the same as the one introduced in the RNG k-ε model, while the turbulent viscosity $\mu_t = a_1 \rho k / \max(a_1 \omega, SF_2)$ is quite different. The coefficient φ of the SST k-ω model is calculated from the constant φ_1 and φ_2 by equation (5.12).

$$\varphi = \varphi_1 F_1 + \varphi_2 (1 - F_1) \qquad (5.12)$$

where φ stands for α, β, σ_k and σ_ω in the forgoing equations. The blending functions F_1 and $F_2$are given as follows:

$$F_1 = \tanh\left\{\left\{\min\left[\max\left(\frac{\sqrt{k}}{\beta^* \omega y}, \frac{500\mu}{\rho y^2 \omega}\right), \frac{4\rho\sigma_{\omega 2} k}{CD_{k\omega} y^2}\right]\right\}^4\right\} \qquad (5.13)$$

$$CD_{k\omega} = \max\left(2\rho\sigma_{\omega 2} \frac{1}{\omega} \cdot \nabla \mathrm{k} \cdot \nabla \omega, 10^{-10}\right) \qquad (5.14)$$

$$F_2 = \tanh\left\{\left[\max\left(\frac{2\sqrt{k}}{\beta^* \omega y}, \frac{500\mu}{\rho y^2 \omega}\right)\right]^2\right\} \qquad (5.15)$$

The parameters α_1, α_2, β_1, β_2, β^*, σ_{k1}, σ_{k2}, $\sigma_{\omega 1}$, $\sigma_{\omega 2}$, and a_1 are model constants.

5.2.4 Simulation results

5.2.4.1 Comparison of turbulence models

Combining the conservation equations for global mass, momentum, energy and species with the foregoing turbulence models, computational fluid dynamic simulations were performed using the commercial finite volume package ANSYS Fluent 14.5 [43]. In what follows, the

three cases with the different turbulence models are referred to as 'RNG k-ε', 'Realizable k-ε' and 'SST k-ω'.

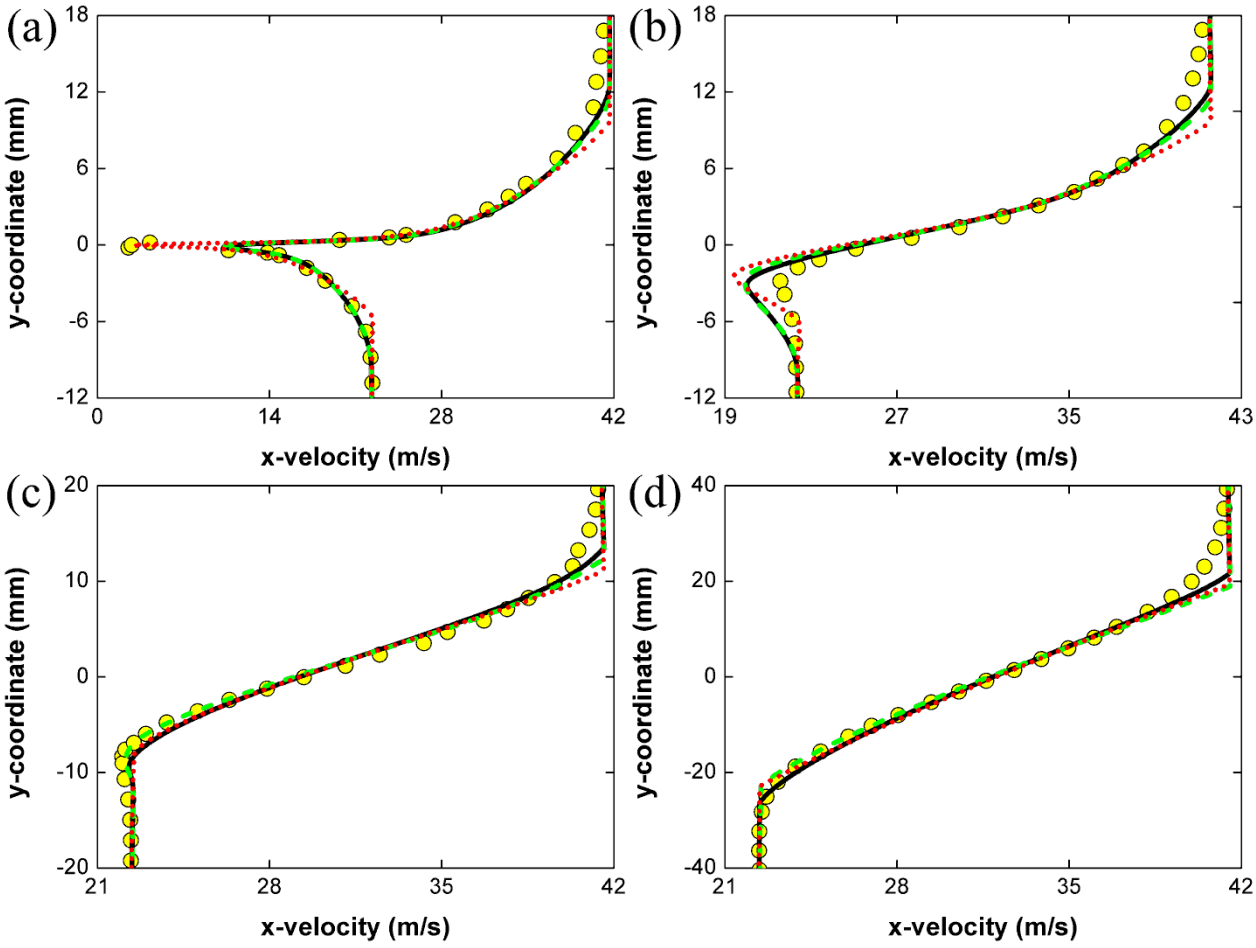

Figure 5-3: Profiles of x-velocity as a function of y-coordinate at different x-locations: (a) x = 1 mm; (b) x = 50 mm; (c) x = 200 mm; (d) x = 650 mm. ○ - experimental data; ▬ - RNG k-ε model; ▬ - Realizable k-ε model; ● ● ● ● ● - SST k-ω model.

The x-velocity profiles as a function of y-coordinate at different x-locations for the 2D mixing layer flow case are depicted in Figure 5-3. It is worth noting that the axes of the x-velocity and the y-coordinate are reversed to be consistent with the configuration of the experimental facility shown in Figure 5-1. It is observed that the x-velocity decreases gradually from a 42

m s^{-1} in the upper stream to 22 m s^{-1} in the lower stream. This transition is rather smooth in the downstream locations (x > 50 mm, Figure 5-3 (b), (c) and (d)) while for x = 1 mm, the x-velocity drops sharply near the center of the mixing layer, mainly due to the stationary point at the end of the taper. Although all three turbulence models provide similar results, only the SST k-ω model successfully captures the near-stationary flow at the end of the taper at x = 1 mm.

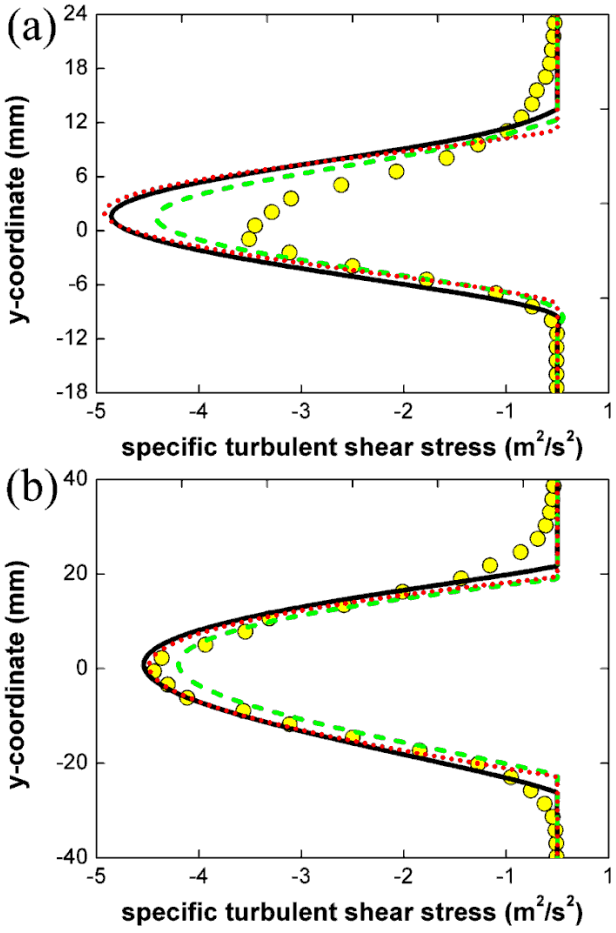

Figure 5-4: Profiles of specific turbulent shear stress as a function of y-coordinate at different x-locations: (a) x = 200 mm; (b) x = 650 mm. ○ - experimental data; ▬ - RNG k-ε model; ▬ ▬ - Realizable k-ε model; ● ● ● ● ● - SST k-ω model.

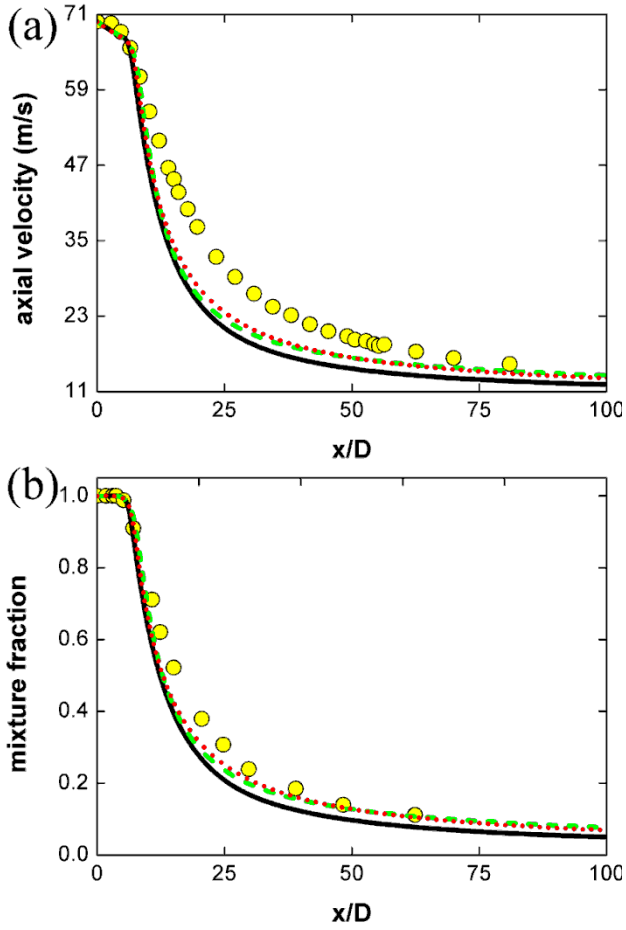

Figure 5-5: Profiles of (a) axial velocity and (b) mixture fraction along the centerline. ○ - experimental data; ▬ - RNG k-ε model; ▬ - Realizable k-ε model; ● ● ● ● ● - SST k-ω model.

Figure 5-4 shows the specific turbulent shear stress at x = 200 mm and x = 650 mm. It can be observed that all turbulence models overpredict the value of shear stress at x = 200 mm while the results at x = 650 mm are generally in good agreement with experimental data. In addition, the Realizable k-ε model yields lower values for the shear stress compared to the other two models. Despite the minor inaccuracies of the calculations in some locations (mainly in the region with large velocity gradients), the simulation results obtained with all three turbulence models match the experimental data reasonably well. This means that they are all suitable for

simulating shear layer flow. However, the SST k-ω model is preferred as it provides more precise predictions of the x-velocity in the region with strong velocity gradients.

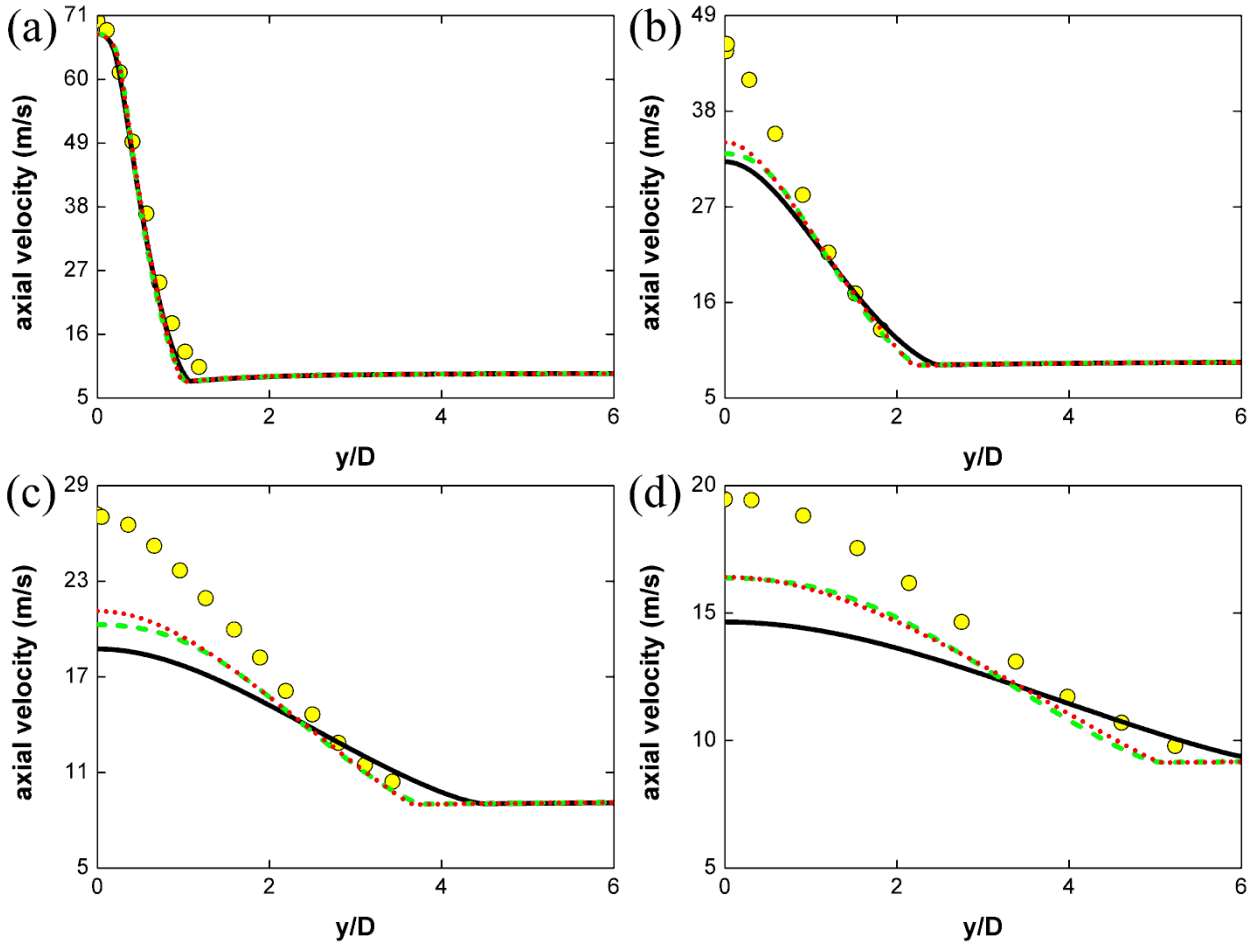

Figure 5-6: Radial profiles of axial velocity at different axial locations: (a) x/D = 4 ; (b) x/D = 15; (c) x/D = 30; (d) x/D = 50. - experimental data; - RNG k-ε model; - Realizable k-ε model; - SST k-ω model.

To further test the validity of the three turbulence models, simulation results of the non-reacting propane jet into co-flowing air are compared against experimental data. As shown in Figure 5-5, overpredictions of the axial velocity and mixture fraction decay along the centerline of the propane jet flow are observed in all three models. In particular the simulated

axial velocity of the propane jet decreases too rapidly after entering into the co-flow air compared to the experimental data. The maximum difference between measurements and simulations is located at a distance of about 25 jet diameter downstream the nozzle exit. This discrepancy can be explained by the fact that the simulations overpredict the spreading rate of the round free jet [22], which implies that the simulated propane jet has a wider turbulent core with a higher entrainment of ambient air. This is verified by the profiles of the axial velocity as function of the radial coordinate, depicted in Figure 5-6 (b), (c) and (d). the simulated jet flow is more flattened with lower axial velocity at the centerline (y/D = 0) and higher velocity at the edges of the shear layer (for RNG k-ε) compared to the experimental results. The radial profiles of propane mixture fraction show similar trends as shown in Figure 5-7.

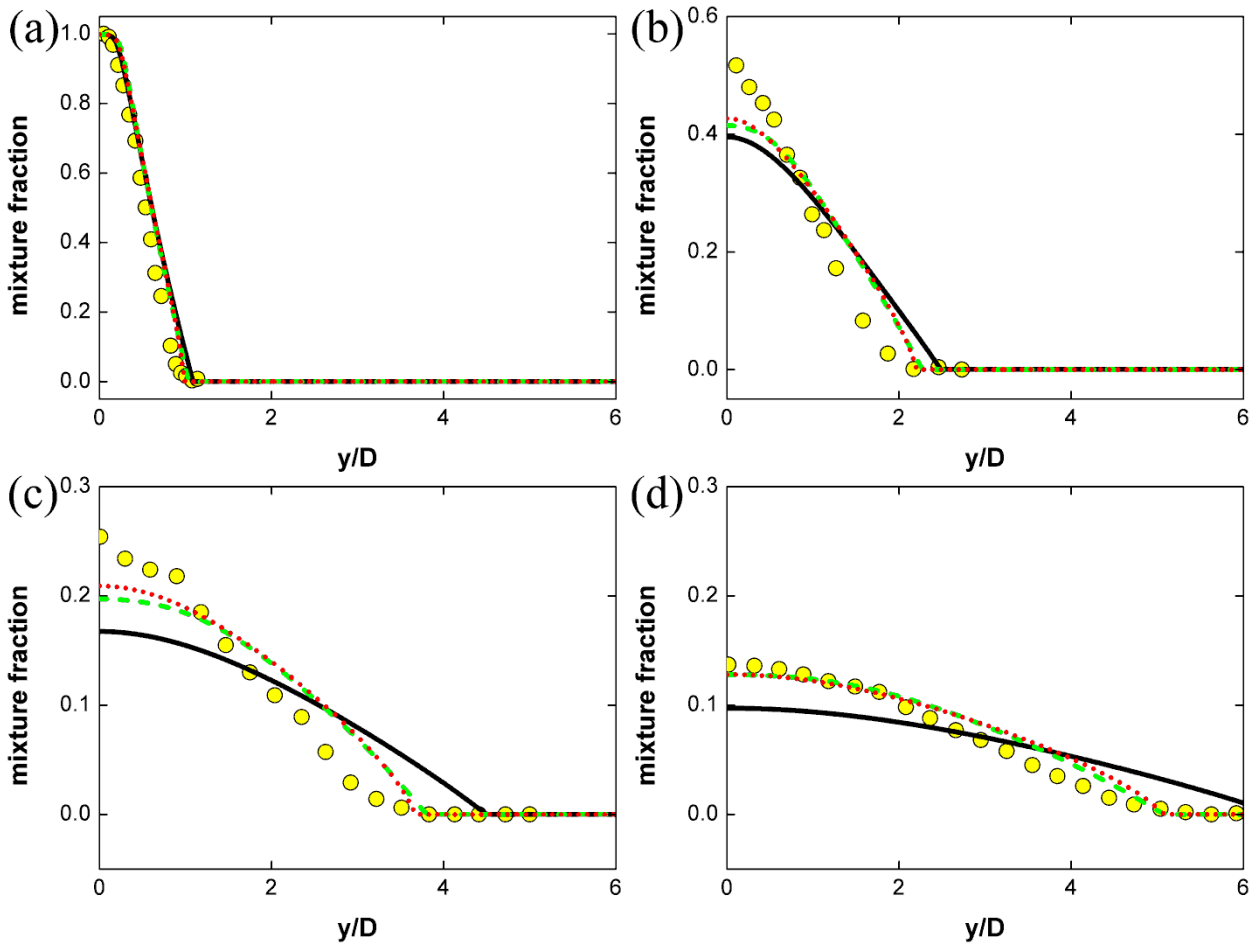

Figure 5-7: Radial profiles of mixture fraction at different axial locations: (a) x/D = 4 ; (b) x/D = 15; (c) x/D = 30; (d) x/D = 50. ○ - experimental data; ▬ - RNG k-ε model; ▬ ▬ - Realizable k-ε model; ● ● ● ● ● - SST k-ω model.

Although the differences between the results obtained with the SST k-ω model and those obtained with the other two models are minor, the SST k-ω model again shows the best performance, closely followed by the Realizable k-ε model, which provides nearly identical results as the SST k-ω model. On the other hand, the RNG k-ε model shows considerable deviations in both axial and radial velocity profiles.

5.2.4.2 Modified SST k-ω model

As suggested by Barlow and Frank [44], it is important to adjust the turbulence model to match the velocity profiles of a jet flow in order to be able to compare different combustion kinetic models with experimental data. Moreover, different sets of model constants were suggested for different turbulence models to correctly simulate the spreading rate of round free jet flames [22, 42, 45]. The SST was selected as the base model because the original set of model constants for the SST k-ω model provided the best performance in the three tested models. Based on the work of Scott [46], the diffusion coefficients σ_{k2} and $\sigma_{\omega 2}$ corresponding to the free stream region of the SST k-ω model were adjusted to improve the model predictions with respect to the axial velocity and mixture fraction for the propane jet flow problem. A series of parameter studies showed that $\sigma_{k2} = 1.25$ and $\sigma_{\omega 2} = 0.645$ were the optimal values. Simulations of the non-reacting propane jet flow case were repeated using the modified SST k-ω model with the two parameters as described above.

Figure 5-8 compares the profiles of axial velocity and mixture fraction as function of the dimensionless axial coordinate calculated by the original SST k-ω model and the modified

SST k-ω model. The performance of the modified SST k-ω model is significantly better than that of the SST k-ω model despite the slight underprediction of the axial velocity and overprediction of the mixture fraction. Profiles of the axial velocity as function of the radial coordinate at different axial positions are also in much better agreement with the experimental data, see Figure 5-9.

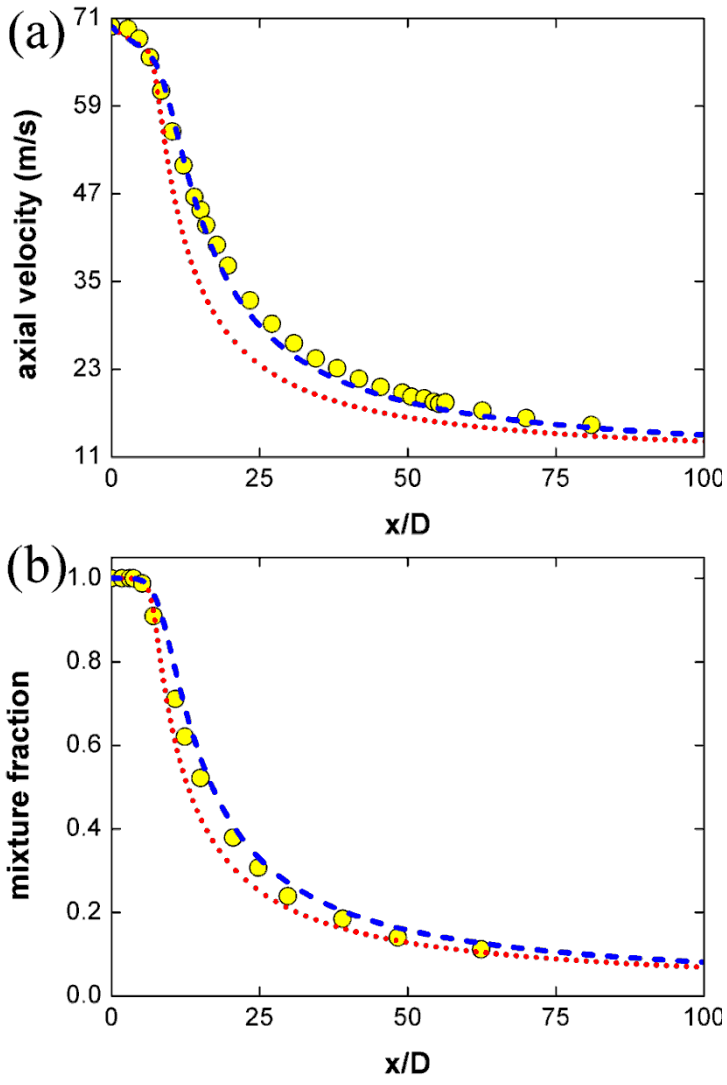

Figure 5-8: Profiles of (a) axial velocity and (b) mixture fraction along the centerline. ○ - experimental data; ● ● ● ● ● - SST k-ω model; ▬ ▬ - modified SST k-ω model.

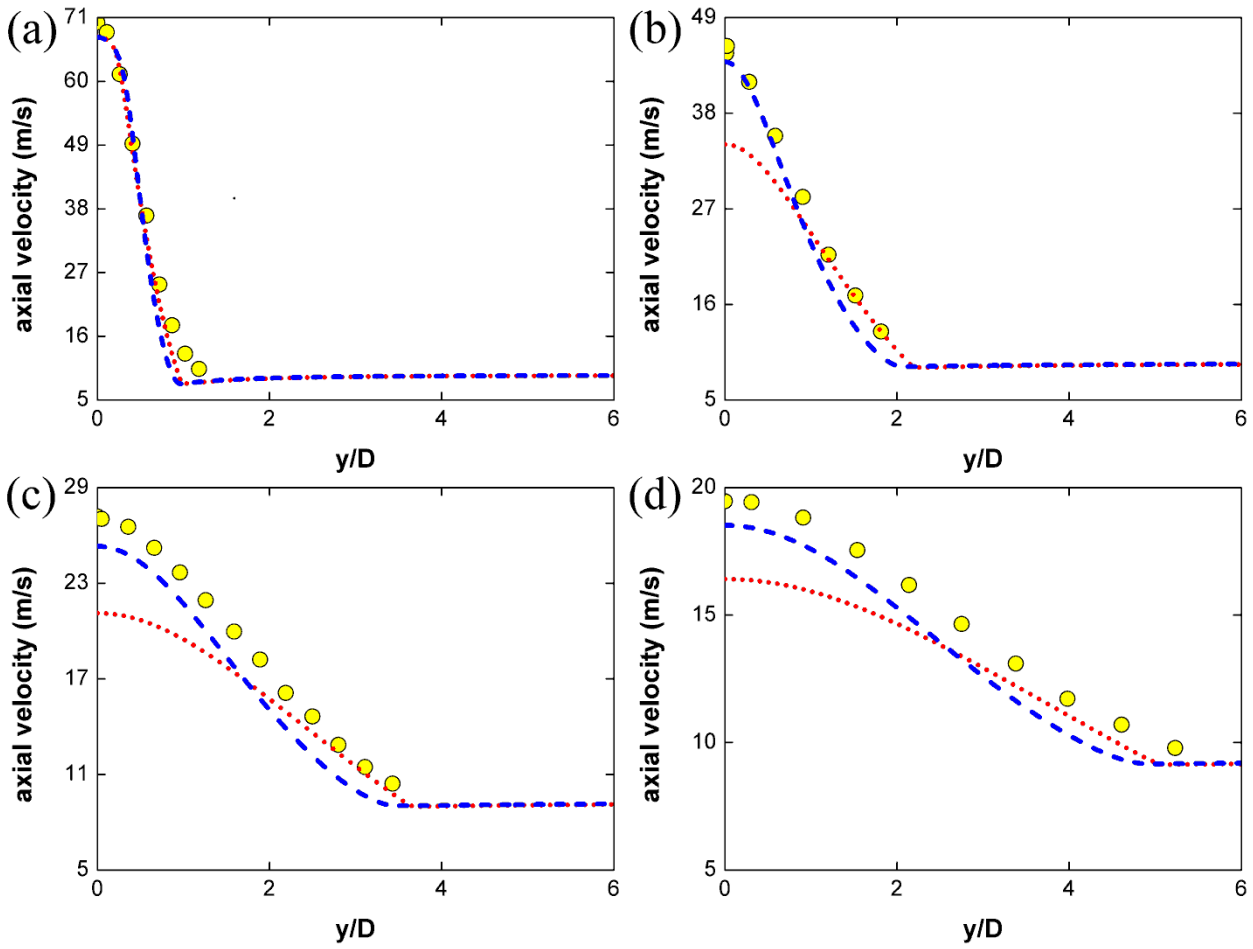

Figure 5-9: Radial profiles of axial velocity at different axial locations: (a) x/D = 4 ; (b) x/D = 15; (c) x/D = 30; (d) x/D = 50. ○ - experimental data; ● ● ● ● ● - SST k-ω model; ▬ ▬ - modified SST k-ω model.

The reason for the improvement can be mainly attributed to the fact that the modified coefficients cause less diffusion of the peak turbulent kinetic energy towards the edges of the shear layer, leading to lower turbulence in the core of the propane jet and therefore a narrower axial velocity distribution along the radial direction. This can be further verified by 2D fields of axial velocity and turbulent kinetic energy as shown in Figure 5-10.

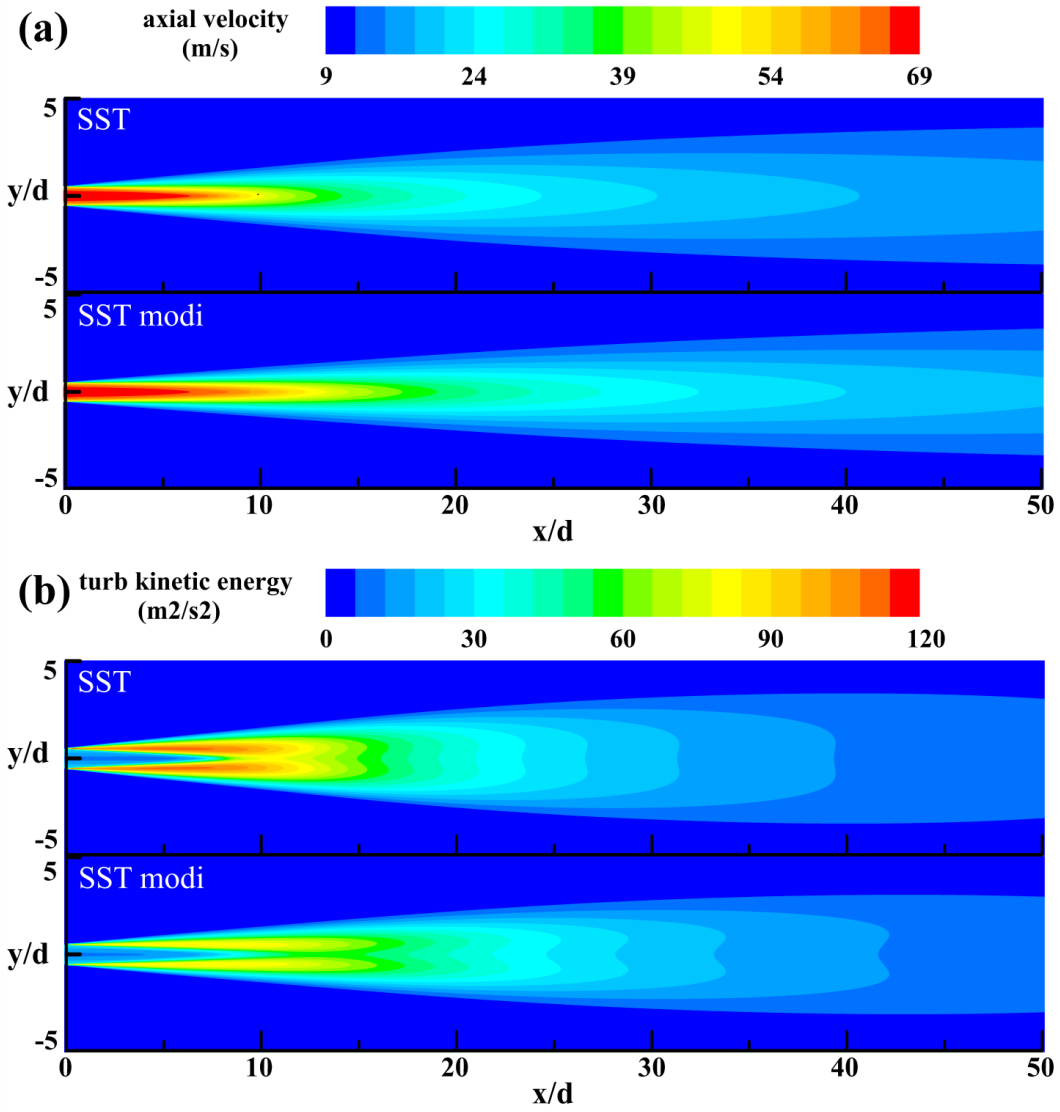

Figure 5-10: (a) axial velocity and (b) turbulent kinetic energy simulated using the SST k-ω model and the modified SST k-ω model.

So far it has been demonstrated that the modified SST k-ω model is able to accurately calculate turbulence characteristics of a non-reacting jet into co-flowing air. However, Scott stressed the necessity of utilizing several benchmark cases representing different types of flow to evaluate the performance of a modified turbulence model [46]. This is to ensure that the modification is not only beneficial for the flow problem of interest but also does not decimate the generality of the model in predicting other flow problems. Therefore, the modified SST k-

ω model was also validated by the 2D mixing layer flow presented before. Other complex flow problems are mentioned in the literature [46] but these are deemed less relevant for turbulent jet flames and therefore those cases were not considered to further validate the modified SST k-ω model.

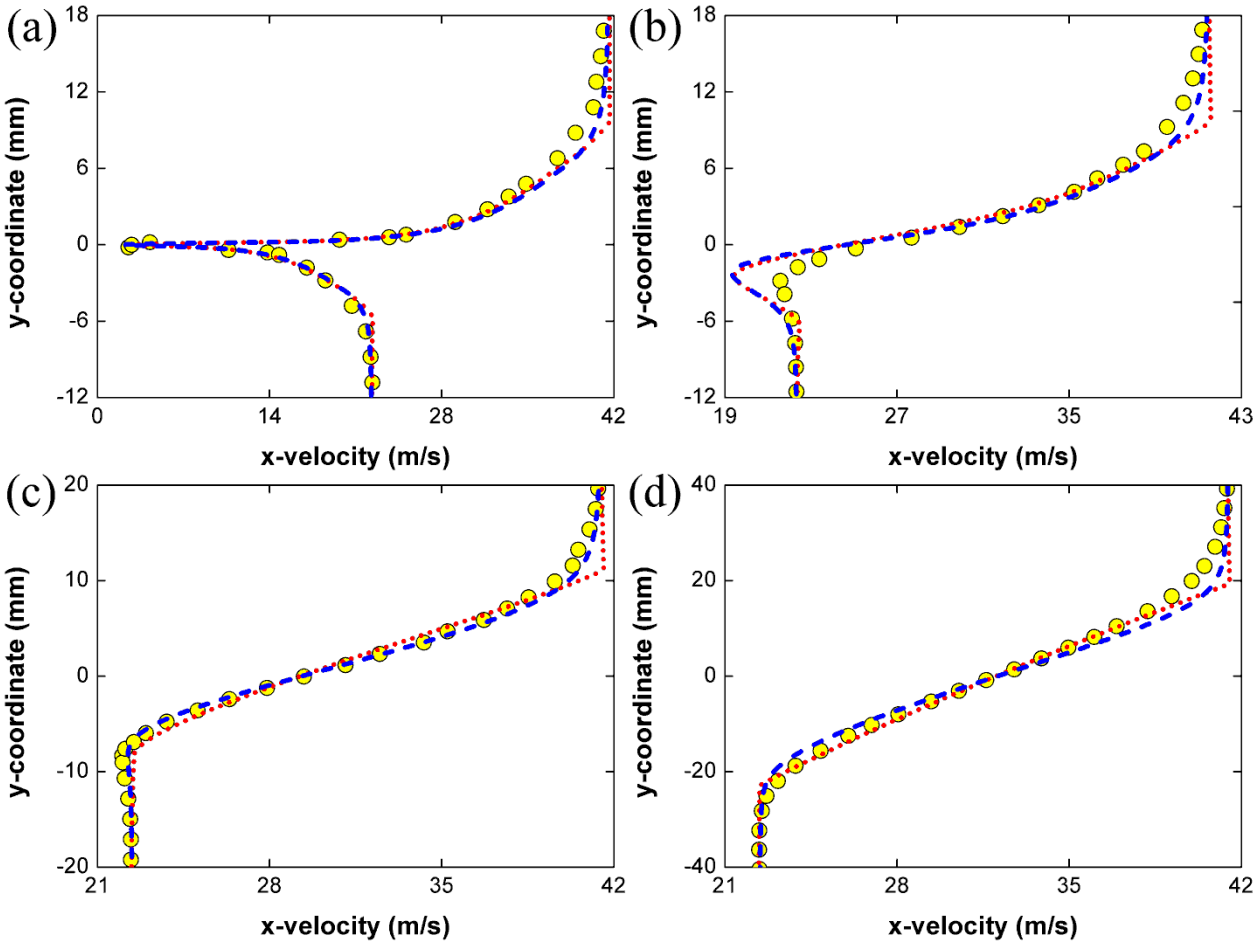

Figure 5-11: Profiles of x-velocity as a function of the y-coordinate at different x-locations: (a) x = 1 mm; (b) x = 50 mm; (c) x = 200 mm; (d) x = 650 mm. ○ - experimental data; ● ● ● ● ● - SST k-ω model; ▬ ▬ - modified SST k-ω model.

Results of the 2D mixing layer flow calculated by the modified SST k-ω model are compared to those of the SST k-ω and the experimental data. It is demonstrated in Figure 5-11 that

modifying the SST k-ω model slightly improves axial velocity predictions near the edges of the shear layer where velocity approaches the free stream velocities of the respective streams. As depicted in Figure 5-12, the modified SST k-ω model gives lower values for the specific turbulent shear stress, which improves the agreement with experimental data for x = 200 mm but reduces the agreement for x = 650 mm.

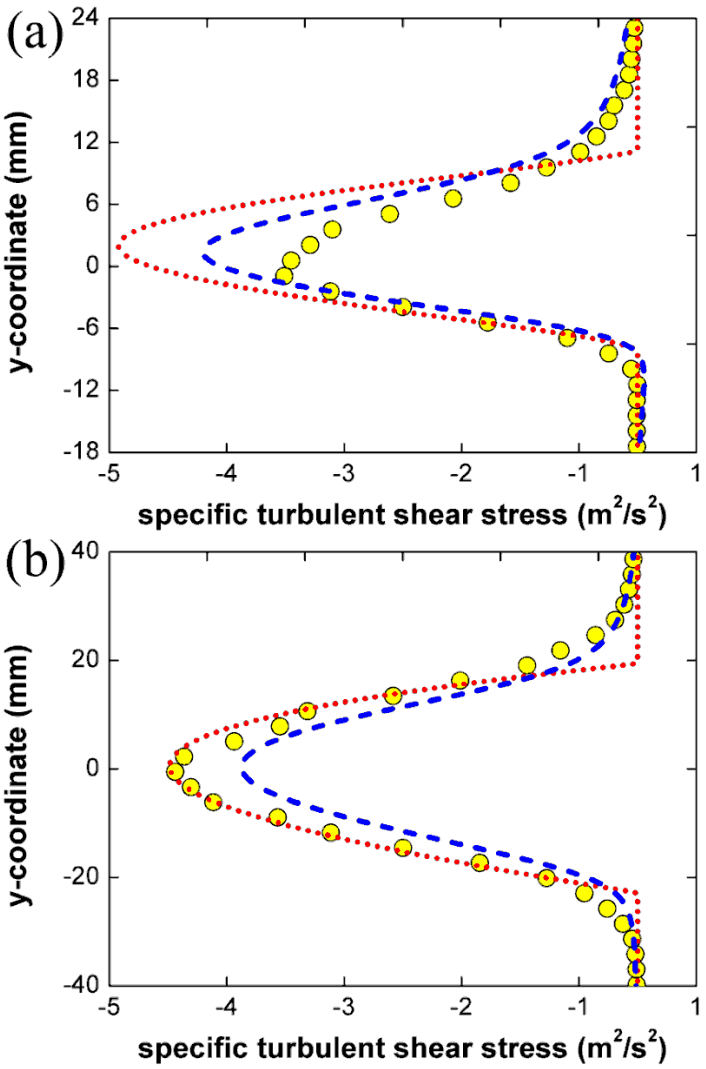

Figure 5-12: Profiles of specific turbulent shear stress as a function of y-coordinate at different x-locations: (a) x = 200 mm; (b) x = 650 mm. ○ - experimental data; ● ● ● ● ● - SST k-ω model; ▬ ▬ - modified SST k-ω model.

In conclusion, the validation of the modified SST k-ω model against experimental results of a 2D mixing layer flow case and a non-reacting propane jet into co-flowing air case shows that the model is a suitable turbulence model for CFD simulation of turbulent jet flames.

5.3 Validation for reacting flow

In this section, several reduced methane combustion mechanisms are validated against experimental data of a methane-air jet flame studied in the Sandia turbulent diffusion flame facility, i.e. the so-called Sandia flame D. The impact of the turbulence model, the radiation model and the reaction mechanism on model predictions of flow velocity, flame temperature and NO emission is investigated.

5.3.1 Experimental dataset

The Sandia flame D is a methane/air jet diffusion flame stabilized by a concentric and co-flowing pilot stream. To avoid any effect of the pilot on the measurements of temperature and mixture fraction, the chemical state of the pilot is equal to the that of the reacting mixture at equilibrium. [47]. The main jet consisting of 25% methane and 75% air by volume enters the wind tunnel at a velocity of 49.6 m s^{-1}. The concentric co-flowing pilot stream with a temperature of 1880 K acts as the ignition source and stabilizer for the jet flame. The configuration of the wind tunnel is identical to that of the non-reacting propane jet flow case shown in Figure 5-2. The only difference is that the non-reacting propane jet is replaced by a piloted methane jet depicted in Figure 5-13. The most important geometric dimensions and inlet conditions of the Sandia flame D facility are listed in Table 5-2. For a more detailed description of this flame such as the measurements and their uncertainties, the reader is referred to the work of Barlow and Frank [44]. A summary of the experimentally measured axial and radial profiles including axial velocity, flame temperature, and species

concentrations can be found on the TNF website [35]. It should be noted that for minor species, only NO and OH radicals are available in the dataset. For the inlet boundary condition, the velocity and turbulence intensity profiles are also available in literature [48].

Table 5-2: Dimensions and inlet conditions of the methane/air piloted jet facility.

Burner dimensions	
Tunnel cross section (m^2)	0.3×0.3
Tunnel length (m)	2
Main jet inner diameter (10^{-3} m)	7.2
Pilot annulus inner diameter (10^{-3} m)	7.7
Pilot annulus outer diameter (10^{-3} m)	18.2
Burner outer wall diameter (10^{-3} m)	18.9
Main jet inlet conditions	
Main jet velocity (m s^{-1})	49.6
Main jet temperature (K)	294
Reynolds number	22400
Composition (vol.%)	
CH_4	0.25
Air	0.75
Pilot inlet conditions	
Pilot velocity (m s^{-1})	11.4
Pilot temperature (K)	1880
Composition (vol.%)	
N_2	7.342×10^{-1}
O_2	5.40×10^{-2}
O•	7.47×10^{-4}
H_2	1.29×10^{-4}
H•	2.48×10^{-5}
H_2O	9.42×10^{-2}
CO	4.07×10^{-3}
CO_2	1.098×10^{-1}
OH	2.8×10^{-3}
NO	4.8×10^{-6}
Wind tunnel inlet conditions	
Co-flowing air velocity (m s^{-1})	0.9
Co-flowing air temperature (K)	291
Composition (vol.%)	
N_2	0.79
O_2	0.21

Figure 5-13: Sandia flame D with a close-up of the pilot flame.

5.3.2 Modeling approach

Due to the relatively simple configuration and high Reynolds number, a lot of numerical studies have considered the Sandia flame D as a benchmark case to investigate the accuracy of different combustion kinetic models [20, 23, 42, 45, 49]. A two-dimensional computational domain can be established to simulate the flame because of its axisymmetry, which considerably reduces the computational cost associated with testing different combustion kinetic mechanisms. Therefore, the same set of governing equations as in section 5.2.2 are used for simulating the Sandia flame D. One difference is that the R_i in equation (5.4) is enabled to account for construction/destruction of species due to chemical reactions and that the energy source term S_E in equation (5.3) is enabled to account for the enthalpy of the chemical reactions. Molecular viscosity of the gas mixture is calculated using kinetics theory. Detailed information on the calculation is documented in Appendix B.

Computational fluid dynamic simulations of the Sandia flame D were performed using the commercial finite volume package ANSYS Fluent 14.5 [43] in which the conservation equations for global mass, momentum, energy and species are solved. Multiple reduced combustion mechanisms and multiple strategies for radiation modeling, which are discussed in the next following sections in details, were implemented via user-defined functions (UDFs) in ANSYS Fluent. The pseudo-steady state assumption was applied to the radicals in the combustion mechanisms. A computational domain of 20D × 80D suggested by Cao and Pope [45] was used in the present work. Grid refinements were also performed and a final gird size of 136,929 was found to be sufficient to meet the following criteria: 1) the residuals for all conservation equations were lower than 10^{-4}, except for the energy conservation equation where the residual criterion was set to 10^{-6} and 2) the flow variables such as temperature and species concentrations at the outlet did not change in subsequent iterations. The final gird size of the Sandia flame D case is.

5.3.3 Combustion kinetics

Various kinetic mechanisms for methane/air combustion have been developed by different research groups [50-54]. Despite their high accuracy in predicting the concentrations of both species and radicals, coupling the complete mechanisms with three-dimensional computational fluid dynamic simulations is prohibitively expensive due to the large number of species and reactions associated with these detailed kinetic mechanisms. Hence the detailed kinetic mechanisms are often reduced to mechanisms with significantly less species and reactions but that are still capable of capturing the most important trends in the combustion mechanism and that combine well with turbulence-chemistry interaction models. Development of the above-mentioned mechanisms are usually based on pseudo-steady state assumption (PSSA). Although the accuracy of the detailed mechanism based on which the

reduced mechanism is established, determines the best performance it can achieve, the reduced mechanisms can still be greatly affected by the selection of the PSS species in the course of the model simplification. Hence it is useful to validate these reduced mechanisms based on experimental data from benchmark turbulent combustion cases. In this section, the well-known Sandia flame D was simulated with four reduced methane combustion mechanisms that include NO_x chemistry.

(a) A 12-step, 16-species reduced mechanism developed by Chen [55] based on GRI-Mech 2.11 [53], referred to as "ChenCH4".

(b) A 16-step, 19-species augmented reduced mechanism (ARM) [56] based on GRI-Mech 2.11, referred to as "ARM2". This model was also used to simulate the Sandia flame D by Cao and Pope and showed superior performance compared to other reduced mechanisms [45].

(c) A 17-step, 21-species reduced mechanism based on GRI-Mech 3.0 [54] from the work of Lu and Law [57], referred to as "Lu21". This model is used as a representative of GRI-Mech 3.0 to compare the performance of the reduced kinetics based on the two versions of the Gas Research Institute (GRI) family. The GRI mechanisms, which was designed to model natural gas combustion including NO formation and reburn chemistry, were developed by research groups led by Frenklach from University of California, Berkeley and Bowman from Stanford University.

(d) A 35-stpe, 39-species reduced mechanism for methane/ethylene combustion by Luo et al [58] based on the USC Mech-II [52] grafted with the NO_x sub-mechanism in GRI-Mech 3.0 with updated reaction parameters for prompt NO formation, referred to as "C1C2NO".

5.3.4 Turbulence-chemistry interaction

For turbulent combustion processes, a larger number of chemical reactions take place for which the characteristic time scales vary over several orders of magnitude. Depending on the reaction rate relative to the mixing rate, reactions can be classified as controlled by the intrinsic reaction rate, the mixing rate or by both. Hence a mixing model is required to fully consider the interactions between chemistry and turbulence. In this chapter, the eddy dissipation concept (EDC) model [59] is used. This model has been successfully applied to model many turbulent reaction problems [4, 21, 22, 49]. It is based on the energy cascade model and the assumption that molecular mixing and chemical reactions occur in so-called fine structures. The characteristic length and velocity scales of these fine structures are of the same order of magnitude as the Kolmogorov scales [60]. The length fraction of the flow occupied by the fine structures is expressed as follows:

$$\gamma = \frac{2}{3}\left(\frac{3C_{D2}}{4C_{D1}^{1}}\right)^{1/4}\left(\frac{\nu\varepsilon}{k^2}\right)^{1/4} \tag{5.16}$$

where $C_{D1} = 0.134$ and $C_{D2} = 0.5$ are the model constants. According to this definition, the volume fraction of the fine structures in is calculated as γ^3. The time scale for the mass transfer between the fine structures and the surrounding is given in equation (5.17).

$$\tau = \left(\frac{C_{D2}}{3}\right)^{1/2}\left(\frac{\nu}{\varepsilon}\right)^{1/4} \tag{5.17}$$

Each of the fine structures are assumed to react as a perfectly stirred reactor where the rate of chemical reactions can be calculated by integrating a system of non-linear ordinary differential equations consisting of conservation equations of mass, energy and species over the time scale τ. As the temperature and species concentrations for this calculation are obtained from the mean value stored at the center of each computational cell instead of the

local value prevailing at the fine structure level, the averaged source terms R_i in the species conservation equation (5.4) is computed as follows:

$$R_i = \frac{\rho\gamma^2}{\tau(1-\gamma^3)}(Y_i^* - Y_i) \tag{5.18}$$

where Y_i^* is the species mass fraction in the fine structure after reacting over time τ. It is calculated based on numerical integration of combustion reaction kinetics over time τ using temperature, pressure, and mass fraction of all species in the volume fraction γ^3 of the fine structure of the current cell. Since the species conservation equations are stiff and their integration is computationally expensive, the in-situ adaptive tabulation (ISAT) algorithm [61] was adopted in the present study to accelerate the calculation of the chemical reaction rates. The resulting Y_i^* is then used to determine the net reaction rate in the cell using equation (5.18). ISAT stores and retrieves the results of the integration of chemical reaction that includes a sensitivity analysis. When ISAT receives an integration request, one of three actions is performed: (1) if the new condition is within a region of accuracy centered around the initial conditions to a stored integration, ISAT will simply retrieval the result of the stored integration to avoid repetition; (2) ISAT will perform an integration when the new condition is outside of the region of accuracy, however if the subsequent integration shows that the new integration is within a specified error tolerance, the range of the accurate region of initial condition will be extended; (3) if new condition is still outside of the region of accuracy after integration, ISAT will grow by adding this new condition.

5.3.5 Radiation models

NO_x levels in turbulent methane flames depend mainly on the local temperature due to the dominance of the thermal NO_x mechanism . A moderate increase in flame temperature of 50-100 K can dramatically increase the NO production rate [42]. As heat loss due to radiation to

the environment is significant in the Sandia flame D case, its effect should be incorporated in the CFD simulations to be able to accurately predict the flame temperatures and thus the NO_x emission. Raman et al. demonstrated that incorporating radiative heat losses in the Sandia flame D simulation can decrease the peak flame temperature by 200 K [42]. Cao and Pope found that including radiative heat losses decreases the simulated NO peak up to 20%.However, earlier work by Tang et al. contradicts this statement as they found that including radiative heat losses has a negligible influence on the NO formation in the Sandia flame D [62]. Most of the previous studies implemented an optical thin model for the flue gas radiative absorption coefficient, which was found to overpredict the radiative heat losses of in this particular case [45]. As literature agrees on the importance of radiative heat transfer in the simulation of the Sandia flame D but disagrees on the most appropriate simulation strategy, a comprehensive study of the impact of the radiation model is required.

5.3.5.1 Optical thin model

The optical thin model for the flue gas radiative absorption coefficient assumes that the optical thickness of the flame is so small that the radiation emitted from the high temperature region will pass through the surroundings without being reabsorbed. In this case the heat loss term is straightforwardly given by equation (5.19) [63].

$$Q = 4\sigma(T^4 - T_b^4)\sum_i (p_i a_{pi}) \tag{5.19}$$

where T_b is the background temperature of the flame case which is set to 291 K, i.e. the temperature of the co-flowing air. Four gas-phase emitting species H_2O, CO_2, CO and CH_4 are included in this model, their Planck mean absorption coefficients a_{pi} were calculated by RADCAL [64] and expressed as polynomial as function of the temperature. The fitted parameters are summarized in Table 5-3.

Table 5-3: Expressions for Planck mean absorption coefficients [63].

CO_2 and H_2O

$$a_p = c_0 + c_1 T_r + c_2 (T_r)^2 + c_3 (T_r)^3 + c_4 (T_r)^2 + c_5 (T_r)^5$$

	H_2O	CO_2
c_0	-0.23093	18.741
c_1	1.12390	-121.310
c_2	9.41530	273.500
c_3	-2.99880	-194.050
c_4	0.51382	56.310
c_5	-1.86840E-5	-5.8169

CH_4

$$a_p = 6.6334 - 3.5686E - 3T + 1.6682E - 8T^2 + 2.5611E - 10T^3 - 2.6558E - 14T^4$$

CO

	$300 \leq T \leq 750\ K$	$750 \leq T \leq 2500\ K$
c_0	4.7869	10.09
c_1	-0.06953	-0.01183
c_2	2.95775E-4	4.7753E-6
c_3	-4.25732E-7	-5.87209E-10
c_4	2.02894E-10	-2.5334E-14

$T_r = 1000/T$
Valid only for temperature between 300 K and 2500 K.

5.3.5.2 Weighted sum of gray gas model

The weighted sum of gray gas model (WSGGM) represents a non-gray gas by a number of fictitious gray gases N, each of them having a constant absorption coefficient κ_i and a temperature dependent weight factor a_i. Hence, the total emissivity over a path length L can be expressed as:

$$\varepsilon = \sum_{i=0}^{N-1} a_i(T)(1 - e^{-\kappa_i L}) \tag{5.20}$$

To take the spectral window into account, the absorption coefficient for the first fictitious gas $i = 0$ is zero so the weight factor for $i = 0$ is evaluated using the following expression guaranteeing that the total emissivity is limited to unity.

$$a_0 = 1 - \sum_{i=1}^{N-1} a_i \tag{5.21}$$

It is common to represent the temperature dependence of a_i via a polynomial function:

$$a_i = \sum_{j=1}^{M} b_{i,j} T^{j-1} \tag{5.22}$$

Values of $b_{i,j}$ and κ_i can be found by fitting equation (5.20) to the experimental total emissivity curve at different partial pressure ratios of the absorbing species. The model developed by Smith et al. [65] including H_2O and CO_2 as participating species is adopted in this work. The absorption coefficient κ calculated from WSGGM is used in the gray gas form of the discrete ordinates (DO) model for the radiative transfer equation (RTE).

$$\nabla \cdot (I(\vec{r}, \vec{s})\vec{s}) + (\kappa + \sigma_s) I(\vec{r}, \vec{s}) = \kappa n^2 \frac{\sigma T^4}{\pi} + \frac{\sigma_s}{4\pi} \int_0^{4\pi} I(\vec{r}, \vec{s}') \Phi(\vec{s}, \vec{s}') d\Omega' \tag{5.23}$$

5.3.5.3 Five-band model

The five-band model is developed and validated in chapter 2. The non-gray properties of the flue gas are described by dividing the wavelength spectrum into five regions, i.e. four absorption bands and one transparent band. In each of the absorption bands, the spectral absorption coefficient κ_i is expressed as a function of temperature and concentration of the participating species H_2O and CO_2. In the transparent band, the spectral absorption coefficient κ_i is zero.

5.3.6 Results and discussion

5.3.6.1 Effect of the turbulence model

One important feature of the Sandia flame D is that it has a small degree of local extinction due to strong turbulence, making it a good case for validating the turbulence model as well. Therefore the SST k-ω model and the modified SST k-ω model discussed in section 5.2.4.2 were compared to check whether the modification of the model constants is beneficial when simulating this turbulent jet flame. The C1C2NO kinetic mechanisms was used in these simulations without considering radiation.

Figure 5-14 clearly shows that the modified SST k-ω model results in a narrower but longer high-velocity core. The slower mixing of the jet with the co-flowing air leads to delayed ignition of the fuel and hence a longer flame. Figure 5-15 shows the profiles of temperature and major species along the centerline of the flame. The peak and the valley of the temperature and species concentrations are moved downstream towards the right positions when changing from the SST k-ω model to the modified SST k-ω model, indicating that the rate of turbulent mixing is well predicted by the modified SST k-ω model. It is worth noting that the profiles of other species are also in good agreement with the experimental measurements.

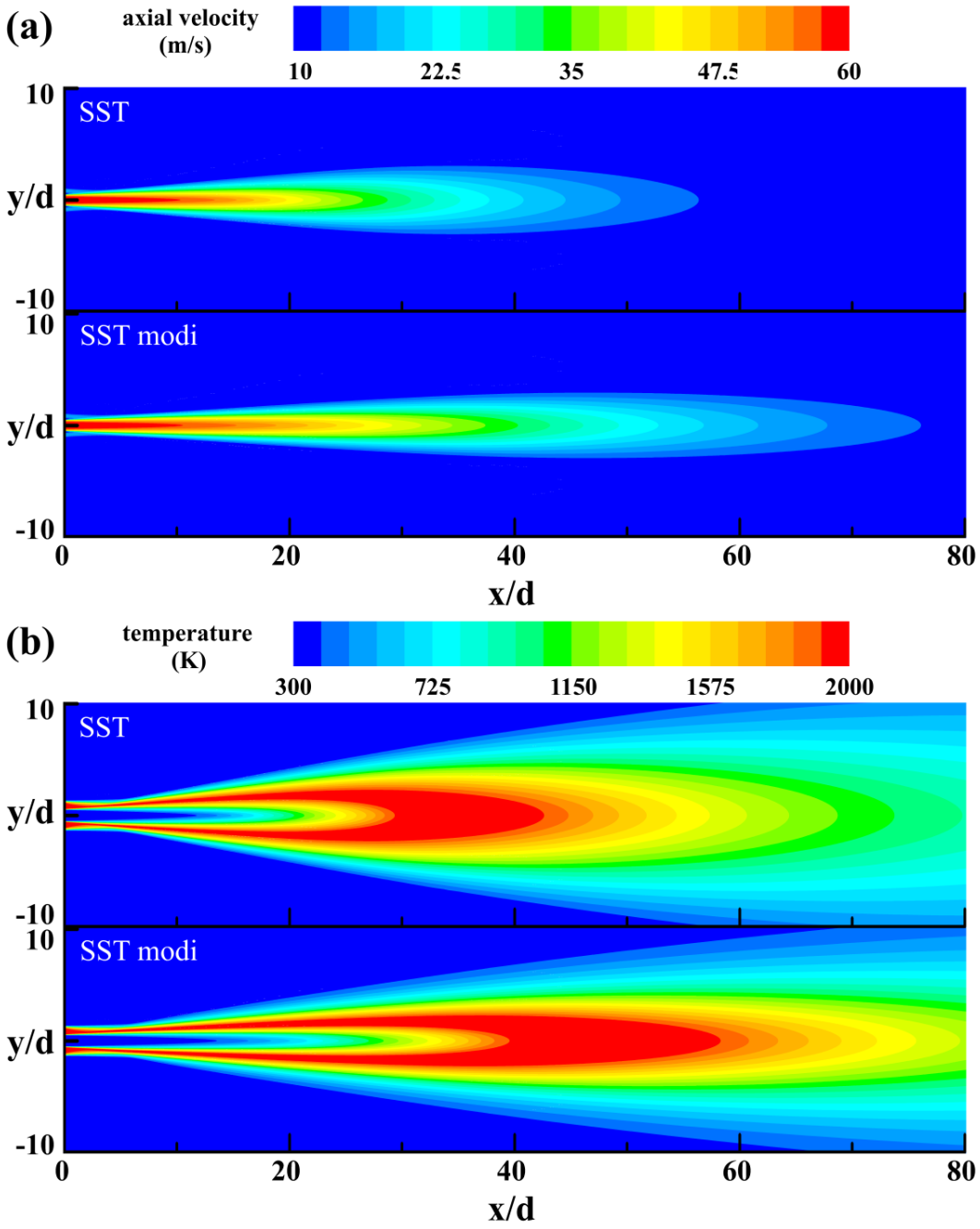

Figure 5-14: (a) axial velocity and (b) temperature for the Sandia flame D simulated using the SST k-ω model and the modified SST k-ω model.

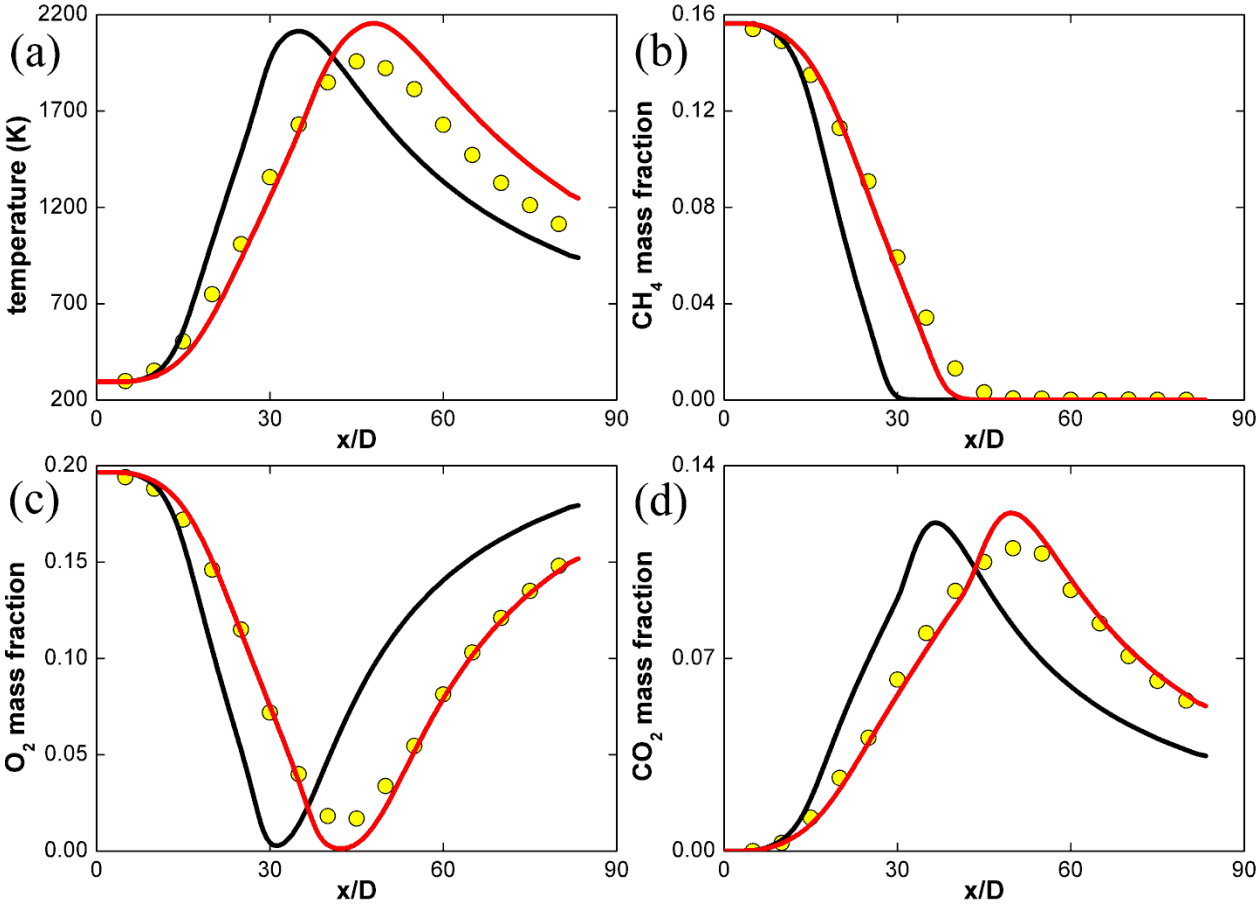

Figure 5-15: Profiles of (a) temperature; (b) CH_4 mass fraction; (c) O_2 mass fraction; (d) CO_2 mass fraction along the centerline. ○ - experimental data; ▬ - SST k-ω model; ▬ - modified SST k-ω model.

5.3.6.2 Effect of the radiation model

Simulations disregarding radiation and accounting for radiation via the optical thin model, the weighted sum of gray gas model, and the five-band model were carried out respectively using C1C2NO as the combustion mechanism. The modified SST k-ω model was used to describe turbulence in all cases.

Figure 5-16 shows the centerline profiles of temperature and species concentrations calculated by different models. The case disregarding radiation predicts the highest flame temperature. All cases considering radiation predict a lower flame temperature, especially in the region

x/D > 40 where CH_4 is almost completely consumed. The WSGGM and the five-band model predict nearly the same temperature profiles, which are somewhat higher than those of the optical thin model. This can be explained by the fact that the optical thin model considers the thermal radiation emitted from two more species (CH_4 and CO) compared to the two other radiation models. Also, it assumes that the radiation emitted from the high temperature region of the flame will not be reabsorbed by the colder surrounding gas.

The mass fractions of the major species are not very sensitive to the applied radiation model. However, it can still be observed that the mass fraction of CH_4 decreases slightly faster using the WSGGM and the five-band model. The explanation for this is that these two models consider CO_2 and H_2O as both emitting and absorbing species. Hence the radiative thermal power emitted from the flame center can be transferred upstream and absorbed by the upstream flow as long as CO_2 and H_2O are produced. The absorbed heat results in a higher predicted upstream temperature for the WSGGM and the five-band model, which can be seen in Figure 5-16 (a) as well. This in turn accelerates the combustion reactions and results in faster CH_4 and O_2 consumption and higher CO_2 and H_2O concentration as shown in Figure 5-16 (b), (c) and (e). For NO emission, it is observed that considering radiation reduces the predicted NO profile by nearly a factor of 2. Therefore neglecting radiative heat transfer, even in a lab-scale flame, is not acceptable as it will cause a large discrepancy in the NO_x calculation.

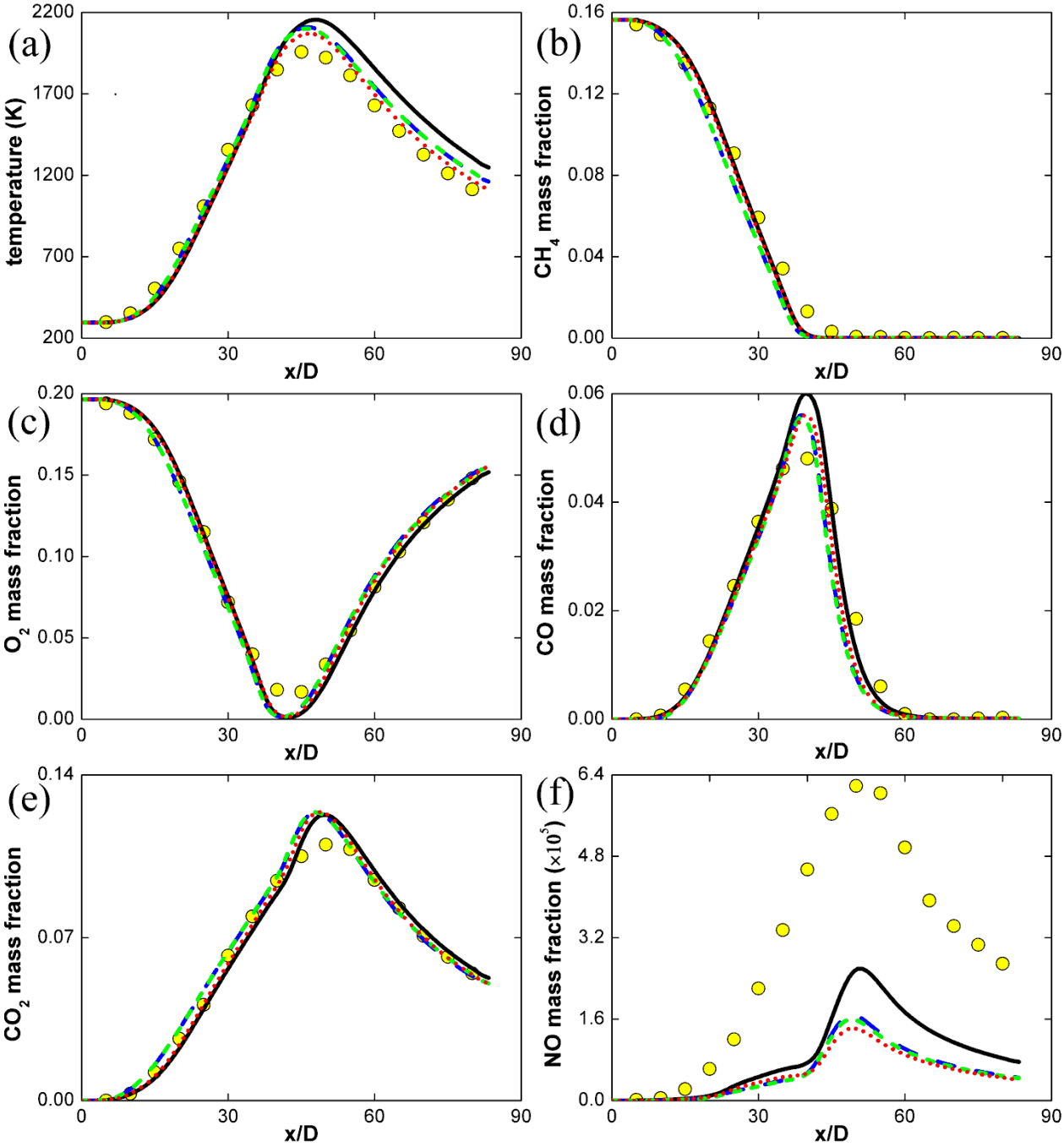

Figure 5-16: Centerline profiles of (a) temperature; (b) CH_4 mass fraction; (c) O_2 mass fraction; (d) CO mass fraction; (e) CO_2 mass fraction; (f) NO mass fraction. ○ - experimental data; ——— - no radiation; ——— - WSGGM; - - - - five-band model; ····· - optical thin model.

Table 5-4 lists the heat loss and flame peak temperature calculated by the different radiation models. The experimental data for the heat loss is obtained from the work of Frank and Barlow [66]. The heat loss calculated by the optical thin model is nearly 2 times larger than the measurement, which is also the major cause of the lower predicted NO emission by this model. This was already observed in literature [22, 45]. The WSGGM and the five-band model predict the heat loss reasonably well, with the flame peak temperature calculated by the five-band model agreeing slightly better with the experimental value compared to that of the WSGGM. Although lower simulated flame peak temperatures are obtained when considering radiative heat transfer, there is still about 150 K difference between the model predictions and the experimental results, which may be attributed to the inaccuracy of the turbulence-chemistry interaction model, i.e. the EDC model applied in this work.

Table 5-4: Simulation results for the Sandia flame D using different radiation models.

	Heat loss (%)	Flame peak temperature (K)
Experiment [66]	5.10	1957
No radiation	0.00	2156
Optical thin model	10.26	2070
WSGGM	5.56	2109
Five-band model	5.56	2102

5.3.6.3 Effect of the kinetic mechanism

The four reduced kinetic mechanisms presented in section 5.3.3 are compared for the Sandia flame D case. The modified SST k-ω model and the five-band model are applied in the simulation to account for turbulence and radiative heat transfer respectively. The centerline profiles of flame temperature and species concentrations are depicted in Figure 5-17. All reduced mechanisms give very similar results for temperature and major species, which are

also in good agreement with the experimental data. However, all kinetic mechanisms overpredict the mass fraction of the OH radical. Nonetheless, Raman et al. [42] showed that the OH mass fraction in the Sandia flame D is accurately predicted by GRI-Mech 2.11, GRI-Mech 3.0 and a 16-species reduced mechanism based on GRI-Mech 2.11. Therefore the reason for this overprediction cannot be attributed to the reduction of the detailed mechanism. Lysenko et al. [49] observed a large overprediction of the OH mass fraction when using the EDC model to describe turbulence-chemistry interaction. A comparison in which the β-PDF model was used provided a much lower OH mass fraction peak.

There are large discrepancies in the mass fraction of NO simulated by the different mechanisms. Lu21 overpredicts the NO mass fraction by a factor of 2. This was also observed in the work of Cao and Pope [45] using the detailed mechanism GRI-Mech 3.0, the base mechanism for Lu21. Other studies have shown that GRI-Mech 3.0 results in higher NO formation due to the overestimated production of the CH radical from C_2H_2, which has an important effect on prompt-NO formation. This is more important in rich methane flames as it promotes the CH radical from C_2H_2 [67, 68]. Hence the reason for the inaccurate NO calculation using the Lu21 mechanism can be attributed to the inherent deficiency of the original mechanism GRI-Mech 3.0. The C1C2NO mechanism conversely underpredicts the NO formation, which is also due to its base mechanism, i.e. USC Mech-II grafted with the NO sub-mechanism from GRI-Mech 3.0 [58]. However, this time the blended mechanism predicts lower NO emission. Among the four kinetic mechanisms, ChenCH4 and ARM2, both reduced from the GRI-Mech 2.11 mechanism, yield the most reasonable results, with the ChenCH4 being slightly better than ARM2.

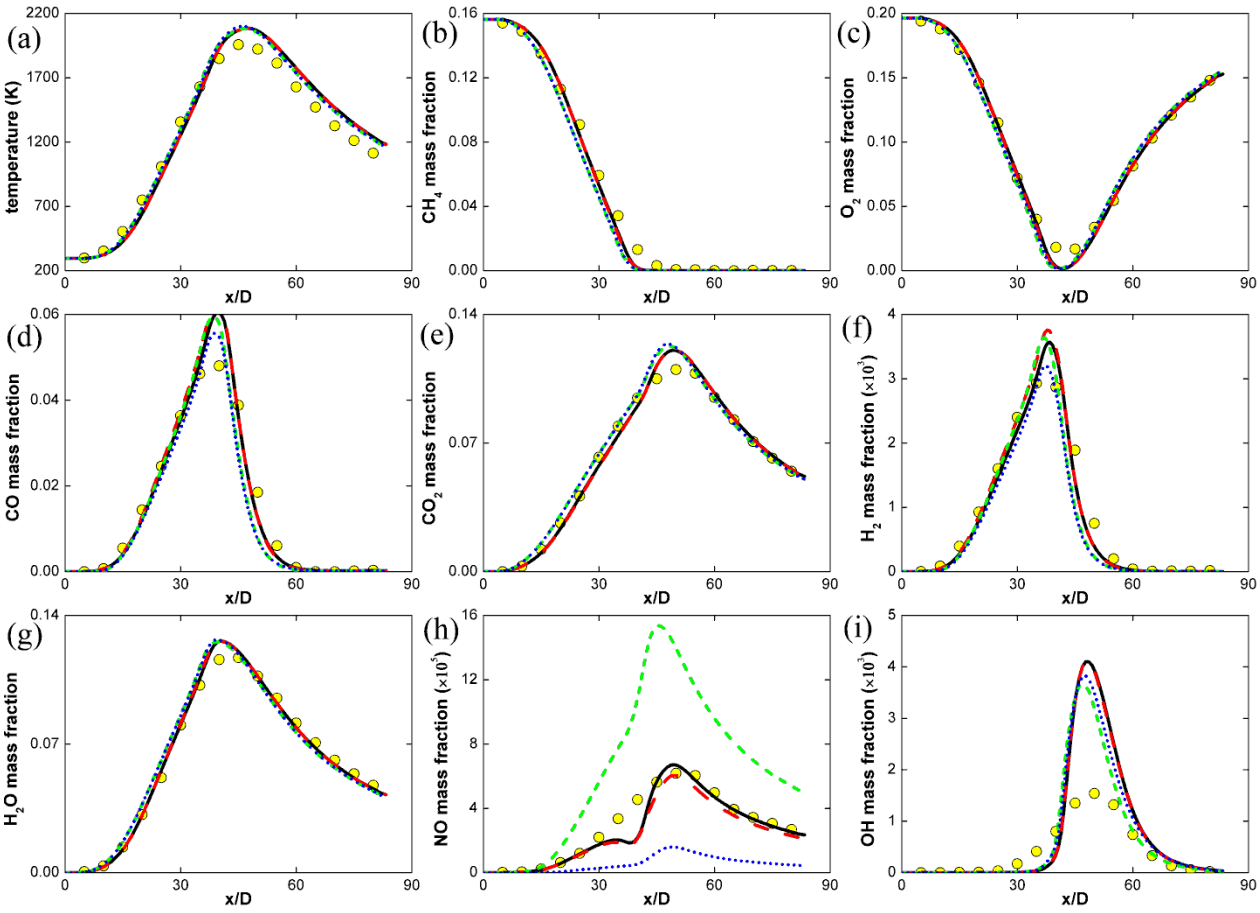

Figure 5-17: Centerline profiles of (a) temperature; (b) CH_4 mass fraction; (c) O_2 mass fraction; (d) CO mass fraction; (e) CO_2 mass fraction; (f) H_2 mass fraction; (g) H_2O mass fraction; (h) NO mass fraction; (i) OH mass fraction. ○ - experimental data; ——— - ChenCH4; ——— - ARM2; - - - - Lu21; ••••••••• - C1C2NO.

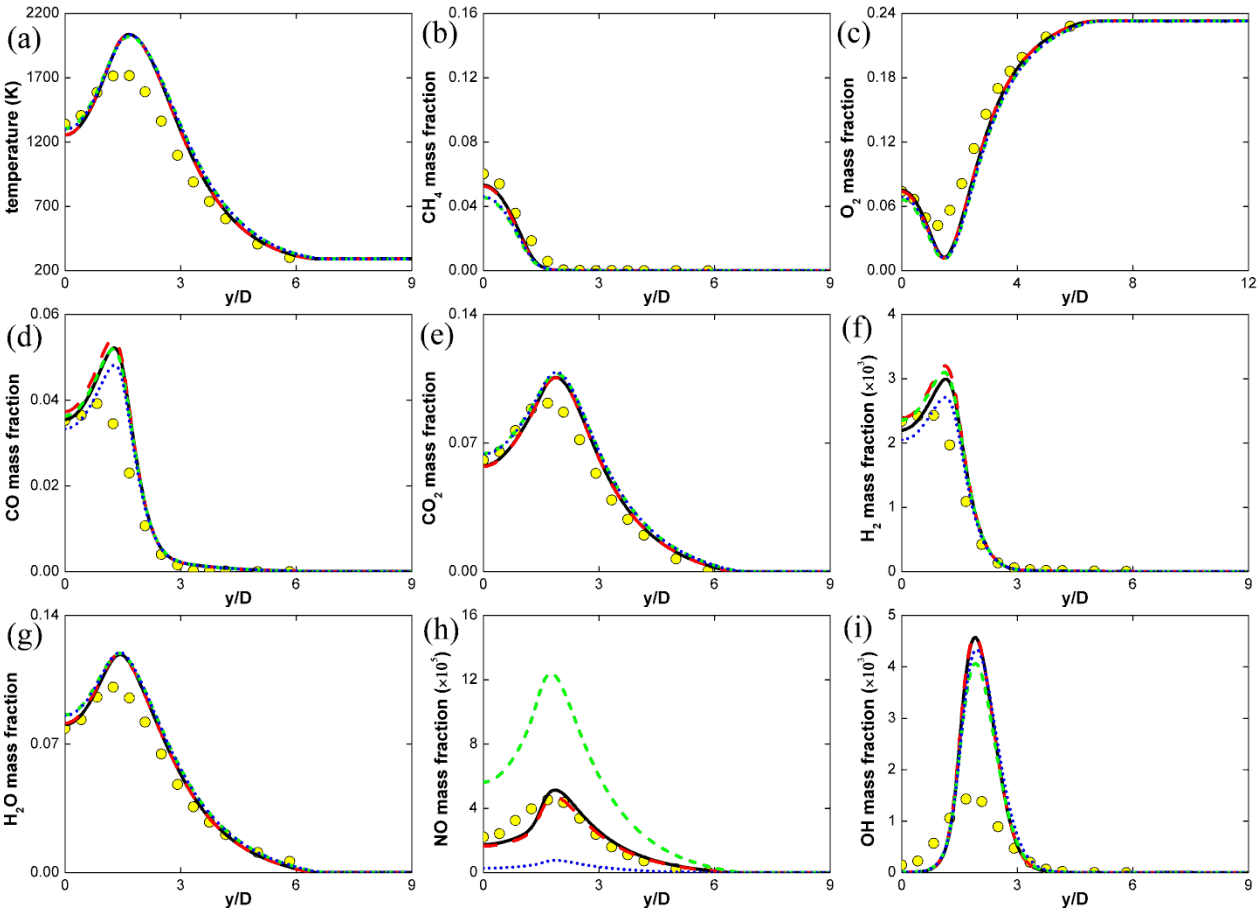

Figure 5-18: Radial profiles of (a) temperature; (b) CH_4 mass fraction; (c) O_2 mass fraction; (d) CO mass fraction; (e) CO_2 mass fraction; (f) H_2 mass fraction; (g) H_2O mass fraction; (h) NO mass fraction; (i) OH mass fraction at x/D=30. ○ - experimental data; ——— - ChenCH4; ——— - ARM2; - - - - Lu21; ••••••••• - C1C2NO.

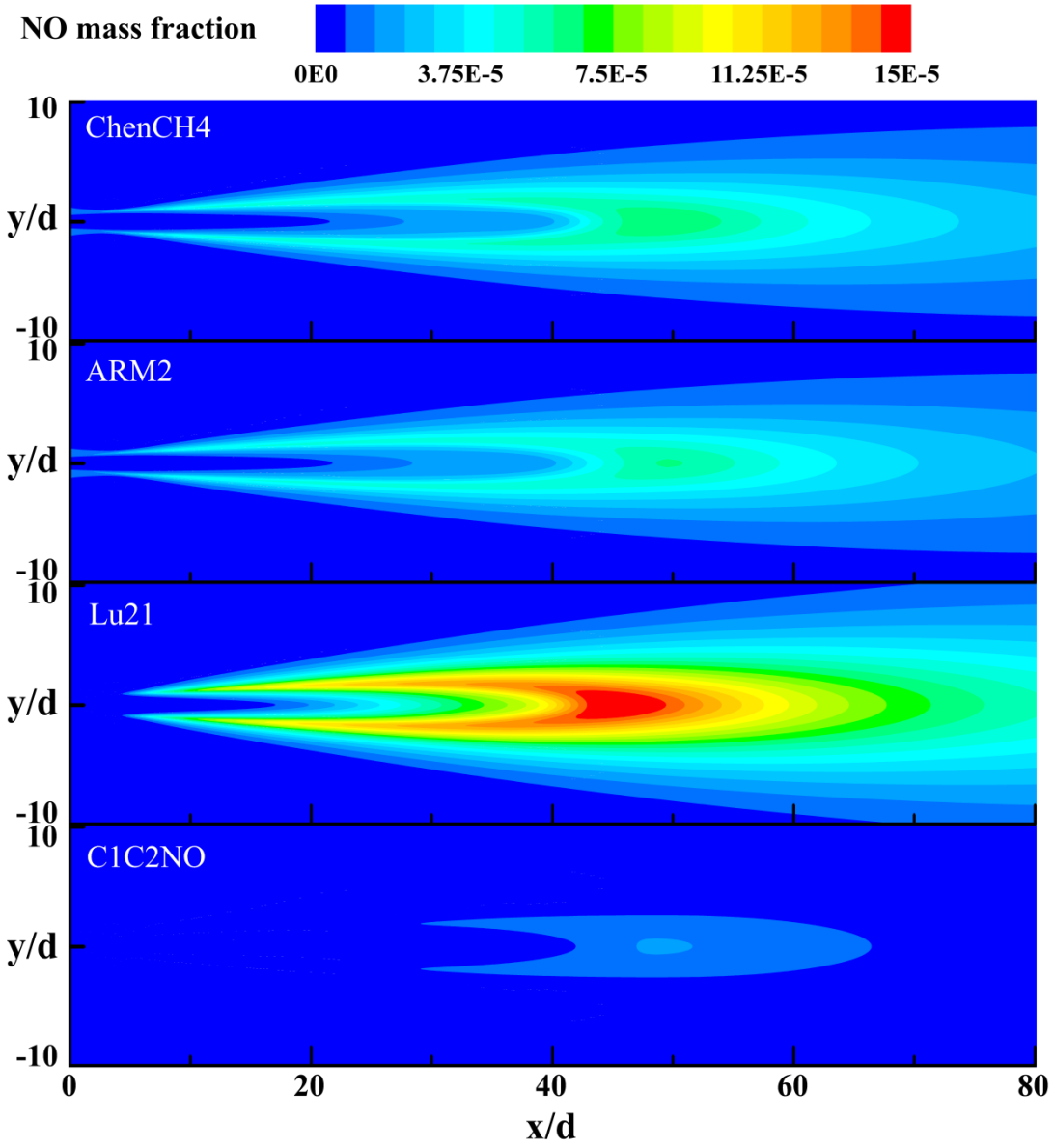

Figure 5-19: NO mass fraction for the Sandia Flame D calculated using different kinetic mechanisms.

Radial profiles of the flame temperature and species concentrations at different axial locations downstream to the flame jet exit are also in good agreement with experimental data. To avoid redundant information, only the ones at the axial location x/D = 30 are presented in Figure 5-18. Temperature and major species mass fractions agree well with measurements, the OH mass fraction is overpredicted by all mechanisms, NO emission is well captured by ChenCH4 and ARM2 while overprediction and underprediction are observed by Lu21 and C1C2NO.

Finally, a 2D representation of the NO mass fraction calculated using the different kinetic mechanism is depicted in Figure 5-19. The regions with a higher NO mass fraction are associated with higher temperatures, again indicating the importance of the thermal NO_x mechanism in a turbulent methane flame. Therefore both the ChenCH4 mechanism and the ARM2 mechanism are suitable for turbulent flame calculations with special interest in NO emission. The performance of ChenCH4 is slightly better than that of the ARM2.

5.4 Conclusions

In this chapter, a comprehensive study was carried out to investigate the effect of the turbulence model, the radiation model and the kinetic mechanism describing combustion on turbulent jet flame simulations. Two dimensional simulations of a mixing layer flow and a non-reacting round jet of propane into co-flowing air were performed for the validation of the turbulence model. The SST k-ω model with modified diffusion coefficients for free stream region outperforms the other two-equation models in modeling round jet flow. This turbulence model was hence applied to calculate a benchmark turbulent piloted methane/air diffusion flame (Sandia flame D) and proved to be able to provide results that agree well with the experimental data. The effect of radiative heat transfer on modeling the Sandia flame D was also evaluated by implementing three radiation models, among which the five-band model developed in chapter 2 showed the best performance. With respect to NO_x emissions, four reduced kinetic mechanisms describing combustion were compared. Good agreement between the calculations and the experimental data was obtained by the ChenCH4 and ARM2 mechanisms. In conclusion, a combination of the modified SST k-ω model, five-band radiation model, and the ChenCH4 or ARM2 kinetic mechanism provides a reliable and widely applicable modeling framework for new low NO_x burner designs.

References

[1] E. Charles, J. Baukal, E. Robert, The John Zink Combustion Handbook, John Zink Company LLC, Tulsa, Oklahoma, (2001).
[2] B. Jenkins, P. Mullinger, Industrial and Process Furnaces: Principles, Design and Operation, Elsevier Science, 2013.
[3] D.J. Brown, J. Ma, B.R. Adams, Development of an improved prediction model for chemical process furnaces, in: AIChE Spring National Meeting, New Orleans, LA (United States), 2003.
[4] G.D. Stefanidis, B. Merci, G.J. Heynderickx, G.B. Marin, CFD simulations of steam cracking furnaces using detailed combustion mechanisms, Comput Chem Eng, 30 (2006) 635-649.
[5] G. Hu, H. Wang, F. Qian, Y. Zhang, J. Li, K.M. Van Geem, G.B. Marin, Comprehensive CFD Simulation of Product Yields and Coking Rates for a Floor- and Wall-Fired Naphtha Cracking Furnace, Ind Eng Chem Res, 50 (2011) 13672-13685.
[6] D. Brown, P. Smith, B. Adams, Cracking furnace fireside modeling advances, in: Proceedings of the 6th Ethylene Producers' Conference, Atlanta, GA (United States), 1994.
[7] D.J. Brown, M.A. Cremer, P.J. Smith, R.T. Waibel, Fireside modeling in cracking furnaces, in: Proceedings of the 9th Ethylene Producers' Conference, Houston, TX (United States), 1997, pp. 159-193.
[8] A.J.M. Oprins, G.J. Heynderickx, Calculation of three-dimensional flow and pressure fields in cracking furnaces, Chem Eng Sci, 58 (2003) 4883-4893.
[9] G. Hu, H. Wang, F. Qian, K.M. Van Geem, C.M. Schietekat, G.B. Marin, Coupled simulation of an industrial naphtha cracking furnace equipped with long-flame and radiation burners, Comput Chem Eng, 38 (2012) 24-34.
[10] H. Guihua, W. Honggang, Q. Feng, Numerical simulation on flow, combustion and heat transfer of ethylene cracking furnaces, Chem Eng Sci, 66 (2011) 1600-1611.
[11] G.D. Stefanidis, B. Merci, G.J. Heynderickx, G.B. Marin, Gray/nongray gas radiation modeling in steam cracker CFD calculations, AIChE J, 53 (2007) 1658-1669.
[12] A. Habibi, B. Merci, G.J. Heynderickx, Impact of radiation models in CFD simulations of steam cracking furnaces, Comput Chem Eng, 31 (2007) 1389-1406.
[13] Y. Zhang, F. Qian, C.M. Schietekat, K.M. Van Geem, G.B. Marin, Impact of flue gas radiative properties and burner geometry in furnace simulations, AIChE J, 61 (2015) 936-954.
[14] G. Hu, C.M. Schietekat, Y. Zhang, F. Qian, G.J. Heynderickx, K.M. Van Geem, G.B. Marin, Impact of Radiation Models in Coupled Simulations of Steam Cracking Furnaces and Reactors, Ind Eng Chem Res, 54 (2015) 2453-2465.
[15] T. Pedot, B. Cuenot, E. Riber, T. Poinsot, Coupled Heat Transfers in a Refinery Furnace in View of Fouling Prediction, Journal of Heat Transfer, 138 (2016) 072101-072101.
[16] G.J. Heynderickx, M. Nozawa, Banded gas and nongray surface radiation models for high-emissivity coatings, AIChE J, 51 (2005) 2721-2736.
[17] G.D. Stefanidis, K.M. Van Geem, G.J. Heynderickx, G.B. Marin, Evaluation of high-emissivity coatings in steam cracking furnaces using a non-grey gas radiation model, Chem Eng J, 137 (2008) 411-421.
[18] G.J. Heynderickx, M. Nozawa, High-emissivity coatings on reactor tubes and furnace walls in steam cracking furnaces, Chem Eng Sci, 59 (2004) 5657-5662.
[19] S. Barendregt, M. van Goethem, I. Risseeuw, F. Alessio, T. Faravelli, A.A. Cuoci, X.J. Li, The Design Of Ultra-Low NOx Critical Furnaces, in: The Eighth European Conference on Industrial Furnaces and Boilers, Portugal, 2008.

[20] Q. Tang, B. Adams, M. Bockelie, M. Cremer, M. Denison, C. Montgomery, A. Sarofim, D. Brown, Towards comprehensive CFD modeling of lean premixed ultra-low NOx burners in process heaters, in: Proceedings of the 17th Ethylene Producers' Conference, Atlanta, GA (United States), 2005, pp. 594-619.
[21] A. Habibi, B. Merci, G.J. Heynderickx, Multiscale modeling of turbulent combustion and NOx emission in steam crackers, AIChE J, 53 (2007) 2384-2398.
[22] G. Hassan, M. Pourkashanian, D. Ingham, L. Ma, P. Newman, A. Odedra, Predictions of CO and NOx emissions from steam cracking furnaces using GRI2.11 detailed reaction mechanism – A CFD investigation, Comput Chem Eng, 58 (2013) 68-83.
[23] Q. Tang, M. Denison, B. Adams, D. Brown, Towards comprehensive computational fluid dynamics modeling of pyrolysis furnaces with next generation low-NOx burners using finite-rate chemistry, Proceedings of the Combustion Institute, 32 (2009) 2649-2657.
[24] G. Lecocq, D. Poitou, I. Hernández, F. Duchaine, E. Riber, B. Cuenot, A Methodology for Soot Prediction Including Thermal Radiation in Complex Industrial Burners, Flow, Turbulence and Combustion, 92 (2014) 947-970.
[25] T. Lu, C.K. Law, Toward accommodating realistic fuel chemistry in large-scale computations, Prog Energ Combust, 35 (2009) 192-215.
[26] A. Cuoci, A. Frassoldati, A. Stagni, T. Faravelli, E. Ranzi, G. Buzzi-Ferraris, Numerical Modeling of NOx Formation in Turbulent Flames Using a Kinetic Post-processing Technique, Energ Fuel, 27 (2012) 1104-1122.
[27] C.J. Sung, C.K. Law, J.Y. Chen, Augmented reduced mechanisms for NO emission in methane oxidation, Combust Flame, 125 (2001) 906-919.
[28] P.A. Reyniers, C.M. Schietekat, D.J. Van Cauwenberge, L.A. Vandewalle, K.M. Van Geem, G.B. Marin, Necessity and Feasibility of 3D Simulations of Steam Cracking Reactors, Ind Eng Chem Res, 54 (2015) 12270-12282.
[29] S. Hoeven, B.J. Boersma, D.J.E.M. Roekaerts, Large Eddy Simulation of Turbulent Non-Premixed Jet Flames with a High Order Numerical Method, in: B. Koren, K. Vuik (Eds.) Advanced Computational Methods in Science and Engineering, Springer Berlin Heidelberg, 2010, pp. 269-287.
[30] M.R.H. Sheikhi, T.G. Drozda, P. Givi, F.A. Jaberi, S.B. Pope, Large eddy simulation of a turbulent nonpremixed piloted methane jet flame (Sandia Flame D), Proceedings of the Combustion Institute, 30 (2005) 549-556.
[31] J. Delville, S. Bellin, J.H. Garem, J.P. Bonnet, Analysis of Structures in a Turbulent, Plane Mixing Layer by Use of a Pseudo Flow Visualization Method Based on Hot-Wire Anemometry, in: H.-H. Fernholz, H.E. Fiedler (Eds.) Advances in Turbulence 2: Proceedings of the Second European Turbulence Conference, Berlin, August 30 – September 2, 1988, Springer Berlin Heidelberg, Berlin, Heidelberg, 1989, pp. 251-256.
[32] Turbulence Modeling Resource. https://turbmodels.larc.nasa.gov/index.html.
[33] R.W. Dibble, V. Hartmann, R.W. Schefer, W. Kollmann, Conditional sampling of velocity and scalars in turbulent flames using simultaneous LDV-Raman scattering, Exp Fluids, 5 (1987) 103-113.
[34] R.W. Schefer, Data Base for a Turbulent, Nonpremixed, Nonreacting Propane-Jet Flow, Combustion Research Facility, Sandia National Laboratories, Livermore, CA. www. sandia. gov/TNF, (1987).
[35] TNF Workshop. http://www.sandia.gov/TNF/abstract.html.
[36] V. Yakhot, S.A. Orszag, S. Thangam, T.B. Gatski, C.G. Speziale, Development of turbulence models for shear flows by a double expansion technique, Physics of Fluids A: Fluid Dynamics (1989-1993), 4 (1992) 1510-1520.

[37] T.-H. Shih, W.W. Liou, A. Shabbir, Z. Yang, J. Zhu, A new k-ϵ eddy viscosity model for high reynolds number turbulent flows, Comput Fluids, 24 (1995) 227-238.
[38] F.R. Menter, Two-equation eddy-viscosity turbulence models for engineering applications, Aiaa J, 32 (1994) 1598-1605.
[39] B.E. Launder, D.B. Spalding, The numerical computation of turbulent flows, Comput Method Appl M, 3 (1974) 269-289.
[40] C.D. Wilcox, Turbulence Modelling for CFD, DCW Industries, La Cañada, California, 1993.
[41] S.B. Pope, An explanation of the turbulent round-jet/plane-jet anomaly, Aiaa J, 16 (1978) 279-281.
[42] V. Raman, R.O. Fox, A.D. Harvey, Hybrid finite-volume/transported PDF simulations of a partially premixed methane–air flame, Combust Flame, 136 (2004) 327-350.
[43] ANSYS, ANSYS FLUENT User's Guide. Release 14.0, in, ANSYS, Inc, 2011.
[44] R. Barlow, J. Frank, Piloted CH4/Air Flames C, D, E, and F – Release 2.1 15-JUN-2007.
[45] R.R. Cao, S.B. Pope, The influence of chemical mechanisms on PDF calculations of nonpremixed piloted jet flames, Combust Flame, 143 (2005) 450-470.
[46] M. Scott, Evaluating Modified Diffusion Coefficients for the SST Turbulence Model Using Benchmark Tests, in: 41st AIAA Fluid Dynamics Conference and Exhibit, American Institute of Aeronautics and Astronautics, 2011.
[47] R.S. Barlow, J.H. Frank, Effects of turbulence on species mass fractions in methane/air jet flames, Symposium (International) on Combustion, 27 (1998) 1087-1095.
[48] C. Schneider, A. Dreizler, J. Janicka, E.P. Hassel, Flow field measurements of stable and locally extinguishing hydrocarbon-fuelled jet flames, Combust Flame, 135 (2003) 185-190.
[49] D. Lysenko, I. Ertesvåg, K. Rian, Numerical Simulations of the Sandia Flame D Using the Eddy Dissipation Concept, Flow, Turbulence and Combustion, 93 (2014) 665-687.
[50] P. Glarborg, M.U. Alzueta, K. Dam-Johansen, J.A. Miller, Kinetic Modeling of Hydrocarbon/Nitric Oxide Interactions in a Flow Reactor, Combust Flame, 115 (1998) 1-27.
[51] K.J. Hughes, T. Turányi, A.R. Clague, M.J. Pilling, Development and testing of a comprehensive chemical mechanism for the oxidation of methane, Int J Chem Kinet, 33 (2001) 513-538.
[52] H. Wang, X. You, A.V. Joshi, S.G. Davis, A. Laskin, F. Egolfopoulos, C.K. Law, USC Mech Version II. High-Temperature Combustion Reaction Model of H2/CO/C1-C4 Compounds, http://ignis.usc.edu/USC_Mech_II.htm, (May 2007).
[53] C. Bowman, R. Hanson, D. Davidson, W. Gardiner Jr, V. Lissianski, G. Smith, D. Golden, M. Frenklach, M. Goldenberg, GRI 2.11, Gas Research Institute, Chicago, IL, http://www.me.berkeley.edu/gri_mech/.
[54] G.P. Smith, D.M. Golden, M. Frenklach, N.W. Moriarty, B. Eiteneer, M. Goldenberg, C.T. Bowman, R.K. Hanson, S. Song, W.J. Gardiner, V.V. Lissianski, Z. Qin, GRI 3.0, Gas Research Institute, Chicago, IL, http://www.me.berkeley.edu/gri_mech/.
[55] J. Chen, Development of reduced mechanisms for numerical modelling of turbulent combustion, in: Workshop on Numerical Aspects of Reduction in Chemical Kinetics, 1997.
[56] C.J. Sung, C.K. Law, J.Y. Chen, An augmented reduced mechanism for methane oxidation with comprehensive global parametric validation, Symposium (International) on Combustion, 27 (1998) 295-304.
[57] T. Lu, C.K. Law, A criterion based on computational singular perturbation for the identification of quasi steady state species: A reduced mechanism for methane oxidation with NO chemistry, Combust Flame, 154 (2008) 761-774.

[58] Z. Luo, T. Lu, J. Liu, A reduced mechanism for ethylene/methane mixtures with excessive NO enrichment, Combust Flame, 158 (2011) 1245-1254.
[59] B. Magnussen, On the structure of turbulence and a generalized eddy dissipation concept for chemical reaction in turbulent flow, in: 19th Aerospace Sciences Meeting, American Institute of Aeronautics and Astronautics, 1981.
[60] I.S. ErtesvÅG, B.F. Magnussen, The Eddy Dissipation Turbulence Energy Cascade Model, Combust Sci Technol, 159 (2000) 213-235.
[61] S.B. Pope, Computationally efficient implementation of combustion chemistry using in situ adaptive tabulation, Combust Theor Model, 1 (1997) 41-63.
[62] Q. Tang, J. Xu, S.B. Pope, Probability density function calculations of local extinction and no production in piloted-jet turbulent methane/air flames, Proceedings of the Combustion Institute, 28 (2000) 133-139.
[63] R.S. Barlow, A.N. Karpetis, J.H. Frank, J.Y. Chen, Scalar profiles and NO formation in laminar opposed-flow partially premixed methane/air flames, Combust Flame, 127 (2001) 2102-2118.
[64] W.L. Grosshandler, RADCAL: A Narrow-Band Model for Radiation Calculations in a Combustion Environment, in, National Institute of Standards and Technology, 1993.
[65] T.F. Smith, Z.F. Shen, J.N. Friedman, Evaluation of coefficients for the weighted sum of gray gases model Journal of Heat Transfer, 104 (1982) 602-608.
[66] J.H. Frank, R.S. Barlow, C. Lundquist, Radiation and nitric oxide formation in turbulent non-premixed jet flames, Proceedings of the Combustion Institute, 28 (2000) 447-454.
[67] S. Naha, A.M. Briones, S.K. Aggarwal, EFFECT OF FUEL BLENDS ON POLLUTANT EMISSIONS IN FLAMES, Combust Sci Technol, 177 (2004) 183-220.
[68] R.V. Ravikrishna, N.M. Laurendeau, Laser-induced fluorescence measurements and modeling of nitric oxide in counterflow partially premixed flames, Combust Flame, 122 (2000) 474-482.

Chapter 6: Conclusions and perspectives

6.1 Conclusions

In this thesis, several important aspects for accurately modeling of the fire side of industrial steam cracking furnaces have been systematically studied via computational fluid dynamic (CFD) simulations.

As 75-90% of the heat transfer from the fire side to the process gas takes place via radiation, radiative heat transfer modeling was extensively studied. The most widely applied radiation model for simulating an industrial cracking furnace treats the flue gas radiative properties as gray, i.e. the absorption coefficient of the flue gas is assumed to be independent of the wavelength. This is a very rough approximation and deemed too inaccurate for large-scale combustion applications, leading to an underprediction of the flame temperature by up to 100 K. Several alternatives are available in literature: the non-gray radiative property methods that capture the variation of the flue gas radiative properties as function of the radiation wavelength. Due to their significantly higher computational cost, these non-gray models are less frequently used. To confirm the necessity of using a non-gray model in steam cracking furnace simulations, the impact of the flue gas radiative properties on heat transfer coupling between the furnace and reactor coils was quantified by analyzing the heat flux and coil outlet temperature (COT).

A nine-band non-gray flue gas radiative properties model was developed in Chapter 2 based on the exponential wide band model (EWBM) to account for the non-gray radiative properties of the major participating species in the flue gas, i.e. H_2O and CO_2. The model considers five

spectral windows that are fully transparent and four absorption bands at wavelengths of 2.7 μm (CO_2 + H_2O), 4.3 μm (CO_2), 6.3 μm (H_2O) and 15 μm (CO_2). It was validated using total emissivities calculated by Leckner's correlation and radiative heat transfer problems in a 2D rectangular enclosure with benchmark solutions using the statistical narrow band (SNB) model. Good agreement between the nine-band model and the benchmark solutions was observed. To decrease the computational cost, the nine-band model was reduced by combining the five spectral windows into one band, resulting in a five-band model with the same accuracy as the nine-band model, assuming that the emissivity of the radiating surfaces in the furnace is independent of the wavelength.

The impact of flue gas radiative properties on steam cracking furnace simulations was investigated by simulating an industrial ultra-selective conversion (USC) furnace using ANSYS Fluent 14.5 with the newly implemented non-gray five-band model and comparing it to a simulation implementing the well-known gray implementation of the weighted sum of gray gases model (WSGGM). Results showed significant differences between the two cases: the gray gas model predicts a 70 K lower flue gas outlet temperature compared to the non-gray gas model, resulting in a 3.6% higher thermal efficiency and 44 K higher average coil outlet temperature for the reactors. This indicates the necessity of using a model that accounts for the wavelength dependence of the flue gas radiative properties in simulating large-scale furnaces. The five-band model developed in the present work is able to provide reasonably accurate results at an acceptable computational cost.

In addition, the effect of the detailed floor burner geometry on the mixing and reaction of fuel and oxidizer streams has been studied as well. When simplifying the burner geometry by omitting the smallest-scale details, the predicted flame is wider and the location where the maximum flame temperature occurs, shifts upwards towards higher elevations in the furnace.

This eventually alters the distribution of the transferred thermal power, coil outlet temperature and production yields of ethene and propene over the reactor coils, even though the absolute values are in the same range when accounting for the detailed burner geometry. Therefore, despite the higher computational cost, the design details of the floor burners must be considered in the simulation of the full-scale furnaces.

Chapter 3 is dedicated to quantifying and mediating the uneven distribution of thermal power over the different reactor coils in a steam cracking furnace as a result of geometry factors such as burner position, shadow effects and asymmetry of the reactor coil layout. The furnace layout alone can induce a coil outlet temperature difference between different reactor coils up to 29 K. Differences are more pronounced if the feedstock is heavier. A direct consequence of this phenomenon is the difficulty in operating all reactor coils of a furnace at optimal conditions, i.e. the performance of the furnace is likely to be limited by only one of the many coils while all the other coils are not achieving their full potential in between subsequent decoking operations.

This has prompted the study of pass balancing, that is, adjusting the feedstock mass flow rate through individual coils in a reactor module. Coupled furnace-reactor CFD simulations were performed to evaluate four different feedstock flow distribution strategies: realizing equal values for a) coil outlet temperature, b) propene to ethene mass ratio, c) maximum coking rate, and d) maximum tube metal temperature over all the reactor coils in a module. Applying feedstock flow distribution on a per-coil level can effectively reduce the intra-module nonuniformities, resulting in a larger operating window and nearly 28% and 13% longer run length in a tube metal temperature constrained and a coil inlet pressure constrained scenario, respectively. Among the four studied schemes, the one with a uniform maximum coking rate, i.e. the case c, proved to be the best strategy. In optimal circumstances, the annual production

capacity of the USC furnace with a nameplate ethene capacity of 130 10^3 metric tons per year can be increased with 1000 metric tons for ethene and 730 metric tons for propene by applying feedstock flow distribution. However, as the coking rate cannot be measured on-stream in an industrial context, a uniform maximum TMT, which is strongly correlated to the maximum coking rate, is proposed as the best indicator for feedstock flow distribution. The optimal feedstock flow distribution is independent of the feedstock, although its effect is less significant if the feedstock is lighter. A so-called fixed heterogeneous distribution was proposed as a way to practically implement feedstock flow distribution in an industrial context. The principle of this method is to optimize the feedstock flow rate through different reactor coils in a module by adjusting the diameter of the venturi nozzles between the convection section and the radiant section in the design stage or when retubing the furnace. The combination of historically measured maximum TMT variations and detailed CFD simulation can offer a sufficiently reliable framework to determine the optimal feedstock flow distribution to maximize light olefin yields over the complete lifetime of the coils.

Based on the CFD model developed in Chapter 2, a fully coupled CFD-based run length simulation was performed for the first time, as described in Chapter 4. In contrast to the standalone run length simulation methodology, in which the total heat flux profile obtained from CFD simulation at start-of-run conditions is scaled uniformly over time to compensate for the decreased furnace efficiency, the CFD-based run length simulation methodology explicitly considers the thermal coupling of the fire side and reactors at each time step. Comparing the results obtained from different run length simulation methods showed that the standalone method underpredicts the run length of the USC cracking furnace by 12%. The reason is that the standalone method cannot not capture the intra-coil and inter-coil thermal

redistribution over time, which leads to a faster increase of maximum TMT and consequently shorter run length.

A disadvantage of the coupled CFD-based simulations is the high computational cost. To overcome this deficiency, a simplified method was developed which utilizes the incident radiative heat flux (IRHF) rather than the total heat flux on the reactor outer walls and correlates it to the flue gas bridge wall temperature obtained from an overall zero-dimensional heat balance. This IRHF-based method was shown to be able to provide similar accuracy (relative errors less than 0.5%) as the coupled CFD-based method but at a fraction of the computational cost, allowing to transfer these run length calculations from a high-performance computing environment to a high-end consumer machine. In addition, the generality of the IRHF-based method when changing operating conditions or feedstock compositions was demonstrated by comparing with coupled CFD-based run length simulations of a set of new cases, with relative errors in all comparisons well below 1%.

In Chapter 5, detailed combustion kinetics including NO_x chemistry were studied systematically, this is to develop a first principles based CFD model for the design and retrofit of ultra-low NO_x burners. Non-premixed turbulent combustion in a large-scale furnace is a process in which turbulence, radiation and chemical reactions are strongly coupled. Hence, each of the relevant sub-models has to be carefully examined first, so that in a second step all models can be grouped, to jointly model all the observed aspects taking into account the computational cost.

To validate the turbulence model, 2D simulations of a mixing layer flow and a non-reacting round jet flow of propane into co-flowing air were performed and compared with experimental data. A modified SST k-ω model allowed to accurately capture the turbulence characteristics of these flows. Different flue gas radiative property models were compared to

investigate the impact of radiative heat transfer in simulations of the well-known benchmark case Sandia flame D. The five-band model developed in Chapter 2 combined with the discrete ordinates model to solve the radiative transfer equation provided superior results compared to the weighted sum of gray gases model combined with the discrete ordinates model and an optical thin model. Four combustion mechanisms, referred to as ChenCH4, ARM2, Lu21 and C1C2NO, were tested for the Sandia flame D case as well. The simulation results show that ChenCH4 and ARM2 provide excellent agreement between the measured and calculated NO emissions. Combining and applying all of the validated sub-models will allow to perform accurate CFD simulations for the design and retrofit of ultra-low NO_x burners in steam cracking furnaces.

6.2 Perspectives

This work aims to construct a comprehensive CFD-based model for simulating industrial steam cracking furnaces. The ultimate goal of this modeling framework is to fulfill the requirements of developing, testing and verifying new technologies designed to improve furnace thermal efficiency, to increase production of light olefins, and to reduce NO_x emission. To this end, future research work should focus on several aspects outlined below.

There is a continuous concern about improving the energy and exergy efficiency of steam cracking furnaces motivated by both financial and environmental considerations. As heat transfer from the fire side towards the reactor coil surface is dominated by radiation, applying high emissivity coatings on the external surface of the reactor coils and on the refractory walls seems a promising way of improving furnace efficiency. However, this requires the non-gray radiative properties of both flue gas and solid surfaces to be well-known and modeled accurately. Although the five-band non-gray gas radiative properties model developed in Chapter 2 combined with the discrete ordinates model to solve the radiative transfer equation

proved to be suitable to describe industrial applications, it treats the solid surfaces of the furnace as gray, i.e. with a constant emissivity independent of the wavelength. This approximation is too rough when high emissivity coatings are of interest, hence the current modeling framework should be extended to consider more emission bands and provide temperature and wavelength dependent values for the emissivity of radiating surfaces, both for the reactor coils and the furnace refractory.

Another drawback of the five-band non-gray model is that the upper and lower limits of each spectral region are fixed and corresponding to an absorption band of a real species as defined in the exponential wide band model (EWBM). This feature makes extending the model to include one or more additional bands of a real species inherently tedious as it will lead to at least one additional spectral region in the model, which inevitably increases the computational cost. The currently considered species H_2O and CO_2 have some absorption bands which are only of considerable importance at either higher or lower temperatures and are hence not included in the present model. However, CH_4, CO and NO are also participating species which have several absorption bands that may have some impact on the local flame temperature. In light of this, a non-gray gas radiative properties model for the flue gas with the flexibility to include or exclude contributions from some absorption bands and/or species when necessary would be welcome. Ideally, the computational cost of this model should not be affected by the contributions that are added or neglected. Such a model can be developed using the concept of the weighted sum of gray gases model (WSGGM). Currently the most widely used WSGGM only considers H_2O and CO_2 as participating species and was validated against total emissivity data in a limited range of H_2O and CO_2 ratios. Therefore the new non-gray model should not only consider additional species such as CH_4, CO and NO, but should

also be valid in a wide application range, which will allows to apply it to study radiative heat transfer problems at different scenarios.

One important discrepancy between the current simulation and industrial measurement is the percentage of radiation contribution to the total transferred energy. This value is typically around 90% in radiant section of steam cracking furnaces, however, the CFD simulation in the present work shows that radiation accounts for only 80 - 82% of the total transferred energy. Literature survey indicates that this underprediction may be caused by soot formation and turbulence-radiation interaction (TRI), both of which were not taken into account in the model developed in the present work. It is reported that soot formation in gas fired furnace will result in 5% - 40% more emission depending on the type of the fuel. In addition, TRI is able to increase emission from the flames by 30% - 60%. As heat transfer inside steam cracking furnaces is dominated by radiation, the effect of soot and TRI on furnace simulation will be significant not only in the ratio of radiative heat flux to the convective heat flux, but also in the thermal efficiency of the radiant section. Therefore implementing models for soot formation and TRI in CFD calculation, which will improve the modeling framework, is also an interesting topic for future research.

Due to the increasingly stricter environmental regulations in the past two decades, and even stricter ones in the coming decades, NO_x reduction has become another important aspect in furnace design and operation. The common practice is to design ultra-low NO_x burners using technologies such as staged fuel/air, air preheat and flue gas recirculation. For burner design and retrofit aided by CFD simulations, sophisticated models that are able to account for interactions between turbulence, radiation and chemical reactions are required. The present work has shown that Reynolds-averaged Navier-Stokes (RANS) simulations can provide satisfactory results for important first order characteristics such as the mean temperature,

mean flue gas velocity and mean species concentration. However, turbulent fluctuations of velocity, temperature and species concentrations have a considerable impact on the behavior of the flame and thus the prediction of NO_x. This is because the time-averaged reaction rate is not necessarily equal to the reaction rate calculated from the time-averaged temperature and species concentrations. Hence, the so-called turbulence-chemistry and turbulence-radiation interactions should be considered. In addition, swirl flow has been widely studied in recent years and is considered as a promising technologies to reduce NO_x emission. There is a broad consensus in the scientific community that the characteristics of this type of flow cannot be captured accurately by two-equation RANS simulations where the Boussinesq approximation is applied, i.e. the Reynolds stresses are assumed to be isotopic and a local equilibrium exists between stress and strain.

Large eddy simulation (LES) has a great potential in mitigating the foregoing limitations of the RANS approach. Many studies of complex turbulent combustion problems have used LES yielding quite accurate results. However, performing LES for large-scale industrial furnaces is prohibitively expensive and may not be feasible or sufficiently efficient for routine simulations necessary during the design and validation stages of new burner design. A compromise would be to carry out furnace simulation using hybrid LES-RANS methods, in which LES is performed for the free turbulent flow region where the combustion occurs to obtain accurate results of flame temperature and NO_x emission, while the near wall region is modeled using RANS to reduce the computational cost. Another solution is to combine RANS to resolve the average flow field with presumed probability density functions to describe the probability distribution of flow characteristics such as temperature or species concentrations. It is also interesting to study the performance of diffusion flamelet model in describing the turbulence-chemistry interactions for complex combustion problems.

Beside the foregoing technologies, oxy-fuel combustion, i.e. burning a fuel using pure oxygen instead of air as the oxidizer, also has a high potential to reduce NO_x emissions compared to traditional combustion processes with air as oxidizer. The formation of NO_x in oxy-fuel combustion is limited due to the lack of nitrogen inside the oxidizer stream and the removal of recycled NO_x through re-burn reactions. Another advantage of oxy-fuel combustion is the production of a highly concentrated stream of CO_2, ready for carbon capture and storage (CCS). Applying this technology requires extensive study of the flame behavior and validation of combustion kinetics under pure oxygen conditions. Moreover, as oxy-combustion is associated with very high temperatures, efforts should be made regarding burner design so as to achieve the desired recirculation rate of flue gases, hence diluting the fresh fuel, limiting the maximum reaction rate and reducing the maximum temperature inside the furnace. Finally, due to the much higher concentration of H_2O, CO_2, and CO, a new flue gas radiative properties model which considers the non-gray properties of these species at high partial pressure is needed.

Appendix A: Discrete number and Ray effect

In a spherical coordinate system, the position of a point is specified by three numbers: the radial distance, the polar angle θ and the azimuth angle φ. For the radiation emitted from a single point to a hemisphere, the incident radiation in each direction has the unit of $w/m^2 \cdot sr$, where sr is solid angle and can be considered as the surface that a pencil of ray reaches on a unit hemisphere. As shown in Figure A-1, the area $dA = R\sin\theta\, d\varphi \cdot Rd\theta$, so the solid angle for a certain pencil of ray can be calculated as follows.

$$\int_{\varphi_1}^{\varphi_2}\int_{\theta_1}^{\theta_2} \sin\theta\, d\varphi \cdot Rd\theta \tag{A.1}$$

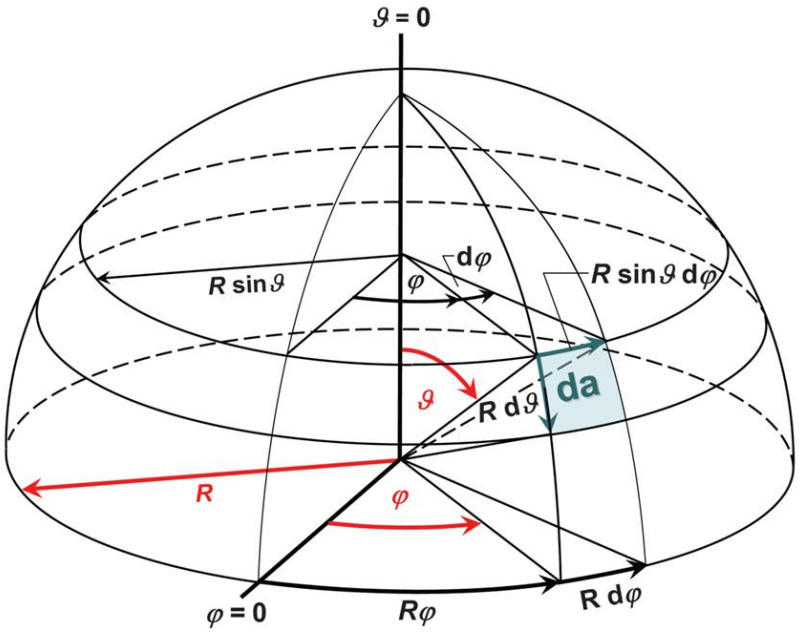

Figure A-1: Scheme of calculating a solid angle

For a hemisphere, $\theta = \frac{\pi}{2}$ and $\varphi = 2\pi$, thus the integration of the above equation is 2π. Ordinates in terms of the polar angle θ and the azimuth angle φ are equaled discretized in DO model implemented in FLUENT, in order to get the total incident radiation I from individual incident radiation I_i, a weight factor w_i for has to be multiplied to the corresponding directional incident radiation.

$$I = \sum_{i}^{n} I_i w_i \tag{A.2}$$

In a three-dimensional problem, FLUENT discretizes each octant into $M \times N$ solid angles, where M and N are the user specified number of individual directions for θ and φ respectively. The more discrete solid angles, the more accurate results of the radiative heat transfer calculation. However, as computational cost in terms of disk space requirements for the data file increase dramatically with the discrete number, it is necessary to evaluate the effect of the numbers of solid angles on furnace simulation results and the computational cost. A sensitivity study was performed using three difference discrete numbers: $M \times N = 2 \times 2$, 4×4 and 6×6, which are referred to as "DO22", "DO44" and "DO66" cases respectively in the following discussion. The heat flux profile calculated using different discrete numbers are depicted in Figure A-2. It is observed that there is a clear ray effect in the DO22 case, leading to over- or under-prediction of the heat flux comparing to the DO44 and the DO66 cases. On the other hand, the differences in heat flux profiles between the latter two cases are much less significant, indicating that a discrete number of 4×4 is sufficient to remedy the influences of ray effect on radiative heat transfer calculations in the furnace. Moreover, comparison of the heat flux profiles of all reactors show that the ray effect results in larger variation of total transferred thermal power within a group of reactor coils for the DO22 case comparing to the other two cases.

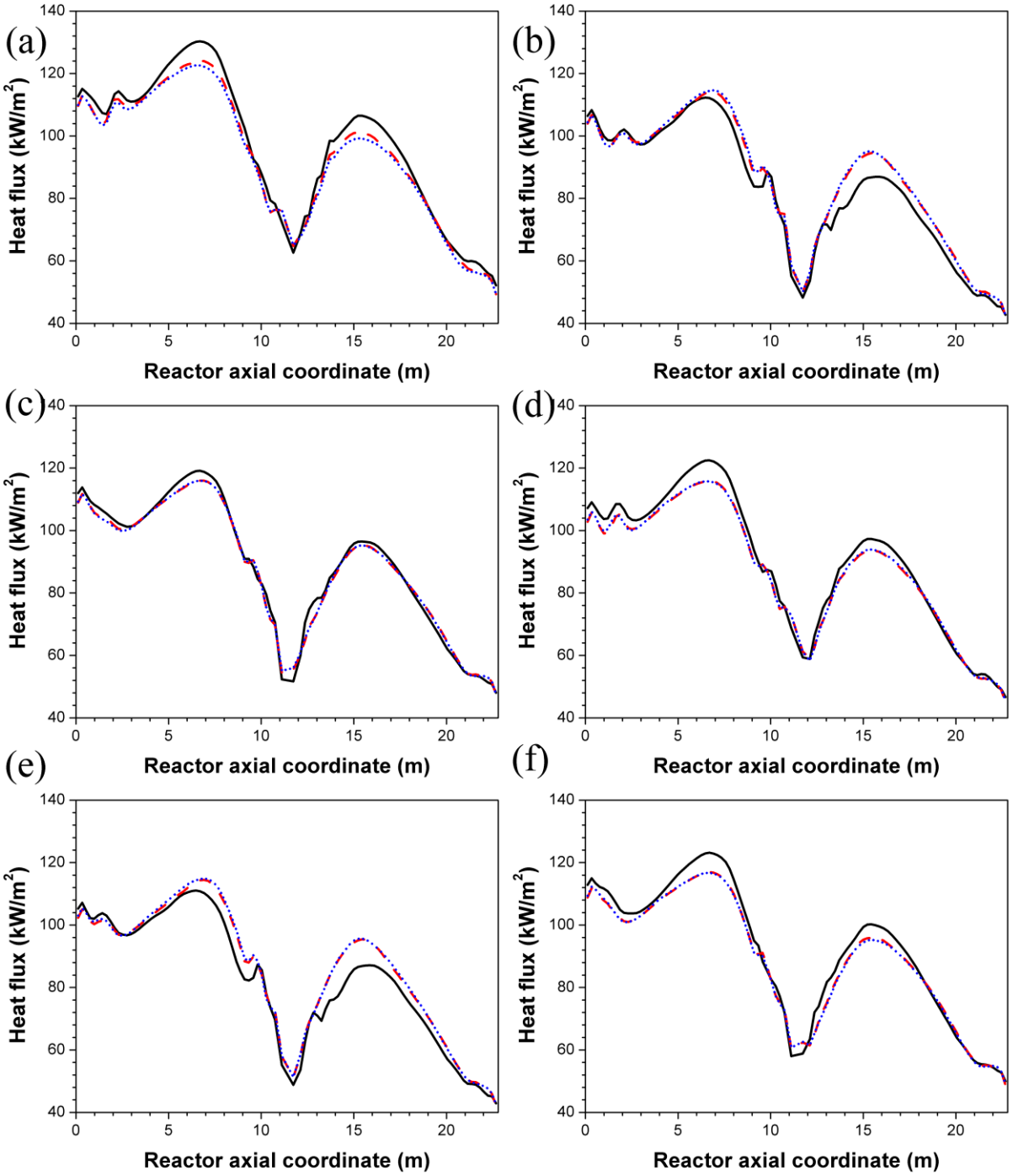

Figure A-2: Heat flux profile as a function of the reactor axial coordinate for reactor (a) NO.1, (b) NO.5, (c) NO.9, (d) NO.13, (e) NO. 17, (f) NO. 21. ——— – DO22 case; – – – – DO44 case; ····· – DO66 case.

Despite of the higher accuracy and less ray effect in the DO44 and DO66 cases, they were not used in the present paper due to the huge disk space requirement. As shown in Table A-1, the size of the DO44 case is nearly 3.5 times larger than that of the DO22 case, making post-processing of the results extremely difficult and time-consuming on local clusters. For the sake of saving computational resources, discrete number of 2×2 was used in all furnace calculation throughout this thesis. Although the downside is that the results have to suffer from a certain degree of ray effect, the overall furnace thermal efficiency does not change much in all these cases and the difference in mixing-cup P/E is still acceptable. Therefore the DO22 case can be considered as a good compromise between the computational cost and the simulation accuracy.

Table A-1: Results of furnace calculation with different discrete number.

Case	DO22	DO44	DO66
$\boldsymbol{M \times N}$	2×2	4×4	6×6
Size of data file (GB)	21	72	155
Heat absorbed by all reactor coils (kW)	6588.8	6580.4	6580.5
Mixing-cup P/E	0.5988	0.6076	0.6084

Appendix B: Calculation of molecular viscosity using kinetic theory

For molecular viscosity calculation using kinetic theory, the following four assumptions were made:

(1) The gas is sufficiently dilute for only binary collision to occur, i.e. the behavior of the gas mixture can be considered as ideal gas;

(2) The motion of the molecules during a collision can be described by classical mechanics;

(3) Only elastic collisions occur;

(4) The intermolecular potential function is spherically symmetric.

With these restrictions, molecular viscosity μ can be estimated using the following expression.

$$\mu = 2.67 \times 10^{-6} \frac{\sqrt{M_w T}}{\sigma^2 \Omega_\mu} \tag{B.1}$$

Where the collision diameter σ and the collision integral Ω_μ must be found. The latter is usually obtained as a function of a dimensionless temperature T^* which depends on the intermolecular potential chosen. For any potential curve, the dimensionless temperature T^* is related to the minimum of the pair-potential energy ε by the following equation.

$$T^* = \frac{T}{(\varepsilon/k_B)} \tag{B.2}$$

Where $k_B = 1.38 \times 10^{-23}$ is the Boltzmann's constant. σ and ε/k_B are the Lennard-Jones parameters for each species (see Table B-1). The collision integral Ω_μ can be estimated by the following empirical equation.

$$\Omega_\mu = [A(T^*)^{-B}] + C\left[e^{(-DT^*)}\right] + E\left[e^{(-FT^*)}\right] \quad \text{(B.3)}$$

Equation (B.3) is applicable from $3 \leq T^* \leq 100$ with an average deviation of only 0.064%. The model constants are listed in Table B-2.

Table B-1: Lennard-Jones parameters for different gas species.

Name	σ (Å)	ε/k_B (K)	Name	σ (Å)	ε/k_B (K)
AR	3.330	136.50	C_2H_4	3.971	280.80
N_2	3.621	97.53	C_2H_5	4.302	252.30
C	3.298	71.40	C_2H_6	4.302	252.30
H	2.050	145.00	HCCO	2.500	150.00
O	2.750	80.00	CH_2CO	3.970	436.00
OH	2.750	80.00	CH_2CHO	3.970	436.00
HO_2	3.458	107.40	CH_2OCH_2	4.760	252.00
H_2	2.920	38.00	a-C_3H_4	4.760	252.00
H_2O	2.605	572.40	a-C_3H_5	4.760	252.00
H_2O_2	3.458	107.40	C_3H_6	4.982	266.80
O_2	3.458	107.40	n-C_3H_7	4.982	266.80
CH_3	3.800	144.00	i-C_4H_8	5.176	357.00
CH_4	3.746	141.40	N	3.298	71.40
HCO	3.590	498.00	NO	3.621	97.53
CH_2O	3.970	436.00	NO_2	3.500	200.00
CH_3O	3.970	436.00	HCNO	3.828	232.40
CH_3OH	3.626	481.80	HNCO	3.828	232.40
CO	3.650	98.10	NH_3	2.920	481.00
CO_2	3.763	244.00	NCO	3.828	232.40
C_2H_2	4.100	209.00	HCN	3.828	232.40
C_2H_3	4.100	209.00	CH_3O_2	3.626	481.80

Table B-2: Model constants of the empirical equation for collision integral calculation.

A	B	Cc	D	E	F
1.16145	0.14874	0.52487	0.77320	2.16178	2.43787